University of Southampton

ASTRONAUTICS AND AERONAUTICS DEPARTMENT

SCHOOL OF ENGINEERNG SCIENCES

Microthrusters Based on the T5 and T6 Hollow Cathode

by

Angelo Niko Grubišić

Thesis submitted in partial fulfillment of the
requirements for the degree of Doctor of Philosophy

December, 2009

UNIVERSITY OF SOUTHAMPTON

ABSTRACT

SCHOOL OF ENGINEERING SCIENCES
ASTRONAUTICS AND AERONAUTICS

Doctor of Philosophy

MICROTHRUSTERS BASED ON THE T5 AND T6 HOLLOW CATHODES
by ANGELO NIKO GRUBISIC

Small spacecraft with limited on-board resources would benefit greatly from the development of a low power, low cost microthruster able to offer propellant savings over conventional alternatives and enable higher energy missions. Such a thruster would also be beneficial in the development of all-electric spacecraft whereby the normally separate reaction control system and primary electric propulsion system were able to operate from a common propellant management system.

In recent years experiments on a T6 hollow cathode have demonstrated the possibility of such a device however the performance, in particular thrust efficiency, falls far short of what would be termed a viable thruster. Nevertheless the means by which hollow cathode discharges are able to produce thrust corresponding to very high velocity propellants is not at all understood, nor is the means by which to improve performance. The relevance of the very high energy ion signatures typical of hollow cathode discharges, synonymous with hollow cathode erosion, has also not been established.

Indirect thrust measurements were made at the University of Southampton on two separate types of hollow cathode, derived from the T5 and T6 gridded ion thrusters, with unique design modifications, primarily of anode geometry. Testing was conducted with argon and xenon and measurements were made via a deflected pendulum micro-thrust balance and supporting architecture constructed specifically for the work. Ion energy measurements were made using a hemispherical energy analyzer in a separate experiment at NASA Jet Propulsion Laboratory on a third XIPS cathode, derived from the XIPS 25cm ion thruster, with xenon and krypton.

These measurements provided unique insight into the influence of terminal parameters such as discharge current, mass flowrate and cathode/anode geometry on thrust production and downstream ion energy distributions. Significant improvements in thrust efficiency have been made with the T5 cathode and in doing so, have taken hollow cathodes a significant step forwards as a viable and competitive propulsion technology.

An analysis of the thrust production is made, and on this basis conclusions are drawn on the existence of electrothermal, electromagnetic and electrostatic mechanisms specific to the cathode and operating regime, as well as their roll in other associated hollow cathode phenomenon. The main conclusions of the work are presented and recommendations made for future experimental work.

ACKNOWLEDGEMENTS

Within the University of Southampton the Author would like to thank his supervisor Prof. Stephen Gabriel for his unwavering confidence, valuable guidance, discussions and support over the past 3-years, technicians Zondy Webber, Simon Klitz and Brian Clarke and also Graham Roberts for valuable feed back at various stages throughout the PhD. Thanks to Cheryl Collingwood for the patience and kindness to proof read the final thesis.

The Author is very grateful to Neil Wallace of QinetiQ Space Exploration Technologies Division for in donating essential hardware and materials early on in the PhD. The author would like pay particular recognition to the late David Fearn who dedicated extensive time to the Author in recalling his past experience on hollow cathodes. David demonstrated unparalleled knowledge, skills and modesty; he was truly one of the greats of advanced propulsion.

Within NASA Jet Propulsion Laboratory the author would like to thank Jay Polk for hosting him with the JPL Advanced Propulsion Group during the PhD and for dedicating extensive time for discussion on all aspects of ion propulsion. Al Owens, Ray Swindlehurst, and Dan Goebel of were also of great support.

Eternal thanks also to my family, particularly Karina, Anita and Milan Grubisic, who have never faltered in their support. Finally thanks to my late grandfather Thomas Richardson, who set me on this path a long time ago by teaching me how to question the world, but also to take a look around occasionally and admire it for what it is.

CONTENTS

LIST OF FIGURES

LIST OF TABLES

NOMENCLATURE

A	Area, m^2
A_R	Richardson constant, $1.201x10^6$ $A \cdot m^{-2} \cdot K^{-2}$
d	Distance, m
e	Electron charge, 1.602×10^{-19}C
E	Electric field, $V \cdot m^{-1}$
f	View factor
F	Thrust, N
g_0	Gravitational constant, $9.81 m \cdot s^{-2}$
G_{dBm}	Gain, expressed in dBm
h	Planck's constant, 6.626 x 10^{-34} J.s
I_{ci}	Critical ionization current, A
I_{sp}	Specific impulse, s
I	Current, A or moment of inertia, $kg \cdot m^2$
j	Discharge current, A
J	Current density, $A \cdot m^{-2}$
k	Boltzman's constant, 1.381 x 10^{-23} $J \cdot K^{-1}$
K_n	Knudsen number
K_e	Kinetic Energy, J
L	Characteristic length, m or Inductance, H
M	Particle mass, kg
m	Mass, kg
$\dot{m}$	Mass flow rate, $kg \cdot s^{-1}$
n	Particle density, m^{-3}
N	Number or particles
p	Internal cathode pressure, $N \cdot m^{-2}$
P	Power, W

q	Heat flux, W
R	Resistance, Ohms
R_{sp}	Specific gas constant, $J \cdot kg^{-1} \cdot K^{-1}$
R_e	Reynolds number
R_{ct}	Ratio of the L_{cog} to the L_{cot}
r	Radius, m
t	Time, s
T	Thrust, N or Temperature, K
T_p	Period, s
v	Velocity, $m \cdot s^{-1}$
V	Voltage, Volts or Volume, m^{-3}
x_0	Peak amplitude
x_n	Peak amplitude n periods away

Greek letters

α	Degree of ionisation or
α_a	Angular acceleration, $rads \cdot s^{-2}$
β	Angle of reflection, rads
B	Magnetic flux density, T
γ	Ratio of specific heats
ε	Electromotive force, dW/dq
ε_i	Ionisation potential, eV
ε_0	Permittivity of free space, 8.85 x10-12 $F \cdot m^{-1}$
ε_A	Anode emissivity
λ_d	Debye length, m

ρ	Resistivity, Ohms-m or density, kg·m^{-3}
ς	Damping ratio
δ	Logarithmic decrement
σ	Electrical conductivity, Ohms·m^{-1}
ϕ	Work function, eV or phase, rads or flux
θ	Angle, rads
τ	Torque, N·m
Λ	Plasma parameter
μ	Efficiency
μ_0	Permeability of free space, $4\pi\times10^{-7}$ N·A^{-2}
ω	Angular velocity, rads·s^{-1}
ω_0	Natural frequency, rads·s^{-1}

Subscripts

A	Anode
b	Burn time or thrust balance
c	Cathode
crit	Critial
cb	Counter balance
cot	Centre of thrust
cw	Counterweight
cp	Calibration point
cg	Centre of gravity
C	Cathode
d	Debye or downstream
D	Discharge
em	Emitter
eff	Effective
eq	Equivalent
ex	Exit
f	Fall or final
h	Heater or horizontal component
i	Ions or initial
ins	Insert
k	Keeper electrode
m	Measured
max	Maximum
n	Neutral
oh	Ohmic
or	Orifice
p	Pressure or plasma
pa	Path
prop	Propellant
r	Radiative
s	Static, surfaces or sensor
se	Sensor
sat	Satellite
th	Thermionic
Th	Thrust line
T	True
tot	Total
u	Upstream
v	Vertical component
xe	Xenon

Units: This thesis uses mks units of the Système International D'unités (SI) with the exception that energies are frequently given in terms of electron volts (eV). Sccm ≡ Standard Cubic Centimeters per Minute. For xenon: 1 sccm ≈ 0.09839 mg/s at STP.

CHAPTER 1

INTRODUCTION

1.1 MOTIVATION FOR RESEARCH

The research presented in this thesis focuses on improving the known performance of hollow cathodes as microthrusters in terms of achievable thrust efficiency and specific impulse while lowering total power requirement. This has been done by designing and testing novel configurations of the T5 and T6 hollow cathodes (HC). These particular cathodes are a mature technology developed extensively over the last 35-years for application on the UK-10, UK-25, T5 and T6 gridded ion thrusters [1] [2] [3] [4] [5] [6] and as an electron source for various ion beam neutralization applications.[7] Previous experiments on a T6 discharge cathode at the University of Southampton by Gessini found that usable thrust (1-2mN) could be generated with reasonable specific impulse (up to <300s with xenon) but with power requirements sometime exceeding 1kW. [8] [9] [10] While ISP values are encouraging, associated thrust efficiencies are overwhelmingly low (<0.5%). Such high power requirement and extremely poor efficiency currently makes the application of hollow cathodes impractical. Operation at high specific impulse was also accompanied by large discharge voltages and voltage fluctuations in a transition to a life limiting plume mode.[3] Such ISP performance has however strengthened interest in the use of all-electric propulsion systems composing high specific impulse primary electric propulsion augmented by a HC microthruster reaction control system (RCS).[11] For some missions such a configuration presents considerable mass savings over configurations where the attitude and orbit control system (AOCS) comprises both a chemical RCS and primary electric system, primarily through the sharing of a common propellant bus and power processing subsystems but also through the potentially high specific impulse of the RCS. While secondary chemical RCS systems constitute a relatively large fraction of the overall propulsion system mass[12] [13] [14] [15] these systems also bring substantial expenditure in manufacture, assembly, integration, testing and launch preparation due to the use of hazardous propellants.[16] Attempts to scale down electrostatic and electromagnetic thrusters for such a role have however yielded poor performance, primarily due to high wall loss from the higher surface area to volume ratios, and warrant a more adequate solution.

1.2 NOVELTY AND OBJECTIVES OF THE CURRENT RESEARCH

If hollow cathodes are to have a practical application they must be developed to show higher thrust efficiencies, lower discharge noise and lower power requirements while being able to contend with other propulsion systems such as resistojets and hall thrusters in terms of performance. The goal of this work was to satisfy these criteria and in doing so take hollow cathode thrusters a step further towards technological readiness. Methods by which to improve performance were however unclear since thrust mechanism in HC's was not understood and the influence of factors such as anode geometry in particular on HCT's had not been established.

A number of steps were taken in order to perform this work:

1. A micro-thrust balance and supporting architecture was developed for the accurate measurement of micro-to-milli-Newton thrust levels. The previous inherited system suffered a number of technical problems which limited thrust resolution, gave large uncertainties at low thrust levels and suffered dramatically from thermal drift.[17] It was seen as necessary to develop a new system which was able to give more reliable data.

2. The mechanisms which govern discharge voltage and the operating mode were identified in order to direct the design for improved performance accordingly. A variant on the T6 neutralizer cathode utilizing a conical diverging anode was consequently developed, built and thrust performance was characterized. The influence of terminal parameters such as discharge current, mass flowrate on thrust production was established.

3. An analysis was made of the various loss mechanisms in hollow cathode thrusters and a lower current T5 cathode was identified as a more ideal candidate microthruster. A T5 hollow cathode (STRV-1A flight spare neutralizer) was then acquired and characterized using the micro-balance. The T6 conical anode was developed for the T5 in an effort to increase specific impulse and thrust efficiency.

4. In an attempt to understand the relationship between the existence of high energy ion populations in hollow cathode discharges and the likely thrust production mechanisms, ion energy measurements were conducted at NASA Jet Propulsion Laboratory on a ¼ inch Xenon Ion Propulsion System (XIPS) cathode (discharge cathode to the 16-cm L3 Electron Technologies ion thruster) with a similar geometrical configuration to the T6LA cathode design. An analysis of the thrust and ion energy measurement data was made in order to determine the possible thrust mechanisms responsible for high specific impulse from the T5 and T6 hollow cathodes at low flowrates.

5. Finally, recommendations were made on the further steps necessary for hollow cathode thruster technology development.

1.3 BENEFITS OF ELECTRIC PROPULSION

This section discusses the propulsion options available for satellites, reviews the definitions of rocket propulsion and outlines the impetus for hollow cathode thruster development.

In all rocket engine type propulsion systems, a working fluid is expelled from the system at high velocity. Through the conservation of momentum, a resulting reaction force acts on the system to produce thrust, thus propelling the spacecraft. The method by which the acceleration of the working fluid is achieved defines and encapsulates the subject of rocket propulsion. The origin of this energy to be transferred into the working fluid can be either be potential (pressure storage), chemical, electrical or nuclear. The means by which conversion of this energy into directed kinetic energy is the fundamental basis of rocket engine design.

The propulsion systems of interest for satellites are:

1. Cold-gas thrusters
2. Solid rocket motors
3. Monopropellant engines
4. Hybrid engines
5. Liquid bi-propellant engines
6. Augmented cold/hot gas thrusters
7. Thermoelectric propulsion
8. Electromagnetic propulsion
9. Electrostatic propulsion

Conventional Propulsion

Electric Propulsion

Within the electric propulsion domain electric thrusters are generally classified into:

Electrostatic	Electromagnetic	Electrothermal
Gridded ion	Magnetoplasmadynamic	Resistojet
Colloid ion	Steady state vs Quasi steady	Electrothermal hydrazine
Contact ion	Self-field vs Applied-field	Microwave electrothermal
Field Emission (FEEP)	Pulsed plasma	Pulsed electrothermal Arcjet, DC vs AC vs Pulsed
Microwave or RF ion	Helicon plasma	Steady state vs Quasi steady
Plasma separator ion	Inductive pulsed plasma	Self-field vs Applied-field
Hall Effect (SPT, TAL)	Electron-cyclotron-resonance	Pulsed plasma
	Variable specific-impulse plasma	Helicon plasma

In all the above systems, if the mass of the spacecraft is defined as m and the mass flowrate of propellant is defined as:

$$\frac{\partial m}{\partial t} = \dot{m}$$

If the effective exhaust velocity is defined as v_{ex} then the thrust produced by any system is given by:

$$F = \frac{\partial m}{\partial t} v_{ex}$$

(1.1)

The effective exhaust velocity is simply a measure of the thrust efficiency of the propulsion system. If the velocity of the spacecraft is defined as v_{sat}, then the thrust from the engine will give a rate of change of velocity given by:

$$m_{sat} \frac{\partial v_{sat}}{\partial t} = -\frac{\partial m}{\partial t} v_{ex}$$

(1.2)

Considering the initial and final masses of the spacecraft, m_i and m_f respectively, and rearranging Equation 1.2 to make:

$$\partial v_{sat} = -v_{ex} \frac{\partial m}{m}$$

(1.3)

Integration of the above equation gives:

$$\int_0^{\Delta v} \partial v_{sat} = -v_{ex} \int_{m_i}^{m_f} \frac{\partial m}{m}$$

(1.4)

$$\Delta v = v_{ex} \ln\left(\frac{m_i}{m_f}\right)$$

(1.5)

Or equivalently,

$$m_f = m_i e^{-\Delta v / v_e}$$

(1.6)

As a result the classical Tsiolkovsky equation is derived from impulse conversation law. By knowing the exhaust velocity and the total Δv required, one can define the relative mass fractions and thus fuel load. The specific impulse (ISP) is commonly used to describe the performance of any one engine/thruster by defining the quantity of impulse achieved per unit weight of propellant. Alternatively, it is the time any one system could theoretically produce 1N of thrust with 1kg of propellant.

$$I_{sp} = \frac{t_b F}{m_{prop} g_o}$$

(1.7)

A useful comparison when comparing propulsion systems is the density ISP term. This gives the performance of a system in terms of compactness and is given by:

$$\rho_{sp} = \rho_{prop} I_{sp}$$

(1.8)

Since the specific density term is dimensionless, this gives units of seconds. Hence for a higher density ISP a system will have a lower propellant volume than a low density ISP system. This is an important parameter for small satellites where volume is generally more of a constraint than mass.

If we rearrange Equation 1.7 to give:

$$F = I_{sp} g_0 \frac{\partial m}{\partial t}$$

(1.9)

It can be seen that the effective exhaust velocity is related to the specific impulse through:

$$v_{ex} = I_{sp} g_0$$

(1.10)

Ultimately high specific impulse systems require much lower propellant fractions presenting significant savings on launch mass and volume. Conventional propulsion systems [propulsion options 1-6] are fundamentally limited by the amount of potential or chemical energy that can be stored in the working fluid for conversion to kinetic thrust. Since electric propulsion systems 7-9 rely on the conversion of electrical energy (either solar, radioisotope or nuclear source) to the working fluid they have the advantage of being able to generate much higher specific powers (energy invested per unit mass of propellant) than conventional propulsion systems. The velocity of a working fluid bares the relationship to its kinetic energy:

$$v = \sqrt{\frac{K_e}{2M}}$$

(1.11)

Thrust efficiency is defined as the ratio of transfer of kinetic energy to the propellant in relation to the operating power:

$$\mu_T = \frac{\dot{m} v_{ex}^2}{2P_{tot}}$$

(1.12)

It follows that,

$$\mu_T = \frac{1}{2}\frac{F}{P_{tot}}\frac{F}{\dot{m}}$$

(1.13)

$$\mu_T = \frac{F^2}{2P_{tot}\dot{m}}$$

(1.14)

In Equation 1.13 the quantity F/P_{tot} is the thrust to power ratio, an important figure of merit in thruster performance. From Equation 1.12 it can be seen that for constant increase in ISP the input power follows a quadratic relationship. Electric propulsion systems, which generally have exhaust velocities > 5km/s, are therefore inherently low thrust due to limited power availability. As a result of governing Equations 1.9, 1.12 and 1.13, Figure 1 shows the attainable thrust to power ratios given the specific impulse and total efficiency of a propulsion system and describes the general position of electric thrusters. This shows that high specific impulse is energetically only achievable at the loss of thrust to power ratio and also stresses the importance of total efficiency in providing useful thrust levels at reasonable power. Electric propulsion systems are therefore generally said to be power limited which brings important considerations in their application.

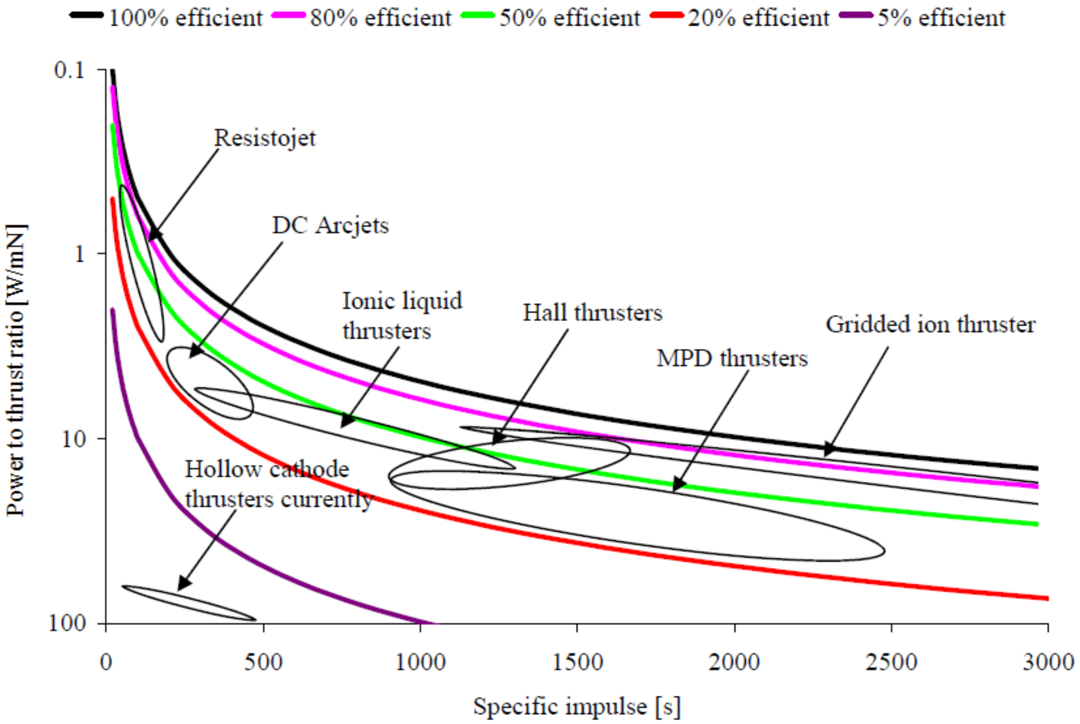

Figure 1 General thruster spectrum based on power to thrust to power ratio, specific impulse and efficiency [Thruster data from[18,19,20,21,22]]

The current placement of hollow cathode thrusters within the thruster spectrum based on the work of Gessini is shown in Figure 1. The comparison shows that although HC thrusters to date have demonstrated exit velocities 1-5 km/s, comparable with resistojets, arcjets and ionic liquid thrusters, their use at a mission level is compromised by inefficiency, which manifests itself as an increase in the power to thrust ratio. To warrant the development of future hollow cathode thrusters they must be able to show power to thrust ratios ~1W/mN and >100s specific impulse to be competitive with resistojets and ~10W/mN with >250s to compete with ionic liquid thrusters and DC arcjets. It should be noted that this involves in some cases increasing the efficiency of HCT's by two orders of magnitude.

1.4 COMPETING TECHNOLOGIES

Many investigations[23-36] have been conducted in the scaling of conventional electric propulsion systems to the level of microthrusters recognizing that current microsatellite platforms however lack the resources to support advanced propulsion systems. The most developed of these investigations involve micro-gridded ion thrusters (GIT) and micro-Hall thrusters. For hollow cathode propulsion systems to be competitive with current technologies an extensive investigation was conducted to determine the necessary performance goals of HC thrusters.

1.4.1 GRIDDED ION THRUSTERS

The deteriorating performance of the existing T5 ion thruster when operated at increasingly low power is shown in Figure 2. A number of practical issues hinder the effective scaling of electrostatic and electromagnetic thrusters to low power. When scaling down ion thrusters for low power operation, factors driving the thruster beam diameter include maximum acceptable beam current density, discharge chamber electrical efficiency, and operating discharge voltage. As the thruster throughput is decreased, the discharge electrical efficiency decreases, as reflected in the power required to produce an ampere of beam ion current. This is a result of the decreasing neutral density in the discharge, and hence the probability that energetic electrons will undergo inelastic collisions prior to being collected at anode surfaces decreases.[23]

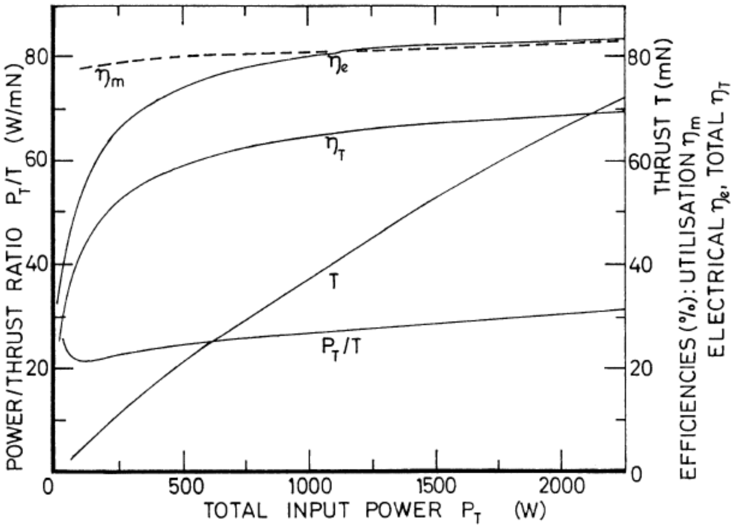

Figure 2 Summary of the overall performance of the T5 ion thruster.[24]

The discharge electrical efficiency also decreases as the thruster diameter is decreased because of the reduction in primary electron containment length. To yield a constant propellant efficiency the discharge must be operated at successively higher voltages as the thruster diameter is decreased, which presents obstacles in power processing unit (PPU) integration.[25] The increase in both discharge losses and operating voltage with decreased thruster size has two consequences. The increase in discharge losses reduces the thruster efficiency, and the increase in discharge voltage decreases the thruster lifetime due to the increase in the energy of ions striking cathode-potential surfaces. The neutral loss dependency on thruster length also reflects directly in the maximum propellant efficiency, and hence thruster efficiency. An exhaustive search of literature reveals that the most efficient and effective design of micro-ion thrusters developed to date was by Wirz at the Jet Propulsion Laboratory. The MiXI thruster performance detailed in Figure 3 operated down to 14W at 700V and 1764s[26] specific impulse giving 31% total efficiency.

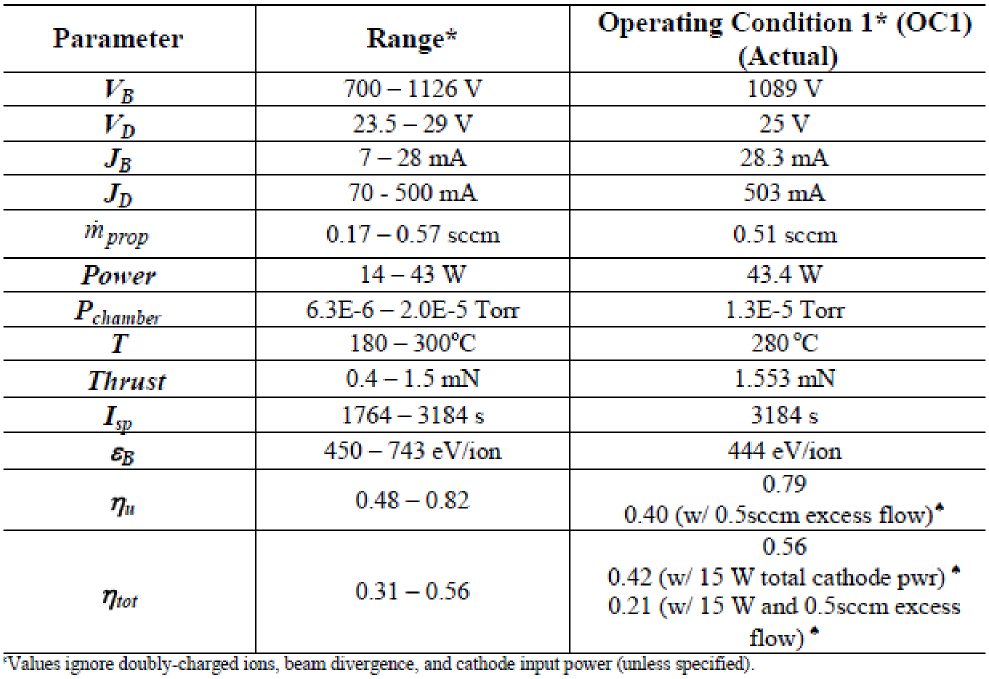

Parameter	Range*	Operating Condition 1* (OC1) (Actual)
V_B	700 – 1126 V	1089 V
V_D	23.5 – 29 V	25 V
J_B	7 – 28 mA	28.3 mA
J_D	70 - 500 mA	503 mA
$\dot{m}_{prop}$	0.17 – 0.57 sccm	0.51 sccm
$Power$	14 – 43 W	43.4 W
$P_{chamber}$	6.3E-6 – 2.0E-5 Torr	1.3E-5 Torr
T	180 – 300°C	280 °C
$Thrust$	0.4 – 1.5 mN	1.553 mN
I_{sp}	1764 – 3184 s	3184 s
ε_B	450 – 743 eV/ion	444 eV/ion
η_u	0.48 – 0.82	0.79 0.40 (w/ 0.5sccm excess flow)♠
η_{tot}	0.31 – 0.56	0.56 0.42 (w/ 15 W total cathode pwr) ♠ 0.21 (w/ 15 W and 0.5sccm excess flow) ♠

*Values ignore doubly-charged ions, beam divergence, and cathode input power (unless specified).

Figure 3 MiXI Propulsive and discharge parameters[26]

Recognizing the limitations in scaling down electrostatic and electromagnetic propulsion systems some researchers have explored the possibility of developing non-magnetic micro-ion thrusters based on hollow cathodes.[26] [27] [28] [29] It is also worth noting the development of a non-magnetically contained gridded ion thruster at NASA Glenn. The Hollow Cathode Micro-Thruster (HCMT) is a magnet-less gridded ion thruster designed to directly accelerate ions emitted from a discharge hollow cathode. [30] This thruster produced low discharge efficiency of 14%. Several low power radio frequency micro-ion thrusters are also currently under development. [191] [192]

1.4.2 Hall Thrusters

Hall thrusters face similar issues since scaling to low power requires a decrease in the thruster channel size and an increase in the magnetic field strength.[31] [32] Increasing magnetic field strength becomes technically challenging since the field can more easily saturate the miniaturized inner components of the magnetic circuit and scaling down the magnetic circuit leaves very little room for magnetic pole pieces and heat shields. This makes it difficult to arrive at an optimal magnetic field configuration. Non-optimal fields lead to enhanced power losses which lower efficiency and result in increased heating and erosion of thruster components, particularly the critical inner components comprising the coaxial channel and magnetic circuit. Erosion of the thruster channel is one of the main life-limiting factors in conventional Hall thrusters.[32]

A cylindrical Hall thruster (CHT)[33] [34] developed between NASA Marshal Space-Flight Centre and the University of Princeton has shown the operation between 90 to 185W in discharge power and result in thrust levels between 3 and 6 mN, thrust efficiencies between 20 and 27% and ISP between 1100 and 1650 s. An exhaustive search reveals the lowest power and highest performing (in terms of ISP) Hall thruster to date is the MHT-9 a developed at Massachusetts Institute of Technology.[35] The thruster operated between 20 and 500W at voltages between 100-300V delivering 1-18mN. Performance parameters are shown in Figures 4a and 4b.

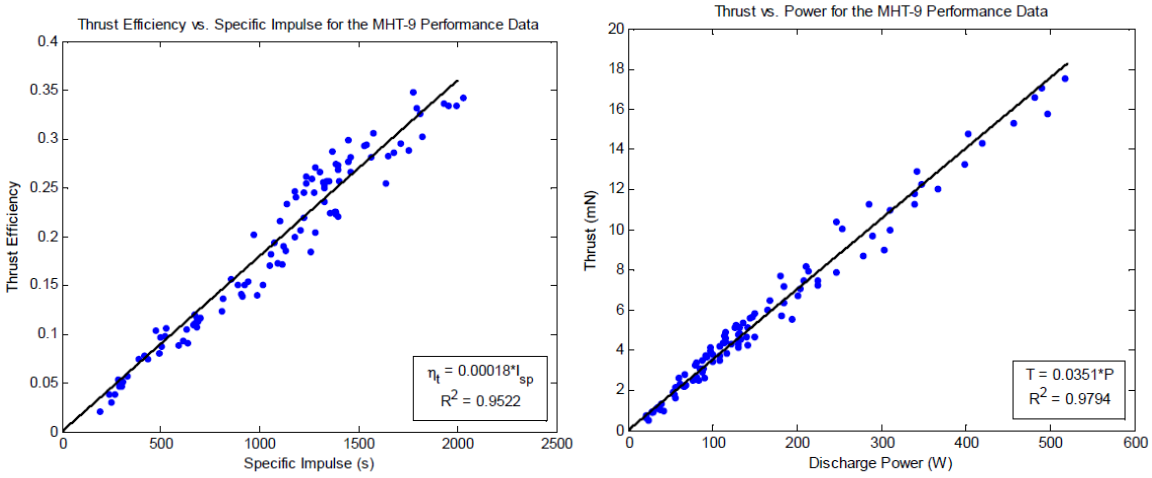

Figure 4a Thrust efficiency vs. specific impulse for the MHT-9. Figure 4b Thrust vs. discharge power for the MHT-9[35]

On the other hand researchers at Stanford have operated a 3.2mm mid-channel annular thruster over the power range 10-40W. The thruster generated 0.6-1.6mN of thrust with total efficiency between 10-15% at 300-850s specific impulse with an applied voltage between 110-275V.[36] The performance of this thruster is shown in Figure 5.

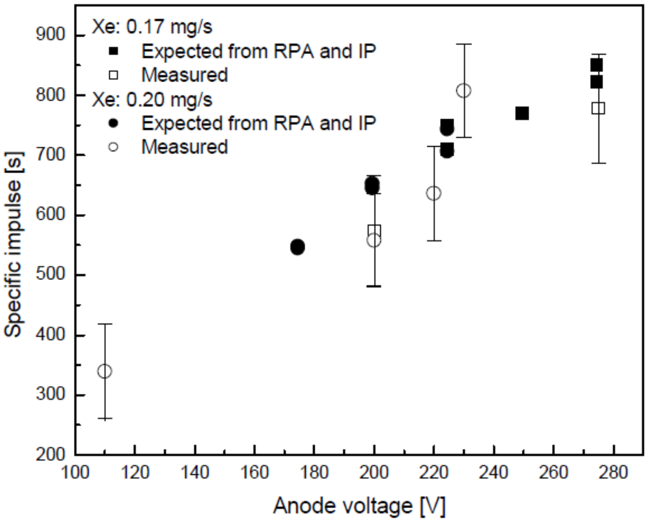

Figure 5 Specific impulse vs. anode voltage for the Stanford miniature Hall thruster[36]

The rapid loss of efficiency evident when attempting to miniaturize Hall thrusters and gridded ion thrusters is endemic. Operation of Hall thrusters at low power is seen to drive down both specific impulse and thrust efficiency regardless of the thruster design. Ion thrusters are able to maintain high levels of specific impulse given the somewhat separated mechanisms of ion creation, containment and acceleration, however discharge voltages in excess of 700V are required to give reasonable thrust efficiencies. None of the low power GIT or Hall thruster concepts have conducted wear tests however even in short term operation some Hall thrusters significant erosion has been noted given the very small scale of device and high throughput.[36]

1.5 APPLICATION OF HOLLOW CATHODES AS STAND-ALONE THRUSTERS

Given that T6 hollow cathodes tests have demonstrated specific impulses comparable to low power Hall thrusters[17], it may be reasonable to suggest the use of a hollow cathode for micropropulsion. This may give a device of comparable capability to low power ion thrusters with possible reduced development cost and requalification given the maturity and space heritage of cathodes. Small satellites (<200kg), have predominantly relied on xenon cold gas and resistojet systems due to their high density-ISP, simplicity and low cost nature, [37] [38] while maintaining the inert propellant storage and feed architectures. Resistojets are however limited in the maximum ISP they can produce since they are restricted by the temperature limitations of the heating element and the high molecular mass limits the performance of xenon cold gas thrusters and resistojets to between 15-48s specific impulse. [37] [38] Previous testing at the University of Southampton on the T6 hollow cathode has shown that at least a basic thruster can be formed, generating moderate specific impulse (<300s with xenon) at thrust levels <2 milli-Newtons, however their inefficiency leads to power requirement sometimes exceeding 1kW to give these ISPs.[8] [9] [39] Based on previous performance testing hollow cathode microthrusters may present an extension of ISP into the hundreds of seconds however they must be able to give this performance while operating in the 20-100W power range to warrant their use on small satellites or as part of an all-electric spacecraft. This is something currently beyond the capability of a hollow cathode thruster based on the current understanding of the T6 cathode and is the goal of this thesis.

Since hollow cathodes would be able to operate from existing inert gas feed architectures their addition to small spacecraft propulsion systems would be a reasonably simple process. As demands on small spacecraft continue to grow for missions such as formation-flying, inspection and rendezvous, requiring drag compensation, constellation phasing and proximity maneuvering,[40] conventional robust microsatellite propulsion systems such as cold gas thrusters and resistojets lack the necessary performance. The diffuse arc in hollow cathodes also permits operation at convenient discharge voltages (10-25V) for small satellites with limited power electronics, especially when compared to other electrothermal, electrostatic or electromagnetic thrusters.[41] Guidelines issued by the Inter-Agency Space Debris Coordination Committee (IADC) also now recommend that spacecraft in low earth orbit have the ability to deorbit within 25-years. This increases the mission delta-V by some 100-500% for typical earth observation missions, beyond the range of traditional small satellite propulsion systems.[42] Hollow cathode thrusters may therefore be a fitting solution only if their performance can be improved substantially.

1.6 APPLICATION OF HCT'S TO ALL-ELECTRIC SPACECRAFT

Hollow cathodes may also represent an attractive propulsion device for spacecraft which operate primary electrostatic or electromagnetic propulsion systems such as gridded ion thrusters and Hall thrusters. These spacecraft are typically required to carry a secondary monopropellant or bi-propellant system for reaction/momentum control or to compensate for thrust misalignment.[12] [13] [14] [43] These secondary systems constitute a large fraction of the overall propulsion system mass while only being required to produce a small fraction of the total impulse and also bring substantial cost increases in manufacture, assembly, integration, test operations, and launch preparation due to special handling considerations of hazardous propellant systems.[44] The use of inert propellants also bears no contamination risk to sensitive spacecraft equipment when compared with other thrusters in the milli-Newton thrust range such as PPT's (Pulsed Plasma Thrusters), colloid and FEEP (Field Emission Electric Propulsion) thrusters.[45]

Concurrent design studies as part of this work have highlighted the possibility of producing an all-electric lunar transfer orbiter utilizing the T5 gridded ion thruster and 8 hollow cathode AOCS thrusters at less than 150kg wet mass (excluding margins).[46] The proposed spacecraft architecture with shared propellant management is shown in Figure 6. A similar NEO rendezvous mission study utilizing 3 microsatellites with T5 gridded ion thrusters for primary propulsion and T6 hollow cathodes for attitude control also generated relatively low-cost spacecraft (50 M€ for the first and 30 M€ for subsequent spacecraft) with a wet mass of less than 120kg each. [47]

Similarly, a hollow cathode RCS system may also present a significant advantage to geostationary telecommunication satellites which utilize gridded ion thrusters for North-South, East-West station keeping and as such may represent one of the most commercially significant applications.[190] To date, 10 of the Boeing 702 communications satellites with a total of 40 XIPS thrusters have been successfully launched and are still in operation. These thrusters have accumulated approximately 33,000 hours of total in-space operation to date in a station keeping role. Including the 13cm XIPS units, there are now a total of 116 XIPS thrusters in orbit with over 150,000 accumulated operating hours. [193]

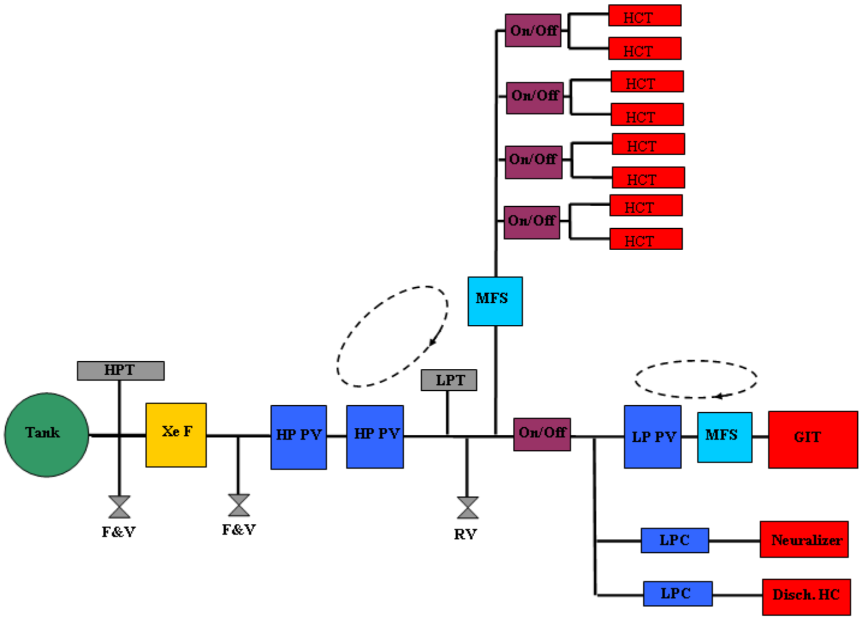

Figure 6 Proposed feed system architecture for the European Student Moon Orbiter (ESMO) electric propulsion system option.

HP PV: High pressure proportional valve, LP PV: Low pressure proportional valve, MFS: mass flow sensor, HPT: high pressure transducer, LPT: low pressure transducer, LPC: low pressure capillary, F&V: fill and vent valve, Xe F: Xenon filter, RV: relief valve

CHAPTER 2

BACKGROUND AND REVIEW

In this chapter some of the background ideas and theory which are of interest to the present research are outlined. An overview of the operation of hollow cathodes is given and this is followed by more detailed descriptions of the operation and plasma processes occurring within three distinct regions of the discharge, namely the internal body, the cathode orifice and the cathode-anode gap. Within each of these descriptions reference is made to the experimental and theoretical work which has been performed to date and shortcomings or inconsistencies in knowledge are indicated. Underlying mechanisms are introduced and the premise by which to improve performance is described.

2.1 HOLLOW CATHODE INVESTIGATIONS

2.1.1 PREVIOUS INVESTIGATIONS OF HOLLOW CATHODE PHENOMENON

Early investigations into HC phenomenon concentrated on understanding discharge characteristics as an electron source since their performance was vastly superior to planar cathodes in terms of the attainable current levels, discharge voltage and lifetime[48] [49] [50] [51] [52] [53] with the first tests conducted using inert gasses in 1978.[54] Most of these investigations focused on empirical investigations systematically modifying cathode geometry to see the influence on discharge performance. Particular attention was given to the different modes of operation now recognized as spot and plume modes. Csiky was the first investigator to use these terms. [55] [56] [57] Extensive work by Fearn and Patterson further characterized these modes[58] [59] [60] [61] [62] [63] [64] with particular attention to discharge noise and ion energy content showing that use of a keeper electrode significantly extended the range of spot-mode-like operation, delaying the onset of discharge noise and helping maintain low discharge voltages. This method was subsequently used to mitigate excessive cathode erosion in ion thrusters.[65] Fearn and Patterson also found the distance between the keeper electrode and the cathode also influenced the voltage required for cathode ignition showing that the initiation voltage is at a minimum when the line of sight distance between the upstream interior edge of the orifice (which has the greatest quantity of free barium during preheating) and the keeper is at its shortest and obeys a classical Paschen breakdown but with modified constants to take into account the heating of the gas. In addition, new information was acquired concerning apparently reproducible instability or oscillatory regimes, showing that some were due to the response of the anode power supply to the negative resistance relationship when attempting to produce a constant current output. The discharge is therefore obliged to adopt a sustained oscillatory mode (typically up to several 100's of Hz). In the T5 ion thruster, the typical oscillation amplitude at any frequency (up to 10s of MHz) is 5 mV. Some of the higher frequency low amplitude oscillations were explicable by other plasma mechanisms.[58] [64] [66] One mechanism for noise generation which is not considered to influence modes of behavior concerns transitory emission from aluminum filaments on the surface of the dispenser.[67] Other noise sources are to be found in the plasma processes[68] occurring within the cathode. A further operational mode was also identified, the so-called neutralizer mode.[69] This occurs when both mass flow rate and discharge current are small, and the cathode is exposed to a hard vacuum. It can then operate very stably, but with significant noise generation, at relatively low temperatures and hence is appropriate for the neutralizer application. It should be emphasized that these operational modes refer specifically to a diode discharge configuration. There is considerable evidence that this behavior is modified when a cathode is used in a thruster, possibly due to the influence of the higher gas pressure within the discharge chamber and to the presence of magnetic fields, however it is a very useful learning exercise for us since a HC thruster would also be operated in a diode configuration with the discharge current being drawn to a single electrode since there is no requirement to provide electrons for external ionization with a discharge chamber. The difference in hollow thruster operation in an open diode configuration and a typical T6 ion thruster is shown in Figure 7.

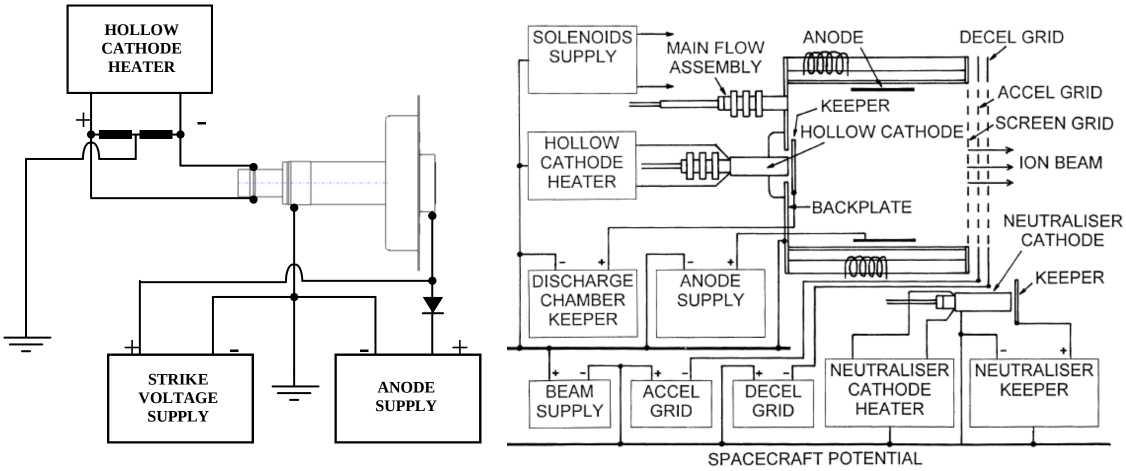

Figure 7 Electrical configuration in the present hollow cathode thruster experiment (left) T6 ion thruster electrical configuration (right) [70]

Previous low-power hollow cathode operation studies include references71, 72 and 73 however much of the cathode development work with inert gases has focused on operation at several Amperes and higher with flows of at least 2 sccm (~0.2 mg/s for xenon) [72] [74] [75] [76] [77] [78]. Historically these operating regimes have been driven by the emission requirements of ion thrusters and later plasma contactors. Investigations on the J-Series ion-thrusters produced high current 6.4mm diameter cathodes operating down to several tens of Watts.[79] Other researchers have produced cathodes capable of operating at much lower power.[80,81] Investigations on hollow cathode miniaturization have shown that scaling down to very small geometries is achievable with the cathode still running in a low voltage self-heated mode. [82] [83] [84] Hutchinson conducted experiments on the scaling of impregnated cathodes to low power which operated between 0.33-2.93W with high voltage discharges between 54-220V.[183]

Several efforts to model hollow cathode processes were reported or started in the 1970's. [85] [74] [75] [54]. There has been an effort to model hollow cathodes to some extent, initially by Kaufman, in an effort to accurately predict lifetimes and avoid costly long duration testing. First attempts to develop scaling laws for orificed hollow cathodes were also introduced by Kaufman[86]. A more rigorous phenomenological model for orificed hollow cathode operation was introduced by Siegfried and Wilbur in 1981[87], and then refined in 1984[88]. The cathode models of Sahli and Turchi[89] allow for some simplification of the problem to observe the effects of geometry on power balance. These models were aimed to establish hollow cathode scaling to permit higher current operation without exceeding the operating temperature limits for inserts. The models also depicted the limiting discharge current for typical operation conditions in ion engines on the basis of the computed cathode temperature or the inability of the model to achieve steady state self consistent solutions. Salhi and Turchi expanded on the model to reduce the number of experimental inputs and to include two-dimensional variations in the heavy particle temperature and also to assess the effect of varying geometry on performance.[186] This research showed that a smaller insert diameter leads to a reduction in the cathode fall voltage for a given discharge current, also showing that the smallest cathode capable of carrying a given current is also the most efficient. The model also predicted that larger cathodes tend to operate at low temperatures relative to small cathodes. Domonkos and Gallimore[90] have tried to establish scaling relationships for low power low current operation, highlighting that power consumption increases with orifice length, while the minimum flow rate decreased. Also the use of an enclosed keeper was shown to reduce power consumption, however the minimum flow rate was observed to increase. A particle and energy balance model of orificed hollow cathodes was developed by the same authors to assist in cathode design however the predicted power consumption exceeded the experimental results.[91] The maximum discharge current for a given cathode has been shown to be proportional to insert inner diameter.[92] [93] [72]

2.1.2 THRUST MEASUREMENT INVESTIGATIONS

Prior to Gessini only one investigation by Snyder and Banks at NASA Lewis made direct thrust measurements from a hollow cathode using a torsion quartz balance both with and without a discharge in an attempt to understand the influence of the neutralizer on the thrust vector of the SERT II ion thruster.[94] The cathode body was 3.2mm in diameter with a 0.25mm orifice and housing a tantalum foil dispenser with a keeper. An additional electrode was mounted downstream to investigate the acceleration of ions or electrons on the measured thrust. However without a method for ion/electron separation/extraction it is difficult to see how this did anything other than provide an additional method of current extraction from the cathode.

Snyder and banks operated a mercury hollow cathode at the nominal operating condition of 47mA equivalent current in both a discharge and no discharge mode where equivalent amps is described as:

$$I_{eq} = \frac{e\dot{m}}{M_i} \tag{2.1}$$

Mass flow rates between 0.05 and 1mg/s correspond for example to I_{eq} flowrates between 0.034A and 0.698A respectively. The cathode was operated at 0.75Amps maintaining a 19V keeper voltage (14.25Watts) and based on the measured value of thrust generated around 66.4μN. Without the cathode operating the thrust was reduced by about 15μN. This was evidence enough to convince Snyder and Banks that the thrust generated by the SERT II neutralizer was negligible compared to the 28,000μN of the SERT II ion thruster. Although the authors did not state the values of propulsive performance a simple calculation reveals that with no discharge the specific impulse of the neutralizer was 53.5s while in a discharge mode the specific impulse rose to 69.2s giving a 0.158% thrust efficiency. Snyder and Banks however also allowed for a correction due to diffuse or specular reflection from the target where, in the worst case of specular reflection the actual thrust would be ½ that of the measured value. In the case of a purely diffuse correction thrust would be reduced by 1/3. Snyder and Banks found that when comparing the thrust generated to the theoretical thrust from a sonic choked orifice with a gas temperature equal to the cathode tip temperature (measured with an optical pyrometer) the actual thrust lay between these two corrections in approximate agreement with the thermal interpretation of propellant velocity. With and without the presence of a discharge the corrected values of thrust were then 52μN and 26μN giving 54s and 27s specific impulse respectively with a 0.097% thrust efficiency. Thrust level was also seen to increase with cathode operating power (presumably by varying discharge current) at constant tip temperature indicating either direct heating of the expellant by the discharge or another acceleration mechanism; it is however difficult to see how this particular test was conducted at constant tip temperature since an increase in operating power generally implies an increase in tip temperature.[95] Nonetheless, these measurements did indicate the potential for electrothermal type operation but also bring to light the very low thrust efficiencies apparent.

More recently Gessini also conducted hollow cathode thrust measurements in an attempt to assess the T6 hollow cathode as a microthruster using an 80mm steel anode disk with a machined 10mm diameter hole and mounted 4.5mm downstream of the cathode. A cantilever beam and laser-optical-lever system was used to characterize thrust. Gessini clearly noted a transition to plume mode at flow rates below 0.5mg/s with xenon at which thrust noise, discharge noise and voltage were shown to sharply increase as shown in Figure 8. Specific impulse scaled linearly with specific power.

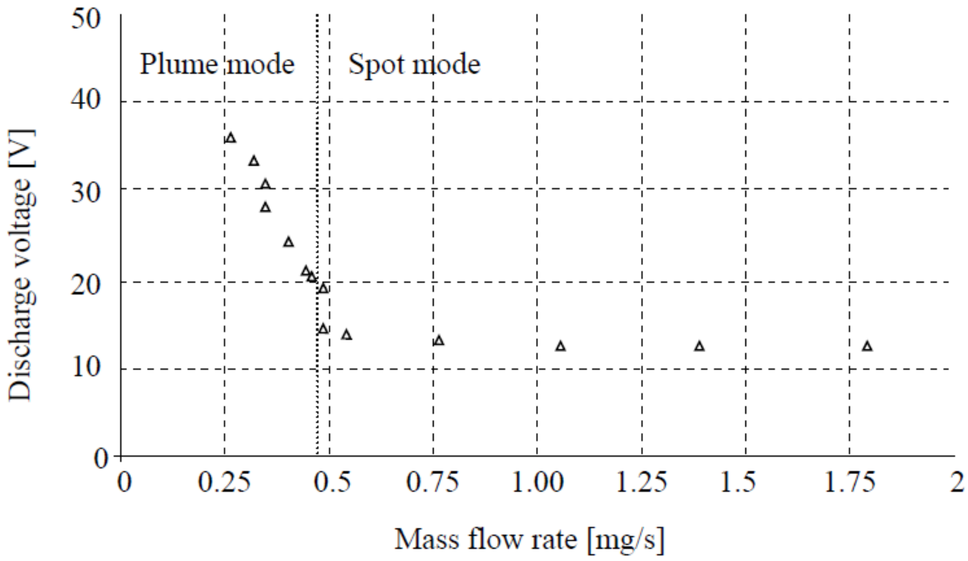

Figure 8 Transition from spot to plume mode at decreasing cathode flow rate with argon at 5A [8]

Gessini also tested both a 0.5mm and 1mm orifice T6 cathode indicating that the larger orifice showed roughly a factor of 2 reduction in specific impulse shown in Figures 9 and 10.

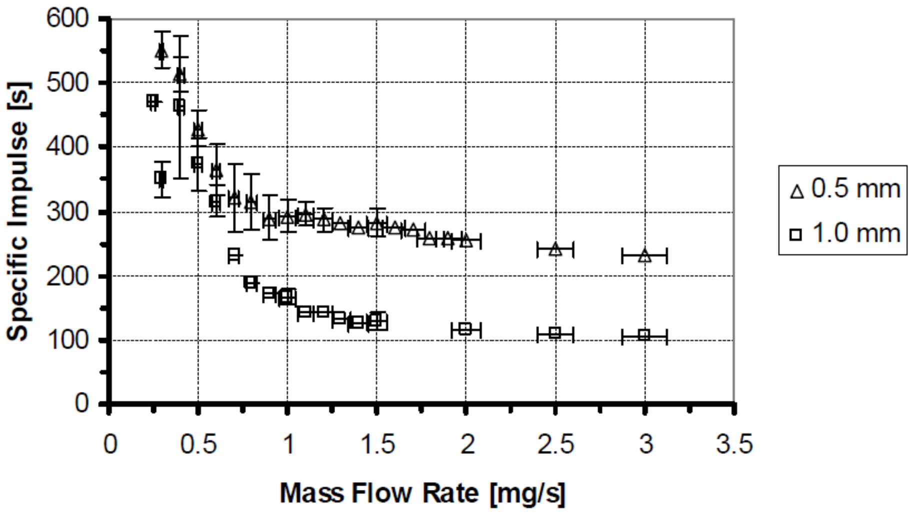

Figure 9 Performance with argon at 25A[17]

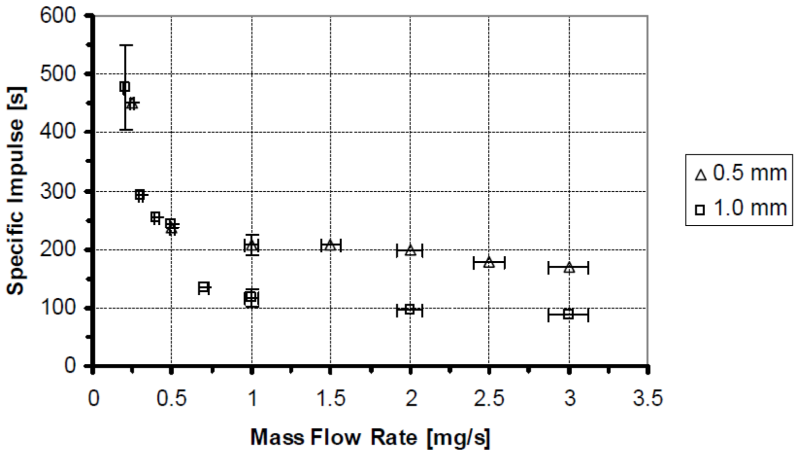

Figure 10 Performance with xenon at 25A[17]

Although the thrust balance developed by Gessini did allow measurement with reasonable accuracy the balance suffered a number of technical difficulties. Since the cantilever beam and target were manufactured from one piece of molybdenum the balance had to be designed for a very specific thrust range which compromised resolution at very low thrust levels. The operating points of most interest turned out to be at low flow rates and low thrust which produced the highest performance and thus measurements in these regions showed large uncertainty as evident in Figure 9. The beam and target also exhibited a large number of dynamic resonant modes excitable by numerous internal and external environmental factors which also compromised accuracy and increased uncertainly. Finally the measurement system also suffered from large thermal drifts due to differential expansion of the cantilever beam and movement in the measurement system and supporting architecture. Chapter 4 therefore describes the design and commissioning of a new kind of micro thrust-balance designed to give better accuracy resolution and range with less ambiguity than the previous system especially in order to better characterize the low thrust, high specific impulse conditions.

2.1.3 HIGH ENERGY ION PRODUCTION

Hollow cathodes have been known for some time to produce streams of highly energetic ions. Since the thrust mechanism in hollow cathode is not understood a review of high energy ion experiments and observations was conducted as a means to better understand potential thrust production mechanisms.

Compton[96] and Tanberg[97] performed early studies that indirectly detected high-energy ion generation in vacuum arc environments. During wear tests of a 10kW ion thruster Rawlin first noted the production of ions from *hollow* cathodes with energies significantly above the cathode-keeper or cathode-anode potentials.[98] Since then their presence has been suggested by many sets of experimental data. [99] [100] [101] [102] [103] Fearn and Patterson also measured the high energy ion content originating from cathodes in a diode configuration.[104] [105] Data obtained by electrostatic energy analyzer (ESA) and retarding potential analyzer (RPA) indicate that these ions are emitted in a roughly collimated beam away from the cathode contrary to preceding studies.[106] Proposed mechanisms have included potential hills[107], charge exchange between ions and neutrals,[108] double ionization,[109] triple ionization,[110] multiple collisions of ions with the cathode orifice wall,[111] magnetohydrodynamic effects,[100] and plasma potential oscillations.[112] The potential-hill model proposed by Friedly and Wilbur[101] postulated the creation, in the plasma near the HC orifice, of a region at a positive potential in excess of keeper potential due to positive space-charge build-up resulting from substantial ion production via collisional ionization by high-energy electrons. Ions would be accelerated to high kinetic energies as they moved off the potential-hill. The orifice-pinch model, proposed by Latham[100] postulates a magnetohydrodynamic (MHD) effect associated with high current densities, in the orifice region, large enough to produce plasma acceleration. Since then Crofton has suggested these to both be incorrect or insufficient for a full explanation while conducting RPA measurements on at T5 hollow cathode.[113] Other researchers have studied the phenomenon of high energy ion production from hollow cathodes since erosion of the cathode and cathode assembly by high energy ion sputtering is considered a major life limiting factor in electrostatic thrusters. The 30,000hr extended life test (ELT) of the spare Deep Space 1 NSTAR ion thruster for instance identified erosion of the keeper and subsequently the cathode assembly as the most probable near-term cause of failure, as well as noting change in the erosion pattern at different discharge power levels. Images from these tests are shown in Figures 11 and 12.[114]

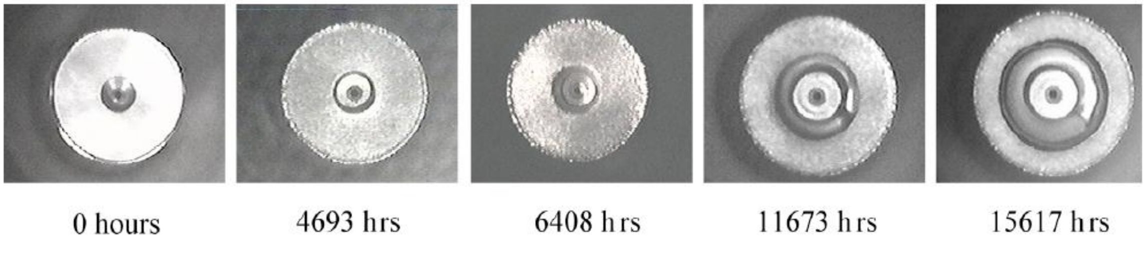

Figure 11 Photo of the NSTAR cathode evolution in the ELT test where the keeper electrode completed eroded out beyond the cathode diameter in 15,000 hours. [114]

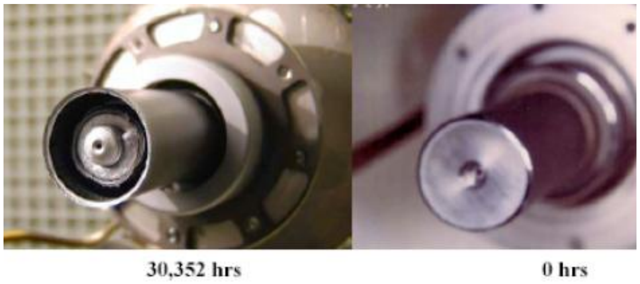

Figure 12 Photo of the NSTAR cathode evolution in the ELT test after 30,352 hours. [114]

Crofton and Boyd[115] focus on measurements of low-flow hollow cathodes where they report both high-energy ions and significant numbers of multiply charged ions as do Davis and Miller.[116] Williams and Wilbur[117] performed studies on low-current, low-flow rate hollow cathodes where high-energy ions were measured and potential hill structures were detected. Kameyama and Wilbur[118] presented data on hollow cathodes operated at high currents (~50 A and higher) where very destructive high energy ions were detected and also showed that these ion originated directly from the orifice and not the downstream plume via highly directional ESA measurements. In work on a free arc, Swift[119] discusses many instances where researchers have detected high-energy ions. Swift goes on to re-propose the potential hill or hump theory of high-energy ion production and then demonstrates its existence using evidence from retrograde motion studies in strong magnetic field environments. In a very high current regime of free arcs, Rusteburg et al.[120] present high energy ion data that display wide variations in zenith angle emission depending upon when the measurements are made during sinusoidal driven emission cycles. The studies discussed above date from the 1930s to the present and all discuss direct and inferred evidence of high-energy ions being generated within arcs. In addition, nearly all of the researchers listed struggle with explaining the mechanism responsible for accelerating the ions, and most suggest the potential hill explanation.

With regard to the ion energy distribution, more recently Foster and Patterson[121] used a fixed-position, highly collimated ESA to investigate the ion energy characteristics of ions flowing along the axis of an open-ended, 40-cm diameter ion thruster discharge chamber (Figure 13). Although they saw some evidence of high-energy ions, the energies were not excessive. Cacey et. al.[122] characterized ion energy distribution as functions of the zenith angle at which the ions flow from the cathode region using a rotating setup. Very few high-energy ions were found flowing along the axis of the discharge chamber which is in general agreement with Foster and Patterson.

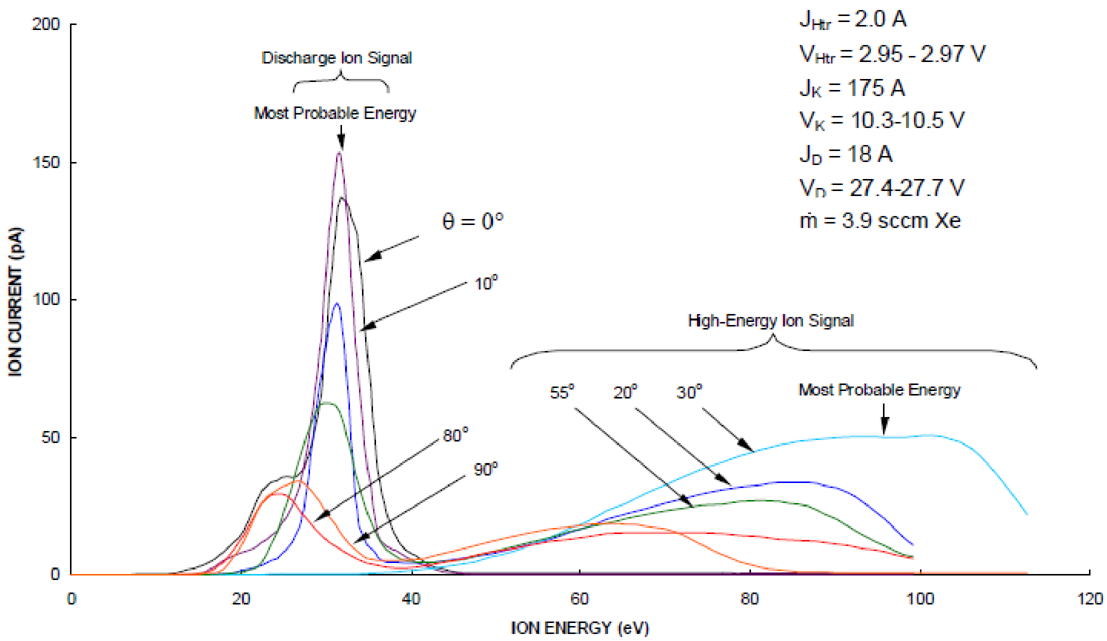

Figure 13 Effect of zenith angle variation on the ion energy distribution with the ESA[122]

Przybylowski performed radial ion energy measurements via an ESA mounted 90° off-axis, immediately downstream of an NSTAR discharge cathode orifice with mixes of xenon and krypton.[123] The investigation found a significant fraction of ion energies in excess of the discharge voltage (>90eV) and also showed that operation with krypton generated ions of significantly higher energy than for xenon for the same mass flow and current conditions indicating that the acceleration mechanism was either mass dependant or a product of the different discharge characteristics. The plasma density and potential profiles downstream of the keeper electrode in the NSTAR geometry have been extensively measured with scanning probes by Herman and Gallimore[124], Jameson, et al.[125], and by Sengupta, et al.[126]. Goebel et al. [127] have made the most substantial investigation of high energy ion production mechanisms by investigation of the DC and RF density and potential profiles measured throughout the discharge by fast miniature scanning probes to give time-averaged plasma parameters and with a 4-grid retarding potential analyzer RPA mounted both radially and axially. [128] Measurements of plasma potential indicate maximum time-averaged voltage differences that are only slightly larger than the discharge voltage therefore, it is unlikely that, in this case, the mechanism for high-energy ion production is an electrostatic acceleration by DC potential structures. Evidence indicates that discharge plasma potential oscillations measured by Goebel et al. had amplitudes about twice the average discharge voltage, large enough to account for high energy ions accelerated through the potential gap between the oscillation peak and cathode potential.[127] This suggests that turbulent oscillations in the characteristic plasma ball observed downstream of the cathode orifice are responsible for both the energy and spatial distribution of the energetic ions. Evidence for this mechanism was compounded by the fact that large amplitude local plasma oscillations up to peak ion energy levels in the 0.5-1MHz range as shown in Figure 14.

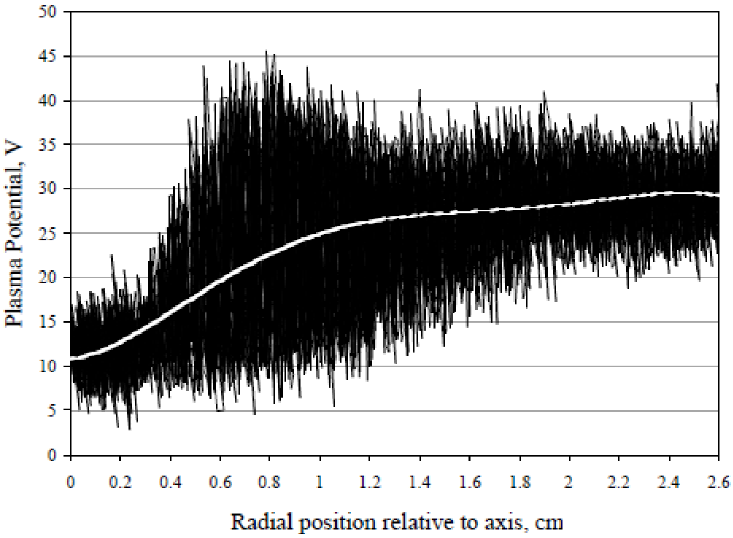

Figure 14 Radial fluctuations in the plasma potential for the NSTAR TH8 throttle condition[127]

The source of the energy to produce these ions has thus been suggested to be RF plasma potential oscillations in the near cathode plume from plasma instabilities.[127] Goebel postulated that the source of these plasma potential oscillations is likely turbulent ion acoustic waves generated in the hollow cathode discharge plasma or ionization instabilities termed predator-prey modes in the near-cathode plume region. Ion-acoustic oscillations are typically current driven and damped at low Mach numbers by Landau damping and by collisional effects. Ionization instabilities are also damped by changes in the local ionization rates. It was found that injection of neutral gas directly into the cathode plume region near the keeper by an exterior gas feed could quench the oscillations and eliminate the high energy ions observed both radially and axially from the cathode exit.

This summary of vast experimental measurements concluding with the work of Goebel demonstrates that the very high energy ion content of hollow cathodes originally provoking research into hollow cathode thrusters as a standalone device, at least at the operating conditions researched, may not a product of an MDH or potential hill accelerating mechanism. On the other hand these mechanisms cannot be discounted as a means for production of bulk ions with relatively high energies on axis. The second part of this thesis makes a similar analysis of the downstream ion energy distribution at higher currents and lower mass flowrates than Goebel in order to investigate the mechanism responsible for such high specific impulse in hollow cathodes.

2.2 HOLLOW CATHODE OPERATION

2.2.1 QUALITATIVE OVERVIEW

HC's generally consist of a refractory metal cylinder enclosed at one end with a tip containing an axial orifice. A chamfer is generally employed on the larger T6 cathode to reduce the orifice length without decreasing the thickness of the orifice plate. A gaseous propellant is supplied from the upstream end thus generating an internal pressure rise and choked flow through the orifice. A schematic of a hollow cathode is shown in Figure 15. The cylinder houses a porous tungsten dispenser (generally 15-20% porosity), impregnated with a mixture of earth metal oxides: barium-oxide, calcium oxide and aluminates (BaO: CaO: Al_2O_3) in various ratios, termed the stoichiometric composition. When heated, impregnates react with the tungsten matrix producing gaseous free barium. The thermal decomposition of impregnate materials may be represented by:

$$6BaO(g) + W(s) \Leftrightarrow Ba_3WO_6(s) + 3Ba(g) \tag{2.2}$$

Impregnate constituents also undergo thermo-chemical reactions and liberate free BaO/CaO, which are adsorbed from the emitting surface during heating and operation. The barium spreads by Knudsen flow over the surface of the tungsten forming a layer. The barium layer is strongly bonded to the surface by an underlying layer of oxygen. These components introduce a dipole and decrease the elecro-negativity barrier of the emitting surface, corresponding to a decrease in work function for thermionic emission from 4.5eV to 2.1eV while operating ~ 1000°C.[129] A tungsten filament heater is wrapped and in this case cemented by ceramic in place around the downstream end (unbound co-axial heaters grounded to the cathode are also used) is employed to raise the temperature of the emitter (>1000°C) sufficient for initial thermionic emission from the dispenser cavity and to begin the thermo-chemical reactions. A potential is applied between the anode (~50V) and cathode forming an axial electric field gradient and a trigger voltage is sometimes applied to initiate the discharge (<200V). While direct measurements have not fully characterized the processes following ignition it is considered that xenon plasma initially forms between the outer orifice edge and the anode; this plasma extends into the hollow core of the cathode insert. Coupling of the electric field into this region drives the ionization electrons that ultimately provide the avalanche breakdown of the main discharge. The discharge current is then drawn from the emitter surface, through the orifice, toward the anode.

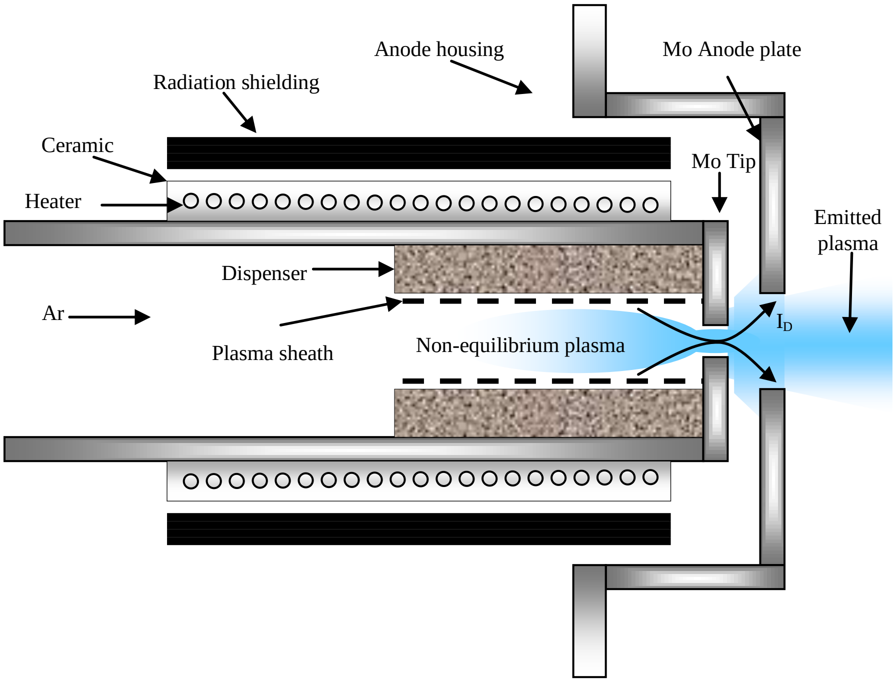

Figure 15 Internal schematic of a T5 cathode

A positive column (a region of higher potential relative to the cathode) then serves as a virtual anode, occupying the interior space of the emitter cavity between two opposing sheath regions at the emitter wall. A change in electric filed distribution occurs forming a radial field and a potential well within the cavity causing a strong radial acceleration of electrons inward leading to an oscillatory motion of electrons as they are accelerated into the virtual anode then repelled from the opposing sheath.[184] Thus the path length of electrons is significantly increased and these pendulum electrons undergo collisions with the background gas. This results in a negative differential resistance characteristic in a normal glow mode and is distinctive of hollow cathode behaviour. The characteristics of the glow transitions are shown in Figure 16. Self-heating is then maintained by the reabsorbtion of energetic electrons and acceleration of ions through the sheath (region between the cathode and plasma column) at the internal cathode surfaces. While electrons deposit their thermal energy to the cathode surface, ions recombine to form neutrals depositing their kinetic, thermal and ionization energy; the cathode then no longer requires the use of the heater. As greater current is demanded the cathode generally experiences an increase in discharge voltage and thus nears the transition to an abnormal glow discharge.

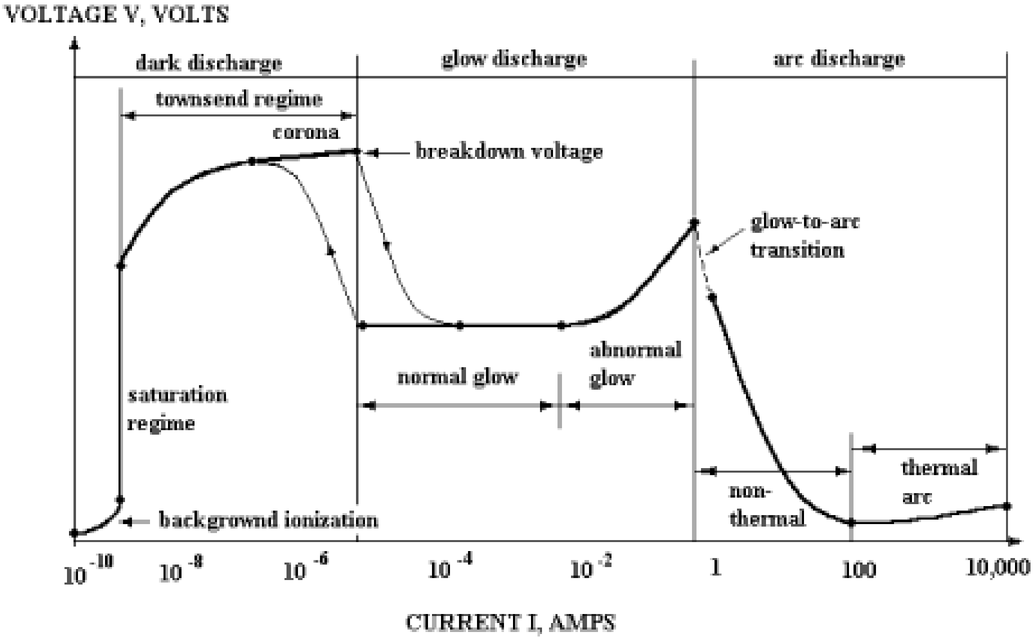

Figure 16 Characteristics of electrical discharge transitions in planar cathodes[130]

At the emitter surface and sheath boundary, the internal plasma column aids in field-enhanced emission due to the intense field ~10^7V/m (sheath voltage at a distance on the order of the Debye length) between the plasma column and cathode potentials. Thermionic current density at the emitter surface is given by the Richardson-Schottky equation[131] for a given cathode surface temperature and emission constant:

$$J_{th} = A_R T_c^{\,2} e^{\left(\frac{\phi_{eff}}{kT_c}\right)} \tag{2.3}$$

Thermionic electron emission from the cathode occurs primarily at the downstream end due to the higher plasma potential, and fall voltages and material temperature.[134] Field enhancement of the emission process lowers the effective work function of the emitter via the Schottky effect is the primary reason why hollow cathodes are able to emit at such high current densities. The effective work function in terms of the electric field at the cathode surface is given by:

$$\phi_{eff} = \phi - \sqrt{\frac{e - |E_c|}{4\pi\varepsilon_0}}$$

(2.4)

Typical values for the work function are between 2.0–2.2eV for 4:1:1-type emitters where 4:1:1 represents the stochiometric ratios of barium oxide, calcium oxide and aluminates. The strength of the enhancing electric field can be estimated from the double-sheathed analysis at the cathode surface governed by Poisson's equation. An approximation to the double sheath analysis was used by Siegfried and Wilbur[88]:

$$E_c = \sqrt{\frac{n_e k T_e}{\varepsilon_0}} \left(\left[2\sqrt{1 + 2\frac{eV_p}{kT_e}} - 4 \right]^{0.5} \right)^{0.5}$$

(2.5)

No significant amounts of secondary emission (electrons liberated by ion or primary electron impact) contribute to the main discharge current.[132] Ion production is generally assumed to be achieved by multi-step processes by two distinct electron populations; firstly by electron impact of primary electrons from the atomic ground state within the emitter volume (8-10eV), and then by lower energy thermalized electrons (2-4eV) within the orifice[133] which then contribute significantly to the ionization process. The plasma potential within the emitter volume generally remains 8-10V above the cathode potential (however lower values are recorded in large orifice cathodes) consistent with the energy required for the excitation of meta-stable states ($3P_0$ ~ 9.45eV, $3P_2$ ~8.32eV for xenon) with the majority of the remaining potential drop occurring over the orifice length, a region of much higher resistive dissipation given the reduced path cross-section and thus higher collision frequency. The total process thus requires transfer of at least the first ionization energy per ion (12.4eV for xenon, 14.4eV for argon). The plasma within the internal volume is considered a quasi-neutral highly non-equilibrium plasma. Processes within the orifice have been shown to dominate both the thermal and plasma characteristics of cathodes.[134] Cathodes with small orifices (0.25mm) have been shown to have an ionization fraction close to 1 at the orifice exit[135] with significant multiply-charged ions in comparison to larger cathodes where gas utilization is typically 5-10%.[136]

2.2.2 POWER BALANCE

The operating regime acts to maintain sufficient emitter temperatures for thermionic emission by balancing power deposition to the cathode (primarily by direct heating from the plasma or conduction from the orifice plate) with cooling by particle efflux and heat transfer to the surroundings. Energy input to the plasma can be attributed to the energy of thermionically emitted electrons accelerated through the cathode fall and through Ohmic (collisional) heating within the orifice channel. A schematic of the energy flux within a cathode is shown in Figure 17.

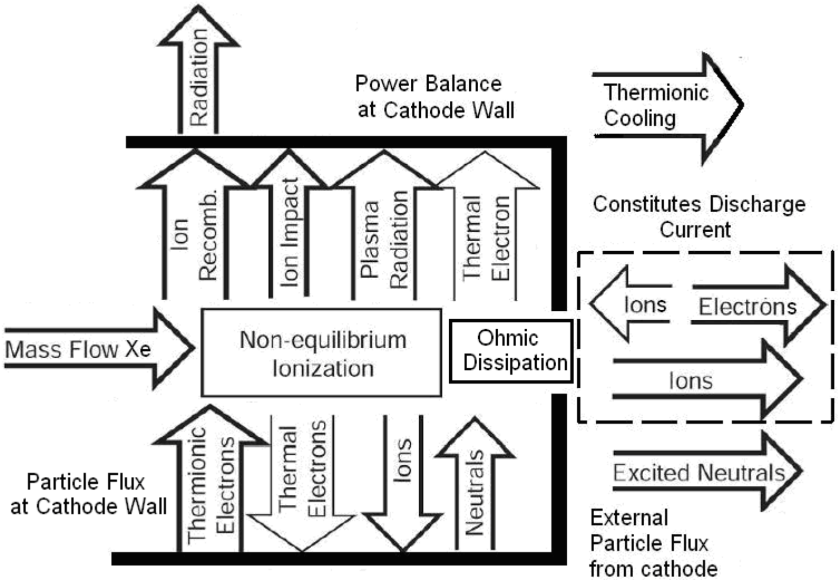

Figure 17 Energy/particle flux within a cathode

The electron or ion temperature in volts is given by:

$$\frac{kT_{i,e}}{e} \tag{2.6}$$

The thermal power of a convected flow is thus given by:

$$I_{eq}\frac{5kT_{i,e}}{2e} \tag{2.7}$$

Again, at the cathode surface thermionic electrons relieve the cathode of thermal energy. This energy is restored by ion recombination and electron back streaming. The power balance can then be represented by:

$$\int J_{th}\left(\phi_{eff}+\frac{5kT_c}{2e}\right)dA_{em}=\int J_i\left(\varepsilon_i+V_f-\phi_{eff}\right)dA_{em}+\int J_e\left(\phi_{eff}+\frac{5kT_e}{2e}\right)dA_{em}-fq_r$$

(2.8)

With a view factor from the emitter to the cathode body:

$$f=A_{e\to S}$$

(2.9)

A similar energy balance has been successfully used by references 87, 88 and 186. Since the emitter temperature profile is not constant along the length of the cathode[137 95], integrals allow for the resulting variation in current density from the emitter. Within the plasma, energy is input by thermionic electrons accelerated through the fall potential and Ohmic heating. The energy invested in the plasma is balanced by the production of thermalized ions, electrons (composed of the back streaming electrons, discharge electrons and plasma electrons), neutrals and radiative flux. The energy balance can be represented by:

$$\int J_{th}\left(V_p+\frac{5kT_e}{2e}\right)dA_{em}+\int\frac{J_D{}^2}{\sigma}dV=$$
$$\int J_i\left(\varepsilon_i+\frac{5kT_i}{2e}\right)dA_s+\int J_e\left(\frac{5kT_e}{2e}\right)dA_s+\left(I_D+\alpha I_{eq}\right)\left(\frac{5kT_e}{2e}\right)+\frac{I_{eq}}{\alpha}\left(\frac{5kT_e}{2e}\right)+q_r$$

(2.10)

2.2.3 SPOT MODE TO PLUME MODE TRANSITION

If the flux of ions into the cathode-anode gap is sufficient to support the electron population, the anode will passively collect the discharge current from the plasma; this type of operation is generally referred to as spot mode. If the ion flux to the cathode-keeper gap is insufficient for the anode to passively collect the electron current, an additional sheath and voltage drop forms between the plasma and anode to facilitate ionization and electron transport/collection so that electrons can traverse the gap within the quasi-neutral plasma. This transition, depicted in Figure 18, occurs as the mass flow rate or discharge current is decreased (both of which intrinsically influence plasma and discharge properties) beyond a critical point and is generally termed plume mode given the bright spot at the cathode tip transitions into a more diffuse-like plume. Since the ions created in the gap have some fraction of the discharge potential to accelerate them toward the cathode, plume mode is particularly associated with ion sputtering of the cathode orifice[138] and discharge instabilities, which limit lifetime[139] and are responsible for high coupling voltages. For these reasons cathodes are normal operated in a spot mode.

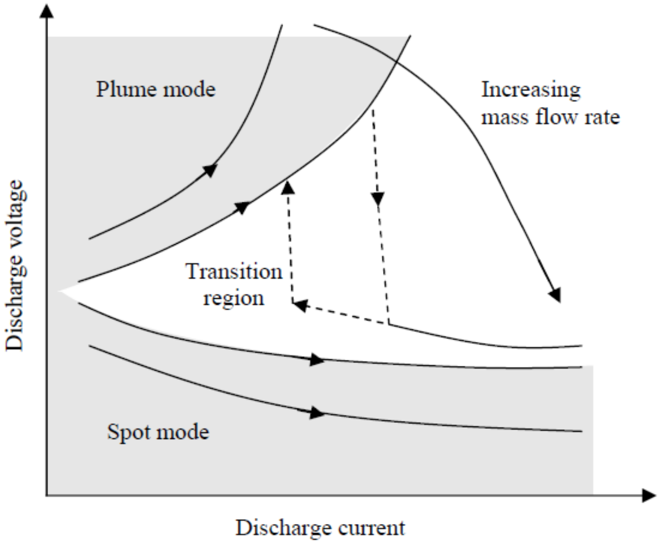

Figure 18 Hollow cathode discharge behaviour with varying current and flowrate

An empirical transition to spot mode criterion[54] has been described by Kaufman, which accurately predicted the transition flow rate. Mandel and Katz[140] have numerically determined this transition on the basis of the contact area of the anode and keeper electrode with the downstream plasma correctly predicting empirical observations of the transition point based on the natural thermal flux of ions and electrons to the anode. Assuming a quazi-neutral plasma, the passive flux of electrons and ions to a keeper electrode immersed in the downstream plasma, based on thermal flux, is given by:[140]

$$I_{e,i} = A_k n_{e,i} \sqrt{\frac{eT_{e,i}}{2\pi M_{e,i}}} \tag{2.11}$$

2.2.4 INFLUENCE OF ANODE GEOMETRY

If the passive current exceeds the demanded discharge current the anode will be negative relative to its local plasma potential in order to repel electrons to fulfill the demanded current condition and achieve current balance. Thus, due to the plasma current density the anode will be surrounded by positive ions forming a positive space charge sheath and hence there will be a negative anode drop. Hence, the discharge fails to exhibit visual evidence of electron-impact ionization in the gap. In this condition it is entirely possible that electron deceleration in fact occurs in the anode cathode gap rather than acceleration to give the necessary excitation/ionization to carry the discharge current and maintain spot mode. If the current demand is increased to a level exactly equal the passive current the anode will simply float at the local plasma potential. If the current demand is increased to a point greater than the natural passive current, the anode will become positive with respect to the local plasma. This mechanism will lead to the accumulation of excess electrons in the vicinity of the anode-plasma boundary forming a negative electron sheath with the negative space charge of the sheath shielding the local plasma from the positive potential of the anode.

Since the electric field of the anode will not penetrate past the outer edge of the sheath, all of the rise in potential between the local plasma and the anode will be concentrated within the sheath itself. The current to the anode can only increase with voltage in proportion to the surface of the outer edge of the sheath, hence it is the increase in sheath voltage which changes the effective area. However if the diameter of the electrode is much greater than the thickness of the sheath, as in our case, the current to the anode cannot increase significantly with rising potential. As the sheath is starved of charge carriers the sheath breaks down to form a highly luminous double layer region with an inner positive space charge and an outer negative space charge which can extend several centimeters from the cathode. The outer edge of the double layer then becomes a virtual anode and its area grows with demanded current. The formation of the double layer marks the cathodes entry into plume mode. Rudwan[187] has described in detail the formation of the double layer and preceding potential profile.

The efficiency of ionization within the cathode in spot mode is hypothesized to be sufficient to emit ions to neutralize the plasma in the cathode-to-keeper gap. In contrast, plume-mode emission exhibits both a luminous plume downstream of the cathode and large current and voltage oscillations at several megahertz, typically. Transition into plume mode is inevitable as the discharge current or mass flowrate is reduced, and where we expect to attain the higher specific impulse. Factors which will enhance ionization processes within the sheath however are the sheath thickness (hence the mean free path of electrons), neutral density (which will determine the collision mean free path and the ionization probability) and the anode potential (which will determine the primary electron energy). Observations have seen that the virtual anode does not extend more than a few cm from the cathode. [188] This is likely due to the neutral density rapidly falling as the plume expands into vacuum. One way in which to maximize the ionization rate in the double layer is to restrict the free expansion of the flow and maintain higher ion/neutral densities in the double layer region. A conical nozzle offers the benefit of constricting the flow close to the double layer where the majority of ionization occurs, yet with sufficient divergence angle the anode also offers significant area for electron collections from the downstream negative sheath.

As already mentioned, ionization rate can also be increased by increasing the anode potential, which when operating in a current limited mode is of course a discharge response to maintain operation rather than a controlled variable. Since the fraction of high energy ions produced by plasma oscillations is only a small fraction of the total flow the electrostatic accelerating mechanism is not likely to be dominant. If electrothermal or electromagnetic mechanisms are considered dominant then the thrust mechanisms are likely to be a function of the discharge current rather than the discharge voltage. With this in mind one way to increase thruster efficiency at a given current and mass flowrate is to reduce discharge voltage through anode design. The significant increase in discharge voltage distinctive of plume mode drastically increases the discharge power for a fixed discharge current based on the relationship:

$$P_D = I_D V_D \tag{2.12}$$

In addition, the extension of spot mode like operation will inevitably enable operation at lower mass flowrates and increased specific powers (J/mg) with higher with specific impulse. To summarize, use of a conical anode on hollow cathode thrusters should:

1. Increases the attainable specific impulse
2. Reduce the discharge voltage for a set current and flowrate
3. Decrease the discharge power and increase thrust efficiency
4. Maintain spot mode operation to lower mass flowrates
5. Reduce voltage fluctuations synonymous with plume mode
6. Ultimately enable operation down to lower mass flowrates
7. Enable higher specific powers

For these reasons the author decided that focusing on a conical anode design in order to improve the efficiency of the cathode thrusters would be of significant benefit.

CHAPTER 3

HOLLOW CATHODE THRUSTER CONSIDERATIONS

This chapter describes the considerations given to the T6 hollow cathode thruster design but also describes the reasoning behind the selection of the T5 hollow cathode as a more ideal candidate microthruster. The means by which to control the operating mode are presented and specifics of anode design are covered including anode-plasma interactions and cooling requirement. Although no physical alteration of the cathode bodies was attempted, the thruster design in this case primarily considers the influence of the downstream anode design based on the current understanding of hollow cathode operation.

3.1 ELECTRON FLUX

The cathode operating power is given by Equation 2.13. Discharge power can thus be decreased for the same discharge current level by decreasing operating voltage. As discussed in Chapter 2, this can be accomplished by increasing the available contact area between the anode and the plasma to aid in current collection and maintain passive current collection. The thermal current for ions and electrons to thermally drift to the anode surface is given by Equation 2.11.

Assuming a quazi-neutral plasma, the plasma density, n_i, can then be calculated by assuming the mass flowrate of propellant equals the thermal efflux through the orifice cross section, ie. assuming the drift velocity is equal to the thermal random velocity in the direction of the outlet with net flux equal to the flow rate. Ion flow is diffusion limited, because of the short mean free path, < 10^{-5}m, for resonant charge exchange with neutrals.[185] Ion temperatures are used for calculation of the plasma density since ions have much lower mobility and thus will drive the density function. At the outlet where a sudden change in plasma density is expected, this can serve as a first approximation.[90]

$$n_n + n_i = \frac{\dot{m}}{A_0 e}\left(\frac{eT_i}{2\pi m_i}\right)^{-1/2}$$

(3.2)

At the anode surface the discharge current is given by:

$$I_A = \int J_i + J_e dA_A$$

(3.3)

Thus for a cylindrical anode:

$$I_{e,i} = J_{e,i}\pi d_A L_A$$

(3.4)

$$I_A = I_e + I_i$$

(3.5)

Again it should be noted that in spot mode operation the local plasma potential is greater than the anode potential in order that electrons be repelled from the surface due to sufficient current collection by the passive mechanism. In plume mode the local plasma potential is negative relative to the anode such that electrons are accelerated to enhance ionization. In this case, at the spot/plume mode transition point of interest to us, the local plasma potential is equal to the anode potential thus the thermal flux current collection mechanism is justified. Thus for a cathode to operate in spot mode with sufficient passive current collection,

$$I_D \le I_A$$

(3.6)

3.2 IONIZATION FRACTION

In cathode development for ion thrusters, one parameter of concern is the propellant mass utilization fraction or ionization fraction. This parameter is defined as the ratio of ion current leaving the cathode over the equivalent current of 100% singly-ionized mass flow. The ratio of orifice diameter to orifice length is optimized for a range of operating conditions to provide high gas utilization without driving up the cost of ion production (energy cost per ion) since the ion flux in hollow cathodes contribute to the total ion population within the discharge chamber. The ionization fraction has been shown to approach unity within the orifice of small hollow cathode such as the T5, however studies have shown that downstream, mass utilization does not exceed 10%.[28] Such change in ion ionization fraction is likely caused by the fact that most of the ions created in the cathode orifice are neutralized before they can escape through the keeper orifice, even though it is located ~2mm downstream of the cathode. Inside the cathode, and even more so in the expanding plume, the electron temperature *Te* is much lower than the first ionization potential for xenon (12.13eV). Recombination of ions and electrons within the emitted plasma is thus bound to be significant.[67]

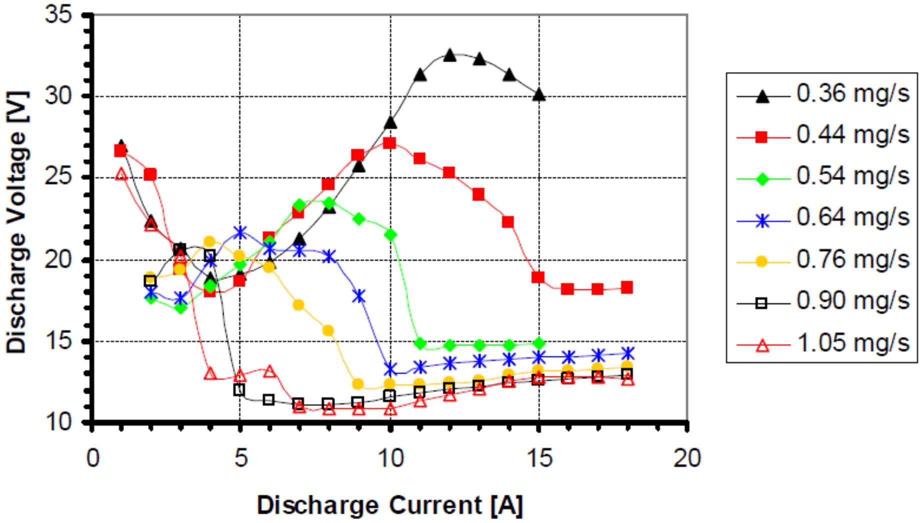

Figure 19 Discharge voltage data from testing by Gessini for the T6 cathode with a 10mm x 10mm cylindrical steel anode on argon

Transition characteristics of Gessini's T6 cathode are shown in Figure 19. With regard to electron temperatures, Pottinger[141] conducted optical probe studies on the T6 hollow cathode at various positions along the emitter length. For a cathode operated at 5A discharge current at 1.1mg/s mass flow rate of argon, probes positioned at 2.7mm upstream and 1.1mm upstream of the cathode orifice determined electron temperature to be ~0.6eV and ~1.0eV respectively. Electron temperature did not vary significantly for discharge currents between 2A to 10A. These measurements show good agreement with the spectroscopic measurements of Malik.[142] Using the value of electron temperature of 1eV close to the orifice, assumption of ion temperature ~0.1eV and Equations 2.11-3.6, the required plasma density for plume mode transition at 5Amps at 0.5mg/s argon for the T6 cathode can be evaluated based the geometrical configuration of Gessini's anode. The ionization fraction required to satisfy the passive current condition of 5A at the anode surface is shown in Figure 20. Since there are no direct measurements of ion temperature at this condition yet it strongly influences plasma density, the ionization fractions for ion temperatures of 0.1eV, 0.2eV, 0.4eV and 0.8eV are calculated, corresponding to heavy particle temperatures of 1160K, 2321K, 4642K and 9284K respectively.

Interestingly increased ion temperature, while being important for the electrothermal thrust production mechanism, serves to lower the plasma density for a particular anode by increasing ion velocity and thus decreases J_e, thus the theoretical ionization fraction required to give spot mode increases. While ion temperature has a strong influence on the plasma density ion flux to the anode remains negligible in terms of constituting discharge current, given the low ion mobility and show in Figure 21. Electron temperature on the other hand does have a strong influence on the total discharge current and the current collection process.

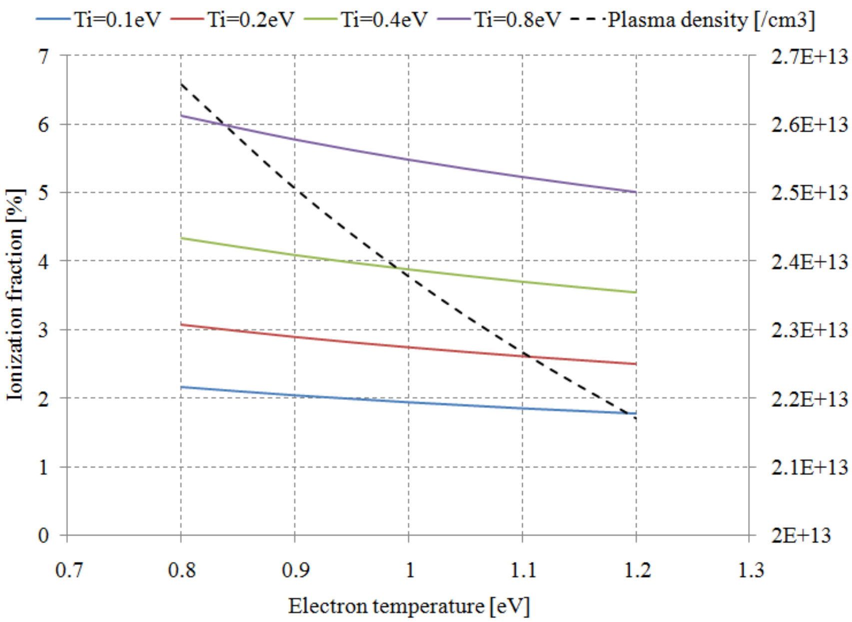

Figure 20 Calculated ionization fraction required to match empirical observations of Gessini for transition to plume mode at 5A and 0.5mg/s with a circular anode of 10mm diameter and 10mm length at respective electron and ion temperatures

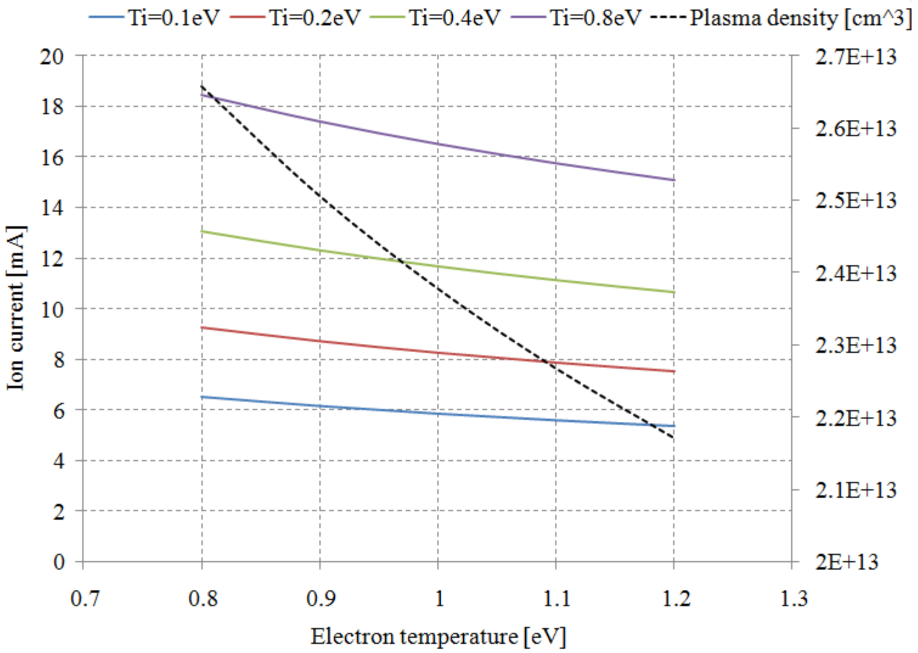

Figure 21 Passive ion current for varying ion and electron temperatures

The increase in ion current with decreasing electron temperature comes about by the increase in the required ionization fraction to give the 5Amps of passive discharge current. Based on the analytical analysis mentioned previously the ionization fraction bares the relation:

$$\alpha \propto \frac{I_D}{A_A}\left[\frac{T_i}{T_e}\right]^{0.5} \tag{3.7}$$

Since T_i, T_e and the attained ionization fraction α are largely functions of the cathode operating regime the most obvious way to increase the maximum passive current a cathode is capable of carrying is by increasing the available anode area to enhance electron collecting area. However, if plasma density significantly decreases (due to decreasing α) downstream of the orifice, so does the anodes capacity to passively collect current from the plasma. Measurements by Goebel shown in Figure 22 confirmed by the plasma models of Mikellides[143] have shown that plasma density can decrease by two orders of magnitude only 8mm downstream of the orifice in the NSTAR discharge cathode. The NSTAR cathode in this case is a useful comparison since the cathode is of identical diameter to the T6 cathode used in our experiments and previous HCT experiments by Gessini on which our model is based.

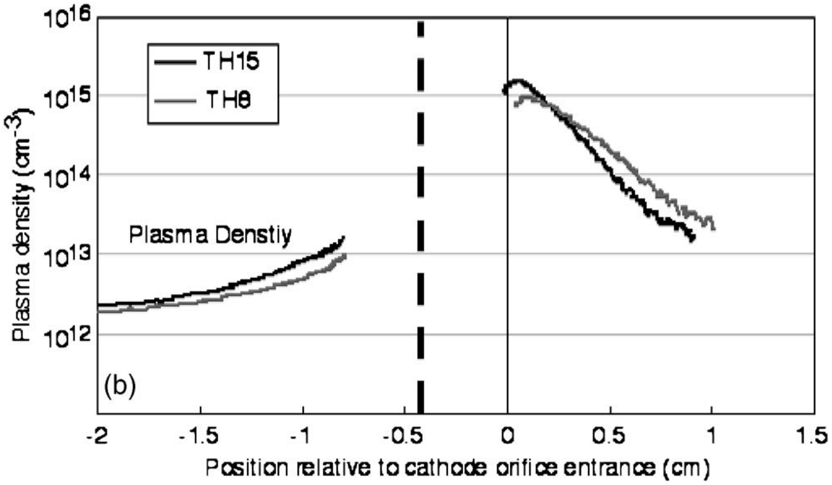

Figure 22 Plasma density falloff downstream of the cathode orifice in the 0.635cm NSTAR discharge cathode with a 1mm orifice[144]

Gessini's anode was mounted at a centre point of 1cm downstream of the cathode. The plasma densities calculated by our model for ion temperatures between 0.8-1.2eV match closely with the observed plasma densities found 10mm downstream of the NSTAR cathode. In this case electron temperatures between 0.8-1.2eV give plasma densities of 2.17-2.65x10^{13}cm^{-3} respectively.

3.3 CONTROLLING SPOT TO PLUME MODE TRANSITION

Gessini also shows the typical transition profile whereby the increased discharge current extends the spot-to-plume mode transition to lower flowrates. Plasma models of Mikellides for the NSTAR cathode operating at 25A on 5sccm of xenon (0.35mg/s) have suggested a maximum heavy particle temperature of 2640K or 0.227eV (only 1300K above the cathode body temperature) thus in the T6 cathode, the ion temperature even for higher currents would not seem to vary enough to have a significant influence on the transition point. Since Pottinger has also shown that electron temperature does not vary significantly for all discharge currents in the T6 cathode in spot mode we can state that the increase in discharge current must be primarily due to increasing ionization fraction at the anode boundary.

Using our analytical model (Equations 2.11-3.6), the theoretical average ionization fraction required to give passive current equal to the discharge current at the spot-plume mode transition points of Gessini (shown in Figure 19) are shown in Table 1. This is calculated using an electron temperature of 1eV, ion temperature of 0.227eV and a cylindrical anode of 10mm diameter and 10mm length.

Mass flowrate [mg/s]	**Discharge current [A]**	**Transition voltage point [V]**	**Theoretical ionization fraction [%]**
0.36	>15	<30	>13.46
0.44	15.4	18.5	11.3
0.54	11.1	14.9	6.64
0.64	9.9	13	5.00
0.76	7	12.2	2.97
0.9	4.9	12	1.76
1.05	4	13	1.23

Table 1 Calculated ionization fractions to meet spot-plume mode transition critical current

These values are extrapolated between 2-35 Amps in Figure 23. R^2 values for the critical mass flow/discharge current and ionization fraction of 0.998 and 0.985 respectively indicate excellent fits to the extrapolations and show that for Gessini's anode configuration, operation in spot mode down to flowrates below 0.3mgs^{-1} would require discharge currents in excess of 30Amps. The majority of Gessini's data did not extend beyond 18Amps, presumably because of overheating of the anode due to the large amount of heat deposition at high currents and voltages. In this case the ionization fraction at such high current densities would be >30%. The critical mass flowrate for spot to plume mode transition bares the empirical relationship:

$$\dot{m}_{crit} = 0.129 I_{crit}^{1.63}$$

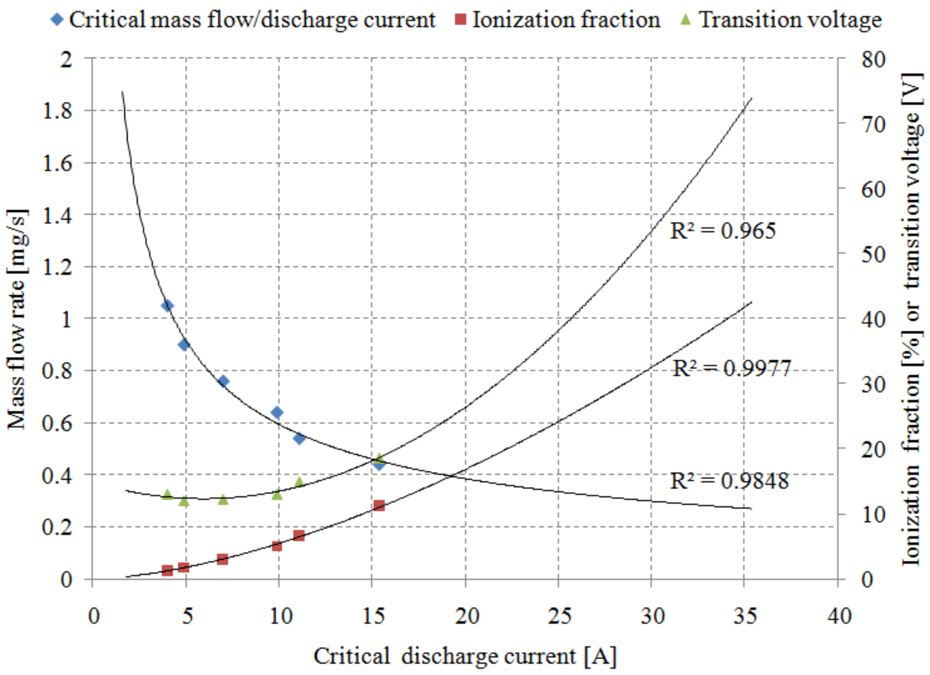

Figure 23 Critical current/mass flowrate for maintenance of spot mode with argon along with theoretically calculated ionization fraction for Gessini's 0.5mm orifice cathode on argon

While increasing the discharge current can enable spot mode operation at lower mass flowrates it cannot, for this anode configuration, stop the increase in transition voltage which would be prohibitively large (>25V) above 20Amps for reasonable cathode life while in spot mode. Since the increase in discharge voltage is not due to the formation of an additional sheath at the anode since the cathode is still in spot mode it is reasonable to suggest that the increase in transition voltage with discharge current is due to the increase in voltage drop within the cathode itself. This can be attributed to the Ohmic drop over the orifice which follows the Ohmic relation:

$$\Delta V_{oh} = \frac{J_e L_{or}}{\sigma} \tag{3.8}$$

Where,

$$J_e \approx \frac{I_D}{A_{or}} \tag{3.9}$$

Since we shall be using a T6 cathode with a 1mm orifice rather than a 0.5mm orifice the Ohmic drop could be up to a factor of 4 less than in this 0.5mm cathode assuming the resistive parameters do not vary significantly.

This data confirms that the model is a reasonable predictor of plume mode transition and strengthens the theory that the plume mode transition occurs when $I_D. \geq I_A$. Figure 24 shows the plasma density falloff external to the keeper in the larger 1.5cm NEXIS cathode which contains a 2.5mm orifice. While being of significantly different geometry to the T6 cathode, the NEXIS data highlights the large drop in plasma density downstream of cathodes even at currents as high as 25Amps.

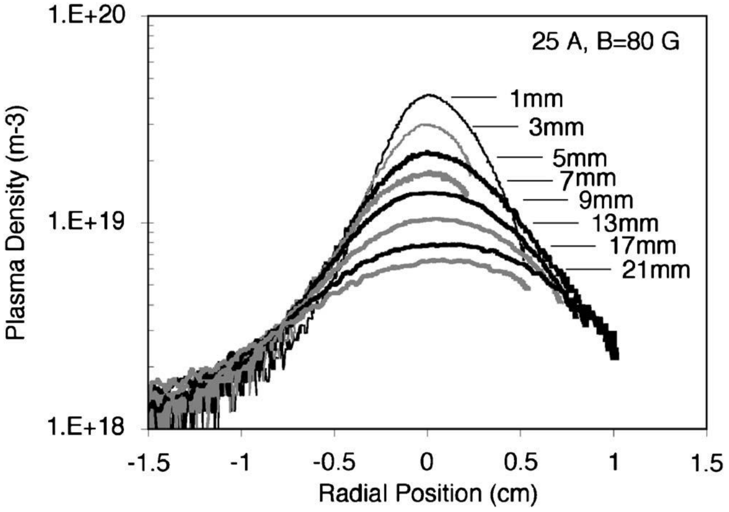

Figure 24 Radial plasma density profiles for different distances from the keeper exit for the 1.5 cm NEXIS cathode operating at 25 A of discharge current.

3.4 ANODE OPTIMIZATION

3.4.1 GEOMETRY

These data suggest that the most effective design of anode for maintenance of spot mode in HCTs may be one which presents as greater area - plasma density product as possible. These two requirements are somewhat contradictory since, for instance, increasing the diameter of a cylindrical anode while increasing the available contact area also increases the path length for electrons and ions to traverse from the orifice, and as we have seen, ion recombination occurs quickly as the plasma exits the orifice, thus plasma density significantly drops. The problem of optimizing geometry may therefore be a complex one based on maximizing passive current collected for a range of operating conditions in which plasma density, ionization fraction, electron and ion temperature will vary as a complex function of the discharge current. Such optimization would require a significant modeling effort. It was thus decided to approach the problem by initially designing an enclosed conical anode with a large surface area available for current collection, this would be designated the T6LA (large area) cathode. Initial investigations were made into the influence of various divergence angles of 15°, 30°, 45°, 90° and it was found that a 30° degree divergence angle gave the lowest discharge voltages at a set current and mass flowrate. The general dimensions are shown in Figure 25 with a solid model shown in Figure 26.

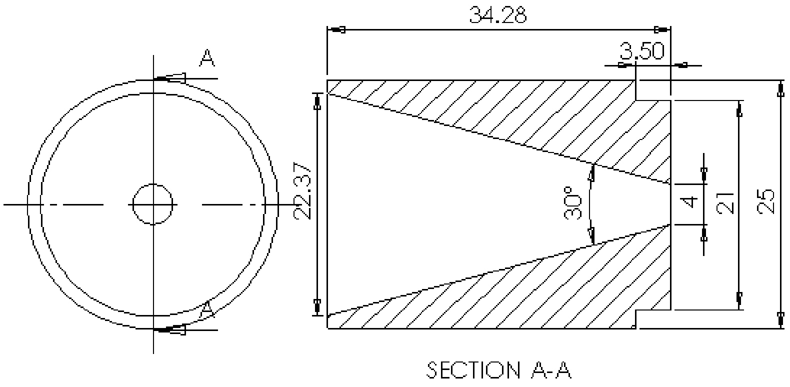

Figure 25 Section view of the T6LA cathode

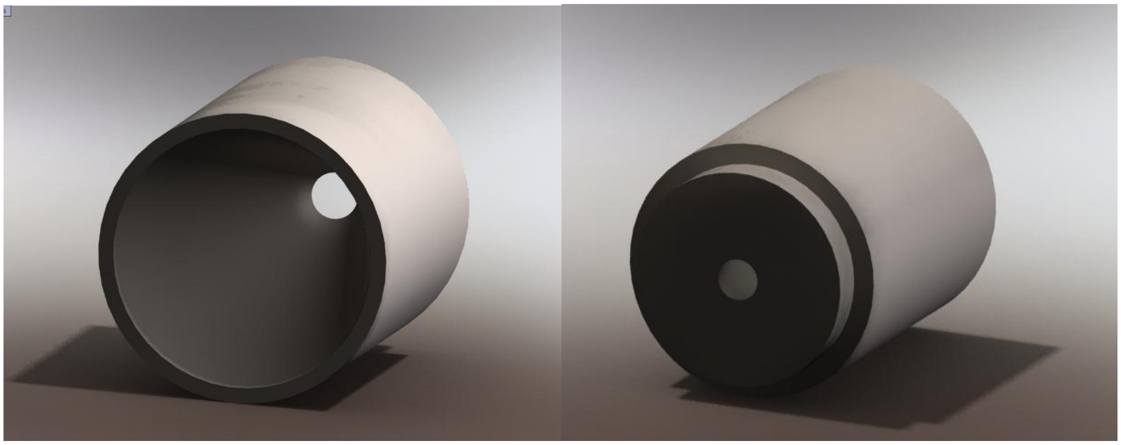

Figure 26 Front and rear face solid model views of the T6LA anode

The contact area of the anode A_A on the basis of the half divergence angle is given by:

$$A_A = \pi r_d \left(\frac{r_d}{\sin\theta} \right) - \pi r_u \left(\frac{r_u}{\sin\theta} \right)$$

(3.10)

$$A_A = \pi \left(\frac{r_d^2 - r_u^2}{\sin\theta} \right)$$

(3.11)

The T6LA cathode, offers 14.70cm^2 of anode contact area, compared to the 0.78cm^2 in Gessini's experiments. An enclosed supporting structure was also designed to position the anode in front of the cathode. A schematic of this design with general dimensions is shown in Figure 27.

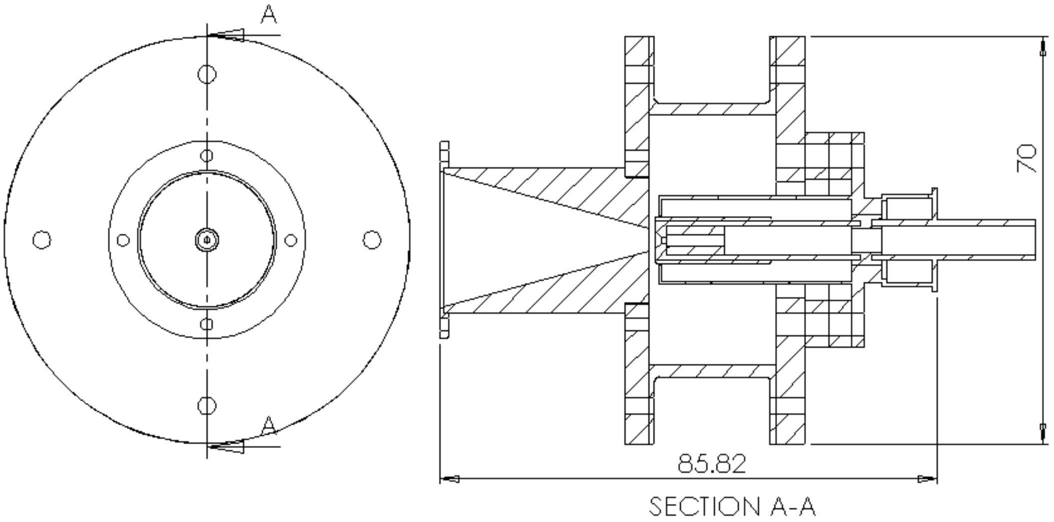

Figure 27 T6LA thruster assembly schematic with general dimensions

Besides the electrically isolating ceramic mounting at the rear of the assembly and the anode itself, the rest of the assembly (anode mounting and cylindrical mounting support) was constructed of steel machined to a high quality finish and polished in order to minimize radiative losses. The cylindrical mounting support was constructed with a thin wall in order to minimize conductive losses. Grafoil gaskets of 0.5mm on all major interfaces provided a hermetic seal to ensure an enclosed design with the full mass flow exiting through the anode orifice. The anode assembly is shown in Figure 28

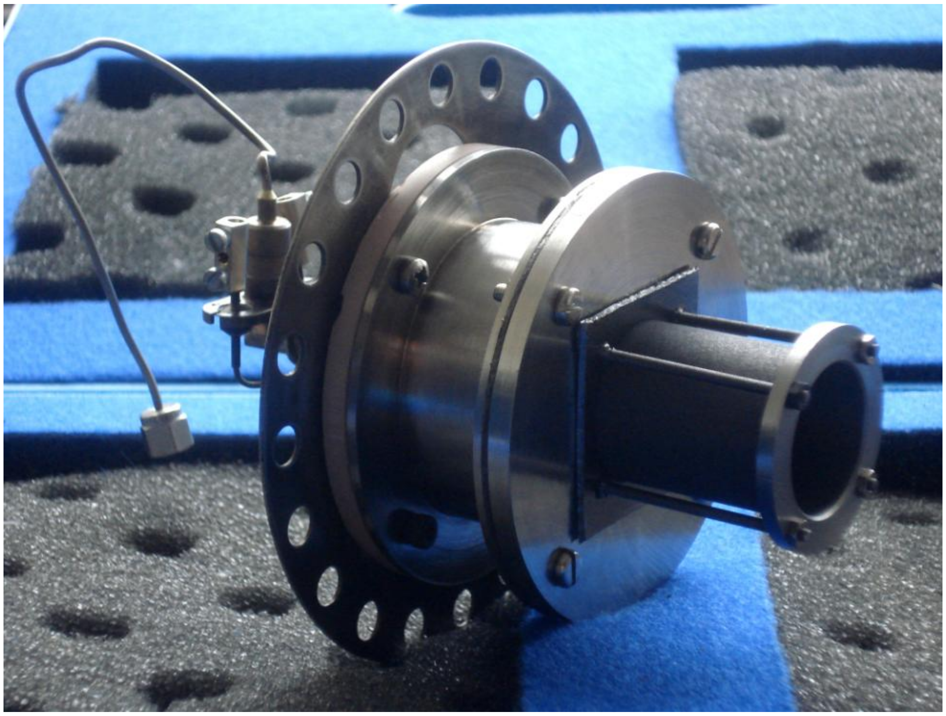

Figure 28 T6LA hollow cathode thruster assembly

3.4.2 ANODE MATERIALS

The anode material is also a driver of operating temperature since thermal radiative power output scales linearly with the materials emissivity. Above 2300K, the total emissivity of refractory metals traditionally used in hollow cathode manufacture is shown in Table 2 as well as the properties of carbon graphite.

Refractory	**Total emissivity above 2300K**	**Thermal Conductivity [W/m-K]**	**Maximum working temperature [°C]**
Molybdenum	0.3	138.0	2617
Tantalum	0.361 – 0.350	83.7	2996
Tungsten	0.37 – 0.36	163.3	3370
Carbon graphite	0.9	24.0	3650

Table 2 Refractory material properties[145]

While also being prohibitively expensive to use in our experiments, the emissivity of all refractory metals is relatively low which generally leads to the use of high emissivity coatings utilizing zirconium, chromium, and cerium to improve the heat shedding capabilities of refractory metals. The only other refractory material capable of operating above 2000K with a high emissivity on the other hand is carbon graphite. Graphite has a higher sputter resistance than all refractory metals,[146] [147] is generally lower cost, is highly machinable and has been used extensively over the last decade for the manufacture of screen, accel. and decel. grids as well as keepers in modern gridded ion thrusters.[147] [148] [149]. The lower thermal conductivity and high emissivity of graphite also aids in maintaining radiative heat shedding rather than conductive heat shedding to the cathode assembly which would serve to heat the thruster and supporting structure. Low porosity graphite was thus selected as the material of preference for anode manufacture.

3.4.3 THERMAL MODEL

Typically no more than 1-Amp is normally drawn to the keeper electrode, however in our case we shall be drawing much higher currents. In anode design we must thus also consider heat dissipation and cooling of the anode. Since active cooling of the anode would be an over complication in design, particularly if we were moving towards flight hardware, here we will assume that the anode can only be cooled by conduction to the anode mountings and radiation to the vacuum. The power balance within the hollow cathode plasma is given by Equation 2.10. In this case the integrals of J_i and J_e are over the cathode and anode area in contact with the plasma. The energy absorbed by the anode from the electron current, ion current and radiative heat transfer from the plasma is given by:

$$\int J_i \left(\varepsilon_i + \frac{5kT_i}{2e} \right) dA_A + \int J_e \left(\frac{5kT_e}{2e} \right) dA_A + q_r + q_c \tag{3.12}$$

Where the total discharge current is defined as:

$$I_D = \int J_i dA_A + \int J_e dA_A \tag{3.13}$$

In this case this energy will be rejected radiatively following the Stefan-Boltzmann law and conductively along the anode housing following Fourier's law, thus:

$$\int J_i\left(\varepsilon_i+\frac{5kT_i}{2e}\right)dA_A+\int J_e\left(\frac{5kT_e}{2e}\right)dA_A+q_r+q_c=\int \varepsilon_A\left[T_A\right]\sigma T_A^4 f_{A\to A}dA_A+k\left[T_A\right]\int\Delta T dA_A \tag{3.14}$$

Where $f_{A\to A}$ is the view factor from the anode unit area to free space, q_r is the radiative flux from the plasma to the anode and q_c is the radiative flux from the high temperature cathode body to the anode. This is in fact an over-simplification of the problem since there are many other important heat transfer routes not defined here such as the radiative and conductive transfer from the anode assembly to the cathode and supporting structure. Even so the evaluation of this problem to achieve a steady state solution is extremely mathematically challenging given the calculation of view factors, changes in thermal gradients, the fact that the analysis is an open radiation system with heat transfer to internal surfaces and as well as ambient vacuum. The evaluation of the q_c component is also an extremely complex problem. In this case COSMOS Flow Works was employed for the calculation of anode temperature.

In order to evaluate the anode temperature heat flux parameters had to be defined which from Equation 3.14 requires the discharge current and the electron temperature as well as the current distribution with respect to anode area to be defined. Ion current is over 2 orders of magnitude (mA/A) lower than the electron current and ions are 2 orders of magnitude lower in temperature hence even thought ions also impart their ionization energy (~12eV), their contribution to the anode heat flux can be neglected. Since in this case we are building a thermal model and not a plasma model we assume that electrons are collected over the entire surface of the anode with constant J_e. In reality this will vary with the attachment point of the current, thus the anode will receive non-uniform heat input. However, since the anode will have a relatively high degree of conductivity and will be small in size, the peak anode temperature should not be substantially different from the mean anode temperature.

So far we have dealt with maintaining operation in spot mode with a low electron temperature, however investigations have shown a two-group electron energy distribution in the 'plume mode'[150 151] for which the anode must be able to deal with as a worst case scenario. These data correspond to the T6 cathode operation data of the references141, 152 and153. According to the data of spectrographic measurements, the plasma inside the cathode in the 'spot mode' is not in a state of LTE[153, 154] and the temperature of the Maxwellian electrons is in the range *T*e ≈ 0.8–

1.1eV. Thermionic electrons accelerated in the cathode layer (≈ 3–5eV) consume their energy for the ionization and excitation of Xe atoms and form the main part of fast electrons in the internal cathode plasma. The slow groups of electrons appear by the ionization processes in the plasma volume and have the same temperature (Te ≈ 0.8–1.1eV) as the slow electrons in the plasma of the external area. The electrons of the slow group have on approximately Maxwellian distribution whilst the fast moving electrons are mono-energetic.

For the evaluation of anode temperature a solid mesh model was constructed with the exact dimensions of the chamber, thruster backplate cathode anode assembly and anodes enabling Finite Element Analysis (FEA) of all volumetric and surface elements. The process of constructing the model is described below.

A. A fine mesh was constructed with a minimum element size much smaller than the cathode orifice diameter since the orifice and insert provide important radiative and conductive surfaces. A smaller mesh yields better results, but takes longer to mesh as well as analyze.

B. A surface contact condition was defined between all adjacent surfaces allowing for a contact thermal resistance and thermal flux between all contacting surfaces.
C. All surfaces were defined as radiative to one another and to the ambient environment and all contacting volumes were defined as thermally conductive.

D. All materials were specified from the COSMOS Works materials library.

The theoretical thermal power of the convected electron flow calculated from equation 3.13 based on discharge current and spot/plume mode electron temperatures is shown in Table 3. The peak steady state temperature calculated by the model as a result of this heat flux in a vacuum environment is shown in Table 4. Figure 29 shows an example thermal profile for the T6 LA cathode with a peak anode temperature of 1058°C.

Discharge current [A]	Thermal heat flux [W]	
	Spot mode Te = 1eV	Plume Mode Te = 5eV
5	12.51	62.53
10	25.01	125.06
15	37.52	187.59
20	50.02	250.11
25	62.53	312.64
30	75.03	375.17

Table 3 Convected heat flux for spot mode and worst case plume mode

Discharge current [A]	Peak Anode temperature [°C]	
	Spot mode Te = 1eV	Plume Mode Te = 5eV
5	473.1	707.5
10	562.6	841.4
15	622.7	931.1
20	669.1	1000.5
25	707.5	1058.1
30	740.5	1107.3

Table 4 Peak anode temperatures calculated from thermal model as a result of electron convective heating

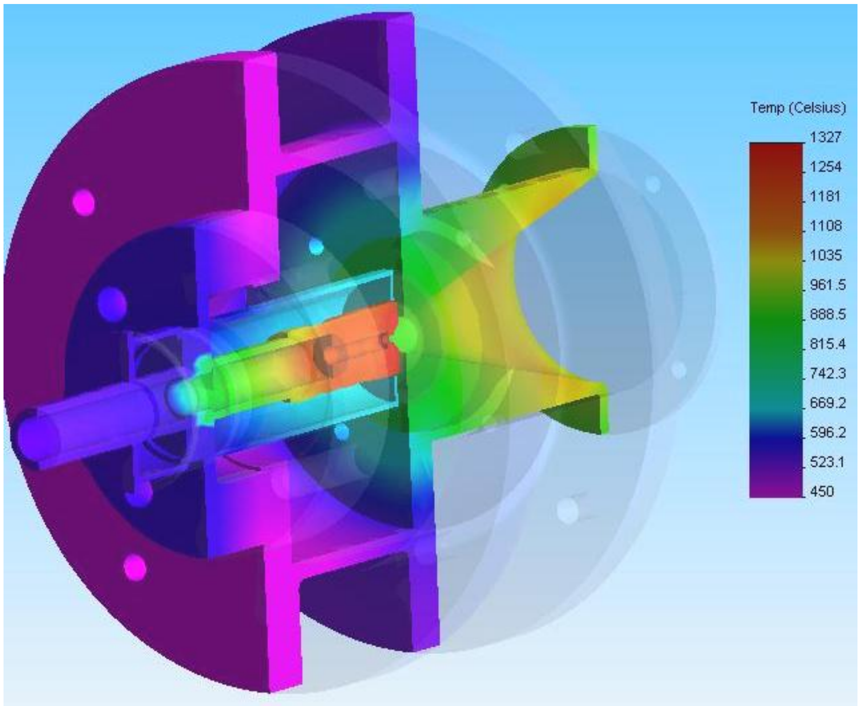

Figure 29 T6 Hollow cathode thruster assembly thermal model operating at 25A in plume mode with an electron temperature of 5eV

3.5 IMPROVEMENTS IN EFFICIENCY AND THE T5 CATHODE

As we have already stated the operating regime within hollow cathodes acts to maintain sufficient emitter temperatures for thermionic emission by balancing power deposition into the cathode surface with cooling by particle efflux and heat transfer to the surroundings. Since for the cathode to maintain operation at thermal equilibrium, the thermal energy liberated from the internal cathode surface by the electron flux must be (primarily) balanced by energy input from ion bombardment and electron back streaming. From Equation 2.10, electron thermal flux is a significant loss mechanism. Table 5 shows the electron thermal heat flux for various discharge currents based on Equation 3.13 for argon, with both a best case 1eV and worst case 5eV electron temperature along with the operating powers recorded by Gessini for the respective current condition in spot and plume mode. Estimates of the percentage power loss due to the convective heat flux are also given.

Discharge current [A]	Calculated thermal heat flux [W]		Experimental comparisons			
	Spot mode $T_e = 1\text{eV}$	Plume Mode $T_e = 5\text{eV}$	Spot mode operating power [W]	Electron heat flux constitution [%]	Plume mode operating power [W]	Electron heat flux constitution [%]
5	12.51	62.53	60	20.9	105	59.6
10	25.01	125.06	110	22.7	245	51.0
15	37.52	187.59	187.5	20.0	450	41.7
20	50.02	250.11	No data			
25	62.53	312.64				
30	75.03	375.17				

Table 5 Thermal flux for various discharge currents with both a best case 1eV and worst case 5eV electron temperatures with the operating powers recorded by Gessini for the respective current condition in spot and plume and the percentage power loss attributable to electron thermal flux.

In spot mode the theoretically calculated electron thermal losses (power convected away from the cathode) represent a minimum 20% of the empirically derived total cathode power. During plume mode however, where electron temperatures have been measured beyond 5eV for cathodes of similar geometry,[155] theoretical electron thermal losses can represent up to 60% of the total cathode power. In reality the convected power may lay between these bounds, however, this analysis does emphasize that the discharge current, particularly in plume mode, is a major source of energy loss, and thus efficiency loss for the cathode. Although some mechanisms of ion acceleration scale quadratically with discharge current such as MHD acceleration (which is only effective at high currents), electrothermal type mechanisms are more likely to scale with the thermal power dissipated into the plasma. Energy input to the plasma can be attributed to the energy of thermionically emitted electrons accelerated through the cathode fall (the sheath voltage drop between the cathode and the adjacent plasma) and through Ohmic (joule) heating by thermionic and plasma electrons given by:

$$\int J_{th}\left(V_p + \frac{5kT_e}{2e}\right)dA_{em} + \int \frac{{J_D}^2}{\sigma}\, dV$$

(3.15)

The thermal energy removed from the emitter by the discharge current is given by:

$$\int J_{th}\left(\phi_{eff} + \frac{5kT_c}{2e}\right)dA_e$$

(3.16)

Since the cathode fall generally remains between 8-10V it is reasonable to suggest that by increasing cathode resistance $\left(\frac{1}{\sigma}\right)$ and decreasing the discharge current, the same power can be deposited in to the plasma at reduced discharge current. In this case however thermal energy loss will be reduced due to the lower thermionic current thus improving efficiency.

The current density within the orifice of the cathode is orders of magnitude higher than in the cathode body therefore it is reasonable to assume the majority of resistive dissipation occurs within the orifice. Assuming the plasma resistance is constant, the voltage drop over the orifice is given by classical Ohms law:

$$\Delta V_{oh} = \frac{J_e L_{or}}{\sigma}$$

(3.17)

Where,

$$J_e = \frac{I_D}{A_{or}}$$

(3.18)

In this case the orifice resistance can be increased by using a smaller or longer orifice. We have seen this effect with the smaller orifice used in some of Gessini's T6 experiments which operated at higher voltage for the same discharge current. Orifice resistance can be approximated to that of a fully ionized gas since the conductivity of fully ionized plasma is considered to be independent of the ion density. [156] Conductivity of the plasma based on electron-electron collisions is given by:

$$\sigma = \frac{1.53 \times 10^{-2}}{\log \Lambda} T_e^{3/2}$$

(3.19)

The plasma parameter Λ is a slowly varying function with a value ~ 10.

It is sensible to suggest that the thermionic loss mechanism is a significant factor in the very low thrust efficiencies shown in T6 cathode performance and reducing the discharge current while maintaining the same power input to the plasma by the method described is likely to substantially improve thrust efficiency. For this reason a T5 cathode was acquired from QinetiQ Space Exploration Technologies Division to test this theory. The orifice within the T5 cathode (0.25mm) is of much smaller diameter than the T6 cathode (1mm) and operates at much higher current densities. It was thus considered that the T5 cathode may well create a more efficient microthruster and show improved thrust efficiencies over the T6 cathode. The comparative orifice resistance for the T5 and T6 cathodes as a function of electron temperature based on Equations 3.16-3.18 is shown in Figure 30.

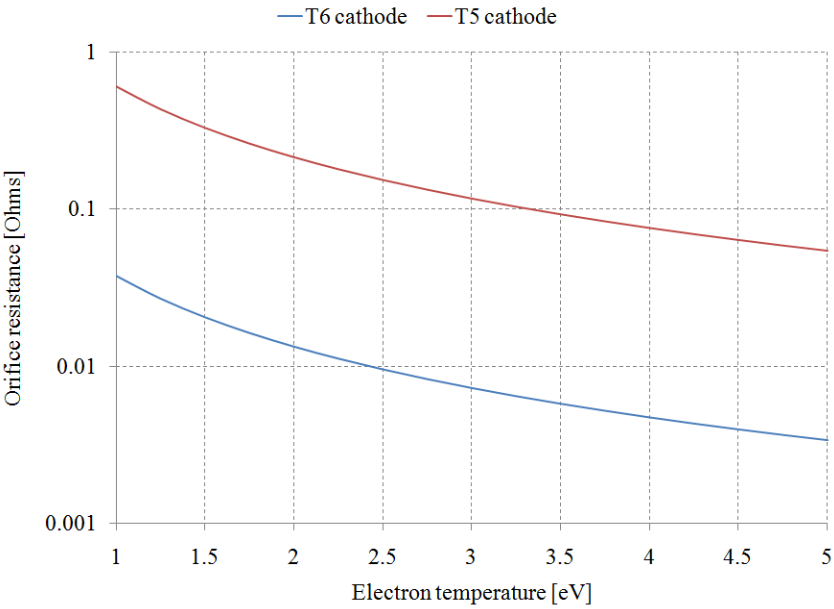

Figure 30 Orifice resistance for the T5 and T6 cathodes as a function of electron temperature.

CHAPTER 4

THRUST MEASUREMENT SYSTEM DEVELOPMENT AND COMMISSIONING

A major part of the research project was the work associated with the design, fabrication and commissioning of the experimental thrust measurement facility. This chapter describes general apparatus used during testing and the philosophy behind the thrust measurement system. The chapter also describes modification and solutions developed to remedy some of the technical challenges encountered during initial testing.

4.1 THE T5 AND T6 CATHODES

The T5 cathode characterized in this experiment is the STRV-A1 (Space Technology Research Vehicle) DRA (Defense Research Agency) neutralization flight-spare launched in June 1994. This included an experiment to allow the hollow cathode assembly to demonstrate spacecraft electrostatic discharging.[157] The cathode is rated at a maximum DC current of 3.2A at flow rates typically 0.04 -1mgs^{-1} operating below 90W and is essentially standard. The T5 cathode was originally designed for the main discharge cathode in the UK-10 ion engine and has been extensively characterized.[158] The cathode contains a tungsten dispenser, 1.0mm i.d. x 2.8mm o.d. x 11mm, impregnated with a mixture of barium-oxide, calcium oxide and aluminates (BaO: CaO: Al_2O_3), and maintains a working temperature ~ 1000°C. Initial hollow cathode designs had the interior surface simply coated with a triple oxide coating. At maximum rated current capacity, the T5 dispenser emits with a current density of at least 400A.cm^{-2}. A solid molybdenum tip, electron beam welded to the cathode body, contains an axial orifice 0.23mm in diameter and 1mm long.

The heater wire is embedded in a flame sprayed alumina. The T5 cathode was used in two configurations, the T5 flat plate orifice (FO) shown in Figure 31 and the T5 conical anode (CA) configuration using the anode designed in Chapter 3 for the T6 cathode. In the case of the T5 FO the open keeper has a 3mm diameter aperture and is mounted 3mm downstream of the cathode tip with the whole assembly mounted on a UK-25 ion thruster back-plate. In typical hollow cathodes a keeper electrode usually draws approximately 1-Amp of current, however in this study the cathode is operated in an open-diode configuration with the full discharge current being drawn to the keeper, which is now termed the anode. Previous studies on this type of hollow cathode have incorporated a much larger anode disk and a secondary discharge between the keeper and the anode and also an applied magnetic field to simulate a Kaufman ion engine environment. Open-diode configuration is more representative of a standalone microthruster configuration with no need for a coupled discharge.

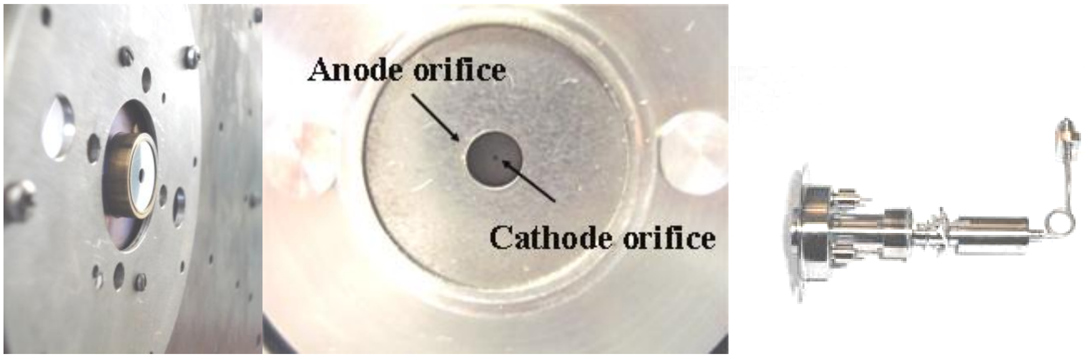

Figure 31 T5FO Hollow Cathode Assembly

The T6 Hollow Cathode used in this experiment is a ROS-2000 HET (Hall Effect Thruster) neutralizer developed by QinetiQ for Astrium under contract to ESA and shown in Figure 32.

Figure 32 ROS-2000 HET neutralizer

The cathode is rated to a maximum of 15-Amps with extended operation up to 30-Amps with flow rates ranging from 0.1-3mg/s, typically operating at a few hundred watts. The tungsten dispenser is 2mm i.d. x 5mm o.d. x 10mm, with an emissions area over seven times that of the T5, while maintaining current densities of at least 1500 $A.cm^{-2}$ at maximum rated current capacity. The cathode is constructed from a solid tantalum piece to avoid the risk of tip weld failure, with a 1mm axial orifice through a 2mm thick orifice plate with a 45° chamfer at the exit to a depth of 1mm leaving an orifice of 1mm length. The heater wire in the T6 cathode is mounted on a machinable ceramic developed more recently for ease and consistency of manufacture. In this case the T6 anode and support housing has been specially designed to maximize available anode-plasma contact area on the basis that this parameter has a strong influence on the minimum attainable flow rate and in reducing the discharge voltage. The T6 cathode is mounted to a ceramic insulator which also connects to the anode housing. A 25mm diameter 30° conical diverging nozzle constructed from graphite with a 4mm orifice at the upstream end, as discussed in Chapter 3, is mounted 0.5mm in front of the cathode and axially aligned. All flanges are sealed with grafoil gaskets of 1mm thickness. The T6LA cathode was shown previously in Figure 28. The general characteristics of the T5 and T6 cathodes are shown in Table 6.

Cathode Type	T5 STRV-A1 (1994)	T6 ROS-2000 HET
Maximum current [A] (qualified)	0.5 – 3.6 @ 15,000hrs	1 – 15 @ 15,000 Extended at 30A
Flow range [mgs-1]	0.03 to 1.2	0.1 – 3
Weight [g]	60	120
Operating Power [W]	<100	<1000
Orifice diameter [mm]	0.23	1
Orifice length [mm]	1	2 (50% chamfer)
Tip material	Molybdenum	Tantalum

Table 6 T5 and T6 cathode characteristics

4.2 EXPERIMENTAL SETUP

4.2.1 VACUUM RIG

The vacuum rig used in this experiment is described in [159] previously used for hollow cathode characterization within the UK-25 ion engine. The rig consists of a 500mm diameter by 500mmm long chamber with ISO and CF flanges. Three main ISO 160 ports allow connection of the pumping system with viewports on either side of the vacuum chamber allowing optical access. Four CF35 ports integrated into the ISO500 door flange allow feed-through access. Pressure gauge heads are located in KF25 and KF40 ports on top of the chamber. A cylindrical water cooled copper shroud fitted around the inside of the vacuum chamber wall is used to dissipate heat load with the water feed-through entering from a CF35 port at the blank end of the chamber.

Pumping is achieved with a water-cooled turbo molecular pump (Pfeiffer Balzers TPH 520KTG, 500l/s) controlled by a TCP 380 power supply (with a TCS303 pump control unit) and backed by a rotary vane pump (Pfeiffer Balzers DUO 016B), achieving an ultimate vacuum of 10^{-7} mbar. This level of vacuum ensures the partial pressure of oxygen in the system is low enough to prevent poisoning of the chemically sensitive thermionic emitter. Propulsion grade argon (99.997% pure) is passed through high and low capacity indicating oxygen traps via an Edwards FCV10K extra fine control needle valve. Vacuum pressure is monitored with a Balzers TPG300 pressure gauge package constituting a pirani ($1000\text{-}5.4\text{x}10^{-4}$mbar) and cold cathode gauge head ($5\text{x}10^{-3}$ – $1\text{x}10^{-9}$mbar). Prior to operation the cathode was allowed to outgas at a pressure $<1\text{x}10^{-6}$mbar for 2 days. After initial outgassing, the heater was operated at a current of 0.5A for 24 hours. This ensures that the flame sprayed heater ceramic is well outgassed and therefore the chances of the heater failing are dramatically reduced.

Propellant supply system is designed to be flexible and accommodate a large range of flow rates. A Spectra Gasses 7120 high accuracy double-stage regulator supplies propellant to the feed system. A sampling cylinder (bypassed during experiment) and Druck PDCR910 pressure transducer are used for flow calibration before each round of testing with a repeatability of better than 4%. Mass flowrate is calculated based on the relation:

$$\frac{dp}{dt} = \dot{m}\frac{R_{sp}T}{V}$$

(4.1)

All external feed lines are above atmosphere pressure to reduce the possibility of air leaks into the flow system. A typical calibration curve for calibration of the needle valve is shown in Figure 33. The system was recalibrated regularly to avoid hysteresis.

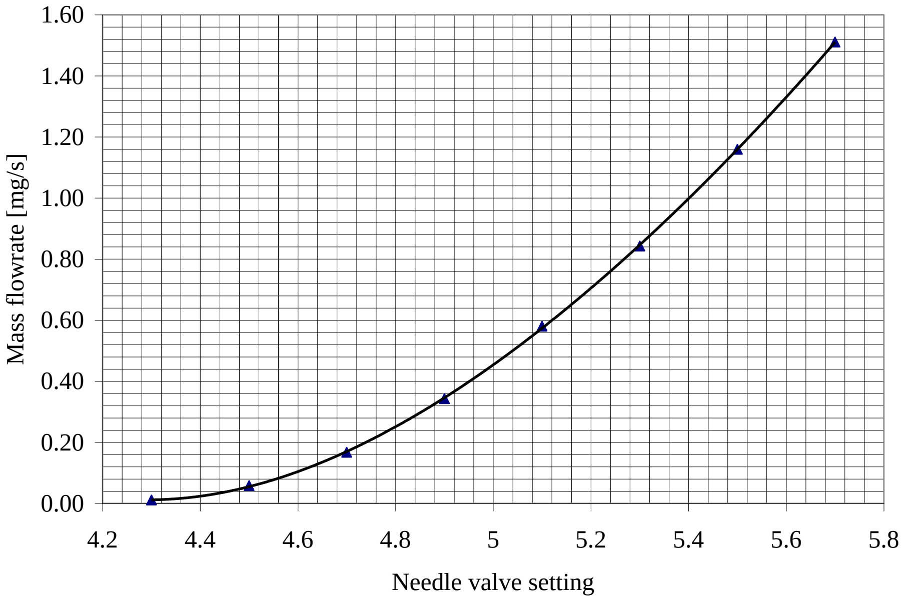

Figure 33 Typical mass flow rate calibration curve with argon

4.2.2 POWER SUPPLIES

The typical T5 gridded ion thruster from which the T5 hollow cathode is derived comprises nine independent supply units to power various elements of the system. In operation of the T5 cathode as a stand-alone thruster, the number of power supplies is reduced to three. It is also worth noting that since the cathode is in effect self-neutralizing, there is no need to electrically float the thruster system to a high positive potential, removing the requirement for electrical isolation of the thruster mounts and propellant feed lines. The electrical wiring system inside the chamber is also designed to minimize the influence of any MHD effects on the plasma both within the cathode and on the externally emitted plasma which may influence the thrust vector.

The power supply system used to operate the T5 hollow cathode is shown schematically in Figure 34. The cathode heater supply (Powerbox Lab605) provides the 2.2A required to heat the cathode to ignition temperatures (>1000˚C) prior to discharge ignition. The heater supply is operated in constant current mode with a common ground to the cathode potential to minimize the voltage difference between the heater wire and cathode body, reducing the risk of heater insulation breakdown. The discharge power supply consists of a high voltage (1kV, 30mA) strike supply and a low voltage (80V, 37A) steady state supply protected by diodes.

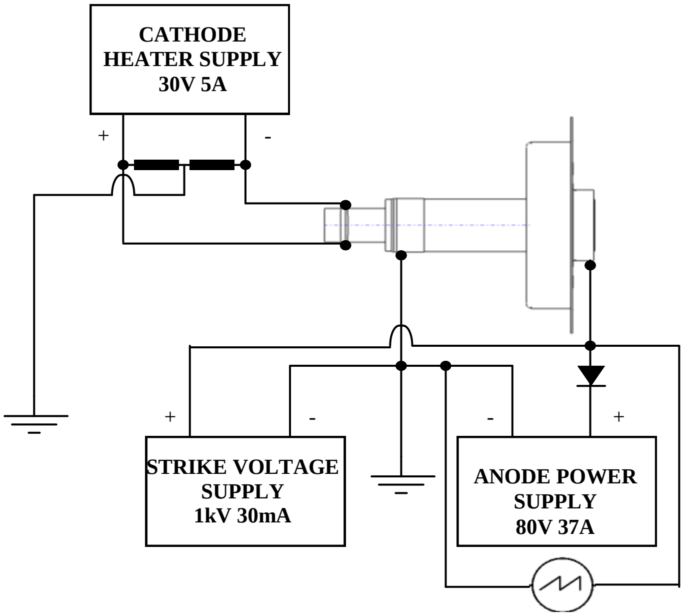

Figure 34 Electrical setup schematic

The strike voltage is supplied by a pair of Farnell Hivolt PM1/DCP photo-multiplier supplies connected in parallel and powered by a pair of Farnell 16RA24012 linear 24V power supplies. Once the discharge is initiated, steady state power is provided by a Glassman LV80-37 DC power supply. This is a 3kWswitch mode supply with load regulation of +/-0.1% and an output ripple of 10mV RMS over the frequency range 20Hz-20MHz. Plasma noise and instabilities in the discharge are monitored with a Tektronics TDS digital oscilloscope connected across between the anode power supply feed-through terminal and chamber ground. Anode voltage current characteristics are monitored via digital meters, limiting the resolution of the readings to +/- 1mA and +/- 1mV, while strike voltage was monitored by a digital multi-meter with a resolution of +/- 0.1V.

4.2.3 THRUST MEASUREMENT METHOD

Providing capability to resolve thrust in the sub-milli-Newton range was essential to the ongoing development of hollow cathode micro-thrusters at the University of Southampton. As discussed, previous measurements by Gessini using a flexible beam suffered numerous challenges associated with thermal expansion, dynamic resonance and measurable range. A decision had to be made concerning the best option for a new thrust measurement system.

Thrusts at the Newton level can be made accurately by direct measurement rigs with flexible propellant lines and thoughtful electrical connections, since mechanical friction and perturbations are small in comparison to the thrust level. As sub-milli-Newton thrusts are approached direct thrust measurements are disturbed by thermal drifts, facility noise and mechanical stress from propellant and electrical connections which can be on the order of the thrust force. Several methods have been used in the past to characterize microthruster performance. The most accurate method is the direct thrust measurement approach and has been developed by a few actors including ARC Siebersdorf[160], Busek and NASA Goddard[161], and NASA JPL[162], using forced feedback mechanisms. In the interests of time, cost and the availability of certain components however, indirect thrust measurements were deemed sufficient for relative comparisons to the measurements of Gessini. With assessment of the level of elastic or inelastic particle collisions with the target the measurement accommodation factor can also be defined thus the absolute thrust measurements inferred. A CAD model of of the in-direct thrust balance is shown in Figure 35.

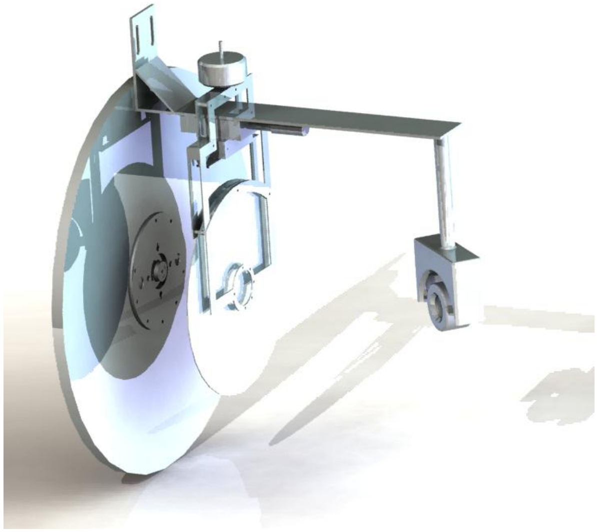

Figure 35 Solid model of the in-direct pendulum

4.2.4 OPTICAL SETUP

Optical setup consists of a Melles Grilot He-Ne (543.5nm) laser passed through a Keplerian beam expander and directed through the chamber on to a mirror, rigidly connected to a molybdenum pendulum target shown in Figure 36. The optics system guides the reflected beam out of the chamber and onto a Hamamatsu 4.7x4.7mm two-dimensional tetra-lateral photo-sensitive-detector (resolution of 600nm) at a path length of 0.9m. The detector is coupled with a C4674 signal processing circuit (output +/-2.5V at 1V/mm on each axis) and designed to provide two-dimensional position data on the incident light spot independent of the light intensity and is powered by a 30V Instec dual-tracking power supply (ripple less than 3mV). The output from the signal processing circuit is displayed on a Tektronix TDS 410A 2-channel digital oscilloscope (resolution +/-0.01V). A pivoting mechanism allows the target to be positioned both perpendicular to the thrust vector and through a full 90˚ sweep of angles while also allowing the pendulum to be electrically floated, grounded or biased. The stand-off distance between the pendulum target and the thruster can also be set between 20-250mm and a micro-translation mechanism is used to finely adjust the position of the target. Unwanted oscillations in the system are passively damped by magnetic induction of weak magnet placed close behind the Molybdenum target, electrically dissipating energy in the system.

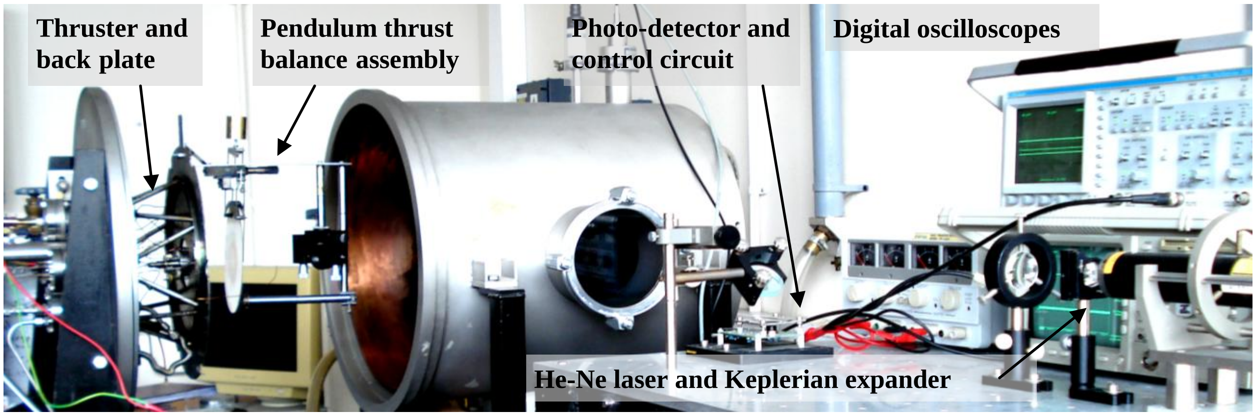

Figure 36 General experimental setup

4.2.5 PHOTODETECTOR

Since the returning spot size is approximately 0.5mm the maximum allowed displacement was set to 2mm, 40% of the total possible displacement. This ensured the full spot diameter was incident on the photodetector. The PSD resolution of 600 nm corresponds therefore, in the present configuration (with an optical path length $P\sim1$ m), to a thrust measurement resolution of ~3 μN although this is an upper limit due to other sources of error. A narrow-bandpass interference filter with a transmission curve centered at the laser frequency, placed in front of the PSD, eliminates ambient light, which may interfere with the measurement. As the peak transmittance is about 50%, this filter also reduces the size of the spot by cutting off the edges of the "spread" beam. The basic principle of operation of the PSD is illustrated in Figure 37. When the laser light spot strikes the detector, an electric charge proportional to the light intensity is generated at the incident position. As the active area is also a resistive layer, this electric charge is driven through it and collected by the output electrodes as photocurrents, while being divided in inverse proportion to the distance between the incident position and each electrode. The use of four electrodes, for a pin-cushion (improved tetra-lateral) type PSD, allows a two-dimensional displacement measurement. Measurement in two directions is important since it insures that the output in the measurement plane (*y*-direction) is a true representation of the full pendulum displacement and that the movement of the beam is perpendicular to the non-measured plane. If the beam is not perpendicular to the non-measured plane (*x*-direction), thus producing negligible output with respect to the measured plane, then the absolute thrust measurement will experience a loss of magnitude and is a source of error. The optical setup therefore allows for this correction with a micro-translation and rotation mechanism of the downward deflecting mirror thus being able to produce small rotations in the lateral and vertical plane of the beam to correct for small errors in alignment.

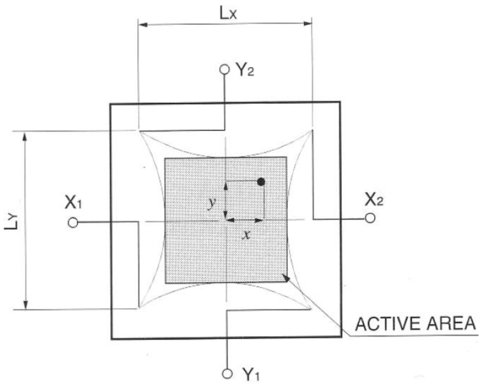

Figure 37 Photodetector measurement plane

Since the sensor delivers a signal independent of the light intensity up to a threshold intensity, (essentially a hi-pass filter) it is important to fully collect the returning signal. The selected sensor displacement range thus ensures that all of the light from the returning spot falls on the sensor given the maximum expected thrust.

4.2.6 PENDULUM MICRO-BALANCE

The pendulum assembly design was vital in dictating the measurement parameters achievable with the system. The pendulum, shown in Figure 38 and Figure 39, consisted of a circular target suspended on the centerline of the thrust vector by two frictionless steel point pivots which rested on a flat steel shelf. The balance was designed to have a centre of gravity below the pivot point which could be controlled by the use of an adjustable brass counterbalance mounted at the top of the assembly. In this design, selection of an appropriate counterweight position can either extend or shorten the measurable thrust range. By knowing the complete mass properties of the balance by 3D computer modeling before manufacture, the pendulum could be built such that its centre of gravity and mass were very close to optimum for the anticipated thrust range to use the full range of the photodetector and thus maximize resolution and signal to noise ratio to minimize error. Based on the work of Gessini with the T6 cathode a maximum thrust range between 0-3mN was initially selected. The maximum allowable laser beam displacement on the photodetector was selected as 2mm; 40% of the full range to ensure the complete beam falls within the detector as discussed in section 4.3. The path length from the pendulum to the beam was measured as 1.323m.

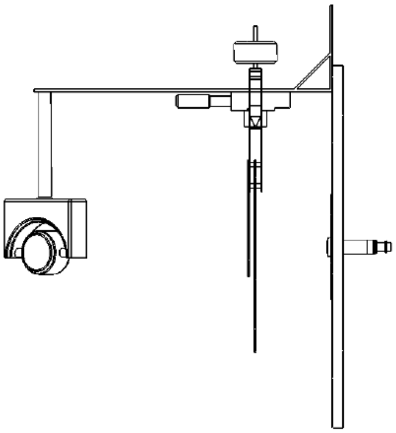

Figure 38 Pendulum assembly schematic

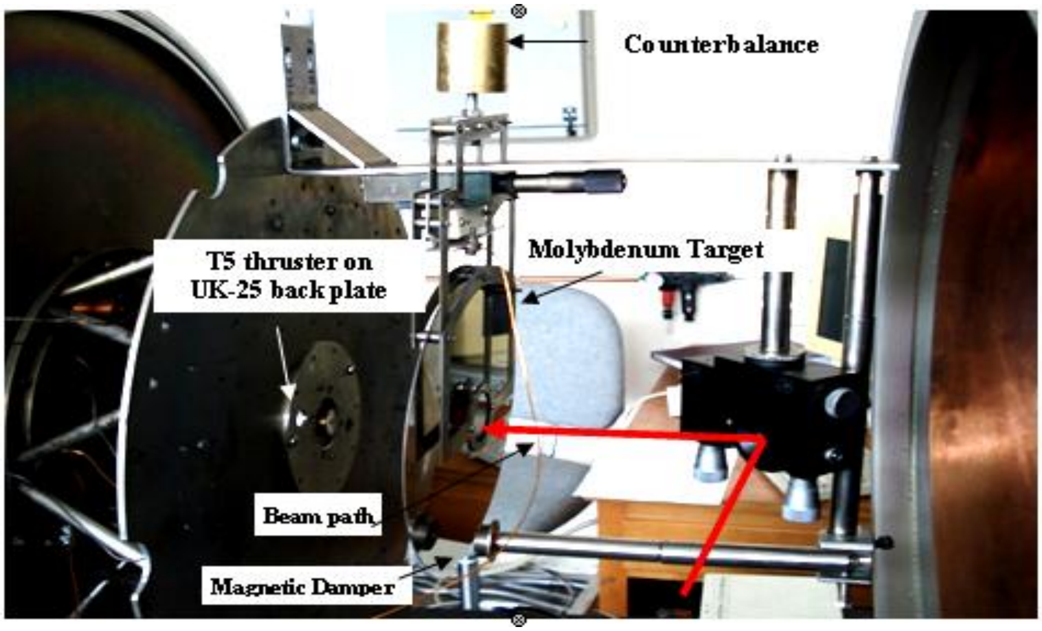

Figure 39 Thrust balance assembly

The pendulum was designed in a sandwich structure to give a high degree of rigidity and reduce the chance of simple or dynamic modes of oscillation whilst being designed symmetrically about the pivot point to minimize the influence of any geometrical changes due to thermal effects in the centre of gravity. Molybdenum was selected as the preferred target material given its small CTE and low sputter yield since the target would be exposed to relatively intensity plasma and high energy ions. Initially the pendulum target was polished to a mirror finish on both sides to enable the measurement beam to be directly reflected off the rear of the target, however even with an optical finish reflections generated by small imperfections in the molybdenum gave excessive signal error. An additional piece of the pendulum assembly was manufactured to enable an optical quality mirror to be held in place behind the target to ensure a good return signal.

4.3 THRUST DETERMINATION

4.3.1 PENDULUM APPROXIMATION

The target can be considered as a pendulum of a mass *m* and length *L* from a fixed pivot point as shown in Figure 40.

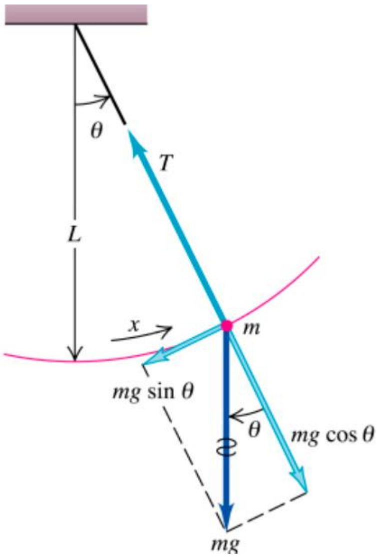

Figure 40 Pendulum force diagram

When displaced to an initial angle and released, the target will swing back and forth with periodic motion. Applying Newton's second law for rotational systems, the equation of motion for the pendulum may be obtained:

$$\tau = I_b \propto_a \Rightarrow -mg_0 \sin\theta L = mL^2 \frac{d^2\theta}{dt^2} \tag{4.2}$$

and rearranged as

$$\frac{d^2\theta}{dt^2} + \frac{g_0}{L}\sin\theta = 0 \tag{4.3}$$

The amplitude of angular displacement is small so that the small angle approximation ($\sin\theta = \theta$) holds true, and the equation of motion reduces to the equation of simple harmonic motion:

$$\frac{d^2\theta}{dt^2} + \frac{g_0}{L}\theta = 0$$

(4.4)

The simple harmonic solution is:

$$\theta(t) = \theta_0 \cos(\omega_o t + \phi)$$

(4.5)

with ω_0 being the natural frequency of the motion. With the assumption of small angles, the frequency and period of the pendulum are independent of the initial angular displacement amplitude. In order to correctly evaluate thrust measurements we must know exactly the position of the center of gravity of the balance. The period for a simple pendulum does not depend on the mass or the initial angular displacement, but depends only on the length *L* of the centre of gravity from the pivot point and the value of the gravitational field strength g_0, according to:

$$T_p = 2\pi\sqrt{\frac{L}{g_0}}$$

(4.6)

The effective *L* can therefore be calculated based on experimental analysis of the natural frequency with.

$$L = g_0\left(\frac{T_p}{2\pi}\right)^2$$

(4.7)

4.3.2 PENDULUM MOMENT OF INERTIA

Since in reality, the pendulum mass is distributed amongst the structure, the moment of inertia is much larger than in the simple pendulum approximation and hence the period will be longer. In this case the period is given by:

$$T = 2\pi\sqrt{\frac{I_b}{m_b g_0 L}} \tag{4.8}$$

The magnitude of the torque about the pivot point is,

$$\tau = m_b g_0 L \sin\theta \tag{4.9}$$

Since as before

$$\alpha = \frac{d\omega}{dt} = \frac{d^2\theta}{dt^2} \tag{4.10}$$

The equation of motion then becomes:

$$mg_0 \sin\theta L + I_b \frac{d^2\theta}{dt^2} = 0 \tag{4.11}$$

With

$$\omega_0 = \sqrt{\frac{I_b}{m_b g_0 L}} \tag{4.12}$$

If we assume simple harmonic motion the natural frequency averages over 50 cycles was determined to be 0.7522s or 1.3295Hz giving an effective length of 0.1406m. The frequency of an underdamped harmonic oscillator based on the natural frequency ω_0 and damping ratio ζ is given by:

$$\omega = \omega_0 \sqrt{1-\zeta^2}$$

(4.13)

Thus given the very small degree of damping in the free system, the approximation based on ω_1 is justified since:

$$\omega \cong \omega_0$$

(4.14)

In this case however L cannot be approximated from the natural frequency without knowing I . The moment of inertia can be calculated by breaking the pendulum down into component parts and using the parallel axis theorem, however this leaves room for error in making assumptions about the distribution of mass amongst the structure. In addition, adding counterweights would require recalculation of the moment of inertia if the C of G location was again going to be estimated from pendulum natural frequency. Alternatively the C of G location can be calculated by very accurately weighing the pendulum on a balance. A small rig was designed and built for this purpose, which enabled the exact measurement of the C of G location through knowing the mass of the balance m and the distance from the pivot point to the calibration point L_{cp} . Through balancing the moments:

$$L_{cg} m_b g_0 = L_{cp} F_b$$

(4.15)

the C of G location is given by:

$$L_{cg} = \frac{L_{cp} F_b}{m_b g_0}$$

(4.16)

The C of G for the pendulum without a counter balance was calculated as 63.2mm from the pivot point.

4.3.3 THRUST DERIVATION

As shown in Figure 40, the total thrusting force required to maintain the pendulum at an angle θ is given by:

$$F_{Tot} = m_b g_0 \sin\theta$$

(4.17)

In this case the total thrusting force F_T includes components of vertical thrust F_v and horizontal thrust F_h. Since only the horizontal component of thrust results in a change in pendulum displacement the total thrust is given by:

$$(m_b g_0 \sin\theta)^2 = F_h^{\ 2} + F_v^{\ 2}$$

$$F_h^{\ 2} = (m_0 g_0 \sin\theta)^2 - F_v^{\ 2}$$

$$F_h = \sqrt{(m_0 g_0 \sin\theta)^2 - (m_0 g_0 \sin^2\theta)^2}$$

(4.18)

However since:

$$\theta << 1,\ m_0 g_0 \sin^2\theta \cong 0 \text{ and } <<\ m_0 g_0 \sin\theta$$

$$F_h \cong m_0 g_0 \sin\theta$$

(4.19)

In reality the pendulum mass is not suspended at the tip of a string but distributed amongst the supporting structure. The calculated force F_h is therefore the force acting about the center of gravity. The actual measured thrusting force F_m is therefore dependant on the relative position of the centre of gravity L_{cg} (0.0632m), and the thrust line $L_{\cot}$ (0.1074m) and is given by:

$$F_m \cong m_b g_0 \sin\theta \frac{L_{cg}}{L_{\cot}}$$

(4.20)

In this case the ratio $\frac{L_{cg}}{L_{\cot}}$ is given the coefficient R_{ct}

$$F_m \cong m_b g_0 \sin\theta R_{ct}$$

(4.21)

4.3.4 BALANCE RANGE AND RESOLUTION

The counterbalanced pendulum principle also gives us a means to control the position of the center of gravity with the counterbalance and thus maximize resolution by using the full swath of the sensor over the expected thrust range. The maximum tolerable angle of deflection (θ_{max}) is calculated based on the measured path length of 1.332m (L_{pa}) and the maximum sensor displacement (L_{smax}). For a small angle deflection where the path length is much larger than the sensor displacement length ($L_{pa}>>L_s$), and accounting for the total reflection angle being the angle of incidence plus the angle of reflection, the maximum tolerable angle of deflection of the balance can be defined by:

$$\theta_{\max} = \frac{1}{2} Arc\tan\left(\frac{L_{pa}}{L_{s\max}}\right)$$

(4.22)

This gives a maximum tolerable deflection of 0.0433°. The pendulum weighs 398.74g without the use of a counterweight, thus the maximum tolerable sensor displacement of 2mm in section 4.2.5, the measured thrust is given by:

$$T_{\max} = m_b g_0 \sin\theta_{\max} R_{ct}$$
$$=3.87\text{mN}$$

(4.23)

By adding counterweights at the counterweight mounting point, located 5cm above the pivot point the center of gravity can be moved closer to the pivot point, decreasing the thrust range and increasing resolution. The thrust range is given by:

$$T_{\max} = m_b g_0 \sin\theta_{\max} \frac{L_{cog} m_{Th} - L_{cb} m_{cw}}{m_{tot} L_{\cot}}$$

(4.24)

Where the new centre of gravity is given by,

$$\frac{L_{cog}m_{Th} - L_{cb}m_{cw}}{m_b}$$

(4.25)

And

$$R_{ct} = \frac{L_{cog}m_{Th} - L_{cb}m_{cw}}{m_b L_{\text{cot}}}$$

(4.26)

As supported by Figure 41, by adding the appropriate counterweight thrust ranges between 3870µN and 1.16 µN can theoretically be achieved. Addition of a counterbalance reduces thrust range and resolution accordingly. R_{ct} between 0.1-1, where the ratio between the centre of thrust lever arm to the centre of gravity lever arm is 0.1–1 represents the most probable ranges of use for these experiments (~3800µN-1000µN).

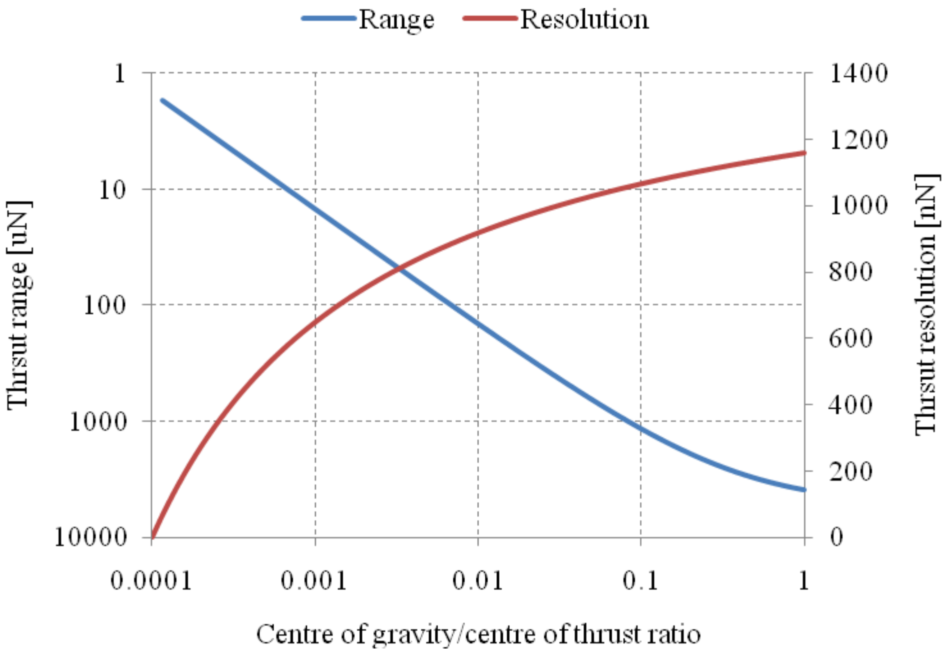

Figure 41 Varying thrust range and resolution by adding counterweights

It should be noted however that with fine tuning of R_{ct} to values < 0.01 enables the measurement of micro-Newton thrust levels accurately. A ratio of 0.001 for example enables a thrust range of ~ 0-11µN at 650nN resolution. This figure however represents an upper limit of accuracy for the balance and supporting measurement system due to external disturbances. The benefit in changing the measureable thrust range however is in the fact that the signal to noise ratio, as a result of external disturbance, will be constant regardless of the thrust range. This occurs since both resolution and range decrease proportionally with increase in counterweight mass, therefore the system maintains its sensitivity. In addition, the pendulum gains mass and thus the moment of inertia will significantly increase. This will have the effect of decreasing the influence of external excitations but will also increase the response time of the balance to changes in steady state thrust. If transitional thrust measurements are required at very low thrust levels the inertia of the balance should be given consideration.

4.3.5 ELASTIC AND IN-ELASTIC PARTICLE UNCERTAINTY AND ERRORS

We also have to consider that the measured thrust force F_m is actually given by:

$$F_m = m_{prop} \frac{dv_{prop}}{dt} = \dot{m}_{prop} \Delta v_{prop} \tag{4.27}$$

Since propellant particles will rebound from the target as they collide with some kinetic energy, the actual transferred impulse to the thrust balance (F_m) will be greater than the impulse originating from the thruster (F_T). The degree of this thrust overestimation will depend on the nature of the physical particle/target interaction. If particles undergo elastic specular recoil from the target with conservation of momentum, the thrust force with respect to the measured force bares the relation:

$$F_T = \frac{F_m}{2} \tag{4.28}$$

$$F_T = \frac{m_0 g_0 \sin\theta R_{ct}}{2} \tag{4.29}$$

If all propellant atoms are reflected diffusely a separate correction must be used to account for F_T. This correction term is the resultant normal force component on the target for a diffuse distribution of reflected propellant atoms. Figure 42 illustrates a cosine distribution of

N number of particles where $N_0 \cos\beta$ equals the number of particles per unit solid angle at any angle of reflection β. Since the resultant force acting on the target is proportional to $\cos\beta$, the resultant thrust can be computed for a cosine distribution by integrating over the total range of reflection.

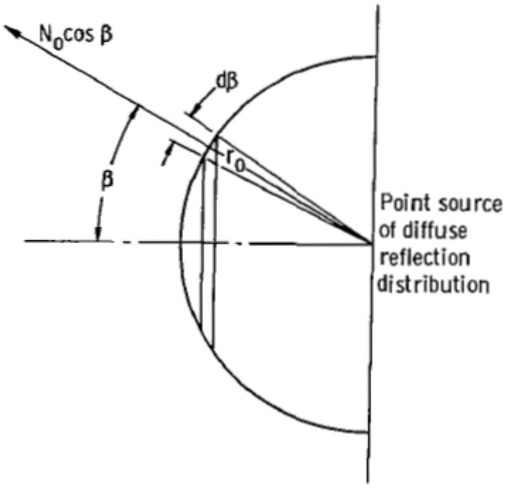

Figure 42 Integration hemisphere for diffuse distribution of reflected atoms

This component may be expressed as a fraction of the measures thrust due to reflection by dividing by the total number of particles.

$$\frac{F_T}{F_m} = \frac{\int_0^{\pi/2} 2\pi r_0^2 \sin\beta N_0 \cos^2\beta d\beta}{\int_0^{\pi/2} 2\pi r_0^2 \sin\beta N_0 \cos\beta d\beta} = \frac{2}{3}$$

(4.30)

$$F_T = \frac{2}{3} F_m$$

(4.31)

In reality the actual correction factor may lay within the bounds of $F_T = F_m$ and $F_T = \frac{1}{2} F_m$ however these bounds mark an upper and lower limit of uncertainly with regards to the perceived and actual thrust in the target measurement system. The degree of diffuse reflection can only be determined by theoretical and empirical comparisons which define the accommodation coefficient for such a measurement technique. Such comparisons and are made in Chapter 5.

In order to limit this uncertainly the surface of the molybdenum target was polished to an optical quality mirror finish such that the propellant atoms recoil with a high degree of specular reflection so as to limit the influence of surface morphology over the target surface. In fact the exact accommodation coefficient will vary with Rutherford/Coulomb scattering by ions and neutrals however this requires extensive analysis and is considered beyond the scope of this thesis.

The main determinant errors with fractional uncertainly in the system include mass flow calibration (±4%), resolution of the optical sensor over the range used (±0.3%), measurement of the optical path length (±0.1%), location of the thruster axis on the target centerline (±0.1%), and the weighing of the balance (±0.025%) giving a total fractional uncertainty of ±4.525%. Indeterminate or systematic sources of error primarily consist of vibration induced deviation.

4.4 SYSTEM RESPONSE

One issue first encountered with the system was the long time constant for the system to reach steady state since the pendulum is almost frictionless. The only mechanism removing energy from the system was therefore a small amount of damping in the ambient gas. Since typical base pressures within the chamber are ~ $2.0\text{x}10^{-7}$ millibar and ~5 $\text{x}10^{-4}$ millibar during operation of the cathode the ambient gas is certainly rarified, however there is a limited transfer of kinetic energy from the swinging pendulum to the gas and very limited friction dissipated as heat at the pivot points. This resulted in some hours for oscillations in the system to dissipate and even when maintaining a quiet background environment external oscillations were sufficient to excite the pendulum, preventing the system from reaching a steady state zero. Figure 43 shows the transient behavior from an initial forced oscillation of ~±1.5V with no damping.

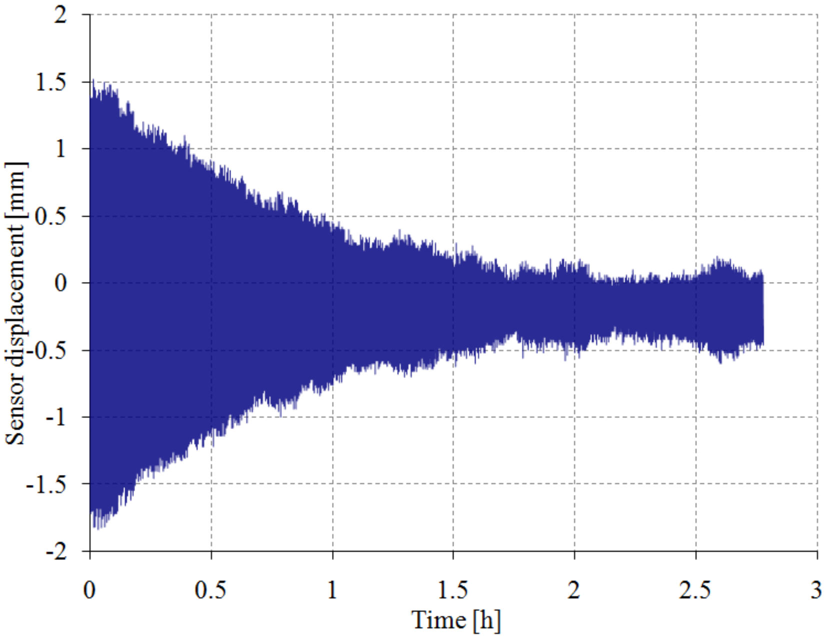

Figure 43 Undamped oscillations from thrust balance as a result of an external ±1.5V input

The damping ratio, ς, of the system can be found from the logarithmic decrement δ by:

$$\varsigma = \frac{1}{\sqrt{1+\left(\frac{2\pi}{\delta}\right)^2}}$$

(4.32)

Logarithmic decrement is used to find the damping ratio of an underdamped system in the time domain. The logarithmic decrement can be found by the natural log of the amplitudes of any two peaks:

$$\delta = \frac{1}{n}\ln\frac{x_0}{x_n}$$

(4.33)

where x_0 is the greater of the two amplitudes and x_n is the amplitude of a peak n periods away. In this case damping factors for the system are shown in Figure 44.

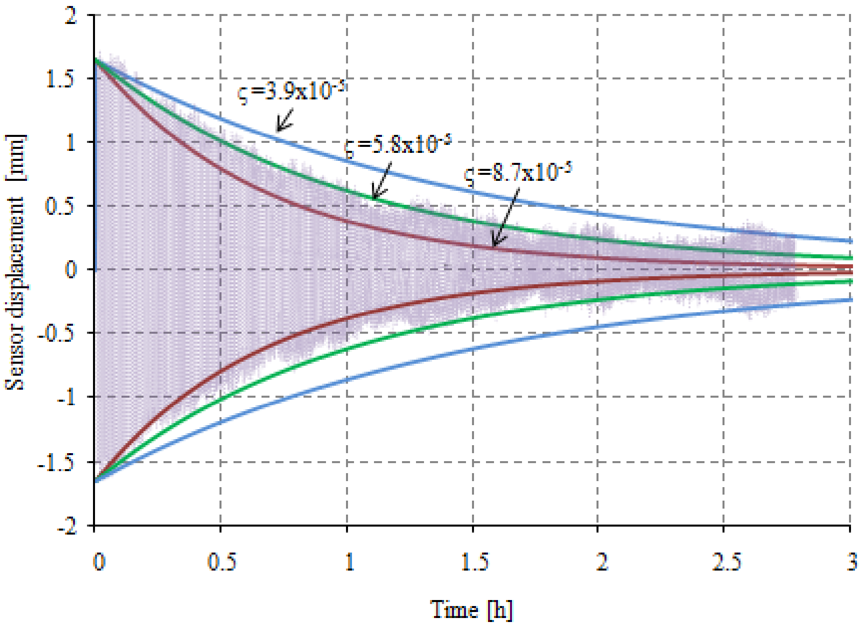

Figure 44 Damping factors calculated for the free thrust balance system

It can be seen that the damping factor for the free thrust balance is approximately 5.8 x10^{-5}, an extremely low value. Such a low damping coefficient generated many technical problems:

1. Oscillations in the system required a substantial time to reside.
2. Steady state was unattainable since, as shown in Figure 43, background excitations induced oscillation into the system
3. Pendulum oscillations were generally much greater than the displacement due to the thrusting force which limited thrust resolution

In this case some form of damping was necessary to reduce the influence of external excitations and to return the thrust balance to steady state sooner. Similarly to Equation 4.2, we can consider the pendulum as a spring mass damped system with a damping constant γ and the equation of motion:

$$\frac{d^2\theta}{dt^2} + \gamma\frac{d\theta}{dt} + \frac{g_0}{L}\sin\theta = \frac{d^2\theta}{dt^2} + \gamma\frac{d\theta}{dt} + \omega_0^2\sin\theta = 0 \tag{4.44}$$

Where,

$$\gamma = \omega_0\left(-\zeta \pm \sqrt{\zeta^2} - 1\right) \tag{4.45}$$

4.4.1 MAGNETIC DAMPING

Various means of damping were considered including active (electromagnetic) and passive (dashpot, magnetic). Active methods have the advantage of being able to tune the system to the appropriate damping constant however a passive system, would avoid the complexity associated with an active system. Thus it was decided to initially investigate a passive system. Dashpot techniques within vacuum chambers generally use mercury to damp by viscous friction since exposure to oil vapor is known to have detrimental effect on cathode dispenser chemistry. It was therefore decided to use a passive magnetic eddy current damping system.

When a nonmagnetic conductive metal, in our case molybdenum, is moved through lines of magnetic flux, eddy currents are generated which circulate within the metal. Eddy currents circulate in such a way that they induce their own magnetic field with opposite polarity of the applied field, causing a resistive force, however due to the electrical resistance of the metal, the induced currents will be dissipated into heat at the rate of I^2R. In the case of a dynamic oscillating system the conductive metal is continuously moving in the magnetic field and experiences a continuous change in flux that induces an electromotive force (emf), allowing the induced currents to regenerate. The process of the eddy currents being generated causes a repulsive force to be produced that is proportional to the velocity of the conductive metal. Since the currents are dissipated, energy is being removed from the system, thus allowing the magnet and conductor to function like a viscous damper. The use of eddy currents for damping of dynamic systems has been known in the application of magnetic braking systems.[163]

An appropriate magnet and setup had to be selected to provide adequate damping to the system without having to significantly modify the system. A magnet placed at the rear of the molybdenum target would function as a viscous damper. As the pendulum swings and cuts the lines of flux its electrons will experience a Lorenz force,

$$\vec{F} = q\left(\vec{v} \times \vec{B}\right) \tag{4.46}$$

Where v is the velocity vector of the charge q and B is the magnetic field vector. The force on the electrons induces a current into the molybdenum as shown in Figure 45.

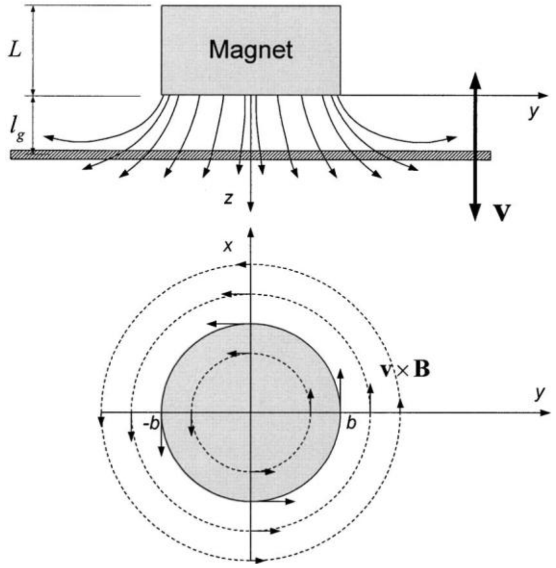

Figure 45 Eddy current direction moving induced into the molybdenum target

Faradays law relates the EMF to the velocity of the plate.

$$\varepsilon = \frac{\partial \phi}{\partial t} = \frac{\partial}{\partial t}\int \vec{B} \cdot \partial \vec{A} \tag{4.47}$$

Besides inducing the eddy currents in the metal plate, the magnet exerts a force on the currents inside its field. This is the retarding force associated with the magnetic braking.

$$\vec{F} = I\vec{L} \times \vec{B} = ILB \tag{4.48}$$

Energy is dissipated by electromagnetic-joule heating by the associated eddy currents within the molybdenum target at a rate:

$$P_{dis} = I^2 R \tag{4.49}$$

4.4.2 MAGNETICALLY DAMPED SYSTEM RESPONSE

A ring magnet of 0.1Tessla was selected and mounted on an adjustable assembly at the rear of the molybdenum target. The distance between the magnet and target was systematically altered to 4 positions of 1mm, 2.5mm, 5mm, and 10mm in order to investigate the dynamic response. Transient ringing data for the 2.5mm and 1mm case is shown in Figures 46 and 47 respectively.

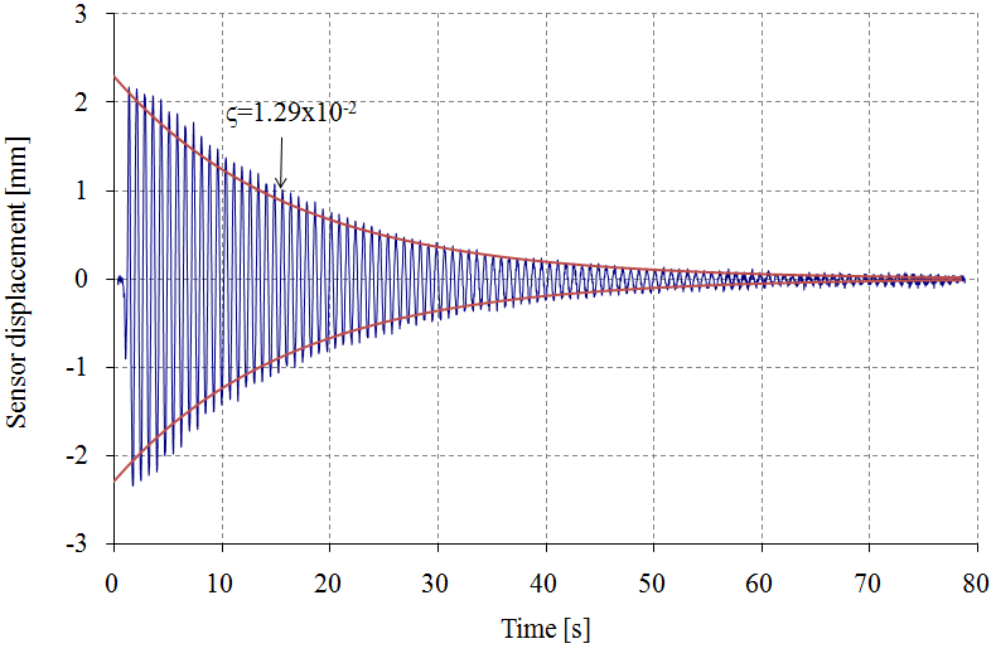

Figure 46 Passively damped oscillations of thrust balance from a step input with a pendulum/magnet separation of 2.5mm

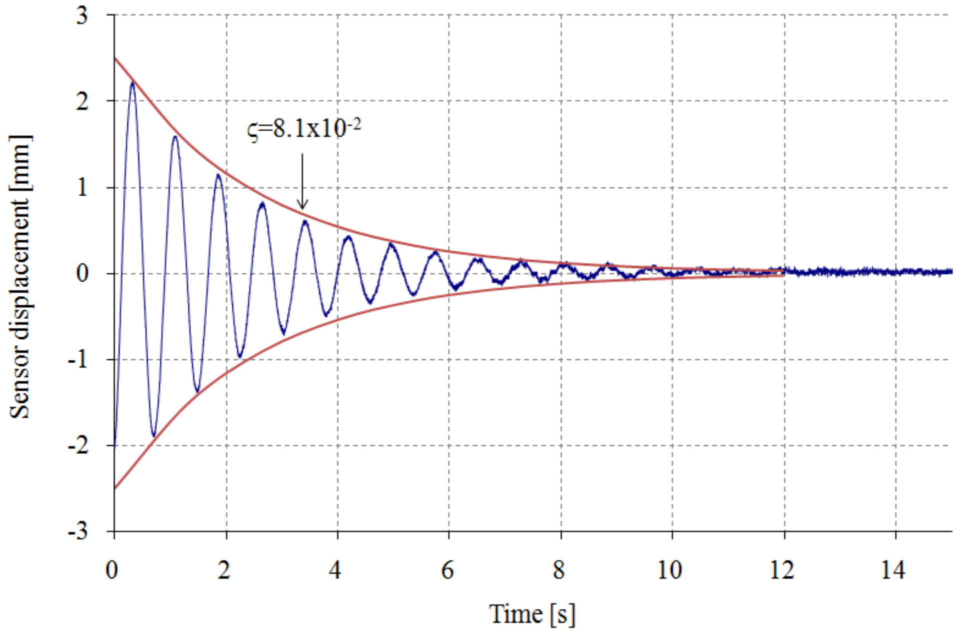

Figure 47 Passively damped oscillations of thrust balance from a step input with a pendulum/magnet separation of 1mm

The corresponding damping factors for respective magnet-target spacing's are shown in Table 7.

Separation [mm]	1	2.5	5	10	No magnet
Damping factor	$6.28\text{x}10^{-2}$	$1.29\text{x}10^{-2}$	$2.17\text{x}10^{-3}$	$5.34\ \text{x}10^{-5}$	$5.79\ \text{x}10^{-5}$
Steady state reached after	12s	71s	~5.5minutes	~2.5hours	~3hours

Table 7 System response due to magnetic damping

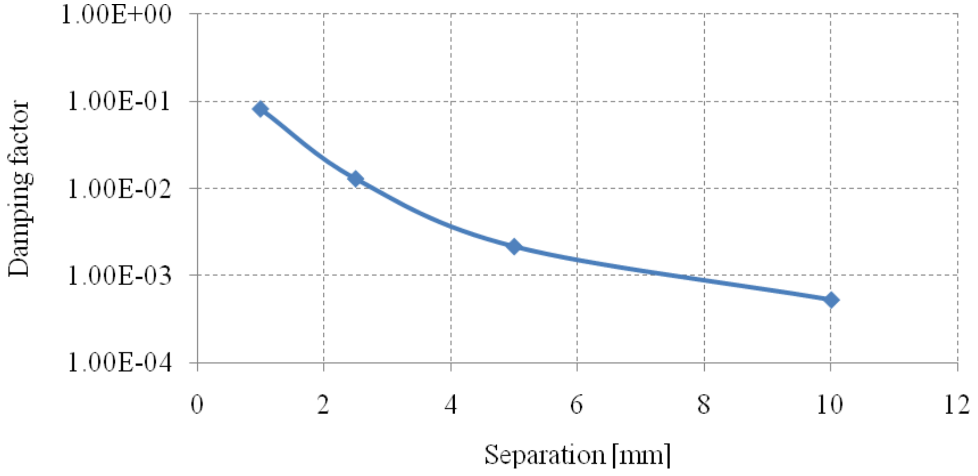

Figure 48 Influence of magnetic damper separation on damping factor

As shown in Figure 47, the addition of magnetic damping at 5mm not only significantly shortens the time for oscillations to decay from hours to seconds, but the background induced vibration oscillations are also damped to give a much cleaner signal with improved signal to noise ratio and allowing rapid transient measurement as shown in Figure 49. With no damping at all the steady state measurement was impossible. Passive damping was deemed sufficient for accurate thrust measurement without the requirement for an active system.

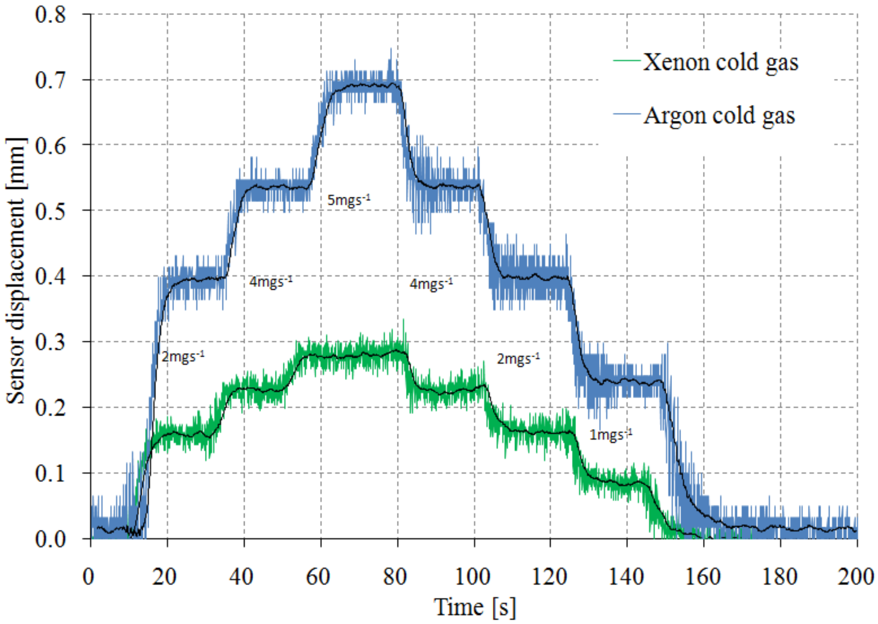

Figure 49 Transient thrust measurement made with step changes in mass flowrate during cold gas operation

4.5 MEASUREMENT SYSTEM NOISE ANALYSIS

In an effort to reduce noise in the system, data was taken to investigate the influence of the roughing pump on the output of the system. Data showing the influence of the roughing pump is shown in Figure 50 clearly showing noise present on signal.

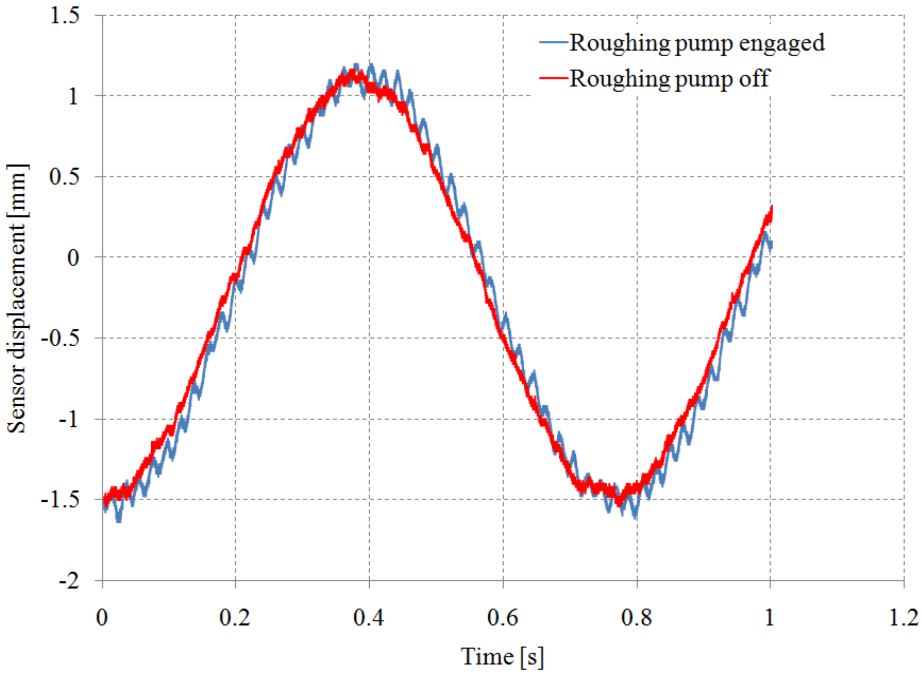

Figure 50 Thrust balance noise with roughing pump on and off

Analysis of the FFT power spectra as shown in Figure 51, helps identify the source of remnant noise in the target measurement system.

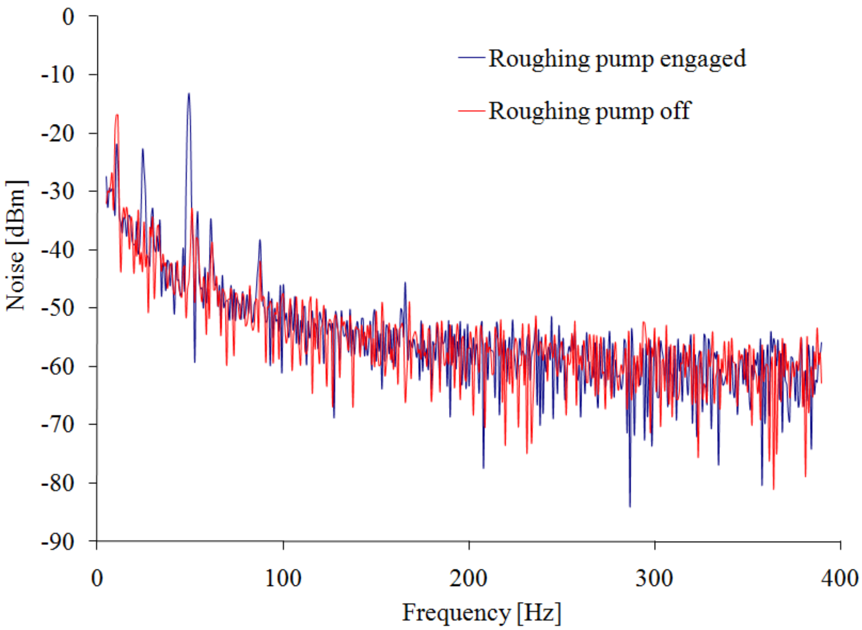

Figure 51 Noise power spectra with roughing pump on and off

The difference in power spectra when the roughing pump is engaged is somewhat obvious. In this case power spectra are displayed in dBm, the power ratio in decibels (dB) of the measured power referenced to one milliwatt. Zero dBm therefore equals one milliwatt with a 3 dB increase representing roughly a doubling of the power. Power gain in dBm is therefore expressed as:

$$G_{dBm} = 10\log_{10}\left(\frac{P}{1\times10^{-3}}\right) \text{ and } P = 10^{(G_{dbm}/10)}1\times10^{-3} \tag{4.49}$$

The FFT reveals peaks primarily of 49.21Hz at 13.12dBm and 24.21Hz at 22.98dBm respectively. The higher frequency peak is consistent with the stated roughing pump 3-phase main motor at 50Hz (3000RPM) with the lower frequency consistent with the second mechanical stage of the roughing pump at a ratio of 2:1 (1410RPM). All other low frequency peaks are present with the roughing pump both engaged and off. The peak at 87.5Hz at 38dBm is consistent with the oscilloscope hard drive rotation speed of 90Hz (5400RPM), action was thus taken to relocate the oscilloscope further from the testing apparatus. In doing so the peaks of 60.9Hz at 34.7dBm also disappeared indicating that the 60Hz signal was likely the oscilloscope fan speed. Noise above 400Hz was negligible. The very low frequency peak of 10.93Hz at 16.9dBm is not likely to be electrical equipment and may well be the natural structural frequency of the building. In order to substantially reduce noise due to the roughing pump, the pump was isolated on a damped mounting.

The resonant frequencies of the system can be analyzed by exciting the system with an externally driven oscillation. In this case the turbopump speed can be monitored during spin-up to the steady state speed of 839Hz. A trace of system response during startup can be seen in Figure 52 with the critical frequencies indicated.

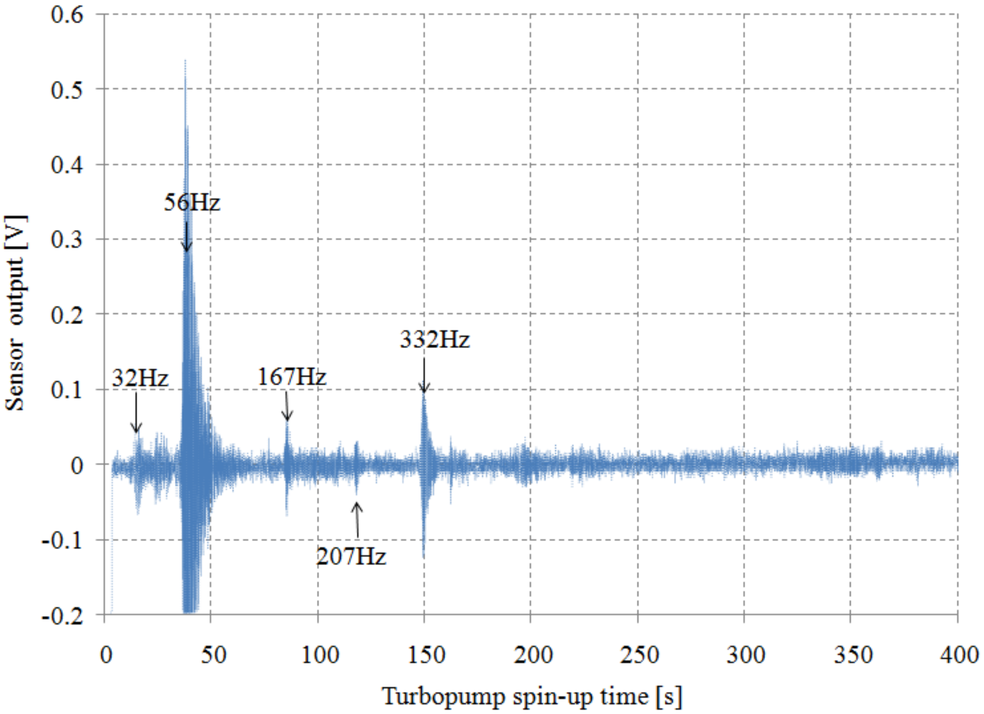

Figure 52 Resonant frequencies of the thrust balance assembly during turbopump start-up

As shown above the main resonant mode of the balance occurs at approximately 56Hz with various lesser modes at 32Hz, 167Hz, 207Hz and 332Hz. This test was important in identifying the roughing pump main motor at operating at 50Hz as a perfect candidate to resonate the thrust balance and a source of significant error. Since the roughing pump was now mounted on a damper the only means of vibrations entering the system at 50Hz was through the vacuum line which connects directly onto the turbopump. In this case a weight was clamped onto the vacuum hose at the mid-point in order to create a standing node and double the transmission frequency to the chamber to 100Hz. A single node was most appropriate since addition of a second may increase the transmitted frequency to 150Hz, close to the 167Hz resonant mode.

4.6 MEASUREMENT SYSTEM THERMAL DRIFT

Since sensor output now showed good resolution tests were conducted to investigate the transient thermal behaviour of the thrust measurement assembly. Firstly heater currents of 2.2 Amps and 2.5Amps were applied to the heater on the T6 cathode without a discharge. As the cathode heats up heat, is transferred radiatively to the supporting beam and pendulum and conductively to the

UK-25 thruster backplate. The sensor outputs are shown in Figure 53. The signal is reasonably noisy since no form of damping was used during this test.

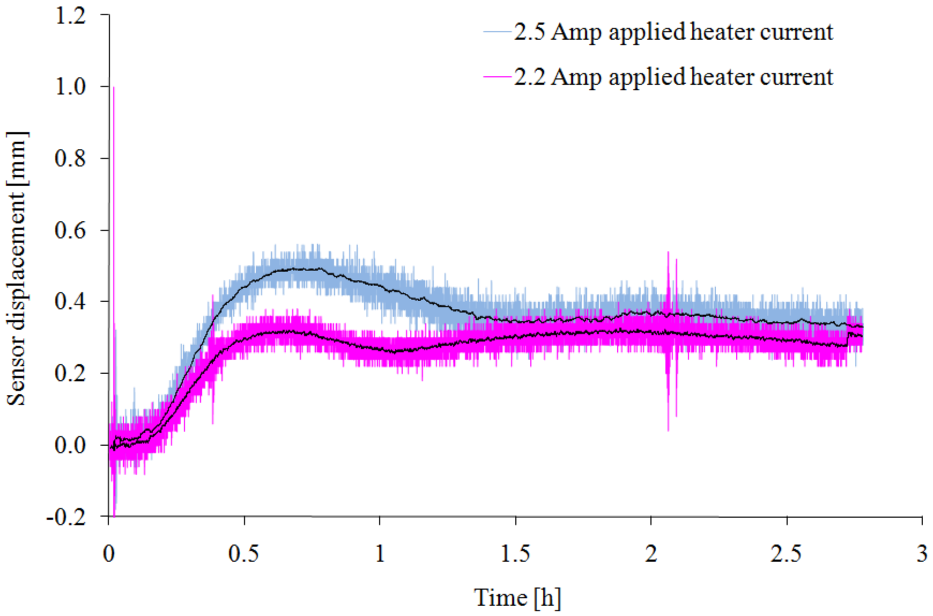

Figure 53 Thrust balance zero-baseline drift with 2.2 Amps applied heater current and 2.5 Amps applied heater current

During operation heat is radiatively and conductively transferred to the supporting architecture on which the thruster and balance is mounted. This results in small but significant movement of the system and a corresponding drift in the photodetector output signal. Because of this shift in the zero/baseline signal readings thrust measurements had to be made followed by a measurement of the relative baseline directly afterwards when the thruster had been switched off. It would seem that this problem is endemic to the method of thrust measurement and the fact that the microbalance supporting structure has to be mounted on the UK-25 thruster backplate. Since the backplate has a large thermal inertia the drift occurred over a fairly long period and the system damping allowed measurements to be made within a few seconds of turning the thruster off. It is worth noting however that in future inclusion of a much more thermally inert or water-cooled mounting plate for the thruster and measurement assembly would be beneficial.

Figure 54 shows the response of the system as the heater is switched off and a separate plot during an actual discharge as the cathode is switched off and the flow turned off. Since both signals drift in opposite directions this indicates that assembly deformation during heated and operation is different, which is reasonable given that the anode radiates much more heat in the direction of the thrust balance assembly further downstream of the cathode during operation than the heater alone. As the figure indicates, as long as the relative baseline was measured immediately (within a few minutes) after the thrust measurement, the error due to thermal drift was negligible.

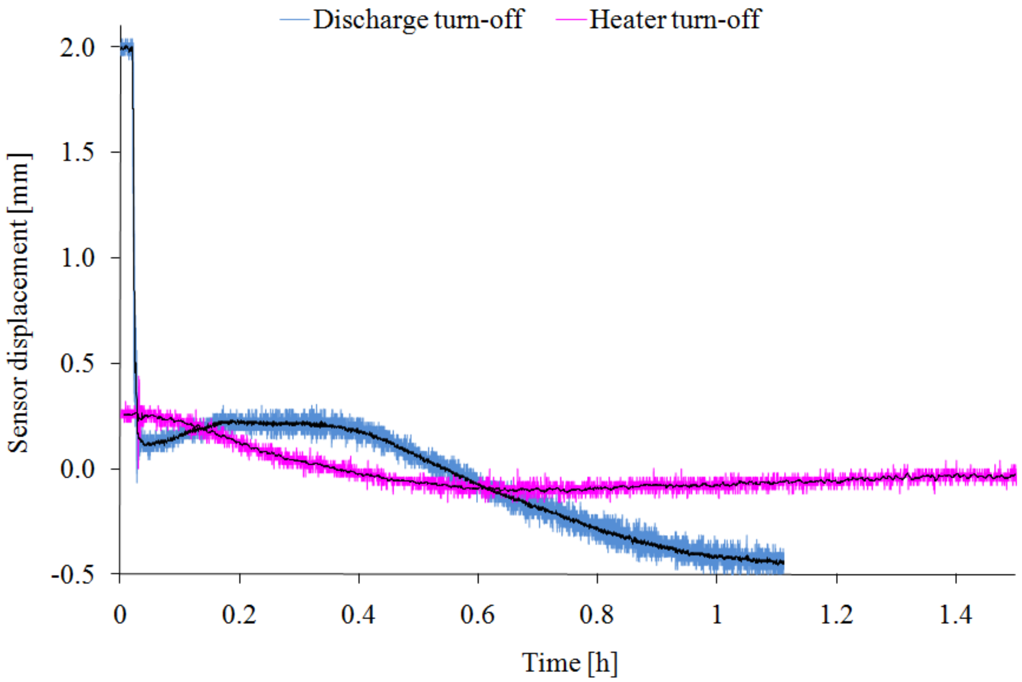

Figure 54 Thrust balance zero-baseline drift during cooling after the application of a discharge and application of only a the T5 heater at 2.2 Amps

4.6.1 TARGET BIASING

One initial concern was that charging of the target could result interaction between the plasma and the target as a result of electrostatic forces acting upon the surface. To ensure the target was not being influenced by the plasma in which it is immersed, the pendulum target was biased +/- 30V, electrically floated and directly grounded during high current and low current operation for the T5 (3.2A, 0.8A) and T6 (30A, 5A) cathodes. The thrust measurement system showed no sign at all of an increase or decrease in the relative thrust measurement at the respective current levels. The target was then left electrically floating for all preceding measurements to ensure that the target was not actively involved in drawing an electron or ion current from the discharge.

CHAPTER 5

EXPERIMENTAL RESULTS I: T5 AND T6 THRUST MEASUREMENTS

This chapter describes the experimental results obtained over the course of the testing with the T5 and T6 cathodes. The experimental apparatus and thrust measurement techniques are described in Chapter 4. It is important to note that thrust measurements in the following chapter are given in their raw form with no correction due to elastic or inelastic collisions. A discussion is made on the validity/correction of thrust measurements due to particle elastic or inelastic collisions and the likelihood of various thrust mechanisms is suggested by analytical comparisons. The data used in the latter discussion on thrust mechanisms for qualitative and quantitative comparisons is corrected based on the calculation of the accommodation factor.

5.1 THRUST MEASUREMENT RESULTS

5.1.1 COLD GAS/RESISTOJET PERFORMANCE

The hollow cathodes can be operated in a cold gas and resistojet mode (with the cathode heater only operating) in addition to the discharge mode. The system therefore allows for 2-levels of partial redundancy if the discharge is not able to ignite. Tests were conducted with argon for the T5 and with argon and xenon for the T6 cathode to characterize possible performance in these two modes and give some indication of the degree of elastic or non-elastic collisions with the target. Figures 55 and 56 show the thrust and specific impulse obtained when operating in a cold gas and resistojet mode. During the heated mode, the T5 cathode was operated at 19.7W heater power with the T6 operated at 50W.

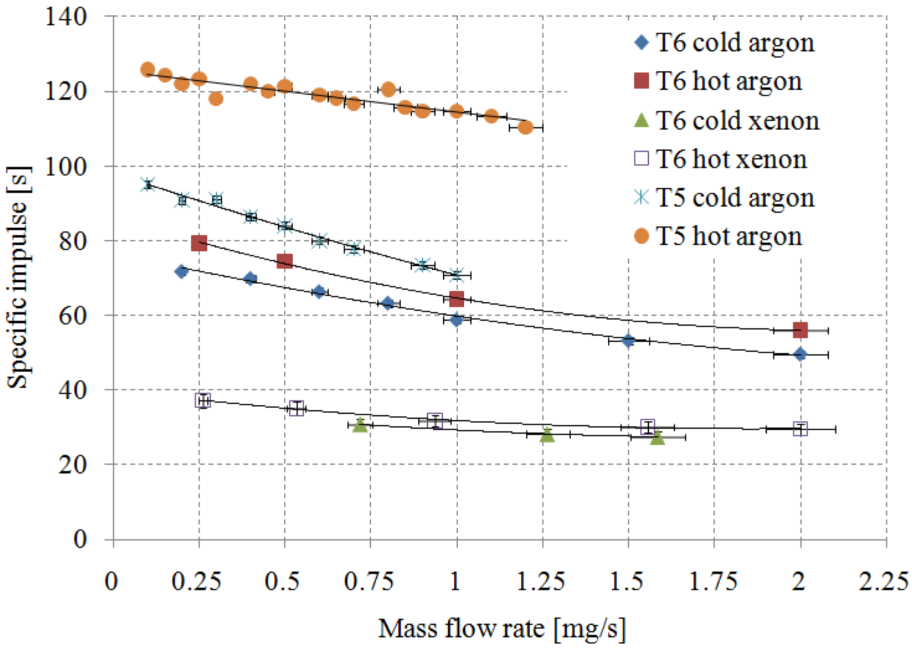

Figure 55 Specific impulse obtainable from operating the T5 (argon) and T6 cathode (argon and xenon) in a cold gas and resistojet mode (using only the heater)

The T5 thruster shows relatively high specific impulse with argon, surpassing the performance of the T6 in both modes of operation. Error bars are indicative mass flowrate accuracy (±4%). Thrust measurements were made with good repeatability down to approximately 0.08mN.

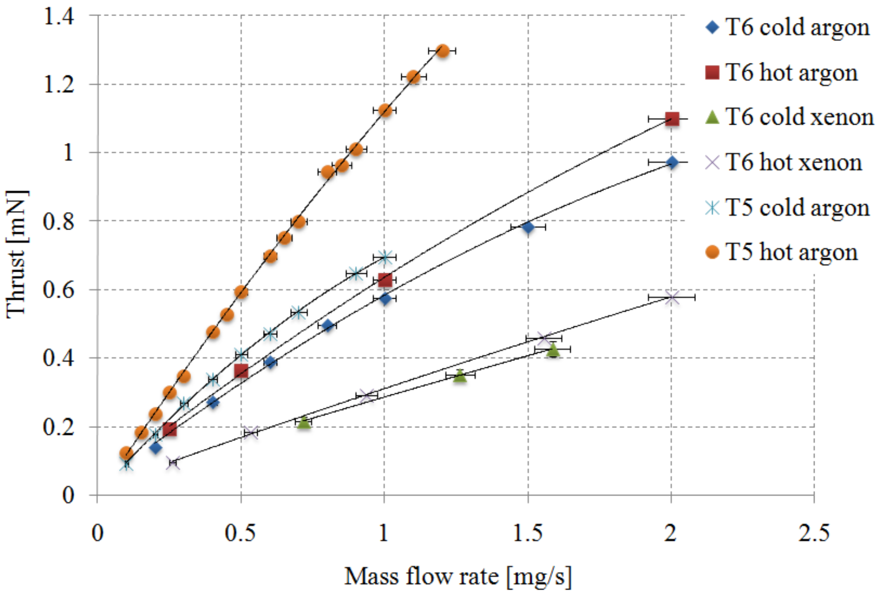

Figure 56 Thrust obtained in operation of the T5 and T6 cathodes in hot and cold gas mode

The T5 cathode achieved a maximum ISP of 125s with argon at 0.12mN. The smaller orifice (0.23mm) of the T5 cathode is shown to be beneficial in thrust production over the T6 cathode for the same mass flow rate both in cold gas and resistojet mode. It should be noted that the area of the T5 orifice is 16 times smaller than the T6 orifice. Since the orifice choked flow velocity will be approximately equal, the internal pressure of the T5 cathode will be on the order of 16 times higher than in the T6. This creates a pronounced difference in performance. In resistojet mode the higher chamber pressure leads to increased thermal conductivity of the bulk gas volume and heat transfer from the hot walls of the cathode. The bulk gas temperature is thus higher at the point of the orifice exit. The T5 resistojet mode therefore produces a marked increase in performance over the cold gas mode, much greater than the T6 even though it operates at lower heater powers. This increase is much less pronounced in the T6 cathode due to the large orifice, lower chamber pressures and thus lower heat transfer to the propellant. As expected, operation with xenon in the T6 cathode leads to a large reduction in specific impulse due to the molecular weight of the gas, with a maximum ISP of 31.8s at 0.29mN obtained in resistojet mode. For the same mass flowrate the neutral density in xenon is much lower, thus so is the cathode internal pressure. Thermal conduction to the bulk propellant is therefore lower for xenon and the improvement in ISP less significant.

The loss of performance at higher mass flow rates is likely due to greater divergence of the plume with higher pressures at the cathode exit. At the time of writing, T5 testing had not been conducted with xenon, however it is very likely that the T5 will also experience a reduction in performance scaling with the reduction found in the T6 cathode. This indicates that attainable ISP for the T5 cathode with xenon would be in the 50-60s range in resistojet mode.

5.1.2 INITIATION OF THE DISCHARGE

One factor which may be important for operation in a discharge mode is the response time of the thruster system. Since hollow cathodes require heating prior to ignition, this has to be taken into account when considering power budgets and the sequencing of thruster firings. Prior to ignition the T5 and T6 heaters were operated at 2.2A +/- 0.1A and 2.5A +/- 0.1A respectively for approximately 20 minutes to raise the body of the cathode to temperatures sufficient for thermionic emission. Since power supplies were current limited, the heater voltage drop determines the input power. Figure 57 shows the results of 15 ignition characterization cases for the T5 and T6 cathodes, including typical heater power profiles.

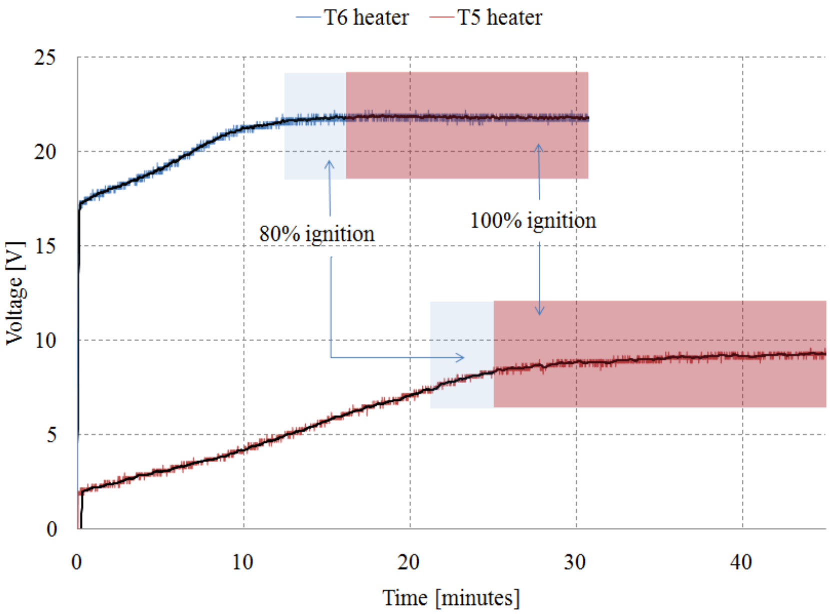

Figure 57 Heater input power over the pre-ignition heating period for the T5 and T6 cathode showing the times at which 80% and 100% of the test cases gained ignition

In the case of the T5 cathode voltage increases slowly during heat-up cycle since the heating element is firmly integrated into the cathode body, and therefore heater resistivity is subject to the thermal inertia of the assembly. Start-up time for the T5 is in the region of 22-minutes for 80% of cases and 25-minutes for the remaining 20%. Small fluctuations in heater power are likely due to thermal and electrical conductivity changes in isolated regions of the heater and insulation. It is also worth noting that purging of the cathode with a gas flow during the preheating time also increases the start-up time in the T5 cathode by some minutes due to convective cooling slowing the assembly heat-up time. Early ignition was possible based on previous operation of the thruster raising the assembly temperature, particularly in the T5 case. In an attempt to quantify the maximum required voltage for ignition an investigation was made recording the breakdown potential for 15 consecutive start-ups. It was found that breakdown voltage could be consistently less than 30V. After operating at high power >60W it was also found that re-ignition of the cathode was possible without the heater voltage being applied up to a minute after switch off due to the remnant temperature of the assembly. Operation at lower powers <15W however required almost the full preheating time to reignite due to the low power deposition into the assembly and thus low remnant temperature. It is interesting to note that at such low temperature emission can only be maintained by the Scotchy effect at the emitter surface.

In the case of the T6 cathode, the heater is primarily radiative rather than conductive; therefore the voltage increases very rapidly at the start of the cycle as the tungsten element rapidly heats. As the assembly heats up there is only a small increase in heater power due to the very limited contact between the heater and assembly. The T6 cathode ignited readily at around 12 minutes, while all ignitions had occurred by approximately 16 minutes. The T6 cathode also does not experience the voltage fluctuations found in the T5 start-up cycle since the radiative heater reduces the possibility of hot spots forming. It should also be noted that in the case of the T6 cathode breakdown voltage could be consistently less than 20V at mass flow rates > 0.5mg/s.

5.1.3 DISCHARGE CHARACTERISTICS

5.1.3.1 T5 CATHODE

Current voltage characteristics were obtained for operation of the T5 with argon over the flow range 0.05-mgs^{-1} to 1-mgs^{-1} and at 3.2A, 1.6A and 0.8A discharge current and with the T6 cathode at 10A, 20A, 25A and 30A with argon and 25A with xenon over the flow range 0.05 to 1-mgs^{-1}.

Typical voltage minimums were found in the T5 case at 0.65-mgs^{-1}, 0.68-mgs^{-1} and 0.82-mgs^{-1} at 3.2A, 1.6A and 0.8A respectively and are shown in Figure 58. This reduction in discharge voltage as flow rate is decreased is likely testament to an increasing ionization fraction within the orifice (and thus also downstream at the anode) which is driven by resistive dissipation and scales quadratically with current. This then corresponds to a lower cathode fall voltage required for the excitation of metastable states of argon to maintain the necessary plasma density at the anode to carry the discharge current. Higher currents therefore show lower voltage minimums.

In an attempt to both understand thrust production and to improve efficiency, the T6LA anode was also mounted on the T5 cathode and operated at lower mass flowrates enabling the comparison in operating performance between the two types of anode. Anode geometry is shown to have a significant influence on both the point of transition to plume mode and also the discharge voltage when operating at a specific discharge current and mass flow rate. With the larger anode and at low mass flowrates the discharge voltage is shown to be 8-10V below that of an orificed flat plate anode. In this case, due to the restricted range of the mass flow meter, the larger anode was only operated below 0.4mg/s. Nonetheless, at the 3.2Amp current condition the conical anode reduces discharge voltage from 34.57V for the flat plate to 19.35V, a reduction of 15.22V. This increases discharge efficiency by 44% and also substantially influences noise generation and the transition point to plume mode.

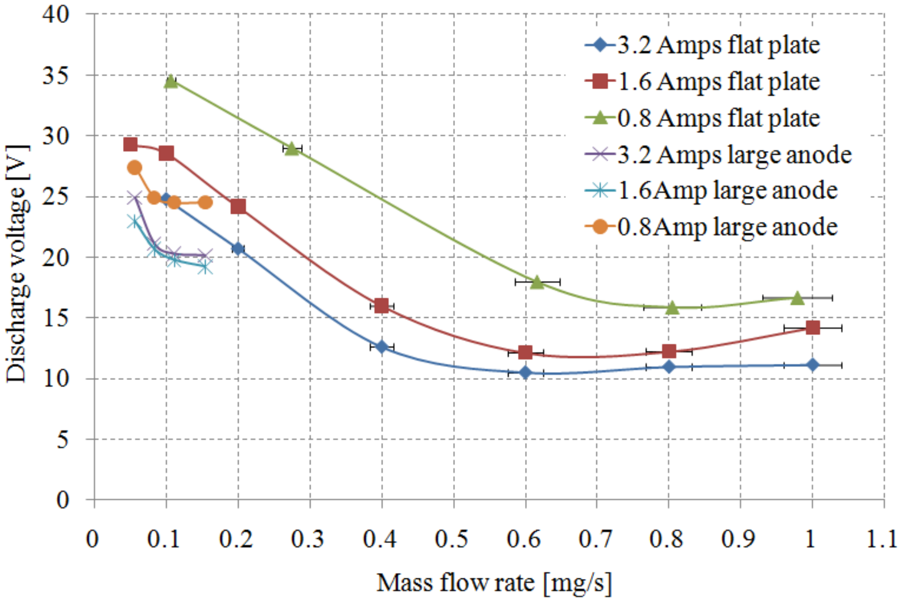

Figure 58 **T5 voltage characteristics when operating in a T5FP and T5CA configuration on argon**

5.1.3.2 T6 CATHODE

Discharge voltage in the T6 case remains very low for higher flowrates and only begins to increase significantly below 0.25mgs^{-1} for even the highest discharge currents (30A). The lowest flowrates achieved being 0.045mgs^{-1} at 28V with argon and 0.040mgs^{-1} at 42V with xenon. Above this flow rate there was little difference in discharge voltage at all current conditions. These discharge characteristics are very unconventional for the T6 hollow cathode and operation at such low flow rates cannot be obtained without suitable anode design to modify the transition characteristics. To the authors knowledge these are the lowest flow rates that a T6 cathode has ever operated at whilst drawing such high discharge currents at low voltages.

Operation with xenon gives consistently lower discharge voltages (testament to the lower primary ionization energy), however at very low flow rates the operating voltage did exceed that of argon. The reasons for this would not seem to be related to secondary or tertiary ionization since these are also lower for xenon but may involve any number of interrelated factors such as the differing ion mobility, recombination rates, field enhancement, plasma potentials or neutral densities.

Operation with xenon showed arguably the most remarkable current voltage characteristics with the cathode delivering 25Amps at only 0.15mgs^{-1} and 12V discharge voltage. Operation at higher mass flow rates gave reduction down to 8V. It should also be noted that discharge voltage was stable in the T6LA cathode design as opposed to conventional cathode operation where the discharge voltage is seen to fluctuate or oscillate over relatively long timescales. Discharge voltage was always stable and down to a critical point of mass flow rate when the cathode extinguishes, the reduction in back pressure encourages an increase in mass flow through the orifice and the cathode then enters into a pulsed mode of operation, continuously igniting and extinguishing until after a short time, the assembly temperature drops and the ignitions do not continue.

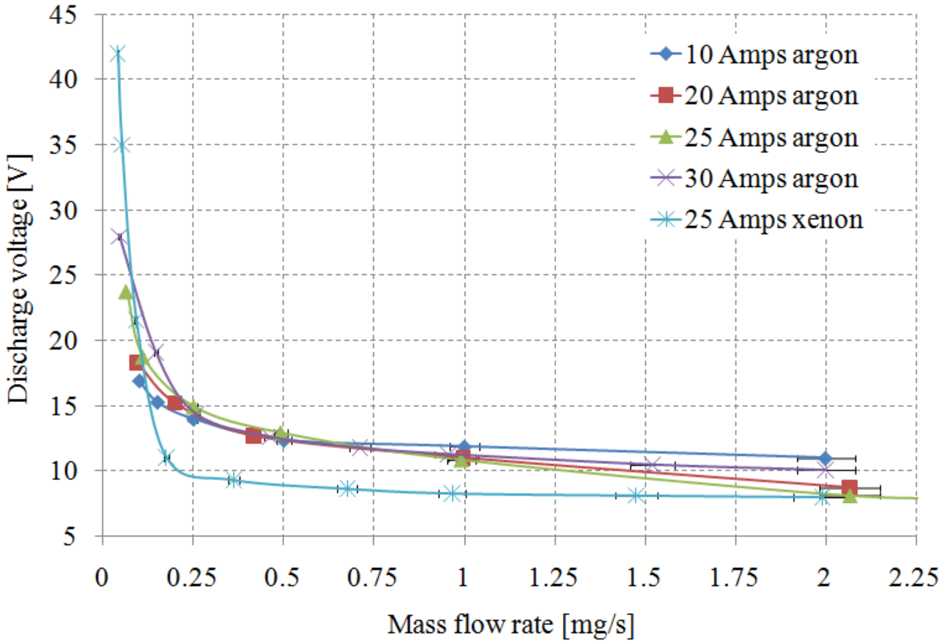

Figure 59 Current-voltage characteristics for the modified T6LA cathode with argon and xenon

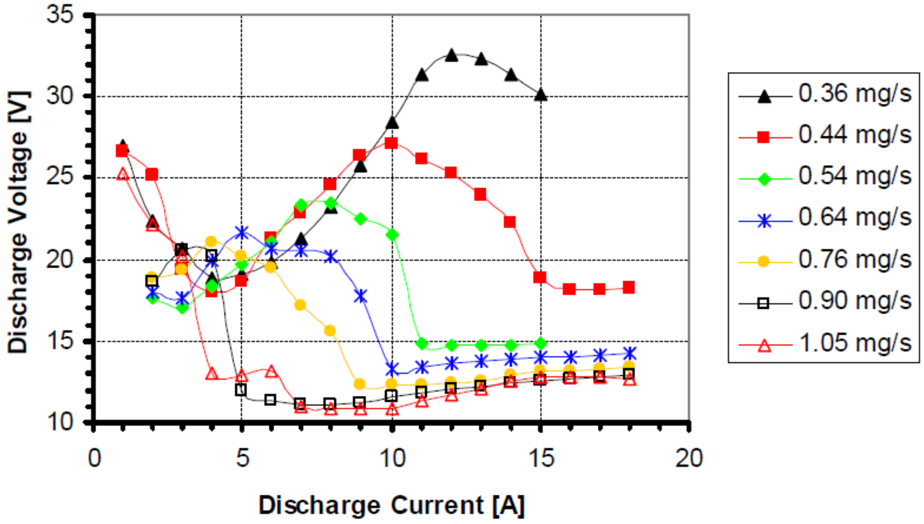

Figure 60 Discharge voltage data from testing by Gessini for the T6 cathode with a 10mm x 10mm cylindrical steel anode on argon

As a comparison, Figure 60 shows testing data of Gessini who used a 10mm x 10mm cylindrical steel anode with the same T6 cathode. With 0.36mgs^{-1} at high currents the newly designed T6LA anode operates at 13V as opposed to 33V for the cylindrical anode. This represents an increase of 39.4% in discharge efficiency. The T6LA anode also enables operation to flowrates over seven times lower than the cylindrical anode (<0.05mgs^{-1}) at twice the discharge current (up to 30A). The T6LA cathode also shows very unconventional discharge characteristics from normal hollow cathode operation with no typical voltage minimums or abrupt change to plume mode.

Noise measurements have shown that, plume mode, at least from a discharge noise viewpoint, does still occur at very low flowrates (<0.1mgs^{-1}) however the jump to high voltage operation with associated hysteresis as seen in Gessini's data is not present. The large surface area available to the plasma by the anode is shown to be remarkable in maintaining spot-mode and with a high degree of passive current collection from the plasma. In this case it is postulated that the voltage increase found at the very lowest flowrates is the essence of the electron flux enhancement mechanism responsible for plume mode (however in its minimal form, whereby electron flux at the desired current is maintained through the formation of an anode-cathode potential drop). A full explanation for this mechanism is given in Section 6.2.5.

5.1.4 SPOT-TO-PLUME MODE TRANSITION

Another significant difference in the two types of anode is the point at which transition occurs. With a flat plate anode the cathode gradually enters plume mode as flow rate is reduced below 0.25mg/s. This type of behavior is typical for conventional hollow cathode geometries where the transition from spot-to plume mode is observed to occur continuously (not a sharp transition) as the gas flow decreases or the current increases.[86, 164] In the case of our anode however spot mode is maintained to extremely low flowrates with a sudden and sharp transition occurring at a critical mass flowrate. Figure 61 shows the T5CA operating in an almost noise free DC discharge when operating on only 0.05mg/s of argon. Further reduction in mass flowrate to 0.03mg/s however results in a step change in operation and substantial noise generation primarily < 5MHz but also extending beyond 120MHz as shown in Figure 62.

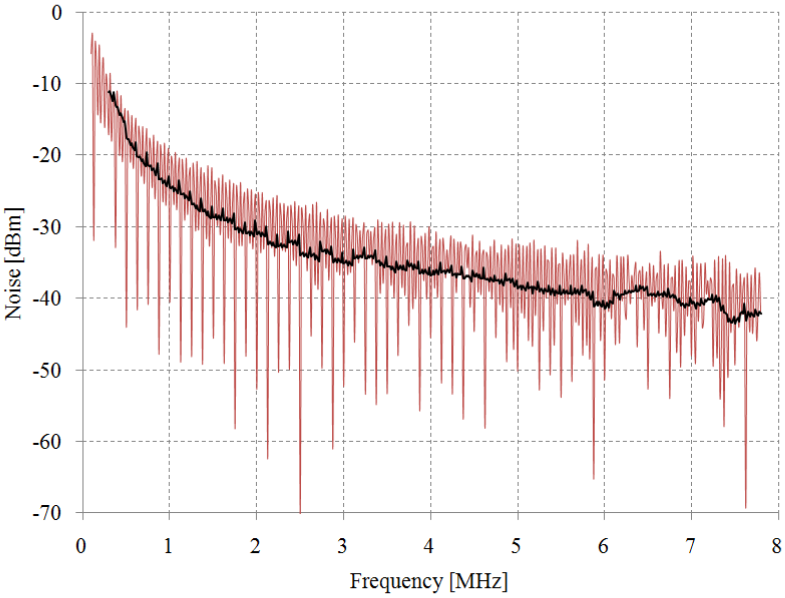

Figure 61 Noise measurements from a T5CA operating on 0.05mg/s argon at 3.2 Amps

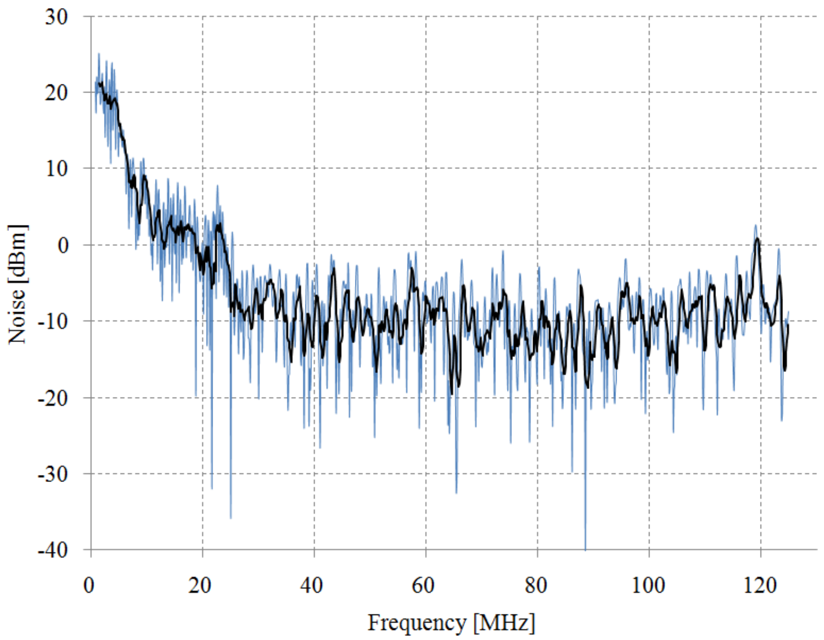

Figure 62 Noise measurements from a T5CA operating on 0.03mg/s argon at 3.2 Amps

This type of transitionary behavior has not been found anywhere in the literature. The voltage fluctuations responsible for this noise when operating the T5 cathode at 0.03mg/s are also found to be extremely large, exceeding +100V and -10V as show in Figure 63. The large fluctuations are periodic as shown in Figure 63, however as the FFT data indicates, it is difficult to identify any other discreet frequencies. Voltage fluctuations of this magnitude will have a serious impact on the life of the hollow cathode and bring into question the feasibility of operating cathodes down to this flowrate, where the highest ISPs are attained, for long periods.

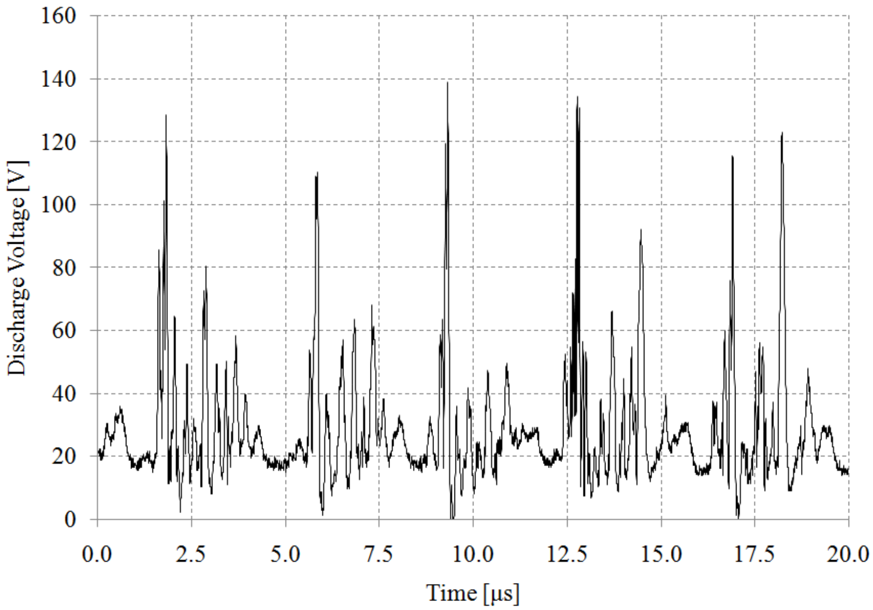

Figure 63 Voltage fluctuations for the T5 cathode operating at 3.2A with 0.03mg/s argon

Similar behavior, shown in Figure 64, is found in operation of the T6LA cathode however transition in this case occurs at an order of magnitude higher flowrates than the T5CA cathode.

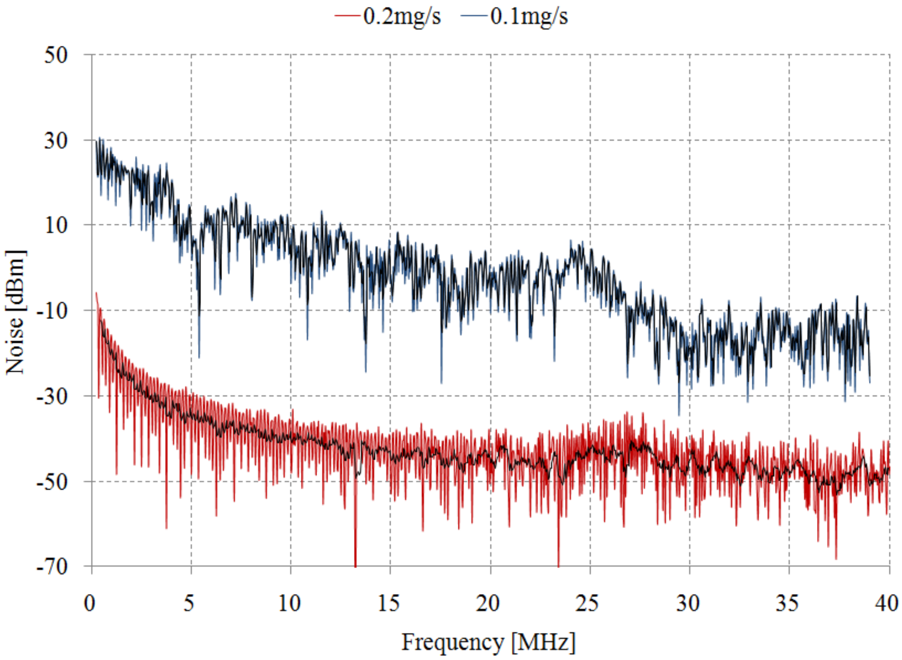

Figure 64 Noise measurements from the T6LA operating at 0.2mg/s and 0.1mg/s on argon at 25Amps

Voltage data highlighting the abruptness of the change to plume mode for the T6 even at low discharge currents is shown in Figure 65. This data was taken at 5Amps with a change in flowrate from 1.5mg/s to 1.40mg/s and back again. The cathode initially shows very little noise, however on decreasing mass flowrate the cathode very quickly establishes a transition to a higher but unstable operating voltage with significant noise generation and peak to peak voltages in excess of 22V.

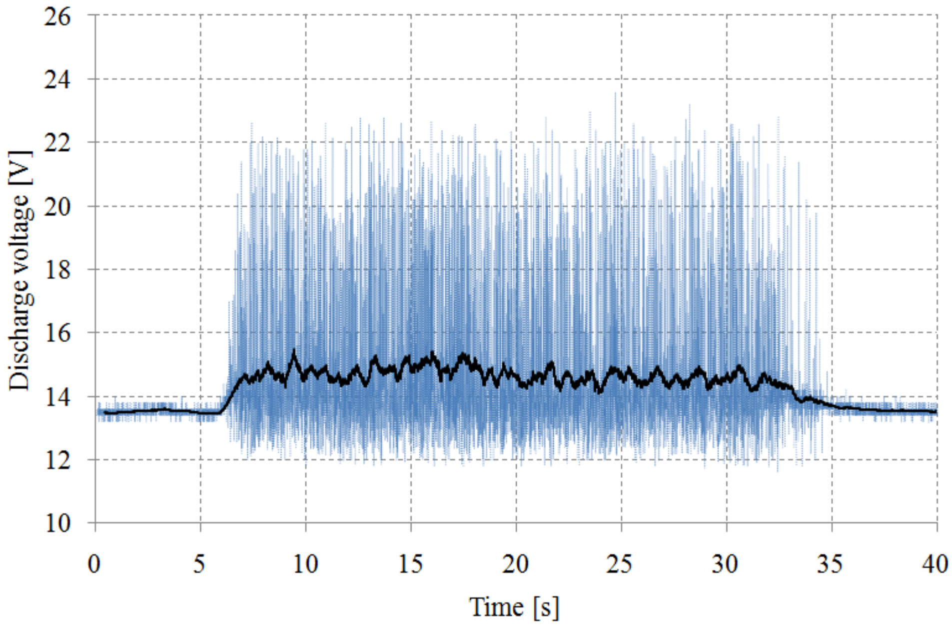

Figure 65 Voltage characteristics of a transition to plume mode at 5Amps on argon between 1.50mg/s - 1.40mg/s and back again.

The extent of discharge voltage oscillations in excess of 600V for the T6 cathode when operating at 0.05mg/s at 30 amps with argon is shown in Figure 66. Similarly to the T5 cathode when operating at 0.03mg/s the T6 cathode shows fluctuations above 120V. Again, voltage fluctuations of this magnitude suggest that the T6 cathode would sustain severe damage if operated in this regime for extended periods. These voltage spikes are a result of the inductance of the circuit and what must be equally large current fluctuations with an EMF given by:

$$\varepsilon = L\frac{\partial I}{\partial t} \tag{5.1}$$

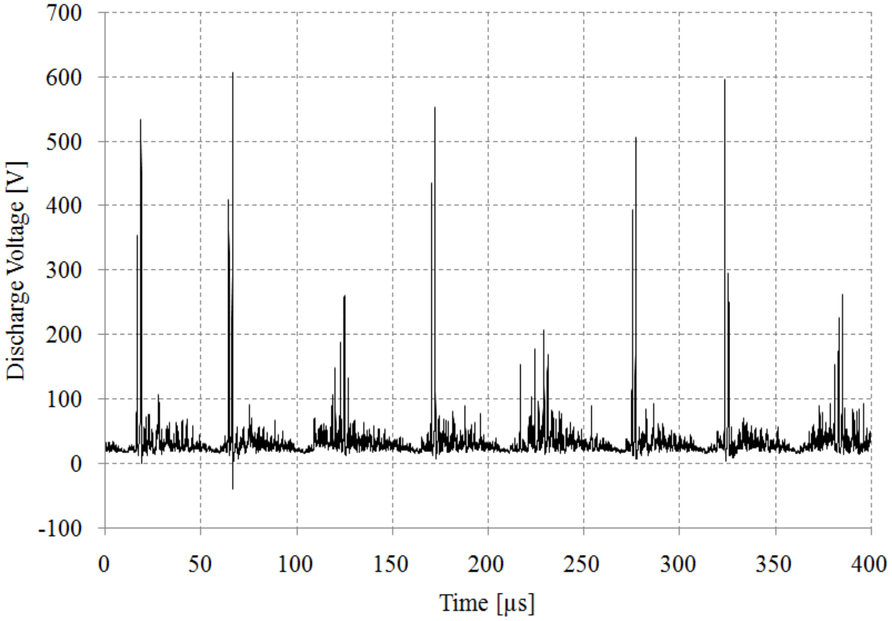

Figure 66 Voltage fluctuations in the T6LA discharge when operating at 30Amps, 0.05mg/s on argon.

In our T6 cathode we can identify a form of breathing mode with a frequency of ~18.1kHz with each decay period having many higher frequency fluctuations. In the T5 cathode the breathing frequency is much higher ~250 kHz. Based on plasma densities the electron plasma frequency in the T6 hollow cathode should be between 1-6 MHz. There are generally three classes of oscillation in hollow cathode discharges[112] [165]:

1. Plasma discharge oscillations in the frequency range of 50-1000 kHz. These are usually incoherent oscillations in the turbulent ion acoustic frequency range with small to moderate amplitude that vary continuously from fractions of a volt on the electrodes in the spot mode to tens of volts on the electrodes into the plume mode.

2. If sufficiently large, these ion acoustic oscillations can trigger regulation problems in the power supply, leading to large discharge voltage oscillations on power supply regulation timescales of 100-1000 Hz.

3. As the discharge current increases the ionization percentage in the cathode plume becomes significant and can lead to ionization instabilities or so called predator-prey oscillations. In this case the plasma discharge burns out a significant fraction of the neutral gas, and the discharge collapses on the time frame of the neutral flow into the

> plume region. The frequency range of these instabilities is in the 25-250 kHz range for xenon, depending on the physical lengths and size of the discharge components. Ionization instabilities can usually be inhibited by selection gas flow and/or magnitudes of any applied axial magnetic fields in the cathode plume region which modifies the local ion generation rate.

The fluctuations found in the T5CA and T6LA discharge extend into much higher frequencies (>120MHz) than oscillations found in typical hollow cathode operation. The fact that the oscillations are coherent however suggests that voltage fluctuations must still be predator prey mode related ionization instabilities with the decay modes extending into much higher frequencies as evident in the Figures.

Simulations have shown that the relative electron-ion drift speed can be several times the electron thermal speed. The latter result supports the hypothesis that electrostatic two stream instabilities, which can grow exponentially, may be excited in the orifice channel and/or near-plume regions of the hollow cathode. High frequency fluctuations of this type, typically in the range of 5-150 MHz, are frequently observed in Hall Effect thrusters and are correlated to decay periods of 'breathing oscillation' component of discharge current.[166] [167] The breathing mode is a low-frequency discharge (typically ~22 kHz) current instability related to predator-prey relation between the electron and neutral propellant atoms in the same way as in the hollow cathode discharge. A large electric field near the channel gives a high ionization rate that acts to deplete the neutral density. The front of the neutral flow retreats upstream to a region where the ionization rate is low. As the front of the neutral flow once again moves downstream into the region of high electric field, the neutral density is replenished and the ionization rate increases, thus the process is repeated. This behavior results in an oscillation in the location of the ionization zone and an oscillation in the electric field. The decay modes frequencies of the breathing oscillation however suggest a mechanism likely responsible for the >150 MHz noise seen in the T5CA and T6LA discharges. The oscillation in electric field is also likely responsible for the fluctuations in discharge voltage of up to +600V to -45V in the T6LA cathode and +120V to -10V in the T5 cathode. It should be noted that the power supply is of course limited to 80V supply.

It is important to realize that the large discharge voltage fluctuations and transition to plume mode is an effect that occurs exterior to the hollow cathode.[165] Plasma density oscillations inside the cathode insert plasma are small in amplitude and uncorrelated to the ionization and large turbulent instabilities observed outside in the keeper plasma region. With both the T5 and T6 cathodes, transition to plume mode occurs at increasingly higher flowrates with decreasing discharge currents consistent with lower ionization fractions. Anode divergence angle and area also has a pronounced effect on the transition point however at the time of writing this data is still being collected. The data does suggest there is an optimum divergence angle for minimization of discharge voltage. It is also noted that during testing, arc root rotation around the anode ring at the exit of the anode orifice which was responsible for approximately 35° alteration of the thrust vector of the visible plume. This was only observable at high mass flow rates and low powers due to the intense brightness of the anode ring shown in Figure 67. It is unclear at this stage what effect this has on the total thrust vector. T6 cathode operation highlighting the rate of convective heat transfer to the anode is shown in Figure 68.

Figure 67 T5FO during operation with argon at 70.3W (3.2A) at 21V with 0.05mgs^{-1} (left) and 12.8W (0.8A) at 15V with 0.8mgs^{-1} (right)

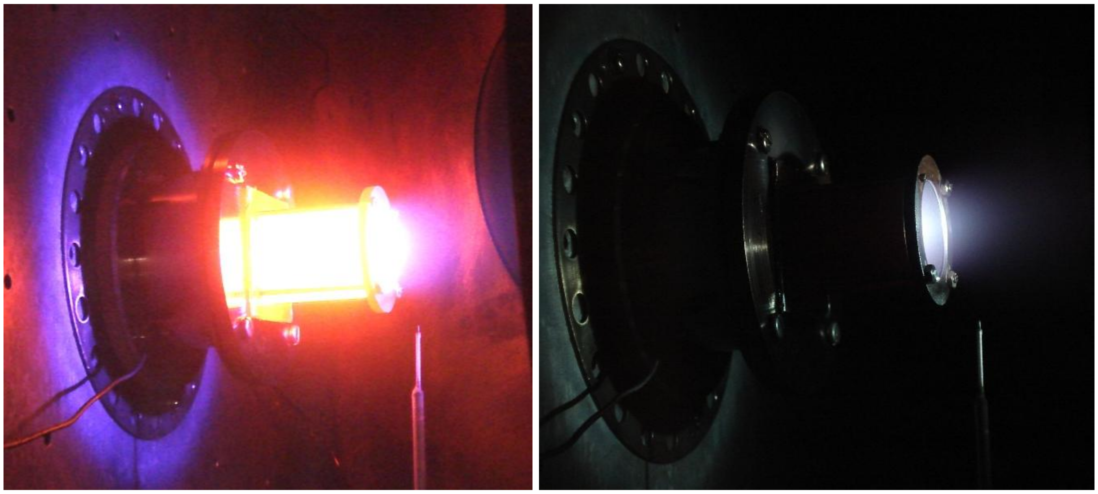

Figure 68 T6 cathode operating stably at 840W (30Amps) on argon at 0.045mgs^{-1}, 28.0V discharge voltage (left) T6 operating on xenon at 200W (25Amps) 0.5 mgs^{-1} at 8.01V discharge voltage (right)

5.1.5 T5 DISCHARGE THRUST MEASUREMENT

All thrust measurement for the T5 cathode were made with argon. Specific impulse at various current conditions for the T5 cathode is shown in Figure 69 with thrust levels shown in Figure 70. Results show near monotonic dependence of specific impulse on discharge current with rapidly increasing performance below 0.4mgs^{-1} for the 3.2A and 1.6A throttle settings with a less pronounced increase at 0.8A.

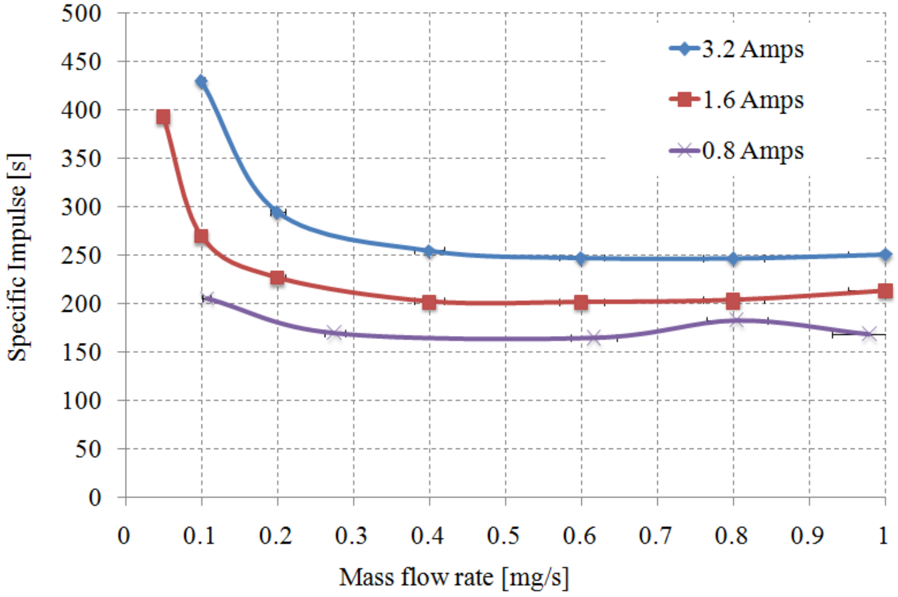

Figure 69 Specific impulse vs. mass flow rate for various throttle levels of the T5 cathode with argon

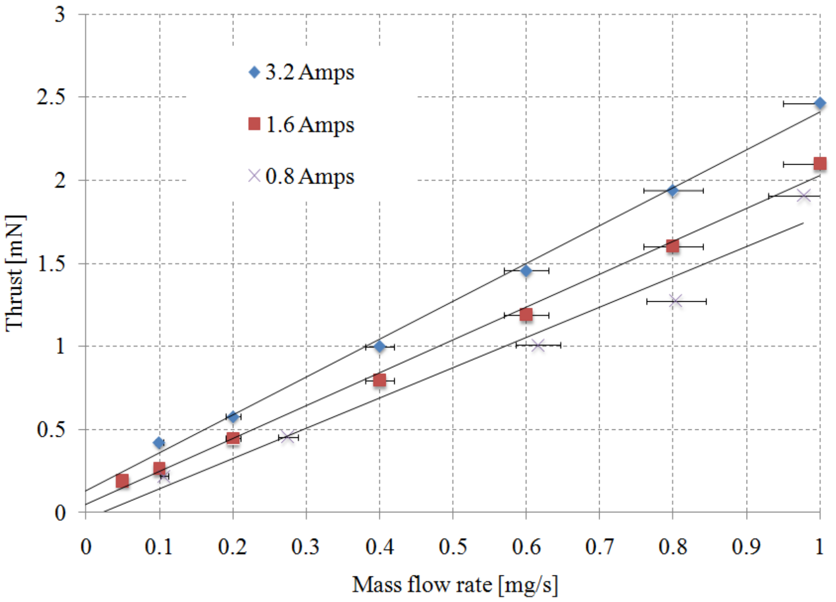

Figure 70 Thrust levels for the T5FO cathode at various current conditions with argon

Since a change in flow rate results in a change in operating voltage it is seen that specific impulse can be correlated with specific power of the flow (J.mg^{-1}) and a product of the discharge current and operating voltage. Figure 71 shows the relationship between operating power and specific impulse and Figure 72 shows associated thrust efficiencies.

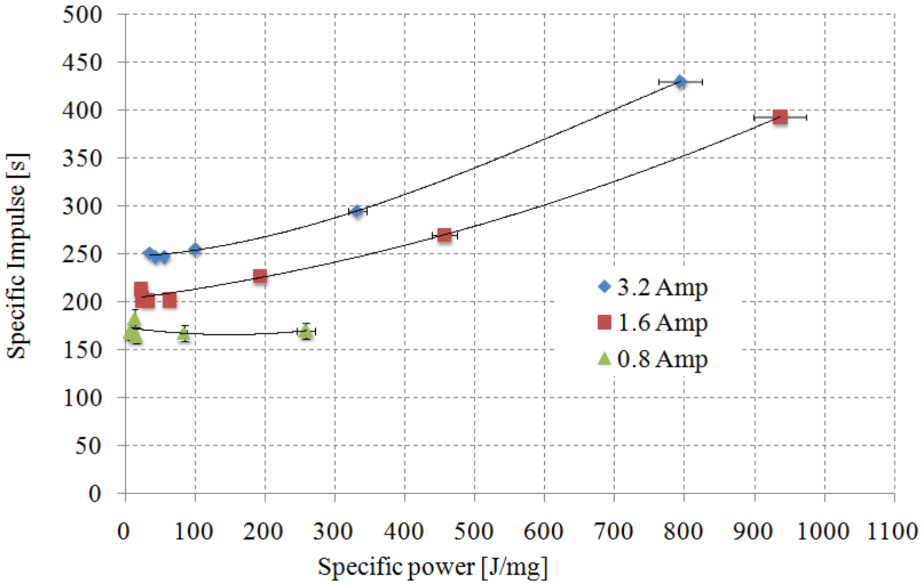

Figure 71 Dependence of specific impulse on specific power for the various current levels with argon for the T5FO cathode

Operation at low powers (<13W) in the low current condition (0.8Amp) brings relatively high specific impulse of up to 165 seconds equal to performance in a resistojet mode (and at lower power), where cathode body temperatures are in the region of 1000°C. At the high current condition operation at powers of below 30W give specific impulse in the region of 250s. Further reduction in flow rate increases operating voltage and power invested in the flow. This results in an increase in specific impulse however with declining thrust efficiency as convective and radiative losses begin to dominate. In this case thrust efficiency is calculated based on Equation 1.12 based on the equivalent exit velocity based on the measured thrust at the respective mass flowrate.

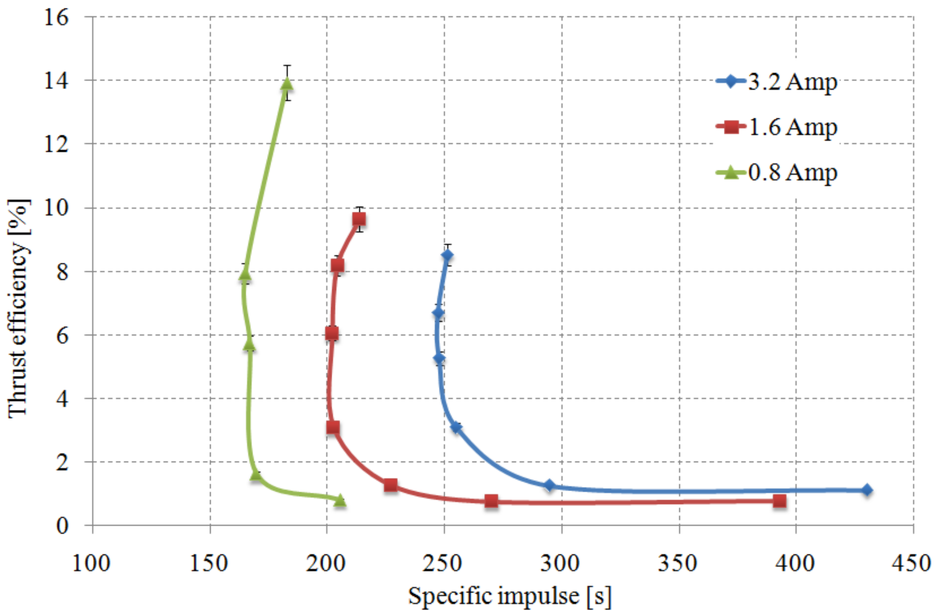

Figure 72 Associated thrust efficiencies in relation to specific impulse at various throttle conditions for the T5FO (flat plate orifice) cathode

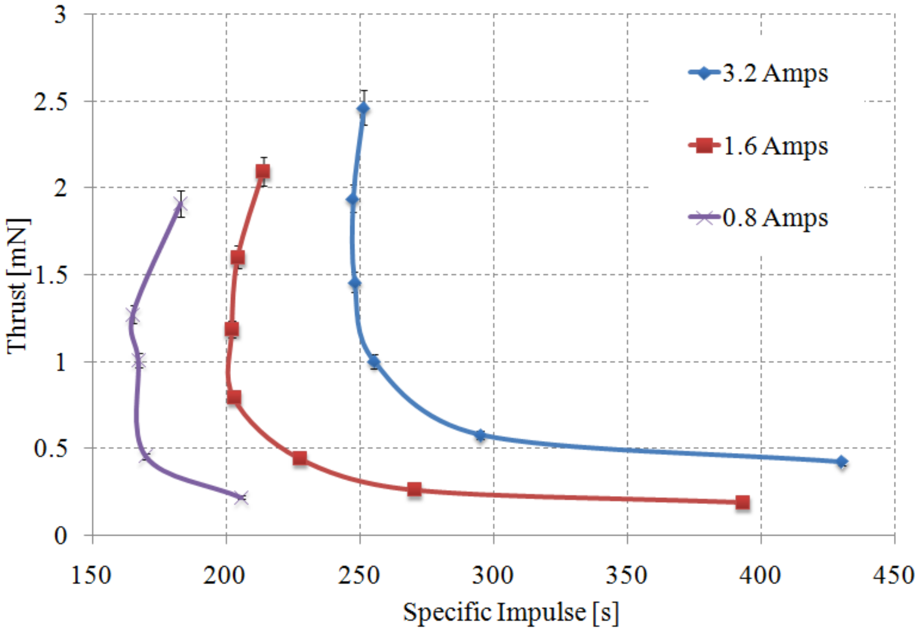

Figure 73 Thrust and specific impulse attained at various current conditions in the T5FO cathode

Figure 73 shows thrust levels achievable with respect to specific impulse. The highest specific impulse of 429s was attained with the T5FO cathode at 3.2A, with 1.1% thrust efficiency, 79W discharge power. Specific impulse can be traded for higher thrust to power ratios by increasing propellant flow rates or decreasing discharge current (however higher thrust efficiencies are obtained at higher discharge currents) generating thrust efficiencies of 14% (200µN/W) and specific impulse of 167s at 0.8Amps, and over 8% at the maximum rated current capacity of 3.2 Amps, with specific impulse ~250s (77µN/W, 35W discharge power). Up to 2.4mN could be generated at higher currents, shown in Figure 22, with the maximum flow rate of 1-mgs^{-1} with specific impulse over 250s.

Respective discharge powers and performance can be seen in Figure 74 and highlights the ultimate power required to generate such performance.

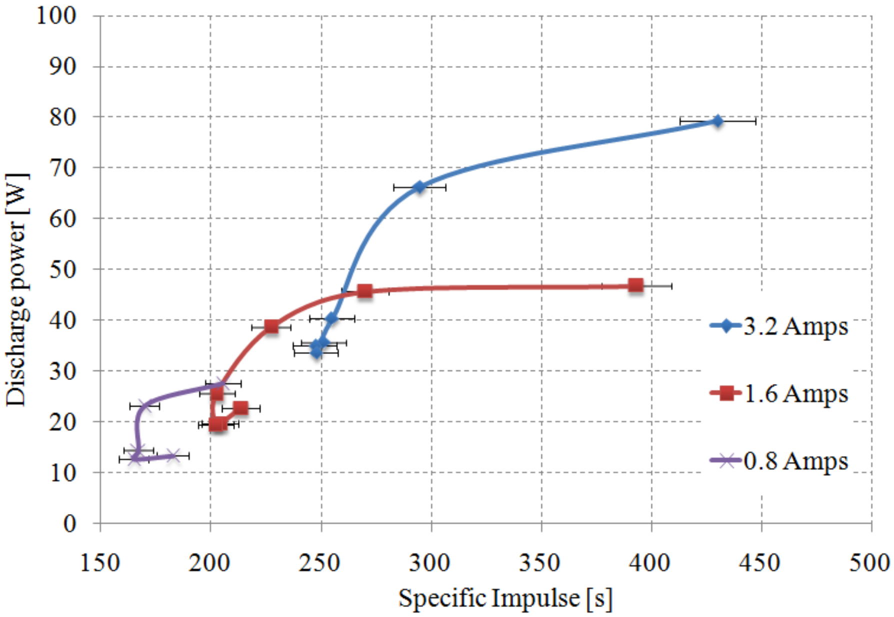

Figure 74 Performance variation with discharge power at various current conditions

In addition some limited data was acquired with the T5 cathode at very low flowrates using the anode from the T6 design with a digital mass flow controller. In this case, comparisons to the T5 flat plate orifice experiments are shown in Figure 75. The data for the conical anode indicates a small increase in specific impulse over the flat plate orifice as expected since the conical anode is enclosed and does not directly inhibit the flow, thus a greater proportion of the gas flow is emitted axially, contributing thrust rather than radially. Since the conical anode was able to operate at lower mass flow rates without the risk of overheating the anode the T5CA was also able to demonstrate greater specific impulse of 657s, 477s and 361s at 3.2Amps, 1.8Amps and 0.8Amps at thrust efficiencies of 4.5%, 8.1% and 17.1% respectively. An image of the T5CA cathode in is shown in Figure 76 and Figure 77.

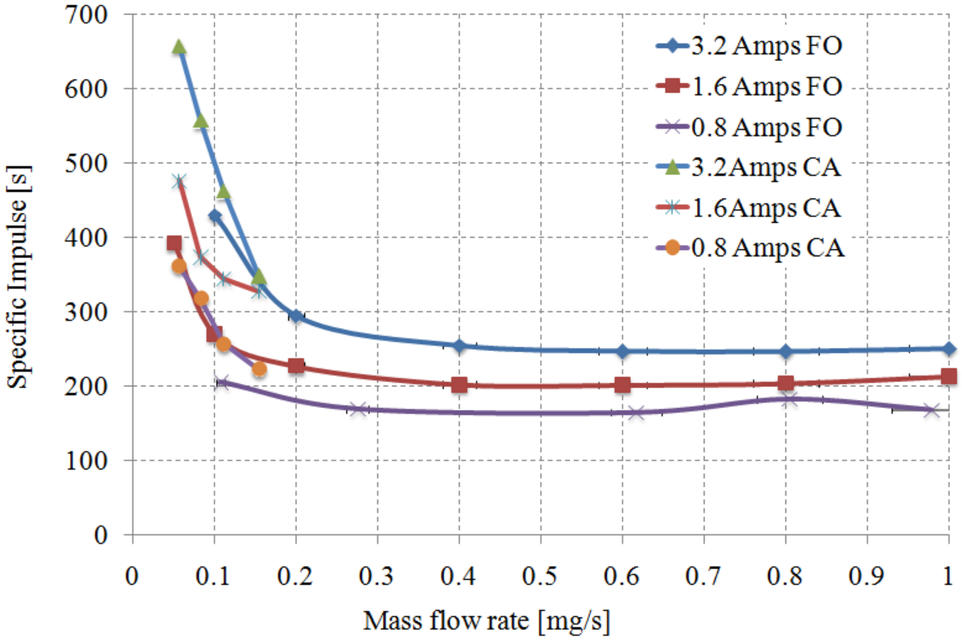

Figure 75 Specific impulse measurements for the T5 cathode operating with a flat plate orifice anode (FO) and a conical anode (CA)

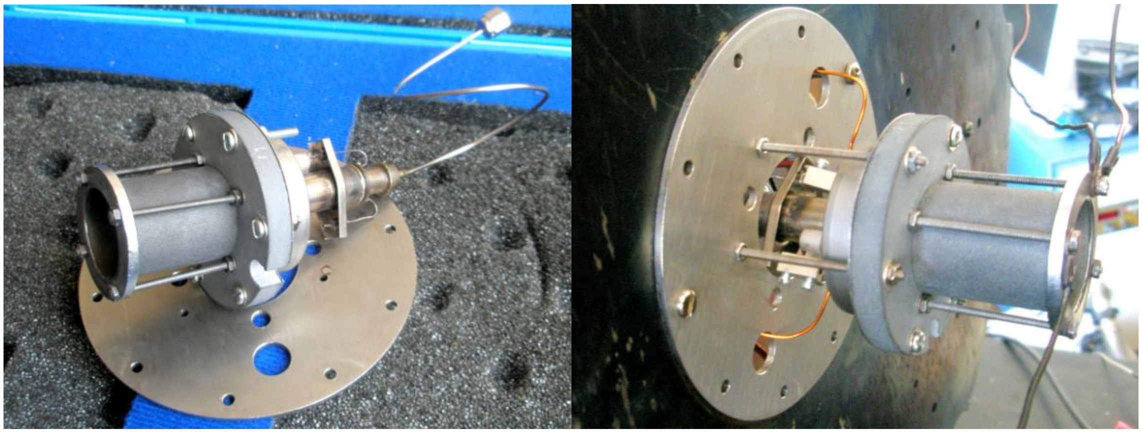

Figure 76 T5CA cathode assembly

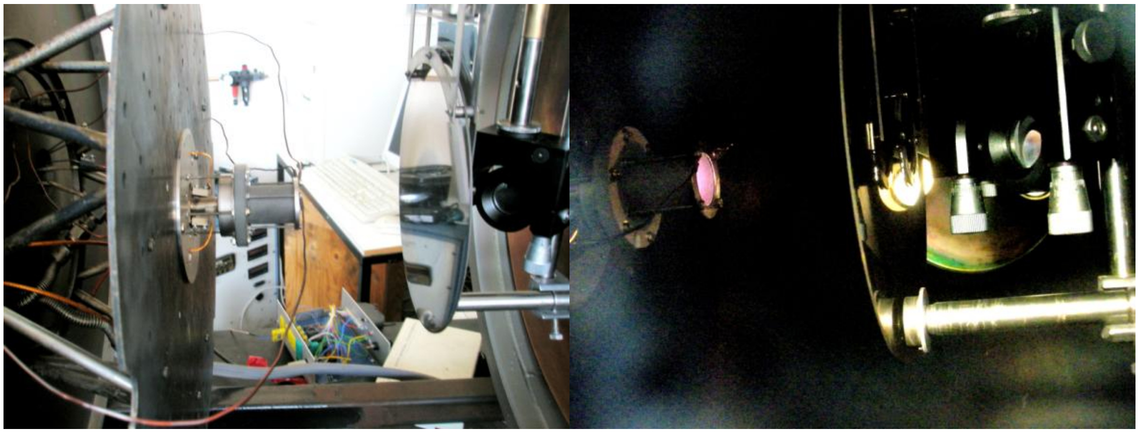

Figure 77 T6LA thrust measurement setup (left) during thrust characterization at 3.2Amps (right)

5.1.6 T6 DISCHARGE THRUST MEASUREMENT

Figure 78 shows that high specific impulse in the T6CA is dependent on the discharge current since higher discharge currents are able to sustain operation at lower mass flow rates and higher powers. Operation with xenon also gives high specific impulse although only at the lowest flow rates. This is testament to the lower primary ionization energy of xenon, which enabled the cathode to operate at the lowest flow rate of 0.04mgs^{-1}.

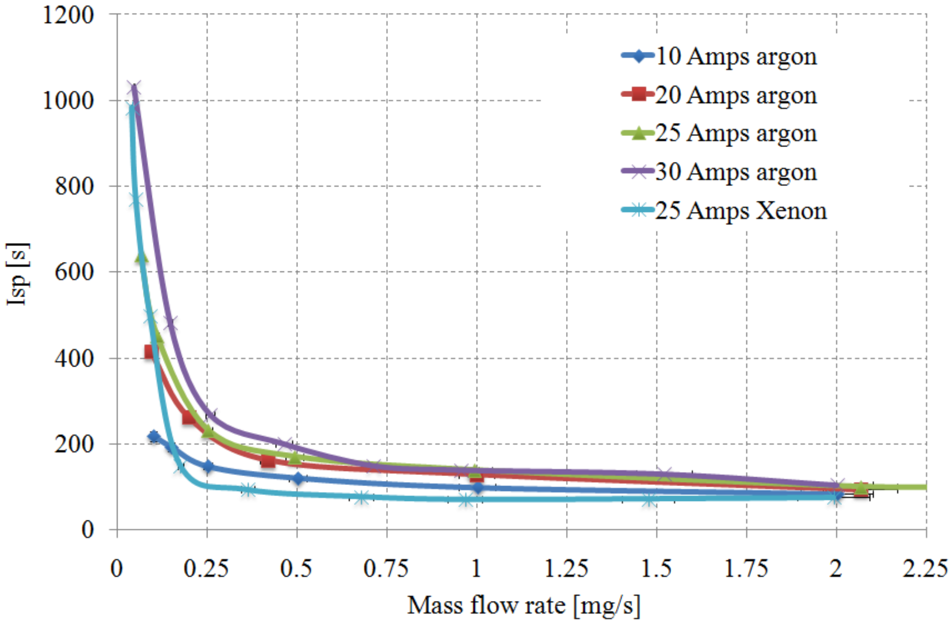

Figure 78 Specific impulse reached with the modified T6 hollow cathode at various current conditions and mass flow rates with xenon and argon

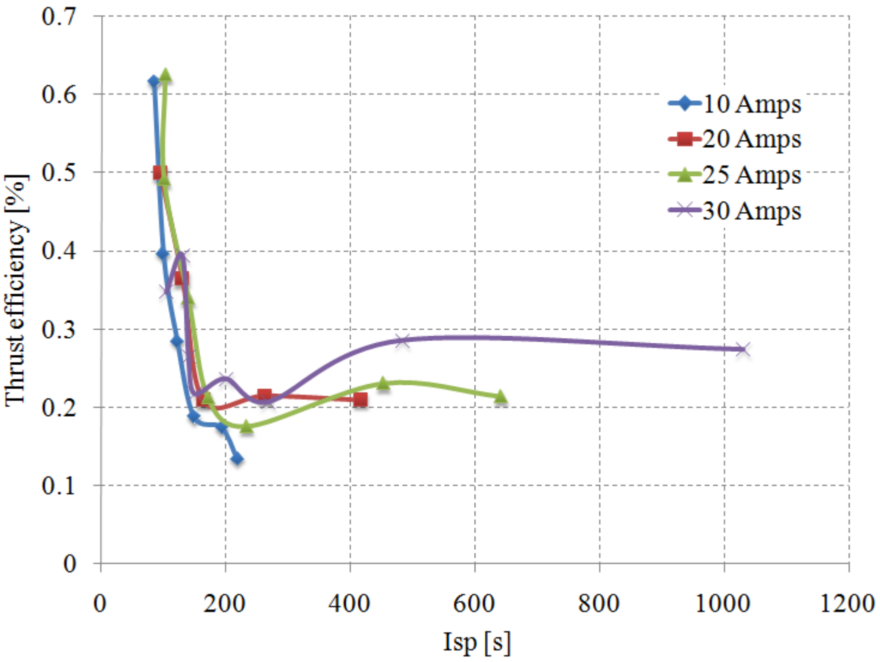

Figure 79 Thrust efficiency of the T6 cathode operating at various discharge currents on argon with respect to specific impulse

Figure 79 shows that although we have demonstrated large reductions in discharge voltage over previous work, thrust efficiency remains very low for the T6LA cathode.

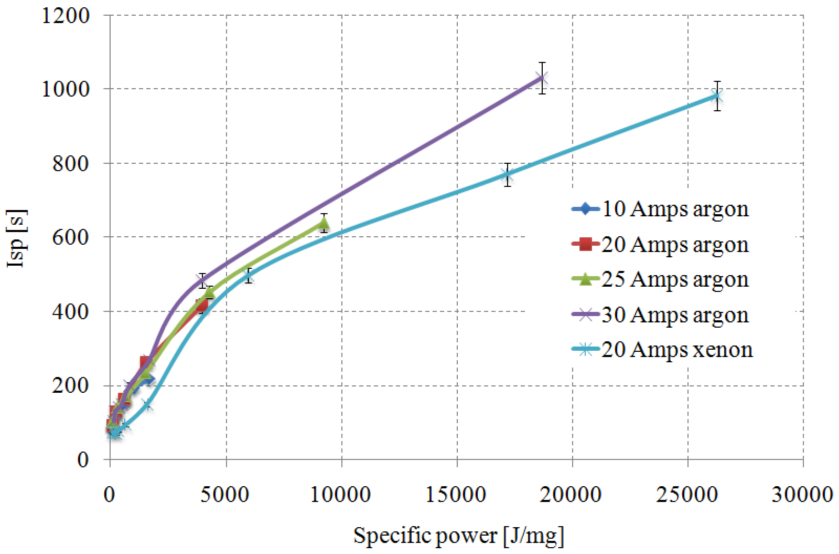

Figure 80 Relationship between specific impulse and specific power for the T6 at various current levels with xenon and argon

Figure 80 shows two distinct gradients in the relationship between specific power and specific impulse which differ substantially from the T5 results. For operation with argon, specific impulse is almost identical for low specific powers, however approaching 5000J.mg^{-1} there is a change in gradient. It is postulated that this change in gradient represents a change in dominant thrust production, with electromagnetic acceleration becoming the dominant accelerating mechanism, since flow rates above 5000J.mg^{-1} are very low and electrothermal thrust would contribute an ever decreasing component. This theory is strengthened when considering thrust level with respect to mass flow rate as in Figure 81. It is clear that when extrapolating thrust level back to zero mass flow a remnant thrust production mechanism exists which scales with discharge current. This of course does not imply that the thruster can generate thrust at zero mass flowrate, but since gas dynamic acceleration mechanisms must scale with mass flowrate, it may imply that there is and additional accelerating component superimposed on top of the mass flowrate dependant gas dynamic mechanism. Interestingly operation with xenon initially shows lower thrust levels more similar to gas dynamic acceleration with xenon until very low flowrates are reached several thrust measurements with xenon at flowrates ~ 0.05mgs^{-1} then show thrust levels to increase to levels similar to that of argon. Error bars indicate ±4% needle valve uncertainly.

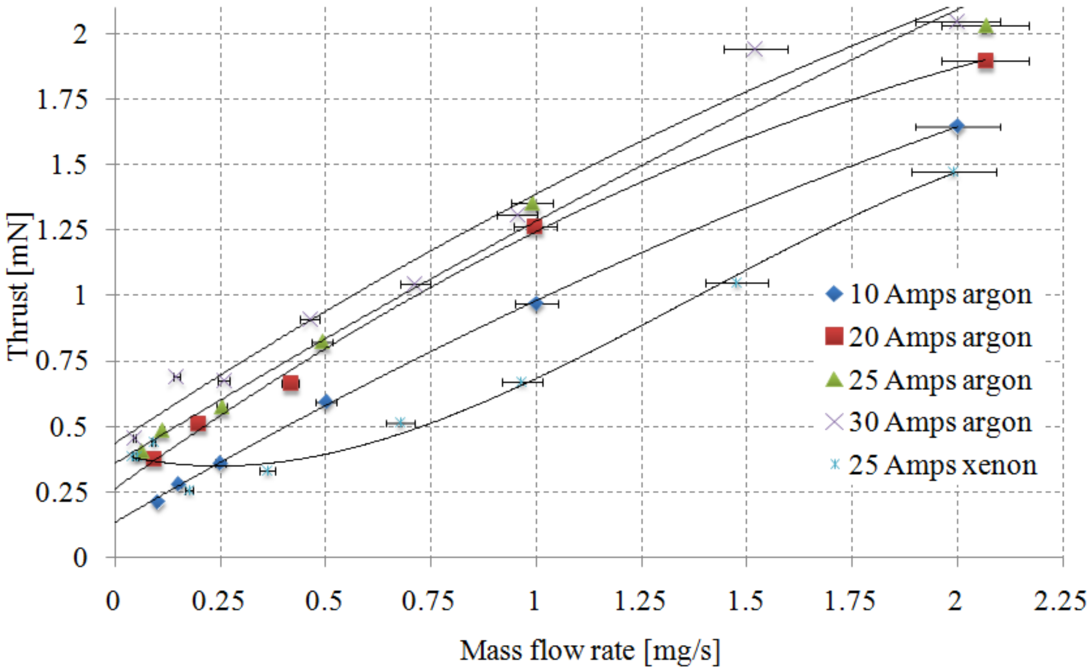

Figure 81 T6 thrust level with respect to mass flow rate at various current conditions with xenon and argon with second order polynomial fits

5.2 THRUST MECHANISM DISCUSSION

There are at least 3 mechanisms which may be responsible for propellant acceleration in hollow cathodes. These are components of electrothermal thrust (consisting of pressure thrust and momentum thrust) electrostatic acceleration, electromagnetic acceleration.

5.2.1 ELECTROTHERMAL THRUST

Plasma models suggest that cathodes are capable of generating heavy particle temperatures greater than 6,000K with wall temperature not exceeding 1,500K[168] while Laser Induced Fluorescence (LIF) has identified neutral temperatures in cathode-keeper gaps between 1800-4000K, well above cathode wall temperature.[103] Experiment has also suggested ion and neutral temperatures between 3200-6000K necessary to explain high backpressures within conventional cathodes.[83] The main mechanism of plasma heating is known to be Ohmic heating by plasma electrons within the cathode orifice with collisional heat transfer to the heavy particles.[169] Neglecting the plume divergence and all other losses, equating the thermal power with kinetic power conversion gives:

$$\frac{5}{2}\frac{\dot{m}}{M}kT = \frac{1}{2}\dot{m}v_{ex}^2 \tag{5.1}$$

In reality this is not achievable due to various losses. Continuum flow theory[170] for a choked sonic orifice predicts that the level of kinetic energy conversion to be:

$$ISP = \frac{1}{g}\left(2\frac{\gamma+1}{\gamma}\frac{kT}{M}\right)^{\frac{1}{2}} \tag{5.2}$$

However the continuum flow theory breaks down just downstream of the orifice and becomes free molecular. If free molecular isotropic non-continuum flow theory is assumed energy conversion is reduced to: [171]

$$ISP = \frac{1}{g}\left(\frac{\pi}{2}\frac{kT}{M}\right)^{\frac{1}{2}}$$

(5.3)

3D Navier-Stokes continuum computations have shown the upstream pressure in cathodes such as the T6 to be between 1000-2000Pa.[172] In this case the cathode orifice can be assumed to act as a conventional constrictor, which is fair given the orifice cross-section is much smaller than the dispenser cross-section. The critical pressure ratio for a choked flow can be estimated:

$$\frac{p_{crit}}{p_{inlet}} = \left(\frac{2}{\gamma+1}\right)^{\gamma/(\gamma-1)}$$

(5.4)

For xenon and argon the critical pressure ratio is ~0.49 and given that chamber pressures, even with low mass flowrates is far above ambient, the assumption of choked flow is reasonable. The collision cross section for ion neutral charge exchange in the orifice of T6 type cathodes is about 88Å^2 at 1eV thus the ion mean free path for charge exchange collisions is only about 1µm. The flow is thus diffusion limited by charge exchange. For relatively slow diffusion in the orifice the *axial ion thermal speed significantly exceeds the drift velocity*, thus the axial velocity can be approximated by the ion thermal speed. In the T5 cathode which operates at much higher pressures than a T6 type cathode the mean free path can be expected to be even smaller still with the ion thermal speed >> ion drift velocity. The thermal velocity is also the sonic velocity and neglecting viscosity a function of the gas temperature[173]:

$$v_{or} = \sqrt{\gamma RT}$$

(5.5)

where the specific gas constant $R = \frac{k}{M}$. As a further confirmation of this condition, the isentropic flow equation relates the mach number of the upstream flow for a given area ratio to the velocity at the choke point.[173]

$$\frac{A}{A*} = \frac{A_{ins}}{A_{or}} = \frac{1}{M}\left[\frac{2}{\gamma+1}\left(1+\frac{\gamma-1}{2}M^2\right)\right]^{\frac{\gamma+1}{2(\gamma-1)}}$$

(5.6)

where *M* is the mach number of the upstream flow. In the case of the T5 cathode, assuming a gas temperature of 298K with an area ratio of 16:1, the required upstream gas velocity is 6ms^{-1}. At 1mgs^{-1} in the T5 cathode, an arbitrary calculation reveals an upstream velocity ~4ms^{-1}, however in our case we have Rayleigh flow with heat addition which significantly heats the gas >> 298K and speeds up the flow within the orifice. In this case we can state with good certainty that the flow does indeed reach M=1 within the orifice.

Since ions created within the orifice cannot be accelerated downstream against the monotonic potential profile we can assume that only neutrals are able to escape the orifice into the downstream plume to conserve mass flowrate and thus the thrust mechanism at the orifice exit can be treated as hot neutral flow with a plasma pressure acting on it immediately upstream. In reality a proportion of the ions must obviously exit the cathode orifice in order to maintain a quazi-neutral plasma while carrying the electron current to the anode, however given the much lower ion mobility than electrons (electron thermal speed at 2eV is 592kms^{-1} as opposed to 456ms^{-1} for an argon ion at 1000K), very little ion flux (low ionization fraction) would be required to carry the discharge current. In addition, in plume mode with the formation of the double layer, sufficient ions are created by the electron acceleration process in the emitted plume itself.

Assuming a uniform velocity profile across the orifice, thrust generated as a result of pressure and momentum thrust is given by:

$$F = \dot{m}v_{ex} + p_{ex}A_{or} \tag{5.7}$$

Assuming that all particles behave like a perfect gas, and neglecting magnetic pinch effects, the plasma pressure at the cathode exit can be evaluated from the equation of state:

$$p_{ex} = n_e kT_e + n_i kT_i + n_n kT_n \tag{5.8}$$

Assuming no form of nozzle is included downstream of the orifice, the thrust contribution at the orifice exit will thus consist of components of momentum and pressure thrust by electrons and ions at the orifice exit given by:

$$F = \dot{m}\sqrt{\gamma R T_n} + A_{or}\left(n_e k T_e + n_i k T_i\right)$$

(5.9)

It should be noted that boundary effects will however also influence the flow regime and velocity profile.

5.2.2 ELECTROTHERMAL ACCOMMODATION COEFFICIENTS

As an example based on the conversion of thermal energy of heavy particles to direct kinetic energy the theoretical limit to specific impulse with xenon, krypton or argon as a result of momentum thrust based on Equation 5.2 is shown in Figure 82.

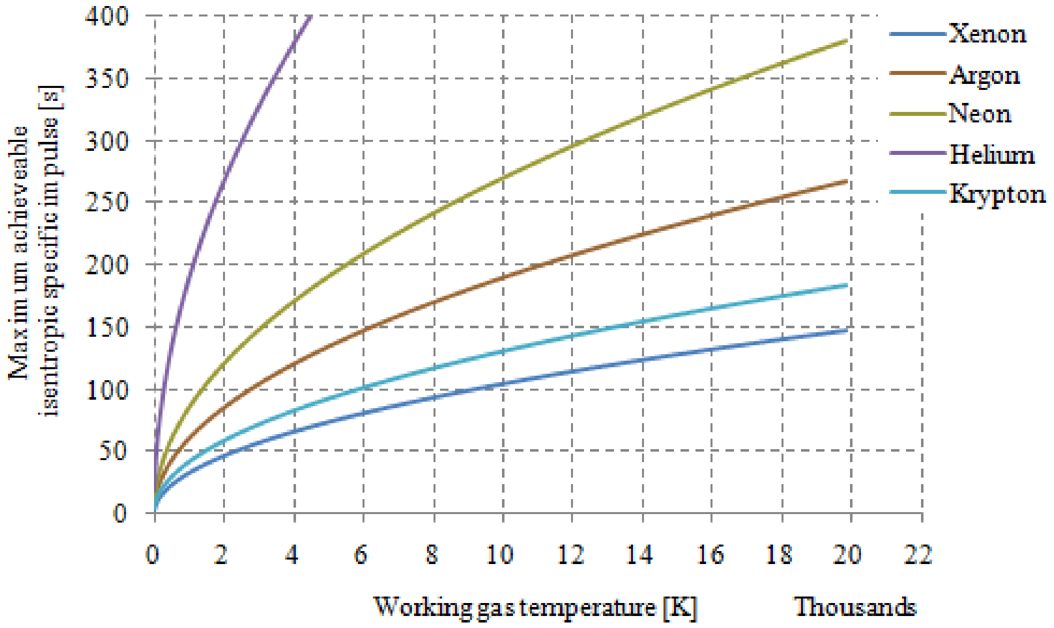

Figure 82 Limiting specific impulse based on momentum thrust for thermalized propellants

Table 8 shows the measured values of thrust for xenon and argon in comparison to the theoretically predicted components of momentum *and* pressure thrust based on Equation 5.8 for the T5 cathode. The accommodation coefficient (the measured thrust value/theoretical thrust value) with respect to mass flowrate is shown graphically in Figure 83. In this case it must be stressed that the accommodation coefficient represents a comparison to the theoretical value rather than a comparison to direct measurements.

Gas	Flowrate [mg/s]	Thrust measurement [mN]	Theoretical momentum thrust [mN]	Theoretical pressure thrust [mN]	Theoretical total thrust [mN]	Accommodation coefficient [Measured/ theoretical thrust]
Cold Xenon (298K)	0.717	0.216	0.155	0.045	0.200	1.079
	1.263	0.350	0.274	0.079	0.353	0.990
	1.585	0.427	0.344	0.099	0.443	0.963
Cold Argon (298K)	0.200	0.141	0.079	0.042	0.120	1.170
	0.600	0.391	0.236	0.125	0.361	1.082
	1.000	0.577	0.394	0.208	0.602	0.958
Hot Xenon (1500K)	0.936	0.146	0.456	0.059	0.515	0.284
	0.533	0.092	0.260	0.033	0.293	0.313
	0.261	0.048	0.127	0.016	0.144	0.332
Hot Argon (1500K)	0.250	0.194	0.220	0.052	0.272	0.712
	0.500	0.365	0.441	0.104	0.545	0.668
	1.000	0.631	0.883	0.208	1.091	0.577

Table 8 Measured values of thrust based compared to the theoretically calculated values of thrust

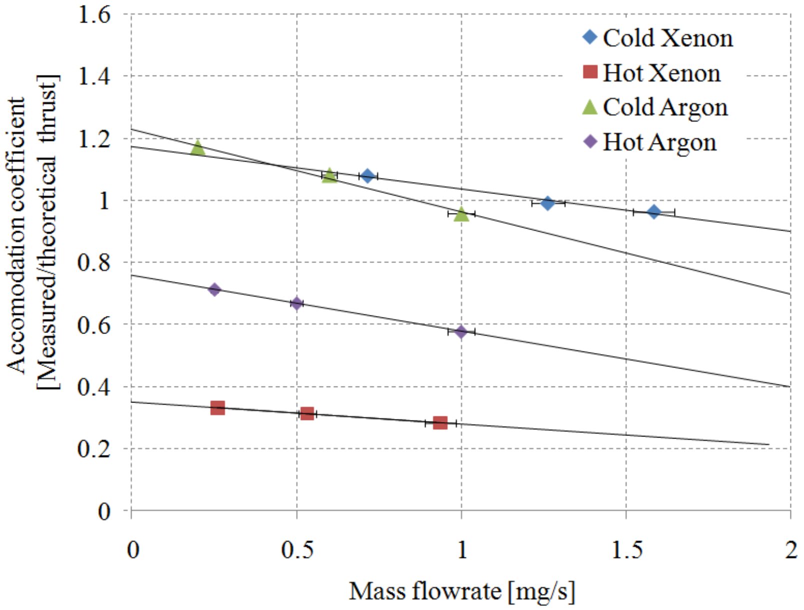

Figure 83 Accommodation coefficients with respect to mass flowrate for hot and cold xenon and argon

Comparing the theoretically predicted thrust to the actual measured thrust gives some insight into the effects of elastic or non-elastic collisions with the target and also divergence of the plume. If all particles collide inelastically with the target the accommodation factor would be 1, however in reality the accommodation factor must be greater than 1 due to particles which undergo elastic collisions and recoil from the target. The loss of ISP at higher flowrates and thus decrease in the accommodation factor <1 may suggest that the plume expands at greater divergence angles with higher flowrates. This effect was confirmed in later undocumented experiments when the target was moved much further away from the thruster resulting in lower thrust measurements. Since argon has lower molecular mass, the same mass flowrate has a higher neutral density than argon. Pressure thrust is given by:

$$A_{\mathrm{or}}\left(n_e k T_e + n_i k T_i + n_n k T_n\right) \tag{5.10}$$

The T5 cathode, when operating on argon operates at higher internal pressures and receives a greater proportion of its thrust from the pressure component (35% for argon, 22% for xenon cold gas). Since the gas velocity through the orifice must be constant at increasing flowrate due to the choked flow condition, higher flowrate results in higher orifice exit pressure which in turn produces a greater divergence angle at the orifice. This may be a reason why the accommodation coefficient shows a steeper gradient for argon than xenon, is consistently lower for argon than xenon and why divergence is greater with increasing mass flowrate.

The hot gas accommodation coefficient for xenon and argon is consistently less than 1 since the residence time of the propellant within the cathode body is not long enough for the gas to reach thermal equilibrium, thus the usual assumption that the propellant temperature is equal to the cathode wall temperature (~1500K) may be invalid. The greater increase in ISP with heated argon over heated xenon is due to the higher internal pressure for the same mass flowrate with argon which increases thermal conduction from the cathode walls.

The cold gas thrust measurements are very useful since we can say with good certainty that the gas temperature is ~ 298K thus we can make good approximations of the theoretical thrust. Although the measured ISP does decline at higher flowrates, which is likely due to increased divergence, tracing the accommodation coefficient back to the intercept should give a value with negligible divergence losses since as mass flow tends toward zero so does the exit pressure, yet the flow velocity is still equal to the choked flow velocity. In this case we can state that the momentum thrust is over estimated by 22.9% for argon and 17.4% for xenon by the pendulum target measurement system, or 20.1% as an average. This is a critical aspect of the analysis since as stated in Section 4.3.5, diffuse and specular particle reflections from the target could lead to overestimates of thrust by up to 66% and 100% respectively. We can now say with some certainty that the overestimate, at least without divergence losses is approximately 20% however we cannot in this case account for increasing divergence losses at higher mass flowrates and exit pressures.

5.2.3 ELECTRON PRESSURE THRUST

As our measurements have shown equivalent particle velocities found in the testing of the T5 and particularly the T6 cathode far exceed the maximum acoustic velocity of the propellant based on typical heavy particle temperatures in cathodes and thus rules out any conventional electrothermal type thrust mechanisms, yet the T5 cathode does not operate at sufficient discharge current for any significant electromagnetic effects based on the Maecker formula. We can however consider the electron pressure as a contributing component to the orifice static pressure at the orifice exit as described previously. Indeed the electron pressure along with magnetic field curvature is responsible for the relatively large divergence angle in hall thrusters.[174] [175] Remembering that the total gas dynamic thrust is given by:

$$F = \dot{m}\sqrt{\gamma R T_n} + A_{or}\left(n_e k T_e + n_i k T_i\right)$$

(5.11)

Calculation of the plasma density at the respective flowrate requires a significant modeling effort however for a quazi-neutral plasma such as in the orifice with a very small Debye length, the electron density can be approximated to that of the ion density. At very low flowrates where we know the plasma is fully ionized in the orifice the plasma density is therefore equal to the equivalent net flux of neutrals at the respective mass flowrate such that:

$$n_e = n_i = \frac{\dot{m}}{M A_o \sqrt{\gamma R_{sp} T_n}}$$

(5.12)

In this case however we do not know the ion/neutral temperature. Assuming momentum thrust is contributed by the neutral flux at the thermal velocity, the required electron temperature at the respective plasma density close to the orifice exit to give the equivalent values of thrust *equal to the measured values* (including the correction of 0.83 accommodation coefficient), for a range of ion temperatures, for the T5 3.2Amp and 1.6Amp conditions is shown in Figures 84 and 85.

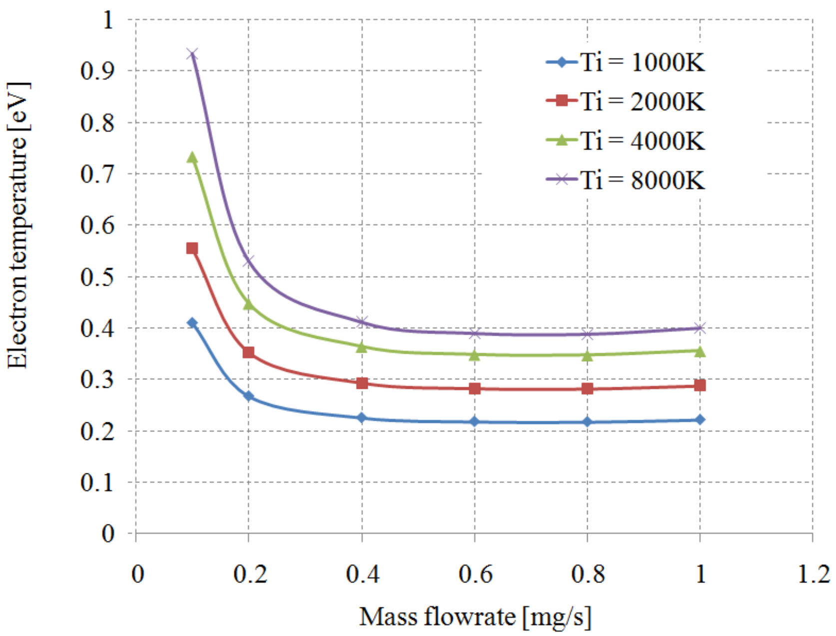

Figure 84 Required electron temperature to match measured thrust values for the T5 cathode operating at 3.2Amps on argon

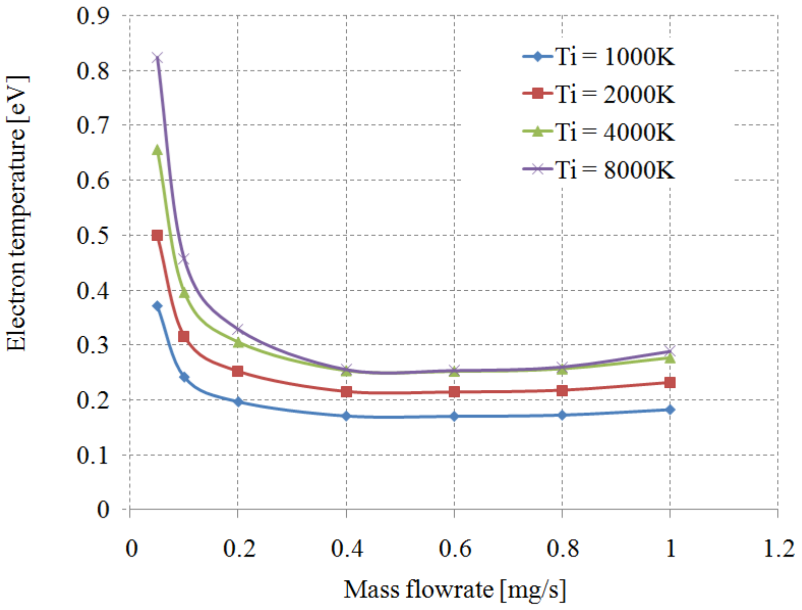

Figure 85 Required electron temperature to match measured thrust values for the T5 cathode operating at 1.6 Amps on argon

As Figures 84 and 85 indicate the required electron temperatures certainly do not exceed reasonable values in all heavy particle temperature cases. In fact the required electron temperature is much lower than the 1-2eV typically found in the orifice of hollow cathodes. This suggests that the electron pressure thrust mechanism would still be able to reasonably account for thrust levels even if ionization fractions were ~20-40%. The evidence for the electron pressure thrust component is strengthened further when considering at low flow rates when the cathode begins to be starved of charge carriers and enters into plume mode electron temperature is known to increase dramatically as suggested by the theoretical comparisons.

A similar analysis is conducted in Figures 86 and 87 for the T6LA cathode operating at 25Amps and 30Amps respectively on argon. The comparison shows that for various heavy particle temperatures it is not unreasonable to suggest that the high electron pressures (~0.6-1.6eV) at the orifice exit are responsible for the high specific impulse found in the 25Amp case. The 30Amp argon case however required much higher electron temperatures ~ 2-6eV. Results for the 30 Amp T6 case with xenon also requires very high electron temperatures (~3-7eV) to account for thrust levels at low flowrates as shown in Figure 88.

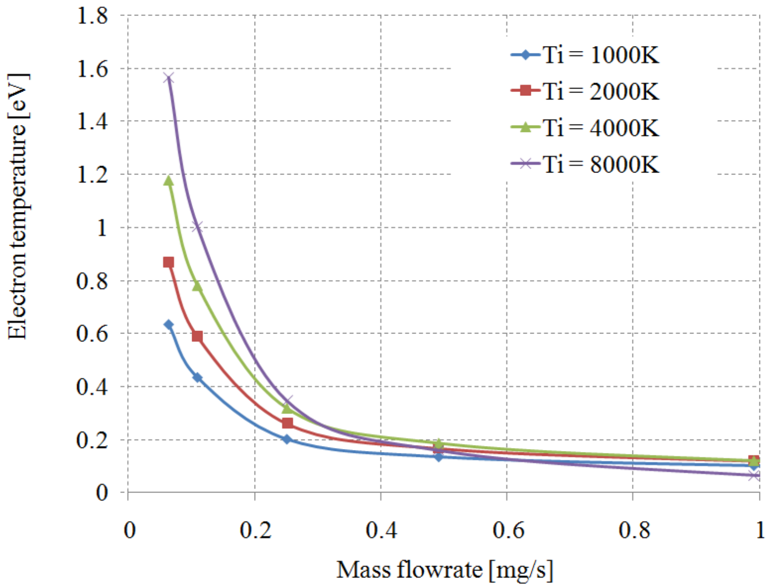

Figure 86 Required electron temperature to match measured thrust values for the T6 cathode operating at 25 Amps on argon

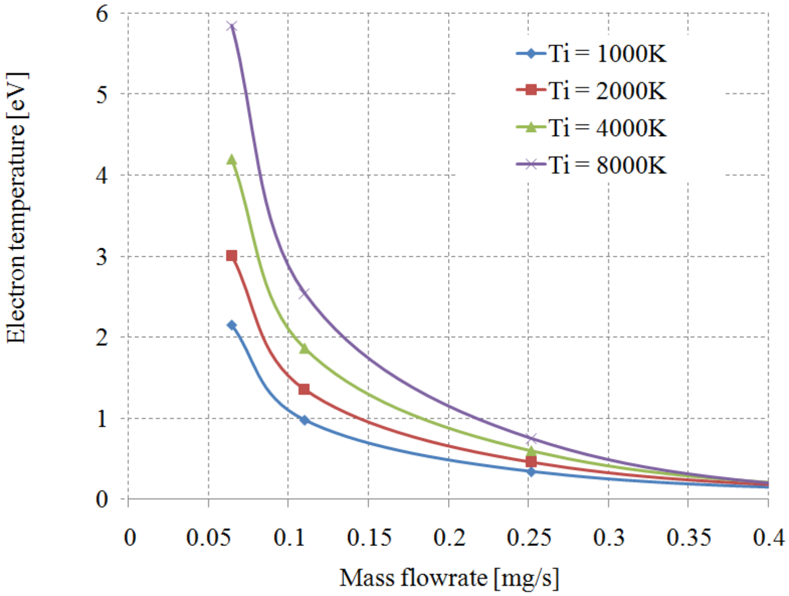

Figure 87 Required electron temperature to match measured thrust values for the T6 cathode operating at 30 Amps on argon

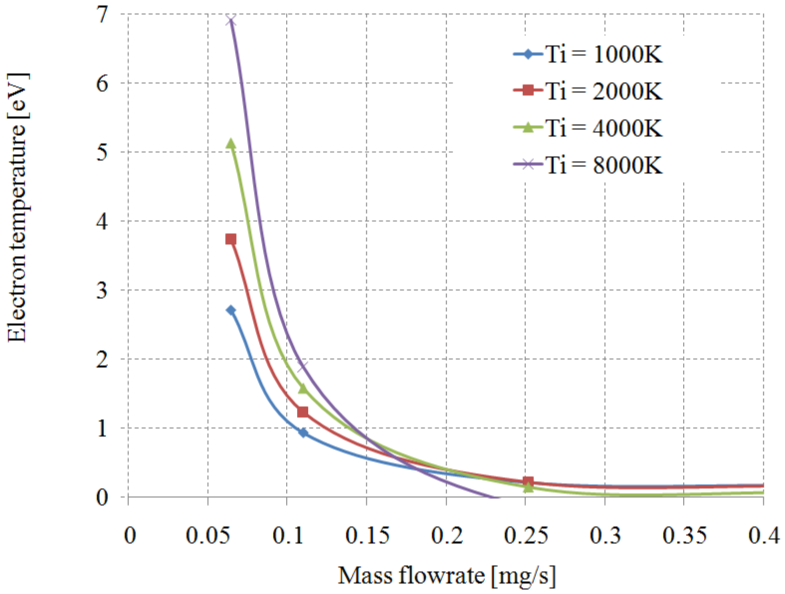

Figure 88 Required electron temperature to match measured thrust values for the T6 cathode operating at 30 Amps on xenon

Mikellides has proposed a mechanism of anomalous heating to produce electron temperatures of > 5eV in the near plume region at high currents and low flowrates which have been experimentally measured by Goebel as shown in Figure 89.

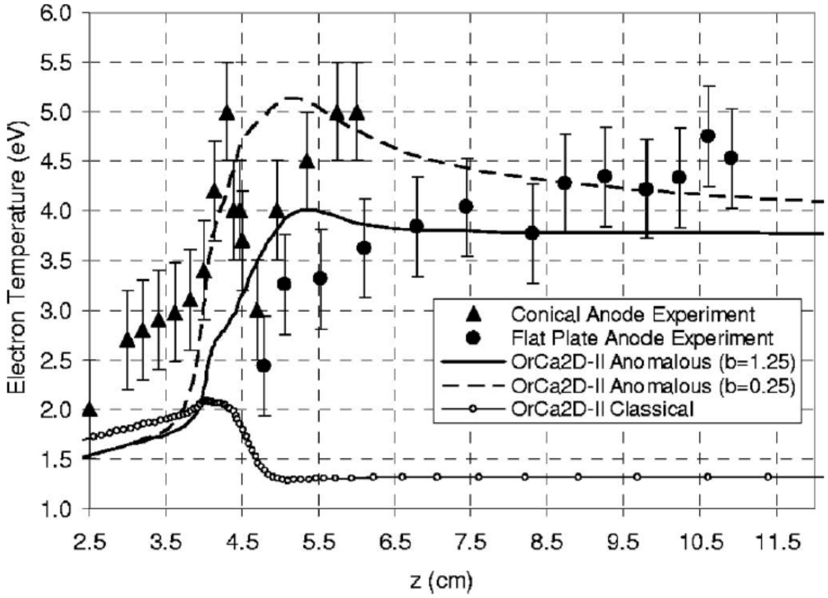

Figure 89 Downstream electron temperature as a function of axial location for the 1.5cm NEXIS cathode[155]

The authors also suggested a double layer mechanism will form if the electron drift speed exceeds the electron thermal speed occurring if the ionization rate in the plume along the current path drops to an insufficient level to support the discharge current. In this case, the double layer accelerates the electrons to higher energies, which increases the ionization rate. Given that we are operating the T6 cathode on the limits of mass flowrate at high discharge currents, well outside of the operating envelope of conventional cathodes, the possibility of attaining electron temperatures of this magnitude cannot be discounted. This evidence is possibly strengthened when considering that specific impulse correlates discharge voltage as shown in Figure 90. The degree of increase in discharge voltage is of course linked to the extent of transition into plume mode with the creation of much higher temperature electrons in the plasma.

One critical piece of information to support this mechanism comes when comparing ISP's of the T6 cathode operated by Gessini and the T6LA cathode. For the same flowrate and discharge current the ISP achieved in the T6LA cathode design is approximately half that of Gessini's T6, although higher ultimate ISP's are achieved by operating at lower flowrates and much higher specific powers. It should be noted that this does not imply higher thrust efficiency since discharge voltage in the T6LA is much lower. This may also suggests that the thrust mechanism is related to the ultimate discharge voltage and/or the electron temperature. Higher voltage operation implies the cathode is operating closer to or further into plume mode. In this case we can expect the electrons to be hotter for the same discharge current and flowrate, the electron pressure thrust component greater, thus a reason why Gessini's cathode exhibits twice the effective exit velocity for the same flowrate and discharge current.

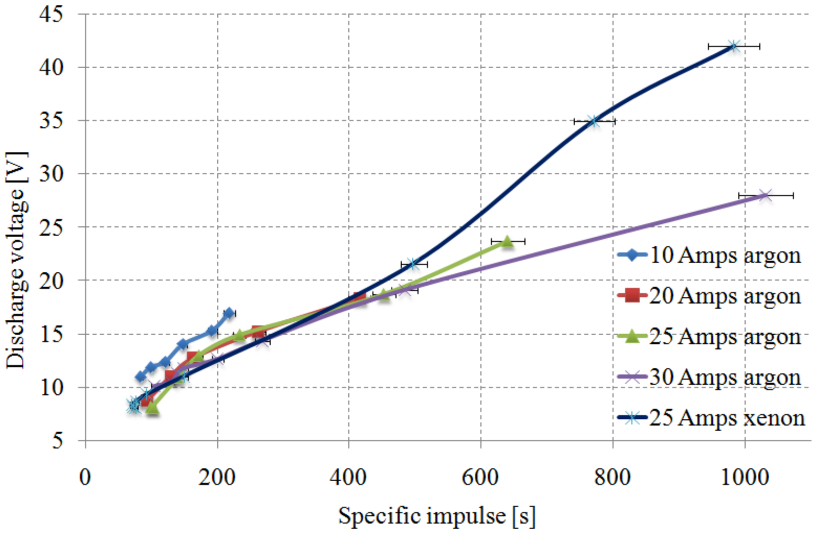

Figure 90 Specific impulse with discharge voltage for the T6 cathode operating on xenon and argon

Limited transient thrust measurements were also made which support the presence of a significant orifice backpressure component. In this measurement the T5 thruster was operated at steady state at 3.2Amps with constant mass flowrate and the discharge was extinguished by switching off the power supply as shown in Figure 91. As the discharge is extinguished a significant and immediate increase in sensor displacement (measured thrust) is observed, generating ~50% additional thrust above the steady state level. The thrust then declines to a level consistent with warm/cold gas thrust. As the mass flowrate of propellant is then switched off the thrust level reduces to zero. The thrust balance in this case was heavily damped and the movement of the balance is not due to its own inertia but a change in the measured thrust.

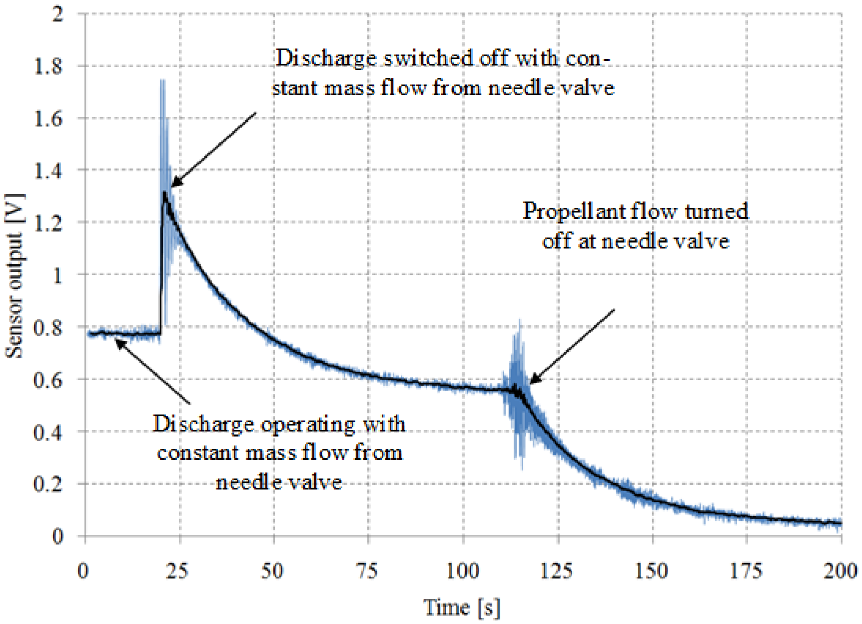

Figure 91 Thrust measurement as the cathode discharge is switched off at t=23s with constant upstream mass flowrate followed by the mass flow being turned off at t=115s. The cathode is operating at 3.2A with 2mg/s xenon

This process may indicate that the thrust increase immediately after the thrust increase at switch-off is likely due to expulsion of an upstream pressure buildup within the cathode and feed lines (which are of significant volume in comparison to the cathode internal volume). This internal 'reservoir' is immediately released immediately as the cathode is extinguished such that the thrust level temporarily increases *above that of the steady state level*. This indicates that the back pressure (static pressure at the orifice entrance) is much higher during operation than without a discharge which restricts the flow and causes the upstream pressure rise (since the gas velocity is choked at the orifice) until mass flow is conserved. It is important to note a common misconception that a choked flow is limited in flowrate. The flow is limited in *velocity* but flowrate can be still increased by increasing the upstream pressure.

The upstream pressure transducer used for flow calibration also allowed for approximate measurement of backpressure in the system at various flow rates and current conditions. While these measurements, shown in Figure 92, cannot give the absolute pressure since the exact head losses in the system are unknown, it can give some idea of the relative changes in operating pressure.

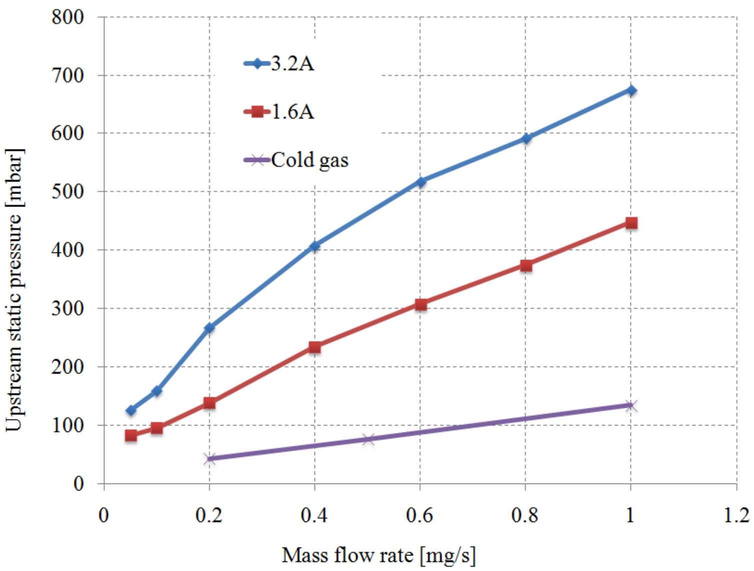

Figure 92 Upstream static pressure measurements for various mass flowrates with the T5FO cathode operating on argon

Approximate static pressures recorded by QinetiQ in the T5 discharge cathode while operating are shown in Table 9. The T5 cathode used in these experiments is representative of the T5 neutralizer; in this case extrapolating the cold gas flow back to 0.041mgs^{-1} gives an operating pressure of 19.47mbar and showing approximately 50% overestimate in the upstream static pressure from that recorded by QinetiQ. During operation our cathode displayed between 82mbar and 125mbar at 3.2A and 1.6A respectively at a mass flow rate of 0.05mg/s in approximate agreement with measurements by QinetiQ.

Component	Mass flow rate (mg/s)	Pressure
T5 GIT	0.07–0.53 ± 0.007	13 mbar (gas flow only) 20 mbar (gas flow and discharge)
T5 discharge cathode	0.1 ± 0.007	10 mbar (gas flow only) 100 mbar (gas flow and discharge)
T5 neutralizer	0.041 ± 0.006	10 mbar (gas flow only) 100 mbar (gas flow and discharge)

Table 9 Typical operating pressures of the T5 GIT components[46]

Previously, the electron temperatures necessary to give the measured thrust levels based on various ion temperatures were calculated. This was done by calculating the required electron pressure component in addition to the ion pressure and momentum thrust components at the orifice exit in order to equal the experimental thrust values. The orifice static pressure components of these calculations for the T5 3.2A and 1.6A condition is shown in Figure 93 and Figure 94 along with the experimentally measured upstream pressure at the respective current.

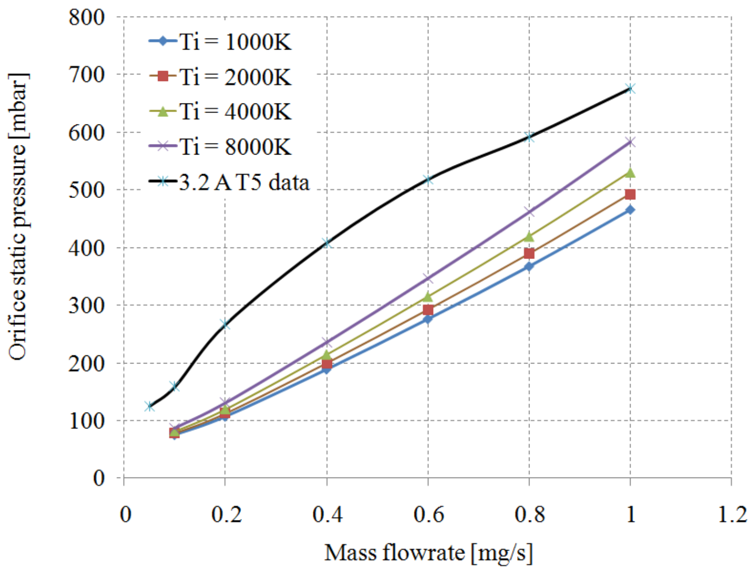

Figure 93 Required orifice static pressure at various ion temperatures required to meet thrust levels of the T5FO cathode operating at 3.2A with argon

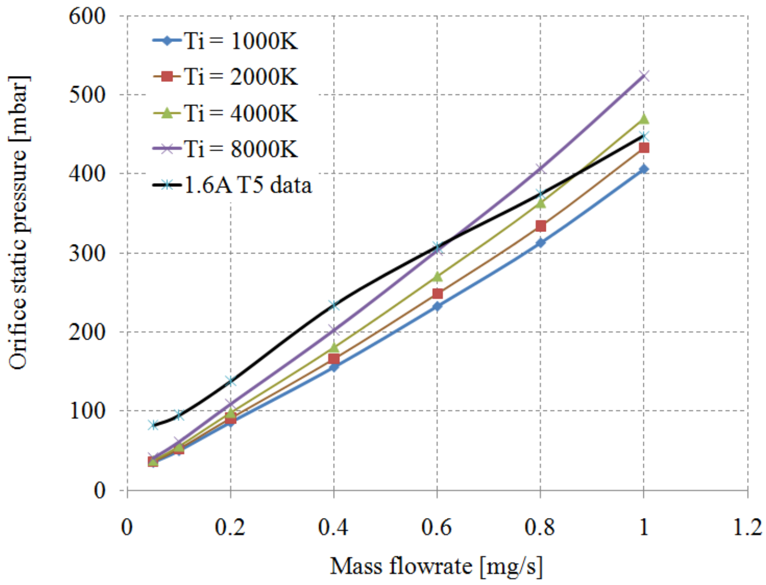

Figure 94 Required orifice static pressure at various ion temperatures required to meet thrust levels of the T5FO cathode operating at 1.6A with argon

Similarly to our cold gas extrapolation, comparison with the measured upstream pressure shows a discrepancy of approximately 50% at lower flowrates in both the 3.2A and 1.6A condition. While this data may not prove that the thrust mechanism is due to an electron pressure component it does show a very large back pressure increase over the cold gas backpressure during a discharge.

The exact analysis of the upstream pressure based on the orifice pressure is extremely complicated for many reasons including:

1. Heat addition in the choked flow region of a plasma discharge constitutes a very unconventional form of Rayleigh flow
2. We have not accounted for contra flowing ions at the double layer at the orifice entrance in producing an additional backpressure component
3. We have not accounted for a non uniform velocity profile in the orifice or the effect of varying temperature on viscosity

Hence assessment of the possible pressures at the orifice exit may be the most reliable way, in the short term, of acknowledging the influence of plasma pressure on the flow since in this region we can make more reliable assumptions of plasma parameters based on the quantity of theoretically validated models, experimental measurements and observations.

5.2.4 ELECTROMAGNETIC ACCELERATION

We have already suggested that an electron pressure component alone, even in a full ionized flow of a T6 cathode, cannot fully account for the thrust measurements found during testing. If a reasonably strong self-induced magnetic field exists within the orifice of the T6 cathode at high current conditions it may be sensible to suggest the possibility of magneto-hydro-dynamic acceleration of the plasma. This effect would be characterized by an almost instantaneous acceleration at which the discharge current and magnetic field interact. The Maecker formula has been used to approximate the thrust scaling of self-field magneto-plasma-dynamic thrusters (MPDTs) with the total current. The formula has been shown to be too simplistic to account for the trends in measured thrust data at low current due to the scaling of gasdynamic pressure distributions induced by the pinching components of the volumetric electromagnetic forces[176] however in this case it can be used as an approximation of the *significance of the Lorenz force* alone.

A stream wise acceleration could be provided by the crossing of the radial arc current *J* with the self generated azimuthal magnetic field through the cathode orifice, an essentially scalar crossed-field interaction, with an anode and cathode radius *ra* and *rc* given by:

$$F_z = \frac{\mu J^2}{4\pi}\left(\ln\frac{r_a}{r_c} + \frac{3}{4}\right)$$

(5.13)

One important factor considered in MPDT's type operation is the exceeding of the critical ionization current. Assuming MPDT theory can serve as a first approximation, it can be shown that if flow rates are low enough the ratios of discharge current I to the critical ionization current, I_{ci} also becomes significant. A key scaling parameter of interest in establishing MPDT like operation is, ξ, the ratio of the discharge current to critical current (also known as the full ionization current).[177] [178] [179] Parameters such as the thrust and voltage have been seen to strongly correlate with ξ in MPDTs. The plasma is considered partially ionized at $I<I_{ci}$ and fully ionized for $I>I_{ci}$. At $I=I_{ci}$ ($\xi=1$), the electromagnetic thrust is equal to the product of the mass flow rate and the propellant Alfven critical ionization velocity. The parameter ξ is given by Equation 5.14, and I_{ci} is given by Equation 5.15 where:

$$\xi = \left(\frac{I^2}{\dot{m}}\,\frac{\mu_0 \ln(r_a/r_c)}{4\pi(2\varepsilon_i/M)}\right)^{1/2} = \frac{I}{I_{ci}}$$

(5.14)

$$I_{ci} = \left(\frac{(\dot{m}\,2\varepsilon_i/M)^{1/2}}{\frac{\mu_0}{4\pi}\ln(r_a/r_c)}\right)^{1/2}$$

(5.15)

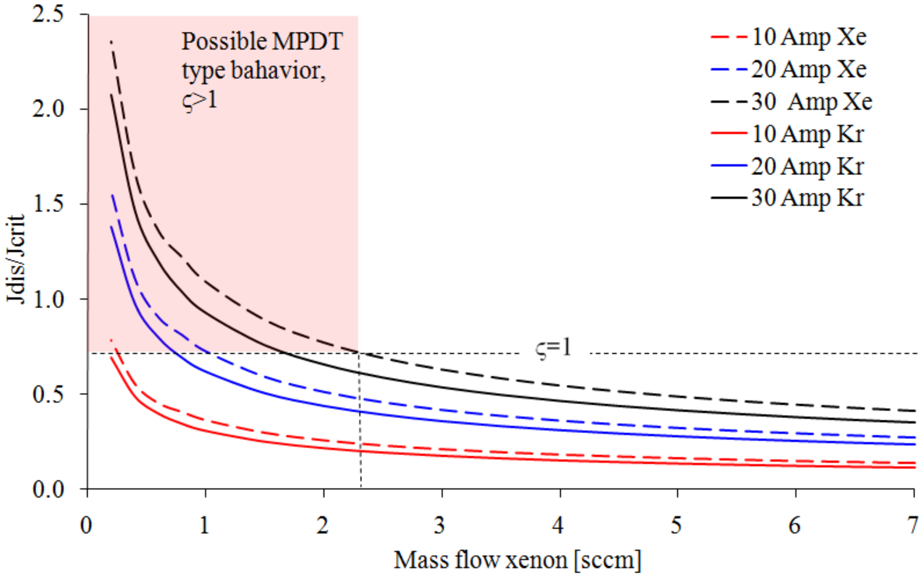

Figure 95 Ratio of critical ionization current to discharge current with xenon and krypton for a cathode anode diameter of 1mm and 25mm respectivley

In Figure 95 it can be seen that for operation with xenon and krypton operation at low flow rates < 1sccm at currents above 30Amps ξ = 1. Below ξ = 1 the flow is only partially ionized while at ξ > 1 the flow can be expected to be highly ionized and may exhibit behavior similar to MPDT's.

This Maecker approximation is sensitive to the particular current density distribution over the disuse arc. In this case the density distribution varies as 1/r. If it were considered uniform over the orifice exit then the contribution would be less. It is also worth noting that the transition may occur at lower value of current than the calculated theoretical value for I_{ci} based on an increase in the effective r_a/r_c due to a decrease in the effective r_c in the cathode orifice via electromagnetic pinching forces acting on the orifice plasma. This effect would result in I_{ci} occurring at a lower value than predicted with the R_a/R_c obtained from the thrusters fixed geometry alone. The strength of the self magnetic field is given by:

$$B = \frac{\mu_0 j_D}{2\pi r} \tag{5.16}$$

In this case we can see that for the T6 cathode operated at 30 Amps the local strength of the magnetic field is indeed significant at 12mT or 120 Gauss, about the strength of a regular iron magnet. The magnetic force will balance the radial gradient kinetic pressure in the current column to give the arc radius. In reality the self-field reacts on the current which produces it with a force density:

$$F = j \times B = \frac{\mu_0 j^2 r}{2} \text{ where } r<r_{or}$$

(5.17)

This magnetic force balances the radial gradient in the gas kinetic pressure in the current column:

$$\frac{dp}{dr} = -\frac{\mu_0 j^2 r}{4}$$

(5.18)

$$p = \frac{\mu_0 j^2}{4}\left(r_{or}^2 - r^2\right) = n_e kT_e + n_i kT_i + n_n kT_n$$

(5.19)

The arc radius can thus be estimated based on empirical measurement of gas pressure within the orifice for this cathode at these operating conditions. Assuming reasonable values of particle densities and temperatures we can see that the magnetic pressure component is far too low to cause any constriction of the plasma thus the effective arc radius can be assumed to be the cathode orifice radius.

As an example, the limiting thrust producible by the blowing force on the plasma with uniform current density within orifices of for the T5 and T6 cathodes with orifice and anode diameters of 1mm and 20mm, and 0.25mm and 3mm respectively is shown in Figure 96. We can see that although current levels are far from the level of MPD thrusters the blowing force in the T6 cathode between 10-30 Amps is still significant.

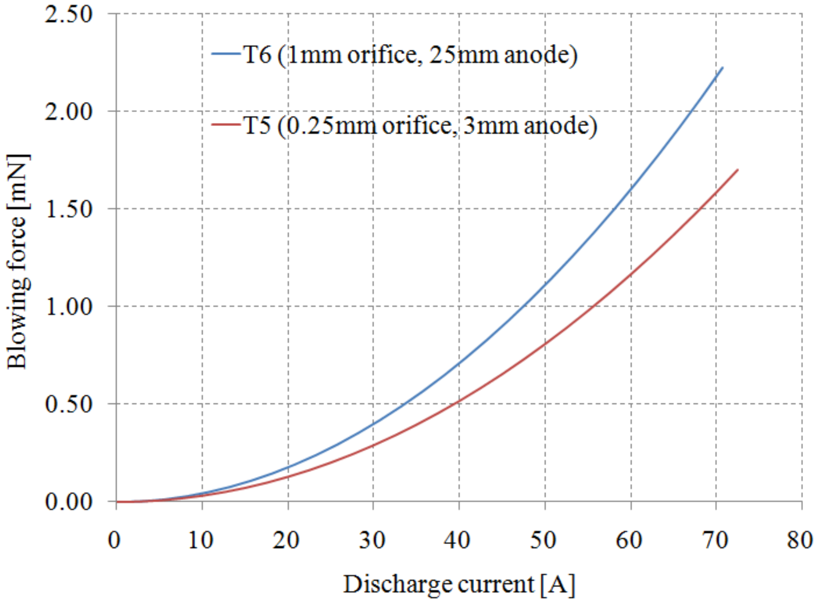

Figure 96 Maximum electromagnetic thrust approximations producible by a diffuse arc hollow cathode discharge with T5 and T6 cathode geoemtries and a 20mm effective anode diamtter

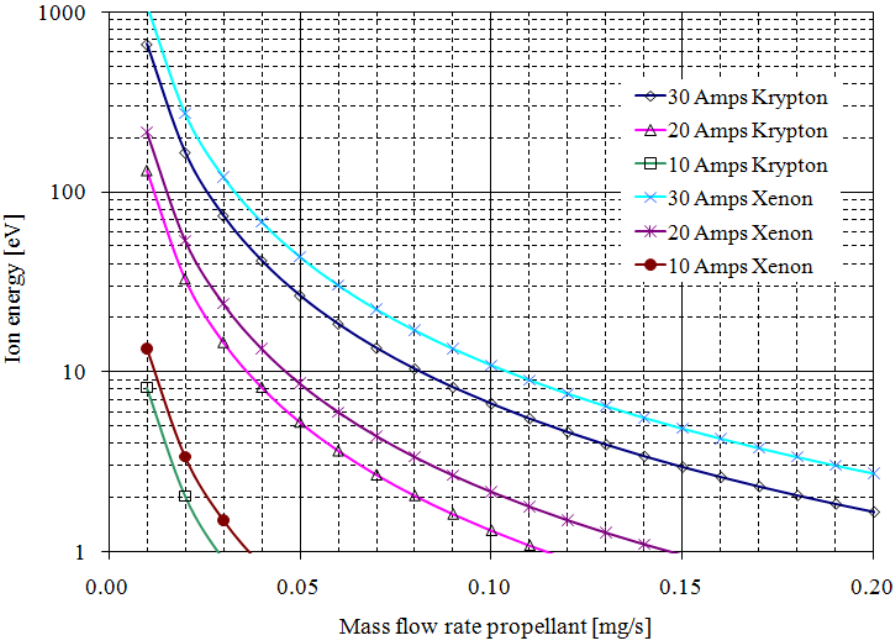

Figure 97 Theoretical ion energies from the Maecker formula as a result of the cross field interaction from a self-generated azimuthal magnetic field for krypton and xenon

Based on the Maecker formula and assuming a bulk accelerating force acts on the total mass flowrate, Figure 97 shows the theoretical particle energies achievable, again suggesting the resulting accelerating force per particle is significant at very low mass flowrates. Alternatively the effective ISP for the T6 cathode at respective current levels and mass flowrates is shown in Figure 98. The limiting factor in this case is the ability to sustain a discharge to sufficiently low flowrate for the accelerating force per particle to become significant.

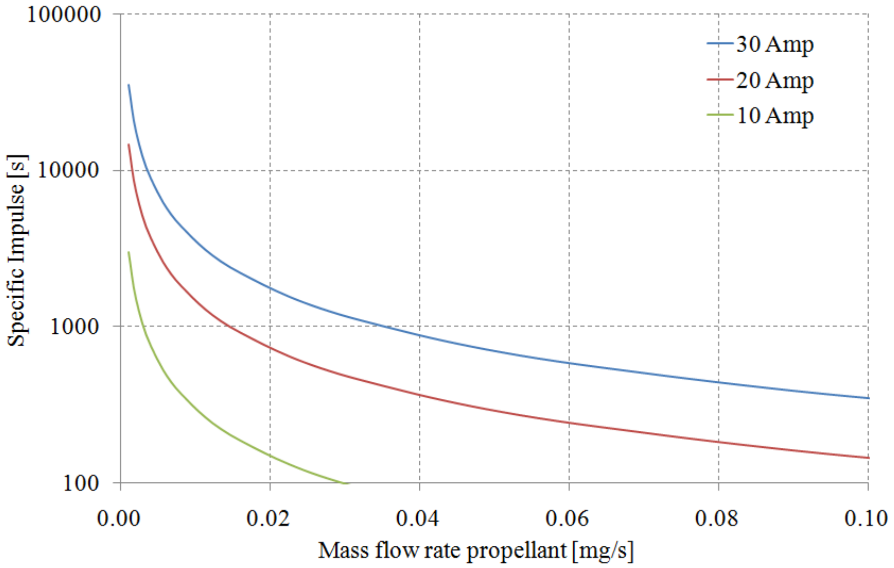

Figure 98 Theoretical ISP developed by the T6 cathode as a result of the blowing component of thrust for an orifice diameter of 1mm and an effective anode diameter of 20mm

Figure 99 shows the T6LA thrust measurement results with the theoretical thrust developed as a result of the theoretical blowing component. Given that the accommodation factor also has to be taken into account which will reduce the measured thrust by about 18%, the theoretically predicted blowing force matches relatively well with the remnant thrust remaining when extrapolating back to zero mass flowrate. This data supports the hypothesis that the very high ISP achievable with the T6 cathode at low flowrates is possibly a result of an MHD effect with an additional gas dynamic component.

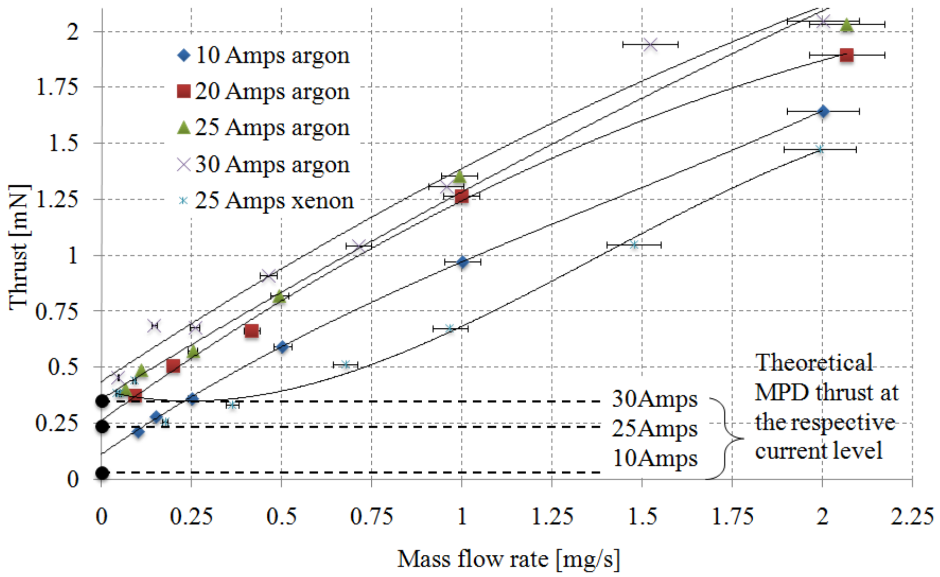

Figure 99 Thrust measurement results for the T6 LA cathode also showing the theoretical blowing force as a result of the MHD cross-field interaction with an identical 1mm T6 orifice geometry and 20mm anode

Figure 100 shows transient thrust balance data with the T6 cathode operating at 25Amps with 0.2mg/s argon where the discharge is powered on at t=21, off at t=48 and the mass flow is switched off at t=71.

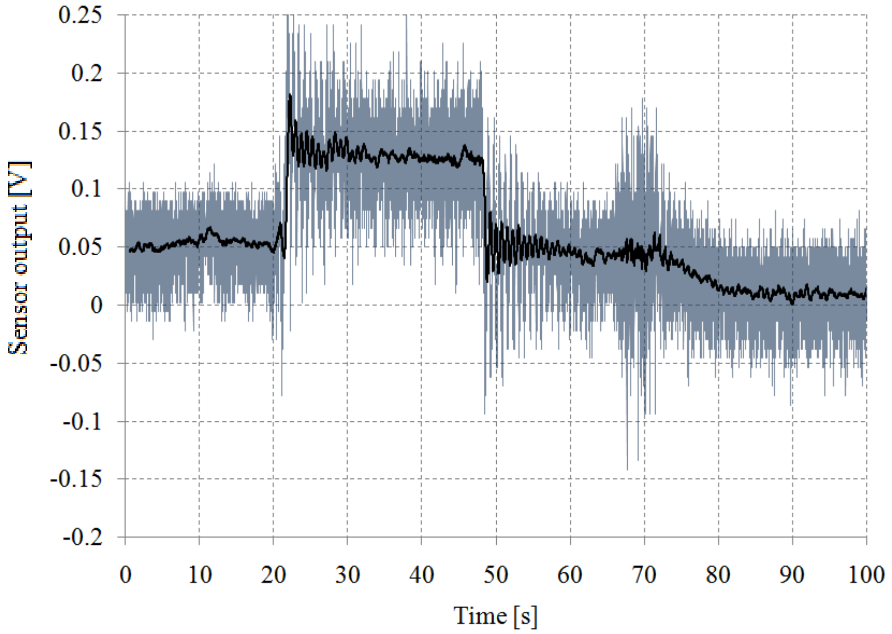

Figure 100 Transient thrust measurement as T6LA is switched on at t=21, off at t=48 and the mass flow is switched off at t=71. Cathode is operated at 25Amps with 0.2mg/s argon

The additional thrust level increase and decrease as the cathode switches on and off would seem to increase and decrease extremely quickly as the discharge is switched on or extinguished. As the mass flow is switched off however a characteristic transient typical of feed lines depressurization is found. If the thrust component which appears during the discharge was indeed electrothermal one would expect it would take 10-20 seconds to reach steady state as the internal body and feed lines pressurize as seen in the mass flow switch-off transient, however it does not. A closer look at the points of interest in Figure 101 confirms that the rate of change in thrust is consistent with the pendulum thrust balance natural frequency and *shows overshoot*, thus from a thrust balance viewpoint the thrust application is instantaneous. Our resolution of the rapidness of this change is however limited by the inertia of the balance. This data strengthens the hypothesis that the T6LA operates in an MPDT type mode at low flowrates and high currents and the blowing force originating from the cross field interaction may play a role in the ion acceleration process with additional thrust contributed by gas dynamic processes. The T5 cathode however operates at a maximum current of 3.2A and therefore is expected to operate in an almost purely electrothermal mode.

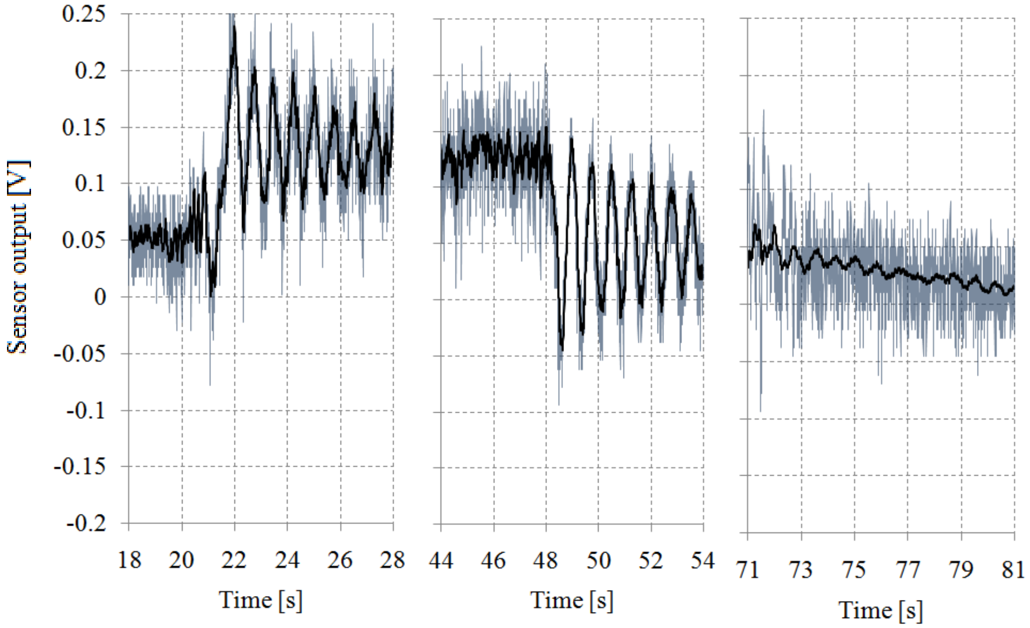

Figure 101 Detailed transient thrust measurement as T6LA is switched on at t=21, off at t=48 and the mass flow is switched off at t=71. Cathode is operated at 25Amps with 0.2mg/s argon

5.2.5 ELECTROSTATIC ACCELERATION

Rudwan[187] has described extensively the formation of the double layer and resulting potential profile within hollow cathodes in plume mode. The potential peak corresponds to a region of intense ionization as electrons focused into this area and accelerated by the double layer give rise to a highly localized ion production region. This mechanism causes the local plasma potential to rise with respect to the surrounding plasma to values which can exceed the applied voltage. Williams and Wilbur[117] clearly mapped this potential profile in when transitioning into plume mode corresponding to a transition from a monotonic to potential hill profile as shown in Figure 102, and the models of Kameyama & Wilbur[180] have demonstrated the creation of potential peaks from 30–50V . Boyd & Crofton[115] have developed detailed numerical fluidic models using particle in a particle based kinetic approach which show good agreement with separate measurements of plasma potential. High peak ion energies were generated in the simulations by the formation of a potential hill downstream of the keeper that is mainly formed by a plasma density gradient. The electron-accelerating upstream side of the double layer provides the energy input to sustain the potential hill. Ions produced at the crest of the hill are accelerated by the potential in all directions consistent with Williams and Wilburs[117] observations of isotropic expansion from a highly localized region in front of the cathode.

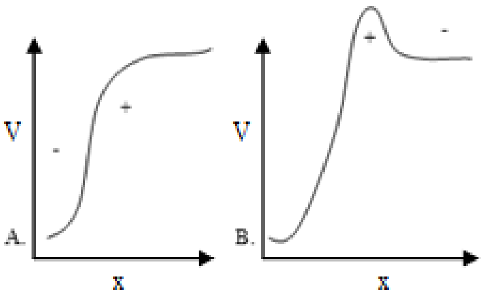

Figure 102 Two of many possible double layer axial potential profiles corresponding to identical potential differences applied to the system boundaries. The structures are due to the presence of at least two parallel charge sheets[189]

If a sufficient quantity of ions are formed on and accelerated off the potential hill produced by the double layer, it is reasonable to suggest that this mechanism may contribute to thrust generation. If an electric field exists across a plasma potential drop:

$$E = -{}^{dV}\!/_{dx} \tag{5.20}$$

as ions move down the potential profile the energy gained is given by:

$$E = q\left(V_{peak} - V_{ambient}\right) \tag{5.21}$$

With the corresponding velocity gained by the ion given by:

$$V_e = \left[\frac{2q\left(V_{peak} - V_{ambient}\right)}{M}\right]^{0.5} \tag{5.22}$$

The ion velocity at any point follows from conservation of energy. It is worth noting that a potential hill of only 20V would therefore be responsible for the acceleration of xenon, argon and krypton ions created at the crest of the potential hill to 5,285ms^{-1}, 6,815 ms^{-1} and 9,818 ms^{-1} respectively. If the bulk of the ions were created at the crest of the potential hill and the flow was highly ionized ions emitted away from the cathode would contribute to an effective thrust. Of course if the ions were accelerated isotropically from the peak the net thrust would be zero, however ions accelerated upstream which contact the cathode surface or which are trapped by the enclosed anode design, would transfer their momentum back to the thruster assembly on recombination and in time may be given the chance to be ionized on the downstream side of the potential peak.

The conical anode configuration developed by the author is significantly different from any configuration previously seen in the literature and its influence on the formation of the double layer in plume mode has not fully been established. Due to the proximity and geometry of the anode, the structure of the ion creation and acceleration mechanism may be substantially different from conventional configurations. As we have discussed, the formation of the double layer is no more than a few centimeters downstream of the cathode and therefore the influence of the anode occupying this region could have a significant effect on the potential structure. The formation of the double layer and potential profile has been shown to be extremely sensitive to the electrode configuration.[187] This is one reason why conducting cathode tests in a diode configuration is extremely non-representative if the normal configuration in the cathodes application is triode or of significantly different anode geometry. For example using a keeper electrode significantly changes the neutral density in the near cathode region while using non-representative anode geometries significantly influences the electron flux. In order to determine the influence of the double layer in the conical anode on the ion energies emitted from a further experiment was conducted at the NASA Jet Propulsion Laboratory. These results are described in Chapter 6.

CHAPTER 6

EXPERIMENTAL RESULTS II: ELECTROSTATIC ION ENERGY MEASUREMENTS

Whist enabling operation at very low flow rates and high discharge currents thrust levels corresponding to equivalent mean propellant velocities of over 10kms^{-1} have been measured in our experiments with the T6LA cathode using both xenon and argon. Whilst an MHD mechanism would seem feasible given the analysis in Chapter 5, the role or even existence of any potential hill acceleration mechanism in producing particles of this velocity, particularly for a conical anode, has not been established. This mechanism becomes even more likely since operation in a diode configuration has been shown to enhance the potential hill formation mechanism due to the uniformity of the various acceleration regions of the double layer.[187] In order to distinguish which acceleration processes are responsible for such high propellant velocity an investigation was made into the downstream ion energy distributions emitted from a hollow cathode with a conical anode in diode configuration.

6.1 HEMISPHERICAL ENERGY ANALYZER EXPERIMENT

These measurements were made at the NASA Jet Propulsion Laboratory and involved the development of an electrostatic energy analyzer (ESA) experiment and manufacture of an anode assembly to replicate the design of the T6 cathode assembly. International Traffic and Arms Regulations (ITAR) prevented the direct testing of the T6LA cathode, however tests were conducted on a XIPS hollow cathode of similar geometry to the T6 cathode with a conical anode built of the same geometry as that used in the T6 experiments. It should be noted that in this case one essential outcome of this investigation was the influence of the conical anode on the formation of the downstream potential structures since similar investigations have already been conducted on the typical discharge chamber and other types of diode configuration and also the possibility of thrust generation from the potential hill. Previous high energy ion characterization experiments were discussed in Chapter 1.

6.1.1 XIPS CATHODE

The XIPS cathode shown in Figure 103 has an outer diameter is 6.35mm with an orifice length and diameter of 2.25mm and 1.5mm respectively. The cathode contains a tungsten dispenser, 3.8mm internal diameter impregnated with a mixture of barium-oxide, calcium oxide and aluminates (BaO: CaO: Al_2O_3). A swaged coaxial heater is used and heater efficiency has been improved with radiation shielding in the form of tantalum foil wrapped around the downstream end. The cathode is welded to a flange which is mounted to a propellant supply fixture and thus directly grounded to the tank. The cathode was run through a 4-hour conditioning sequence prior to ignition by applying various current levels to the heater to ensure the cathode was fully outgassed and activated.

Figure 103 XIPS hollow cathode

The cathode was operated in an open-diode configuration as in T6 experiments with the full discharge current being drawn to the anode as in our T6 experiments. The anode shown in Figure 104 was designed to closely replicate the anode in previous T6 hollow cathode thruster experiments shown in Figure 105. The anode is a conical 30° diverging nozzle constructed from poco-graphite with a 50mm and 4mm diameter orifice at the downstream and upstream end respectively, mounted in a graphite bracket 1mm in front of the cathode and axially aligned.

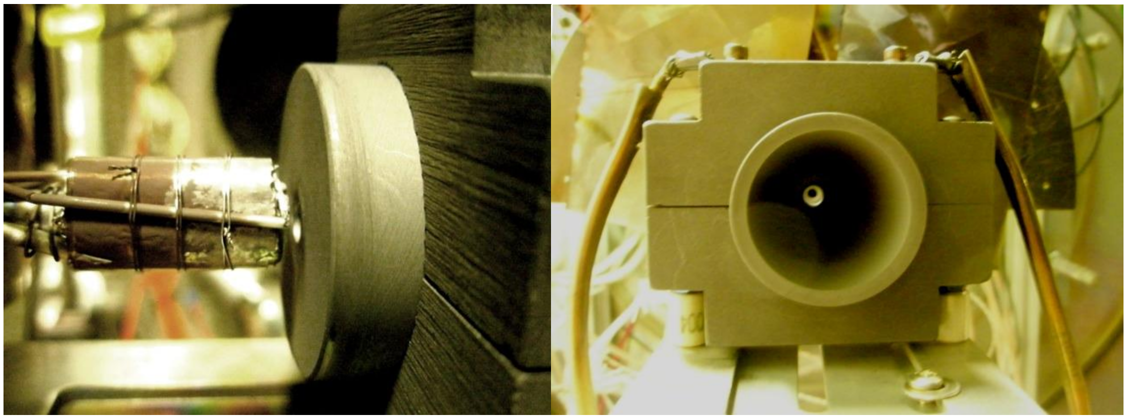

Figure 104 On axis view down conical anode showing cathode orifice at upstream end (left) view of radiation shielded cathode and tip thermocouples mounted 3mm downstream of anode orifice (right

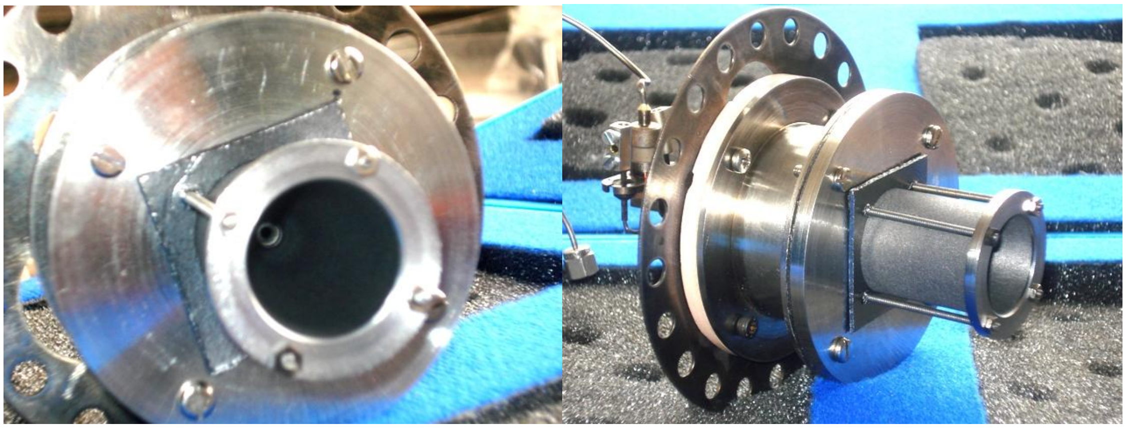

Figure 105 Upstream view of the anode exit of the T6 cathode showing the orifice (left) and view of the enclosed hollow cathode/anode assembly which the experiment was designed to replicate (right)

The most significant divergence in the two configurations is the enclosed design of the T6 experiment using an enclosed anode with grafoil gaskets. The enclosed design ensures the entire mass flowrate of propellant passes through the exit of the anode orifice. The XIPS anode was left open due to time constraints on manufacture of the experiment. In this case a proportion of the flow of ions/neutrals will be lost to the cathode-anode gap. Since the anode was mounted 1mm downstream of the cathode however with a 4mm orifice in comparison to the 1.5mm cathode orifice the loss of neutrals to gap should constitute only a small proportion of the expanding flow.

6.1.2 TEST FACILITY

The experiment was mounted in a 1m diameter by 2 m long vacuum facility and pumped by two 25cm diameter cryopumps. Chamber pressure was monitored with a Granville Phillips Stabil Ion Gauge which was calibrated with xenon gas. The base pressure during operation was typically 5×10^{-5} Torr (6.7×10^{-5} mbar) for operation at higher flow rates and 9×10^{-7} Torr (1.2×10^{-6} mbar) at lower flow rates with ultimate base pressure on the order of 1×10^{-7} Torr (1.33×10^{-5} mbar). Propulsion grade (99.997% pure) xenon and krypton are fed to the cathode with flow rate measured by a Unit Instruments 1661 flow meter, controlled with an MKS 250C controller and an MKS 248 valve. The meter was calibrated by flowing xenon into a known volume and measuring the rate of pressure rise with a precision pressure transducer, yielding flow rate measurements with an uncertainty of less than 2%. An Optomux data system with LabView control software was used for flow setpoint control and flow meter data logging. Heater and discharge power were provided by a Sorenson DLM 40-15 power supply and a Power Ten P62B-5060 power supply, respectively, with the common returns grounded to the vacuum tank. Currents and voltages were measured to within 1% by the data system using calibrated shunts and voltage dividers.

6.1.3 HEMISPHERICAL ENERGY ANALYZER

A custom built HEA (Hemispherical Energy Analyzer) was used to characterize the ion energies emitted from the cathode. There are several types of electrostatic energy selector geometries including parallel plates, cylindrical electrodes and hemispherical electrodes. The hemispherical selector was chosen because its spherical symmetry gives it superior focusing qualities. The ESA operates by establishing a radial, electrostatic field between two graphite coated aluminum surfaces, which form segments of spheres having a common center and different radii. Charged particles that pass through the entrance collimator are focused along different paths depending upon their kinetic energy, charge, and mass. The electrostatic fields within the unit were established by setting potential differences between the inner and outer surfaces and the collimator sets. Under this condition only those ions with a prescribed kinetic energy the transmission energy (TE) at the entrance collimator are able to pass through the unit with a specific curvature of trajectories (155 mm). Ions with greater and lesser energies will strike the outer and inner surfaces, respectively. The hemispheres create a radial electrostatic field given by:

$$\varepsilon(r) = \frac{(V_2 - V_1)R_1 R_2}{(R_1 - R_2)r^2}\hat{r} \tag{6.1}$$

If the kinetic energy with which the ion enters is such that the centripetal acceleration balances the radial electrostatic force, the ion is allowed to pass.

$$\frac{mv^2}{R_c} + q\varepsilon(R_c) = 0$$

(6.2)

Another useful relation that can be derived from the particle trajectory equation is the energy resolution where α is the acceptance angle.[181]

$$\frac{\Delta E}{E} = \frac{\omega}{2R_c} + \frac{1}{2}(\Delta\alpha)^2$$

(6.3)

Power supplies were integrated with Labview to control the potential on each hemisphere within 0.2Vof the specified voltage. Voltage dividers were used to monitor the voltage output from each power supply. To sense the ion-energy distribution, potentials on the inner, outer, and collimator surfaces are swept together with respect to facility ground potential, thereby changing the amount of acceleration or deceleration experienced by ions as they approach the entrance collimator from the cathode-plasma plume. The analyzer was able to translate in the z-plane, as shown in Figure 111, and laser levels were employed to ensure that the energy analyzer was mounted exactly on axis with the cathode. Voltages were independently applied to the inner and outer hemispheres by a Kebco BOP-1M and Sorensen DLM 150-4 respectively with common returns to vacuum chamber ground.

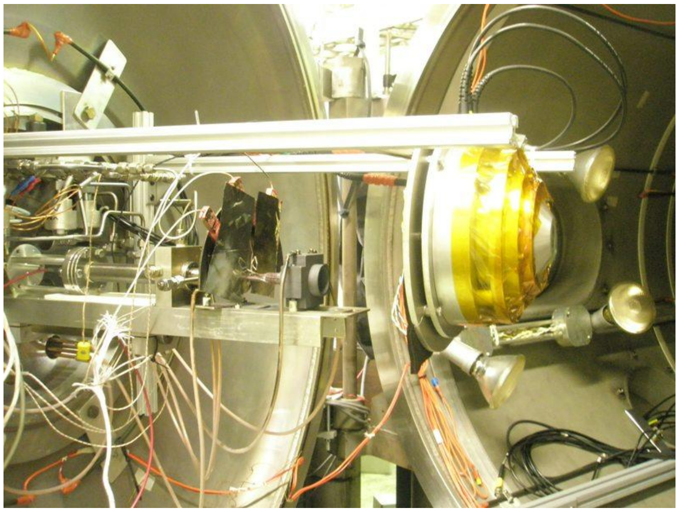

Figure 106 HEA mounted on axis, downstream of the hollow cathode and nozzle assembly

During a typical transmission energy sweep the hemisphere voltages (<40V) were applied in such a way as to keep the centerline path R_0 at near zero potential; in this way discrete filtering of ions with energies of up to 200eVcan be made based on the ratio of energy to charge. A representation of the HEA arrangement is shown in Figure 107.

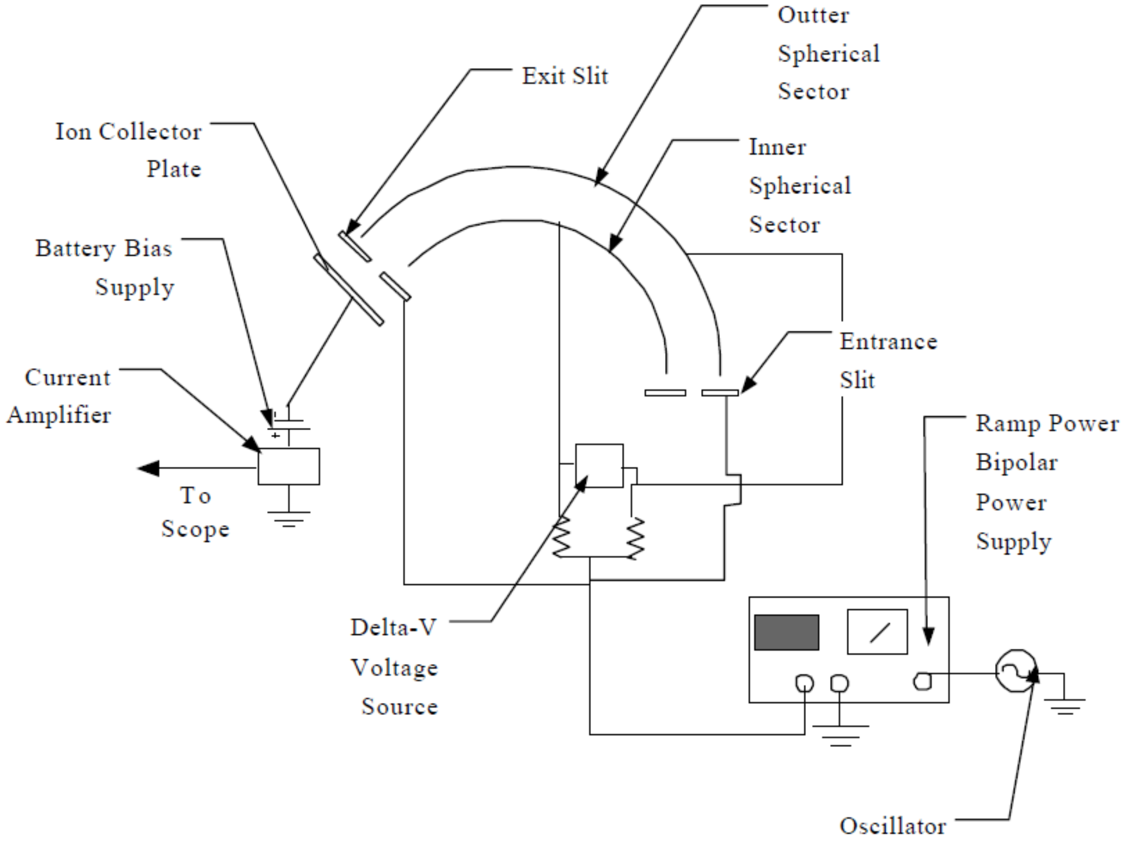

Figure 107 Representation of the electrical connections to the HEA for constant transmission energy

Entrance and exit-collimator slits had 2.0-mm-diamiter apertures. Both the HEA housing and cathode were at grounded. Ions were collected on the stainless-steel faraday cup at the exit collimator, and the currents were sensed by a Keithley Picoammeter, 6485 of 10fA resolution and error <2%, that retransmitted this signal along with the collimator potential measured with respect to ground and the data recorded with a Labview program. The collector plate was biased about 30V negative with respect to the ground potential to eliminate any ion dispersion that could have been induced by space charge effects. A 0.5-mm-thick mimetal enclosure around the HEA also provided shielding against magnetic field effects. The ion currents were measured based on transmission energy, which was established via internal bias conditions, and the absolute bias on the instrument was varied over the range that yielded ion energies from a few to 200eV. A collimator (70mm in length with a 2mm aperture) on the HEA gave a small angle of acceptance (α<2°) and ensured that only ions travelling axially and originating directly from the cathode could reach collector. The HEA was positioned 800mm downstream of the cathode orifice with its entrance-collimator axis aligned with the cathode axis for all of the experiments described herein. This configuration was used because it was anticipated that the energetic ions would be created near the orifice as in the potential hill mechanisms previously described. To confirm this, a series of ESA measurements were made with the probe positioned the same vertical distance from the cathode but moved, so that it was on centerline pointing at the orifice, 1 cm off centerline with its entrance axis parallel to the cathode axis, off centerline and pointing toward the cathode orifice, and off centerline pointed away from the orifice. In first 3 cases the acceptance angle of the ESA was such that some ions created at the orifice or in a plume immediately downstream of it would be collected. In the final case the orientation was such that none of these ions should have been collected. These experiments demonstrated that the distribution of energies among the ions was similar whenever the ESA was pointed at the orifice, there were dramatic reductions in the currents of high energy detected by the probe when it was not pointed at the cathode orifice, and almost no ion currents were detected when the ESA was pointed away from the cathode orifice. Samples were taken at 1kHz and averaged for each energy increment of 1eV, each scan taking 200seconds. Between scans discharge current and flow rate was varied and the cathode was allowed to settle for up to 15-minutes to reach steady state. Figures 108, 109 and 110 show the construction of the HEA and axial alignment procedures.

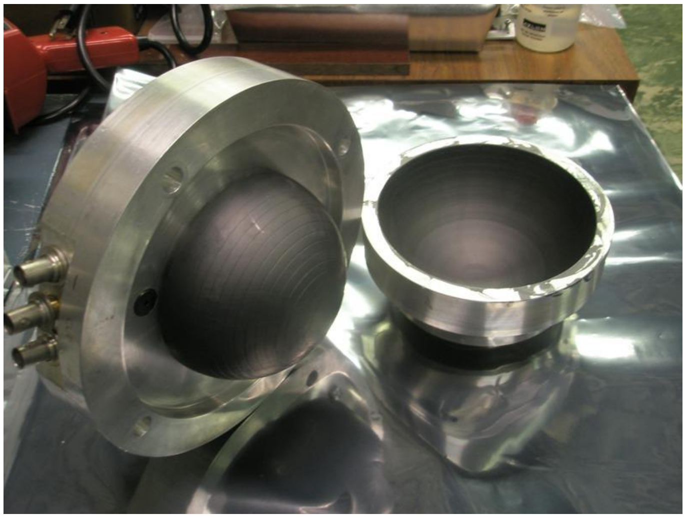

Figure 108 Construction of the HEA showing inner and outer hemispheres

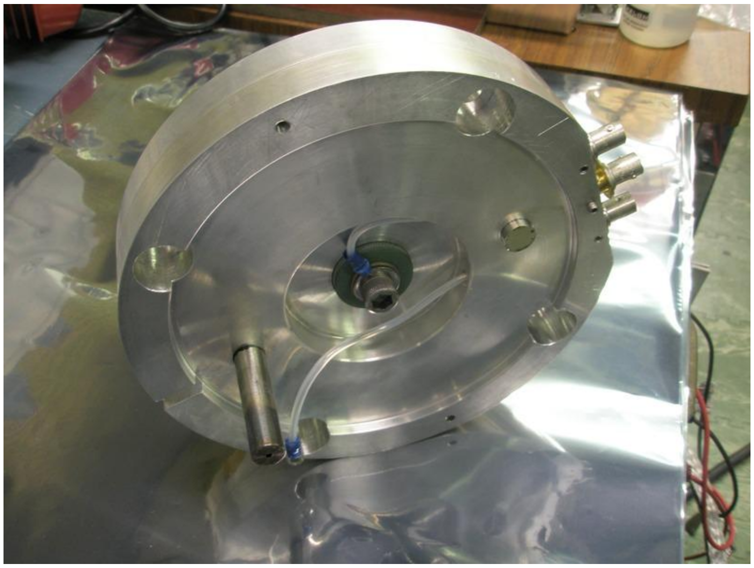

Figure 109 Front face of HEA showing collimator and Faraday cup

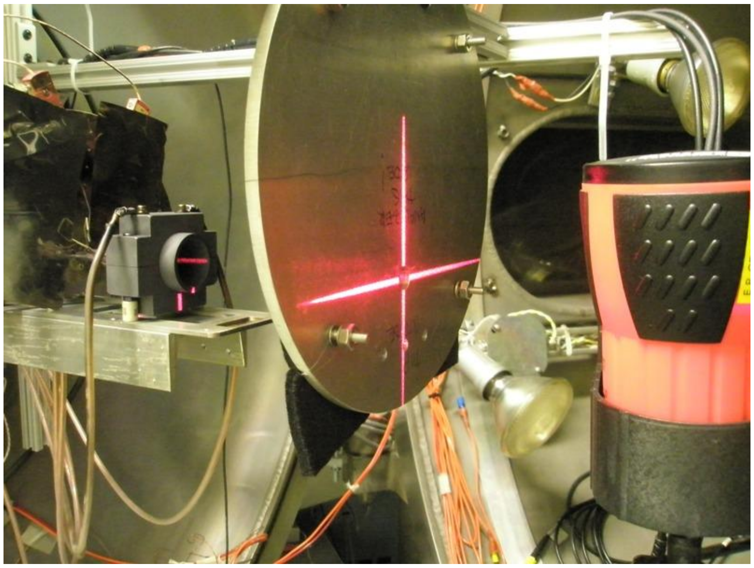

Figure 110 Checking of axial alignment using a laser level

The experiments were initiated by evacuating the vacuum chamber below 2.0 $x10^{-6}$ Torr ($2.7x10^{-4}$ Pa) then beginning a 4-hour cathode conditioning sequence at various heater currents and cathode flowrates. Cathode tip temperature was monitored via S-type thermocouples. Before final startup the heater current was raised to 8.2A, the anode supply was switched on and cathode flow rate increased to 5sccm.

6.2 ION ENERGY DISTRIBUTION RESULTS AND DISCUSSION

6.2.1 XIPS CATHODE REPEATABILITY AND ALIGNMENT

Ion energy measurements were made with excellent repeatability in some cases down to 1.8sccm and up to 18Amps with xenon and krypton. Operation at certain current mass flow conditions generally <1.8sccm or >18Amps resulted in excessive signal noise and thus determined the maximum range of terminal parameters for which ion energies could be measured. Typical examples of measurement repeatability for 4 separate sweeps separated by 15 minutes are shown in Figure 111 and Figure 112. It should also be noted that the hemispherical segment passes ions based on the charge to mass ratio, so a doubly charged ion will look the same as a singly charged ion with half the energy. With the current HEA we have no way of distinguishing between singly, doubly and triple charged ions. However, the abundance of doubly or triply charged ions generally results in bimodal distributions and is generally easy to identify. In our case the data only showed Maxwellian distributions.

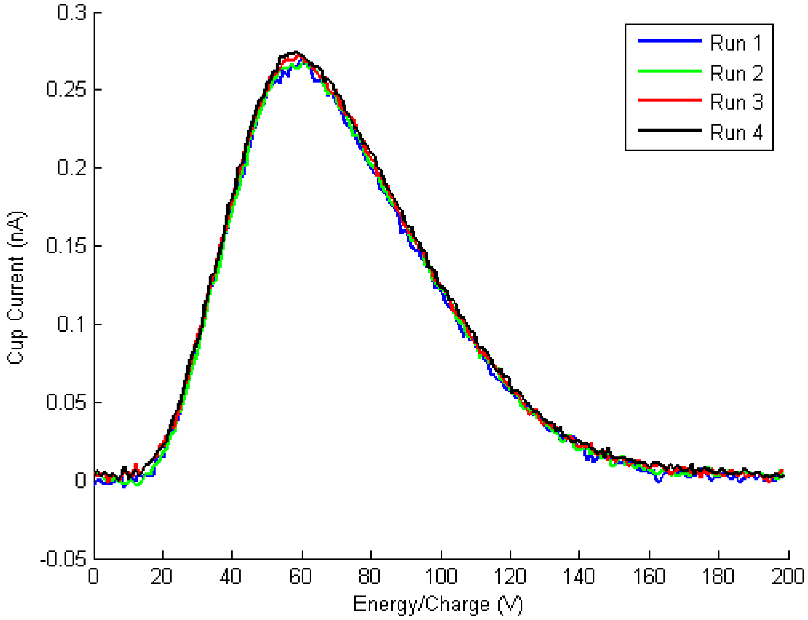

Figure 111 Typical repeatability of readings while operating at 18.25Amps with 6sccm on krypton

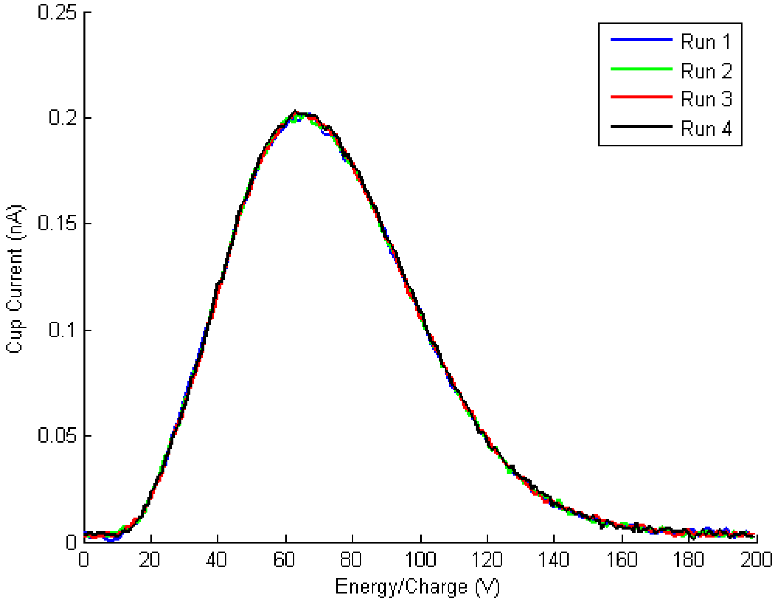

Figure 112 Typical repeatability of readings while operating at 15.25Amps with 4sccm on krypton

Figure 113 shows the experiment in operation. The plume of the cathode is clearly visible and although an enclosed keeper was not used there is no visual evidence of plasma escaping from the cathode anode gap and dispersing radially. The anode received significant heating at higher current levels due to electron convective heat transfer and thus frequently resided >700°C since it was only radiatively cooled. Figure113 also highlights that ESA was mounted accurately on axis with the anode and cathode through the illumination of the analyzer by the cathode spot and shadowing of the anode which fall on axis with the collimator.

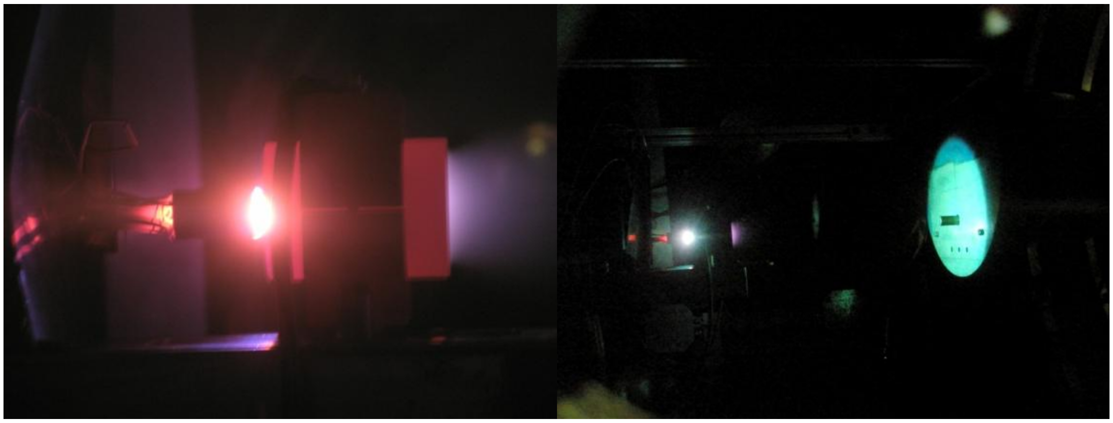

Figure 113 Side on view of the hollow cathode during operation with the cathode tip and plume visible (left) cathode spot illuminating the HEA showing excellent alignment (right)

6.2.2 XENON ION ENERGY DISTRIBUTIONS

Figure 114 shows ion energy distributions obtained at 5 amps with xenon. With decreasing flow rate the total ion current and the peak ion energy significantly increases and broadens to contain a much larger high energy component and high energy tail of over 120eV with a maximum peak of 57.5eV. The low energy tail also shows a lack of ions of energies below the discharge voltage and also an associated anomaly in the distribution, at approximately the discharge voltage, for all mass flow conditions. The anomaly is more difficult to identify for the lowest flow condition and much less prominent. The highest flow rate of 7.96sccm also shows a small reversal in trend with a slightly higher energy peak than the 5.96sccm condition; however total ion current and the distribution are consistent.

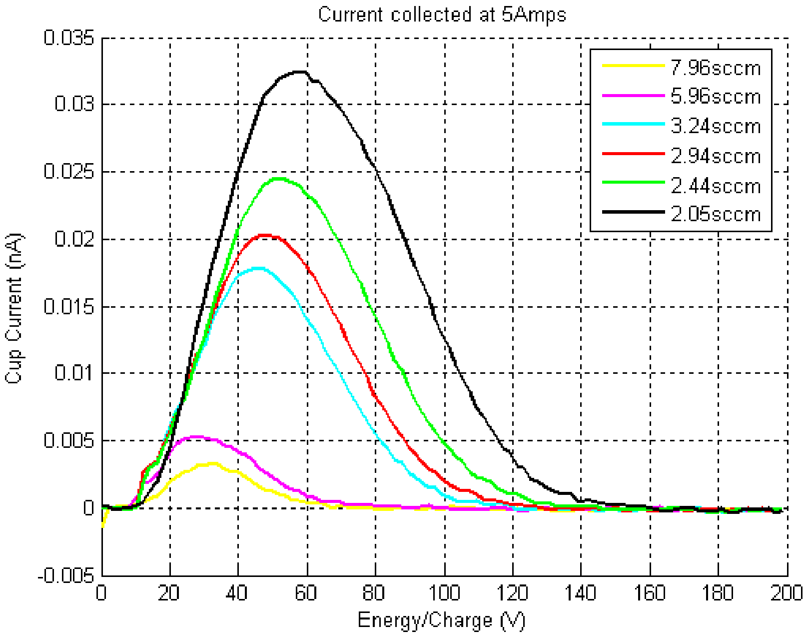

Figure 114 Ion energy distributions at 5 amps with xenon

Figure 115 at 10Amps shows higher energy peaks (up to 62.4eV) in comparison to the 5Amp condition however with only half of the peak collected current and some broadening of the distribution. The plot also shows a similar trend at 2.05sccm where a reduction in collected cup current is found. The increase in peak cup current to a maximum followed by a decrease in peak collected current becomes more pronounced at higher discharge currents as will be shown. The distribution also begins to show a bulk acceleration of the 2.44sccm and 2.05sccm conditions whereby the complete distribution is shifted upwards in energy rather than simply increasing peak ion energy; something exemplified at even higher currents.

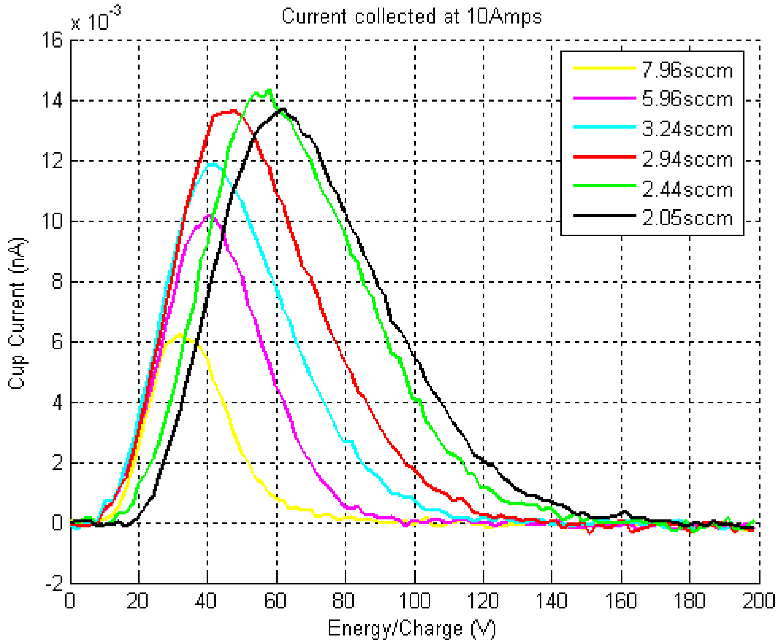

Figure 115 Ion energy distributions at 10 amps with xenon

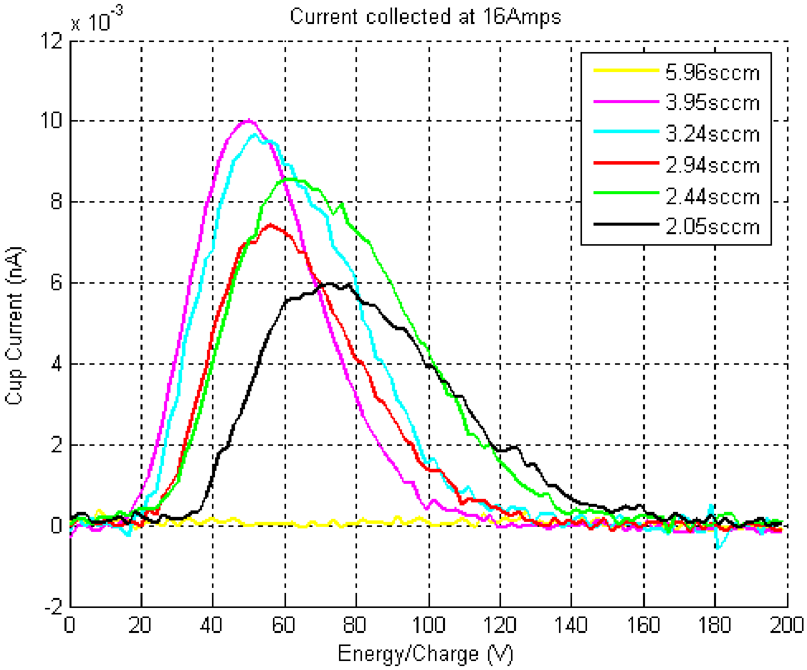

Figure 116 Ion energy distributions at 16 amps with xenon

As shown in Figure 116 the 16Amp condition for xenon displays a very different distribution from both the 5Amp and 10Amp condition. The data shows a rapid drop off to zero collected current for the 7.96sccm and 5.96sccm flowrates. Again a general decrease in collected current and increase in peak ion energy is revealed with decreasing flowrate. Peak ion energies are significantly higher than for the 10Amp condition and with much greater bulk acceleration of plasma; the data for the 2.05sccm flow condition for instance shows little to no ions with energies less than 35eV. The 2.94sccm condition shows a decrease in collected current contrary to the trend which may be due to some thermal movement of the anode or vectoring of the plume.

6.2.3 KRYPTON ION ENERGY DISTRIBUTIONS

Data for operation with krypton, shown in Figure 117, shows much higher energy distributions for the heavier xenon species however at this current condition the discharge was unable to reach steady state and showed long period fluctuations in discharge voltage leading to shifts in the distribution. Nonetheless the data again show a general inverse relationship of peak ion energy to mass flowrate for peak ion energies of up to 95eV and energy distributions extending beyond 180eV; significantly higher in ion energy with a much broader distribution than the xenon data suggesting a mass dependent acceleration mechanism As with the 5Amp xenon case an anomalous blip at approximately the discharge voltage is present. Operation at the 10Amp condition generated too much signal noise for reliable ion energy measurements and comparisons.

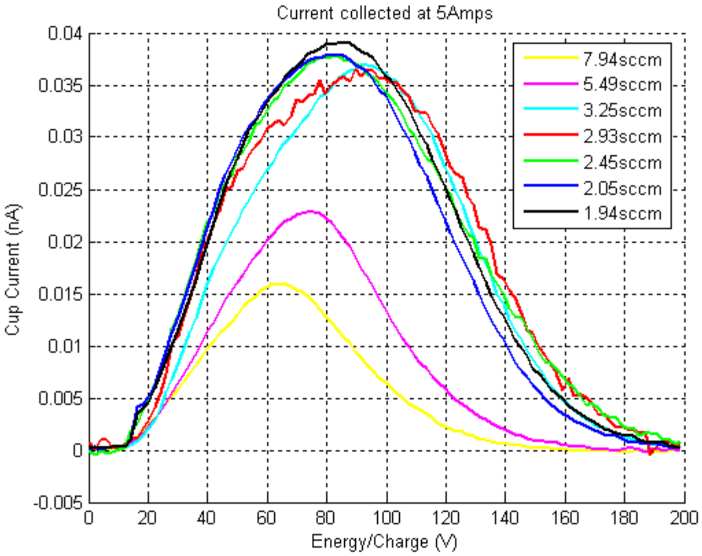

Figure 117 Ion energy distributions at 5 amps with krypton

Figure 118 shows data for operation at 16Amps with peak ion energies of up to 122.5eV. At the lowest flow condition and distributions also take on a more Gaussian form. Bulk acceleration at the 1.94sccm also leaves no ions with energies below 44eVand the data displays a general reduction in collected current when operating below 2.45sccm. The high energy tail extends well beyond the 200eV limit of measurable ion energies for the current experiment however extrapolations would suggest the presence of ions of over 240eV.

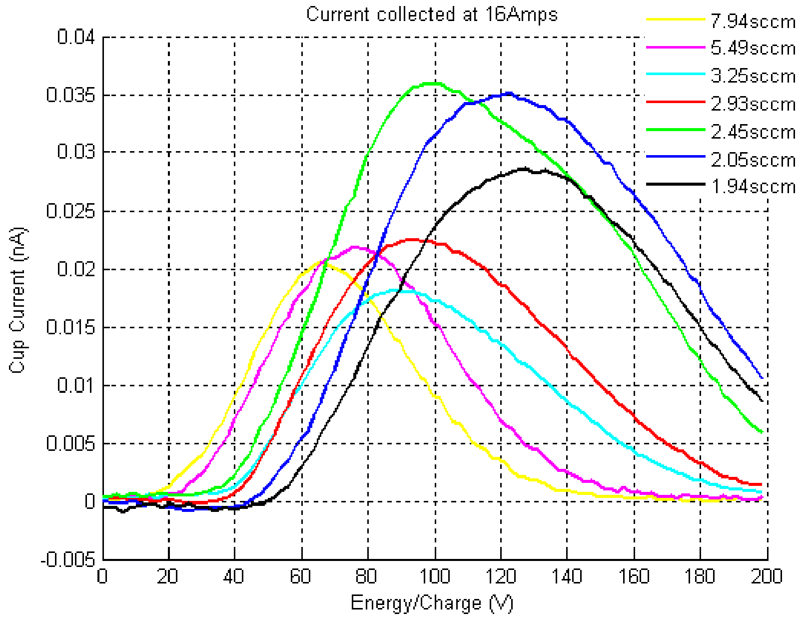

Figure 118 Ion energy distributions at 16 amps with krypton

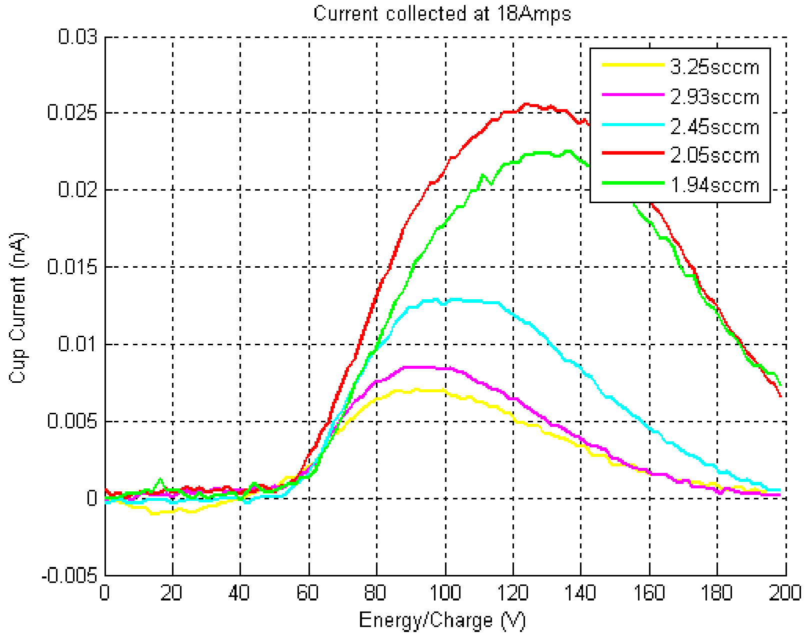

Figure 119 Ion energy distributions at 18 amps with krypton

Operation at 18Amps shown in Figure 119, further increases peak ion energies and bulk acceleration leaves no ions of less than 55eV, although this would not seem to change significantly with decreasing flowrate. High flowrates were not achievable due to excessive signal noise.

6.2.4 DISCHARGE CHARACTERISTICS

The current voltage characteristics were obtained during the HEA experiment over the flow range 1.8 – 7.9sccm with xenon and krypton and are shown Figure 120. Operation with xenon does show low discharge voltage characteristics similar to the T6LA arrangement at high current. There are however significant differences from the T6LA discharge voltage characteristics shown in Figure 59. Principally these are general increase in discharge voltages at low currents and voltage 'humps' between 2-3.5sccm with xenon similar to a plume mode transition although less abrupt.

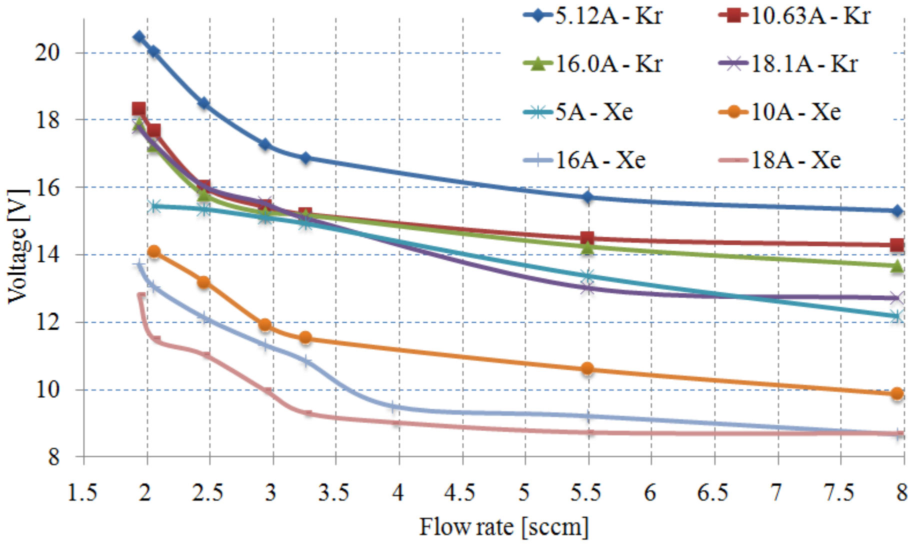

Figure 120 Current voltage characteristics

Both xenon and krypton data sets shown in Figure 121 and122 suggest that at high currents the high energy ion production mechanism strongly scales with discharge voltage at high current for both xenon and krypton. Interestingly there was no correlation between peak to peak voltage oscillations and peak ion energies. This result is somewhat surprising since high energy ion production has been attributed to RF plasma oscillations by Goebel. In this case however we must realize that local plasma potential oscillations can be much larger than the terminal voltage oscillations perceived by the electrodes themselves.

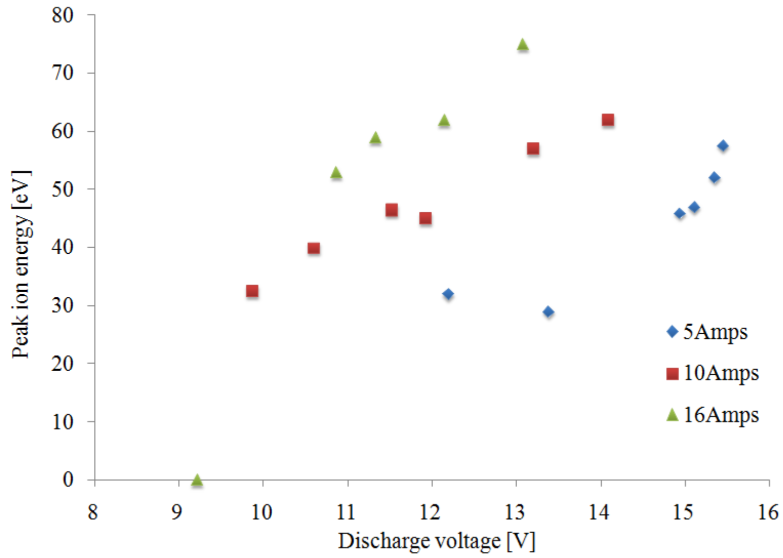

Figure 121 Peak ion energy with respect to discharge voltage for xenon

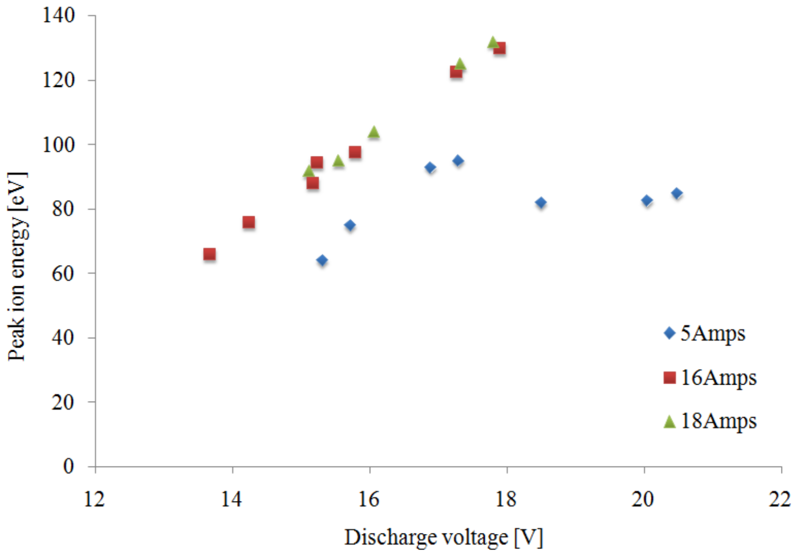

Figure 122 Peak ion energy with respect to discharge voltage for krypton

For the high current conditions in Figure 123 and 124, peak ion energy shows an inverse quadratic dependence on mass flowrate again with the exception of the low current conditions.

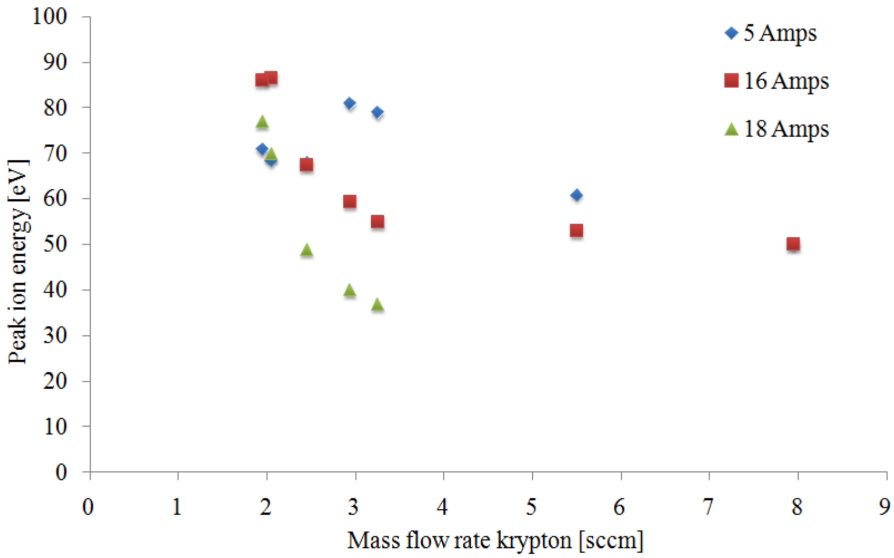

Figure 123 Peak ion energy with respect to mass flow rate for krypton

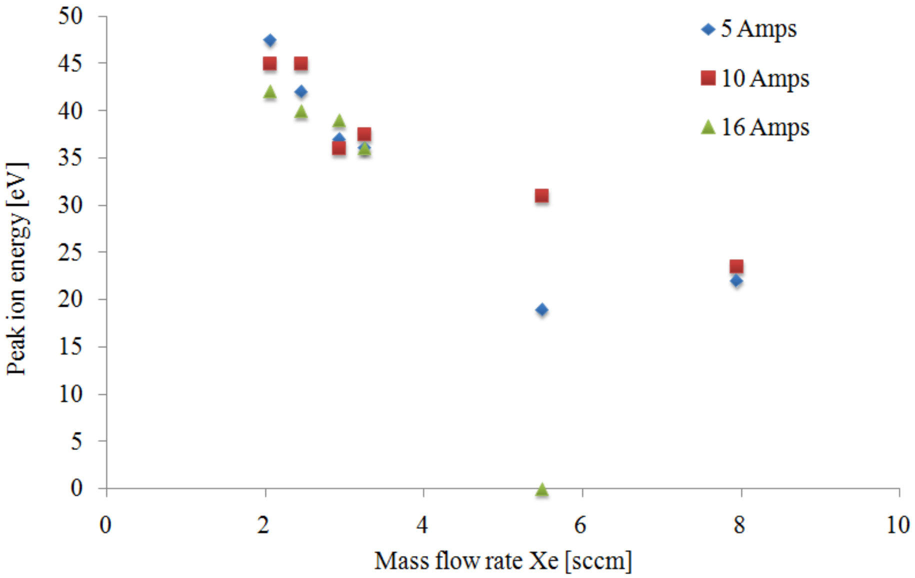

Figure 124 Peak ion energy with respect to mass flow rate for xenon

6.2.5 ACCELERATION MECHANISM OF IONS

The lowest flowrate obtainable with the ¼ inch XIPS cathode was 1.98sccm or 0.136mgs^{-1} at 18Amps with xenon. Calculation shows that the XIPS cathode was far short of operating down at the critical ionization current, sufficiency high such that MHD effects could be legitimate. There are two distinct differences in the HEA measurements made by previous authors. The measured ion populations are of much higher energy and broader in their distribution. Secondly at high currents the complete ion energy distribution is shifted up in energy, a process exemplified as flowrate is decreased. The following mechanisms are proposed.

At high currents and flowrates, as we have in Figure 116, the high energy ion signature is shown to completely disappear. This also corresponds to low voltage operation with very low peak to peak voltage oscillations. We have already shown how during spot mode operation the potential distribution favors the acceleration of ions toward the cathode and only on the transition to the double layer does the potential distribution favor the acceleration of ions created between the peak and the downstream side of the potential hill towards the HEA as shown in Figure 125. It is therefore proposed that these flat ion energy distributions constitute operation firmly into spot mode whereby the natural thermal electron current to the anode is sufficient to supply the current demanded by power supply and a positive monotonic potential profile is maintained.

Reduction in flowrate while operating at 16Amps results in the rapid appearance of highly energetic energy profile as the cathode transitions to double layer potential structure. Distributions show however that the population which appears at the low current condition grows in peak energy less rapidly with the inverse of flowrate since the current density and neutral density within luminous plasma ball region are much lower, consistent with formation of the double layer. An important observation is the appearance of an easily identifiable bulk acceleration of all ions created along with a simultaneous reduction in the collected current of the signal. It is important to note that Goebel has shown the existence of the high energy population is a result of high amplitude RF oscillations, particularly on the outer edge of the luminous ‘plasma ball’ which scaled similarly to our results with respect to mass flowrate and discharge current as discussed in Chapter 1. The distinctive difference here however is large shifts in the complete distribution. In this case the peak of the potential hill and the source of the high energy ions arising from ion acoustic turbulence correspond to the same luminous region at the exit of the cathode orifice. Ions created on the downstream side of the potential hill will therefore receive additional acceleration towards the HEA as they fall down the potential hill. Ions on the opposite side of the potential hill on the other hand will experience acceleration towards the cathode region. The whole distribution will therefore experience a shift up in energy with a loss of ions with energies less than that required to overcome the potential peak. This is represented by the drop in total collected current with decreasing mass flowrate and is not, as one may think, directly related to the reducing mass flowrate itself since this actually results in an increase in collected current due to the promotion of RF oscillations until the potential hill forms. Of those ions created on the upstream side of the potential hill only ions with energy in excess of the potential hill are able to overcome the double layer region and reach the HEA. These ions will of course also be accelerated by the potential drop on the opposite side of the potential hill. The minimum energy which an ion can reach the HEA with is therefore equal to the hill potential and is easily identifiable in the data.

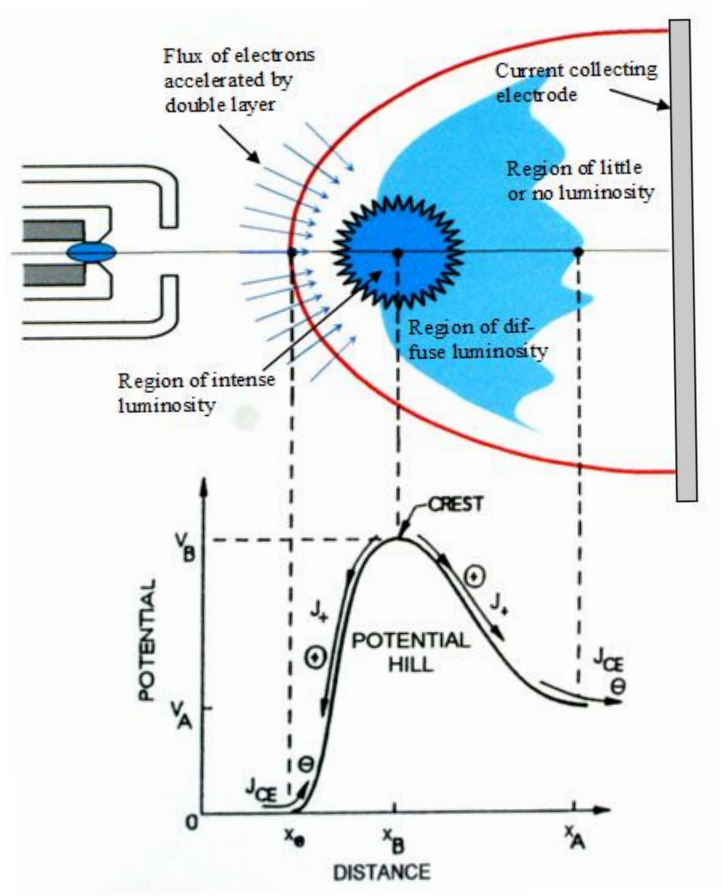

Figure 125 Axial potential profile detected by Williams and Wilbur[117] corresponding to the visual structure of the double layer in the plume mode virtual anode seen by Rudwan[187]

If a potential hill is indeed forming and accelerating/decelerating the complete distribution then subtraction of the potential due to the 'hill' from the peak ion energies should reveal the independent process of ion creation by RF ion acoustic turbulence. The potential hill voltage size is clearly identifiable by the lowest energy at which ions appear in the signal or the 'switch-on voltage'. This represents acceleration in the positive column ~30V for xenon in the low flow high current regime and ~50V for krypton. Figure 126 shows the peak ion energy minus the 'switch-on voltage' with respect to discharge current at the high current conditions for xenon and krypton. This excellent correlation shows that the RF ion acoustic ion acceleration process is relatively independent of the discharge current but is rather a function of the *absolute discharge voltage*. This is a reasonable hypothesis since the peak plasmas potential oscillation amplitudes are very likely to be a function of the absolute discharge voltage since both are related to the extent of operation into plume mode.

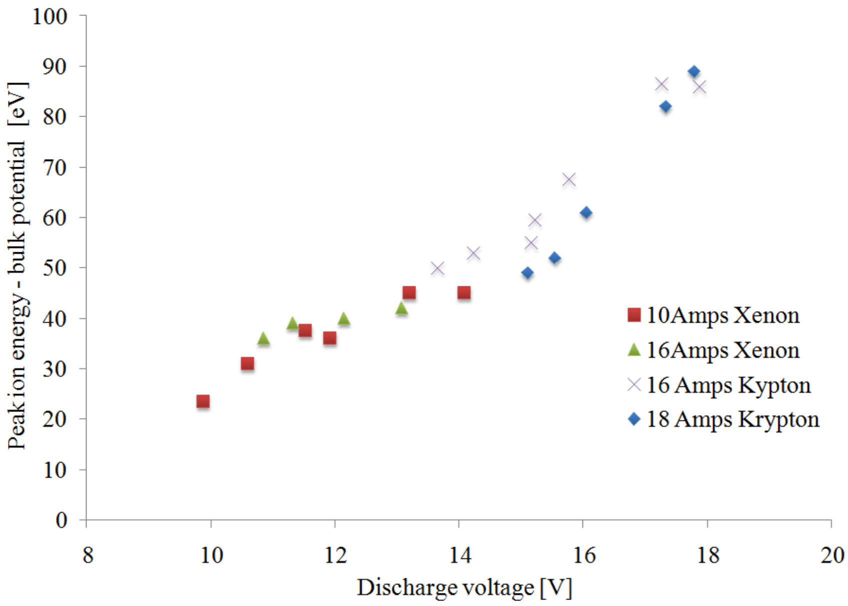

Figure 126 Plot of peak ion energy minus the bulk acceleration energy experienced by all ions for the respective distribution with respect to discharge voltage

One other noticeable phenomenon is that the bulk acceleration mechanism seems to saturate when operating at 18A on krypton at about 45V suggesting that it may not favorable to maintain such a high potential hill beyond 45V even when decreasing the mass flowrate further, although the potential continues to rise for xenon. It may be that space charge limits the formation of higher plasma potentials.

Such evidence significantly strengthens the theory of the plasma potential hill acceleration mechanism. Since at these flowrates and in this configuration however we do not know the degree of ionization in the region of the potential hill we cannot state the significance of the ions accelerated through a potential hill on the total thrust component. Since the anode is not enclosed ions will be emitted isotropically and the net thrust close to zero, except for the fact that a small proportion of ions will transfer their momentum back to the cathode and represent the actual net equivalent thrust. The loss of these ions to the cathode is actually therefore the only mechanism preventing zero net thrust. As a basic approximation of the significance of the emitted ions on the thrust mechanism we can compare the collected current at the HEA in comparison to the total equivalent mass flow and while making some assumptions about the distribution of the ions, calculate the contributed thrust. As an example the mean collected current for operation with xenon at 16Amps and 2.05sccm was 6nA with mean ion energy ~80V. Equivalent flow is defined as:

$$I_{eq} = \frac{e\dot{m}}{M_i} \tag{6.5}$$

This represents an equivalent total mass flow of 0.149A with $8.25\text{x}10^{-9}$mgs^{-1} flowing to the cup collector on the HEA. Based on observations of the plasma ball in front of the cathode a reasonable approximation of the angle of the isotropically expanding distribution which see the cathode orifice face is about 30° which of course implies that a 30° expanding proportion of the flow do not see the orifice face and therefore contribute thrust. As a conical approximation, the downstream area of this 30° expanding flow at a distance of the HEA collimator entrance (0.8m) is 0.144m^2. The collimator entrance has a 2mm aperture (receiving 6nA of current) giving an area of $3.14\text{x}10^{-6}$m^2 thus the total equivalent current, integrating over the entire base of the 30° cone, is 0.275mA or $3.78\text{x}10^{-4}$mgs^{-1} (1.84%of the total mass flowrate). Neglecting divergence in reducing the net thrust component, which is fair given an expansion angle <<60° the mean velocity of each particle is 80eV or 10.57kms^{-1} for xenon giving a net thrust of $3.99\text{x}10^{-6}$N or 3.99μN. This calculation indicates that the thrust generated by the combination of the potential hill and ion acoustic turbulence is negligible in terms of usable thrust. On the other hand this calculation does indicate that pulses of ions originating from the combination of these mechanisms may in fact contribute a significant source of thrust noise in hollow cathode thrusters. Below a critical pressure Song et al.[188] have shown that the discharge mechanism cannot settle into a double layer type operation and observes pulses in current similar to the high frequency oscillations found in our previous measurements. Pulses ~4μN or more at these frequencies could therefore constitute a significant noise component.

6.3 INFLUENCE OF CONICAL ANODES

The conical anode design produces marked difference in ion energy distribution over conventional arrangements. Since the conical nozzle restrict the loss of neutrals from the ionizing double layer region it is likely that this design helps maintain higher local neutral densities, increasing the ionization rate and allows for the production of much higher ion densities and potential hills. Lower voltage operation for the same discharge current is also likely attributable to this mechanism. An interesting phenomenon observed is the formation of distinctive rings on the inner anode regions during operation of the T5 cathode as shown in Figure 127.

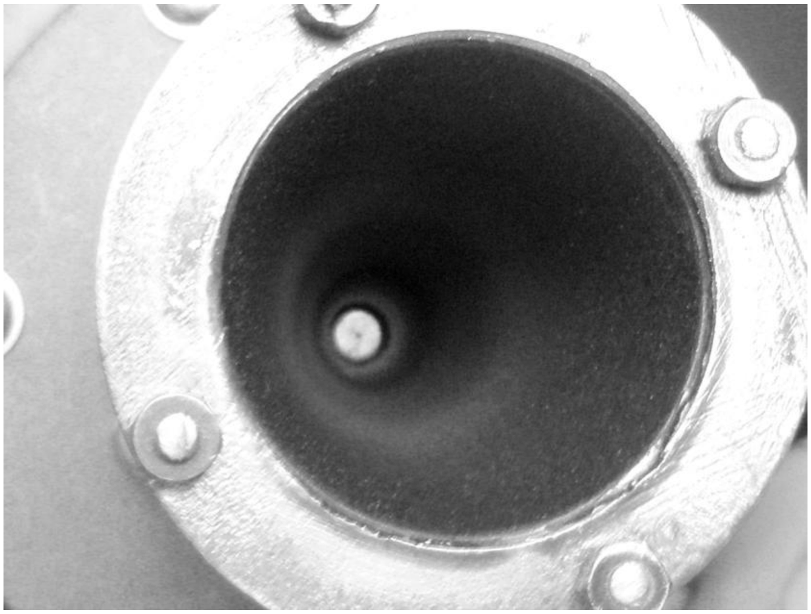

Figure 127 Image showing post test analysis of the T5CA anode with distinctive regions of arc attachment.

This anode operated at three separate current levels, 3.2A, 1.8A and 0.8A, and thus may be an explanation for three distinctive concentric ring patters within the anode cone. It is possible that these rings represent the attachment point of the negative sheath in which the discharge current flows to the anode on the downstream side of the double layer. At this point electrons are no longer being accelerated but are collected by the anode and hence any sputtered material may also be allowed to recombine and deposit in this region.

The investigation has shown that increasing the electron collection area at the anode while increasing its proximity to the dense plasma at the orifice exit through the use of a conical geometry has a pronounced effect in reducing both the general discharge voltage of hollow cathodes and modifying the transition to plume mode. Plume mode is usually identified as peak to peak voltage oscillations >4V accompanied with high frequency oscillations and a sudden and dramatic increase in discharge voltage as flowrate is reduced. This behavior has been found in both diode and triode configurations however, as we have shown, an enclosed conical anode geometry does not display the later characteristic. An enclosed conical anode is shown to maintain low voltage operation to lower mass flowrates than conventional arrangements. As flowrate is decreased further the cathode experiences a steady rise in discharge voltage, with no abrupt jump to higher voltage as found in conventional configurations. The reason for the prevention of the abrupt change with associated hysteresis is unknown; the following mechanism is proposed.

We know the abrupt change in discharge voltage at the transition is a product of the breakdown of the sheath at the anode surface to form a double layer. It is likely that the reason why a conical anode behaves differently lays in the fact that the double layer is enclosed, immediately adjacent to the anode. In conventional configurations the anode is situated further downstream, far from the double layer. In-situ noise measurements confirm that the transition to a double layer does still take place in the T6CA since the discharge displays the characteristic oscillations at ion acoustic frequencies associated with its formation. Visual inspection of the anode surface clearly shows the progression of the arc attachment region further downstream under different operating conditions with the growth of the electron accelerating double layer. In a conventional configuration the distance from the double layer to the point of current collection is approximately fixed as the electron accelerating sheath at the cathode exit grows with reducing flowrate. In the conical configuration an electron collecting area is present immediately downstream of the double layer as it grows. There is therefore no need for an additional voltage drop between the double layer and the anode potential to facilitate ionization and electrons can passively diffuse to the anode surface. In conventional configurations however the double layer may not give sufficient ionization to allow electrons to flow from the double layer to the anode which may be located some distance away, hence an additional potential drop occurs between the double layer and the anode to accelerate electrons further and generation ions.

Electron collection in the electron acceleration double layer region of the conical anode should be minimal due to the focusing of electrons inwards by electric field and due to the lower degree of ionization on the upstream side of the potential hill since electrons will not have reached their maximum kinetic energy. Hence the anode displays dark regions of graphite where relatively little ion recombination and hence deposition has occurred. The geometry also reduces the expansion of the plasma and neutrals from the orifice from a spherical to a conic expansion significantly increasing the downstream neutral density and subsequent ionization rate in the double layer contributing to a lowering of the discharge voltage. In spot mode where the ionization fraction generated within the cathode is sufficient support the collection of the discharge current passively at the anode surface, the conical geometry significantly increases the capacity of the anode to collect the electron current without the formation of a double layer based on the anode surface area available to energetic electrons.

CHAPTER 7

CONCLUSION

This work makes the first objective study of the performance and thrust mechanisms of distinctly different hollow cathodes in various geometrical configurations of as much empirically collected data as possible. The study utilized a variety of instrumentation and investigated the influence of terminal parameters of discharge current, flowrate and geometry on thrust measurements and the ion energy distribution and a considerable attempt was made to identify thrust mechanism responsible. Consequently some new insight has been gained into the underlying physics of hollow cathode operation and thrust production. A study of such scope has not been previously attempted and is unique in the literature. This chapter summarizes the main conclusions drawn from the present work.

7.1 THRUSTER PERFORMANCE AND BEHAVIOR

The investigation has shown that increasing the electron collection area at the anode while increasing its proximity to the dense plasma at the orifice exit through the use of a conical geometry has a pronounced effect in reducing both the general discharge voltage of hollow cathodes and modifying the transition to plume mode. Furthermore the move to a lower current but higher orifice current density hollow cathode utilizing a conical anode has shown dramatic increase of over two orders of magnitude increase in thrust efficiency at no more than a few amps while demonstrating comparable ISP.

The use of a conical anode geometry in the T6 cathode resulted in a significant improvement ~40% in electrical efficiency over cylindrical anodes for the same discharge current and flowrate. Improvement in the current collection mechanism also allowed operation of the T6 cathode down to extremely low flowrates resulting in high specific powers, generating ISP of up to 1031s with argon at 30Amps and 982s for xenon propellant at 25Amps, much higher than that found in previous testing by Gessini[9] and with much greater accuracy. Although large improvements in the current collection mechanism were made, thrust efficiencies still however remained very low at 0.37% for xenon and 0.27% for argon. The inability to significantly improve thrust efficiency in the T6 cathode suggests that losses dominate the total efficiency. We have shown that at high currents and low mass flowrates, where high ISP's are achieved, electron convective losses represent between 20-42% of the discharge power in spot mode, however in plume mode where high ISP is found this can be as high as 60%. Since the cathode body is relatively large, radiative and conductive cooling are likely to represent the majority of the remaining energy loss mechanisms. The T5 cathode was therefore proposed as a potentially better performing thruster based on analysis of the energy input processes and suggested as a candidate cathode more likely to operate at higher efficiencies. At maximum rated current density, the T5 cathode operates at $65A.mm^{-2}$ compared to the T6 cathode at $38A.mm^{-2}$, however for the same mass flowrate the neutral density within the orifice must also be ~ 16 times greater improving energy equipartition between ions, electrons and neutrals.

The T5 cathode was tested with the original flat plate anode with which it was developed and the conical anode used in testing of the T6 cathode. With the flat plate anode the T5 developed a maximum ISP of 430s with argon at 3.2 Amps with 1.1% thrust efficiency. When operating using the large area anode however the T5 cathode was able to develop over 657s ISP at 3.2 Amps with 4.5% thrust efficiency. When operating at higher mass flowrates with the conical anode the T5 developed 349s ISP at 3.2 Amps with 8.1% thrust efficiency and 223s ISP at 0.8Amps with 17.1% thrust efficiency. This improvement when moving to the conical anode is testament to both the improved propellant utilization due to the enclosed design and a significant reduction in discharge voltage.

The pendulum thrust balance developed for the characterization of the T5 and T6 hollow cathode shows significant improvements in measurement sensitivity, uncertainty, thermal drift and noise over the previous measurement system and will provide the ongoing capability make micro-to-milli-Newton thrust measurements at the University of Southampton. For the first time assessments of the accommodation coefficient were made by comparison to the theoretical cold gas performance and were found to give ~20% over estimate arising from elastic collisions with the target.

We have shown that by considering the thrust production and energy loss mechanisms in hollow cathodes the T5CA hollow cathode has been developed as a potential candidate microthruster operating in the 10-80W range. Operation in cold gas and resistojet modes highlights that redundancy in such a propulsion system is possible. Although large improvements in discharge voltage characteristics have been made with the T6 cathode thrust efficiency for this device remained impractically low stressing the need to explicitly understand the thrust mechanism. In particular understanding of energy equipartition between ions, electrons and neutrals through intensive modeling will enable more optimal designs of electrothermal thruster.

With the conical anode both the T5 and T6 cathode were able to maintain low voltage operation down to extremely low flowrates. Beyond a critical flowrate however both cathodes began to exhibit noise characteristics typical of plume mode. We have definitively attributed this change to the formation of the double layer in the anode cathode gap which we will discuss next. At extreme flowrates very large high frequency voltage fluctuations of up to +600V/-45V for the T6 and +120V/-10V for the T5 cathode. Such high voltage fluctuations have not been seen in the literature. Analysis of discharge noise suggests that the voltage oscillations are due to ionization instability related predator-prey modes with breathing frequencies ~ 18kHz for the T6 cathode and ~250kHz for the T5. Both cathodes also exhibit voltage fluctuations in excess of 120MHz which can be linked to the decay modes of the breathing frequencies. Such discharge fluctuations of this magnitude suggest that consideration will have to be given to the maximum allowable noise for reasonable hollow cathode life in any future development which may bring about limitations on attainable ISP. SEM analysis of the T5 cathode shown in Appendix A confirms a high rate of sputter erosion on the orifice plate also with deposition of carbon from the anode electrode from initiation. It is foreseeable that this may present a life limiting mechanism in hollow cathode thrusters.

7.2 ELECTROTHERMAL THRUST PRODUCTION

Theories of the means by which hollow cathodes are able to generate such high thrust levels have been proposed but have never been seriously explored. Neither has the existence of the high energy ion population and its relevance to the total thrust mechanism.

For the first time, this work has proposed the novel concept of electron pressure as a contributing factor in thrust production at the orifice exit in hollow cathodes. We have shown that the electron pressure component thrust combined with that of the heavy particles is sufficient to explain the propellant acceleration mechanism in the T5 cathode. Maximum electron temperatures ~0.4-0.9eV with the assumption of a full ionized flow, have been shown to generate sufficient static pressure at the orifice exit to equal the observed performance based on heavy particle temperatures between 1000-8000K . This is in fact a low electron temperature to those typically found in the orifice hollow cathodes and the actual temperature is likely to be between 1-2eV suggesting that even if the fully ionized assumption is not valid the ionization fractions <40-90% would still be high enough to account for the perceived thrust levels although measurements do state an ionization fraction close to 1 in the T5 orifice at high currents and low flowrates.[113]

We have shown that the internal pressure of the T5 hollow cathode is of at least 100mbar at high currents and low flowrates and significantly increases with mass flowrate to pressures estimated to exceed 600mbar and furthermore that the flow through the orifice is almost certainly sonic. In relatively high pressure discharges such as these the electron pressure component must be substantial. One piece of information to support this mechanism is apparent when comparing ISP's of the T6 cathode operated by Gessini and the T6LA cathode. For the same flowrate and discharge current the ISP achieved in the T6LA cathode design is approximately half that of Gessini's T6, although higher ultimate ISP's are achieved by operating at much lower flowrates and higher specific powers. Is should be noted that this does not imply higher thrust efficiency since discharge voltage in the T6LA is much lower. This does however imply that the thrust mechanism may also be related to the ultimate discharge voltage. Higher voltage operation implies the cathode is operating closer to or further into plume mode. In this case we can expect the electrons to be hotter for the same discharge current and flowrate thus the electron pressure thrust component to be greater, thus a possible reason why Gessini's cathode exhibits twice the effective exit velocity for the same current and flowrate as the T6LA cathode. Since we did not make any measurements of ion energy distributions as in the T5 HC it is difficult to speculate on the role of the plasma potential hill ion acceleration theory in this cathode however measurements made with a XIPS hollow cathode discussed later do shed some light on the general role of this mechanism in hollow cathodes.

7.3 ELECTROMAGNETIC THRUST PRODUCTION

This study has shown that the electron pressure thrust mechanism is insufficient to fully explain the measured thrust levels in the T6 hollow cathode and for the first time shown that cathodes such as the T6 can be operated at such low flowrates so as to significantly exceed the critical ionization current. This ratio marks the bounds by which an axial to radial current driven thruster can be said to exhibit magneto-plasma-dynamic thruster properties with electromagnetic acceleration of the gas flow in a highly ionized state. Calculation of the ‘blowing’ force on the gas correlates reasonably well with the measured values of thrust at low flowrates. Thrust measurements also indicate the possible presence of an accelerating force, superimposed on top of the mass flow dependant gasdynamic thrust mechanism. Extrapolations back to zero mass flowrate show the presence of the force which correlates well with the predicted thrust based on the Maecker formula. This would suggest that the self generated magnetic field in the orifice, which we have shown to be up to 120G, is sufficient enough to generate a cross field interaction and impart a Lorenz force on the plasma. The strength of the magnetic field within the orifice and its role in plasma acceleration was previously thought negligible which is true at higher flowrates.

7.4 ELECTROSTATIC THRUST PRODUCTION

By measuring the beam current downstream of a XIPS cathode the first measurements have been made of the ion energy distribution of an open diode hollow cathode with a conical anode. This was done to explore the role of potential hill and high energy ion populations which have become synonymous with theories of high rates of hollow cathode erosion found in modern ion thrusters. Ion populations of these energies represent extremely fast particles. Many authors have made measurements of the ion energy distribution of conventional configurations and a cacophony of contradicting theories have been proposed as to how hollow cathodes are able to generate ion of such energies. This is not surprising given the unique discharge characteristics of one hollow cathode discharge over another and even less surprising when a fuller understanding of hollow cathode behavior is gained, in particular the vast influence of anode geometry on the discharge itself.

In a study of the literature one is able to definitively attribute the high energy ion signature in hollow cathode discharges to RF ion acoustic oscillations in the ‘plasma ball’ region line with the measurements of Goebel.[128] Local plasma potential oscillations within this diminutive region have been overlooked by previous authors and the potential hill found has been wrongly attributed as the cause of these energetic ions. The potential hill itself on the other hand is almost certainly a byproduct of the intense double layer ion creation mechanism close to the orifice exit. The formation of the double layer and the height of the potential hill have been shown to be sensitive to the particular anode geometry and thus considerable disparity exists between measurements even of the same cathode. This work has presented a scrutiny of measurements and observations, particularly within the cathode-anode region supported by ion energy measurements which describe a unified view of these mechanisms.

Analysis shows that the XIPS cathode was far short of operating down at the critical ionization current when MHD effects could be responsible. Hemispherical Energy Analyzer experiments made with a conical anode arrangement show distinct differences in the HEA measurements made by previous authors. The measured ion populations are of much higher energy and broader in their distribution. Secondly at high currents the complete ion energy distribution is shifted up in energy, a process exemplified as flowrate is decreased. At low flowrates and high currents we can mark the transition to a double layer potential structure as the high energy ion population rapidly appears as a result of high amplitude RF oscillations. An important observation however is the appearance a *bulk acceleration of all ions created* along with a *simultaneous reduction in the collected current* of the signal which we have firmly attributed to the formation of a positive potential hill exceeding the discharge voltage. This represents acceleration in the positive column ~30V for xenon in the low flow high current regime and ~50V for krypton. Ions created on the downstream side of the potential hill receive additional acceleration towards the HEA as they fall down the potential hill while ions created on the upstream side must overcome this potential which corresponds to a reduction in collected current. We also identified a low energy ion population originating from the cathode which was quickly excluded from the distribution as the potential hill forms and that peak ion energy scales linearly with the absolute discharge voltage.

The use of conical anode geometry also reduces the expansion of the plasma and neutrals from the orifice from a normally spherical to a conic expansion significantly increasing the downstream neutral density and subsequent ionization rate in the double layer again contributing to the lowering of the discharge voltage and increase of the local plasma potential. In spot mode where the ionization fraction generated within the cathode is sufficient support the collection of the discharge current passively at the anode surface, the conical geometry significantly increases the capacity of the anode to collect the electron current without the formation of a double layer.

The disappearance of the high energy ion signature at high flowrates is also something not reported in the literature. This also corresponds to low voltage operation with very low peak to peak voltage oscillations. We have proposed that this corresponds to a monotonic potential profile whereby few ions have the energy to overcome the potential and identifies true spot mode operation. In this case the natural thermal electron current to the anode is sufficient to supply the current demanded by power supply and a positive monotonic potential profile is maintained without the appearance of the double layer at the orifice exit hence the lack of the associated highly energy ions. The conventional definition of spot mode based on peak to peak voltage oscillations is therefore deemed insufficient.

Finally we have made a basic assessment of the estimated thrust level produced by these fast ions. We have shown that the production rate of high energy ions by ion acoustic/potential hill mechanism is too low to present usable thrust levels and is on the order of a few micro-Newtons. On the other hand we cannot discount these ions as source of thrust noise, particularly in a discharge with ionization instabilities whereby the ion production rate is not constant. A full model would be required to know if this mechanism can be utilized for thrust production in any significant way. Since the plasma hill region is reasonably downstream of the cathode it is difficult to foresee how it would be possible to accelerate all but a small fraction of the flow. Constriction of the flow to restrict expansion by using an enclosed conical anode would seem the most obvious way to increase utilization however we cannot state without a model the influence on the neutral flux.

7.5 NOVELTY AND SIGNIFICANCE OF THE WORK

A wide-ranging study has been conducted which is geared towards assessing the potential of hollow cathodes as microthrusters by assessing the limitations on maximum attainable performance, improving thrust efficiency to a practical level and gaining a deeper physical insight into the poorly understood thrust mechanisms and general hollow cathode phenomenon. Due to the range of applications of these devices, from primary electron sources in a variety of configurations to spacecraft charge control, the results of this work have wide ranging applicability.

Before the current work began, hollow cathode thrusters had already been considered as an RCS propulsion thruster by mission studies based on previous work on T6 cathode. However we have shown that the performance of this device was, and still remains, completely impractical for any reasonable mission based on thrust efficiencies <<1% and the thruster is entirely outclassed by other miniaturized electric propulsion systems. The only admirable performance parameter would seem to be moderately high specific impulse ~550s with argon and xenon.

Initially, improvement of the T6 cathode was sought, rightly by improving anode design to significantly reduce discharge voltage and decrease the minimum attainable mass flowrate. In doing so this work demonstrated an increase of nearly 100% in achievable T6 specific impulse. An energy flux analysis was performed and identified the source of efficiency loss in the T6 cathode as the convected electron thermal heat flux and recommended a move towards the lower current higher orifice current density T5 cathode. The T5 cathode with a conical anode demonstrated over 657s and 349s specific impulse with 4.5% and 8.1% thrust efficiency respectively. This improvement of over two orders of magnitude in thrust efficiency over the T6 has taken these thrusters a considerable step forward, for the first time demonstrating a viable propulsion technology.

A significant effort was also made to identify the thrust mechanisms responsible for such high propellant acceleration in hollow cathodes in a reasoned investigation of electrothermal, electromagnetic and electrostatic mechanisms. For the first time, the high electron pressure within the high plasma density orifice of hollow cathodes was identified as a possible explanation for such high electrothermal performance supported by analytical comparisons and empirical measurements of backpressure. Also for the first time, a hollow cathode was shown to operate beyond the critical ionization current and as such the T6 cathode can be expected to exhibit electromagnetic acceleration properties. Estimates of the force due to MHD acceleration agree well with measured thrust values however this mechanism was shown to be more interesting than useful as a means of thrust production.

Finally analysis of electrostatic energy measurements emitted from a conical hollow cathode may be able to conclude the long running disagreement over the creation mechanism of the high energy ion population either by potential hills or ion acoustic oscillations. Our data has shown the first clear evidence for *both* phenomenon, however in this case the potential hill is not likely to be the *cause* for ion creation but a *product* of intense ionization in the double layer formed downstream of the hollow cathode. It is in fact the intense local plasma potential oscillations in this double layer region which are the real cause of the ion energy population. It is also likely that the use of a conical anode significantly increases the potential hill creation process by increasing the neutral pressure in the high ionization region. Electrostatic mechanisms were eliminated as viable means of thrust production however they are likely to be a significant source of thrust noise in the micro-Newton range.

7.6 RECOMMENDATIONS FOR FUTURE WORK

The power and performance characteristics of the T5CA cathode would suggest that the application of standalone thrusters for small spacecraft and multiple thrusters for all-electric spacecraft would be well within the respective spacecrafts resource constraints. Furthermore due to the highly qualified state of these cathodes, development as flight hardware may present lessened qualification requirements.

For smaller spacecraft, which generally utilize inert gas propulsion systems, the addition of hollow cathode thrusters to existing architectures may also present reduced development requirements. In this respect it is recommended that the development of hollow cathode thrusters should continue however with the particular near-term objective of proving attainable efficiency well beyond that of other competitive thrusters in the milli-Newton range.

One of the main barriers to entry of hollow cathodes is acceptance by conservative commercial spacecraft manufacturers yet the commercial telecoms market in particular represents one of the main end users of an all-electric spacecraft enabling technology. It is therefore recommended that development continues with application on telecom satellites especially in mind. This means satisfying the potential design requirements for such an application. As yet no serious studies have been conducted in order to identify the needs of geostationary telecommunication satellites for such an application. This possibly represents the critical path in taking hollow cathodes forward as an all-electric spacecraft technology.

If the means by which the T5 cathode generates high ISP primarily relies on a high pressure thrust contribution due to electrons then dedicated design of a hollow cathode thruster with orifice geometry optimized to increase electron temperature while further decreasing discharge current, may present even greater improvements in thrust efficiency and ISP. Increasing orifice current density by the use of a smaller orifice will increase electron temperature by promoting Ohmic heating of electrons while increasing the ionization rate. A full numerical model is also required to support empirical comparisons in order to help identify thrust mechanisms and optimize cathode design.

Since MHD acceleration scales quadratically with discharge current while losses scale linearly, a hollow cathode thruster based on an MHD acceleration principle will always be of poor efficiency, hence MPD thrusters typically operate at many kilo-amps. A thruster based on this principle is therefore interesting however impractical. It is therefore recommended that the T6 hollow cathode and indeed other high current hollow cathodes move in an unsuitable direction with regard to hollow cathode thruster development.

Further improvements in the indirect thrust balance may be possible by thermally isolating or actively cooling the mounting equipment to reduce thermal drift. This way long term thrust measurements can be made to investigate the long term thrust stability. Redesign of the target to control particle paths to limit elastic collisions would also give more certainty in the accommodation factor which would also be beneficial. In the longer term, it is recommended that direct thrust measurements be made particularly of the T5 cathode in order to accurately characterize thrust and give the accommodation coefficient of the indirect balance. Measurements of downstream plasma parameters, in particular electron temperatures are also essential to firmly identify thrust mechanisms in combination with direct thrust measurements.

APPENDIX A

Cathode Wear Analysis

The voltage fluctuations found as part of the cathode discharge characteristics at high current and low mass flowrate are a cause of concern for cathode longevity. We have shown that discharge oscillations in both the T5 and T6 cathode are caused by ionization instabilities which can be defined as plume mode, although the characteristics differ considerably from the conventional terminology. These severe voltage fluctuations encourage energetic ion bombardment of the cathode resulting in sputtering and increase the probability of cathode-orifice clogging, cathode-orifice erosion, anode erosion due to direct-beam ion-impingement and energetic ion production due to plume-mode operation. Here we conduct a post-test analysis of the T5 cathode orifice plate using scanning electron microscopy.

Figure 128 clearly shows the sputter erosion patter across the orifice plate. Depth profiling reveals that the most severe sputter erosion has occurred within 500µm of the orifice and that the orifice face itself has recessed between 150-200µm. The outer 50% of the orifice plate diameter is shown to exhibit less surface modification with some of the surface showing a relatively unchanged surface with visible grain boundaries.

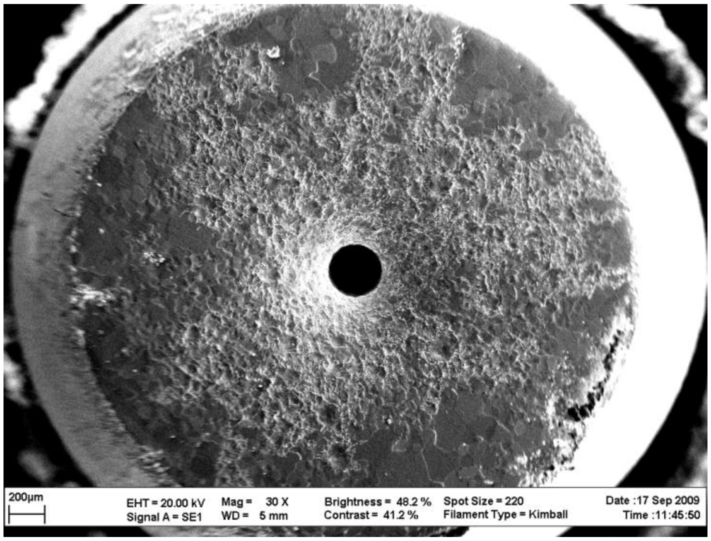

Figure 128 SEM image of the complete orifice plate at 30 x magnification

Figure 129 highlights the change in surface morphology with a view from the outer edge of the orifice plate to the outer edge of the orifice. One clear observation is that while sputter erosion occurs with increasing severity towards the orifice, deposition large particles and groups of particles is seen to mainly occur towards the outer edge of the orifice plate.

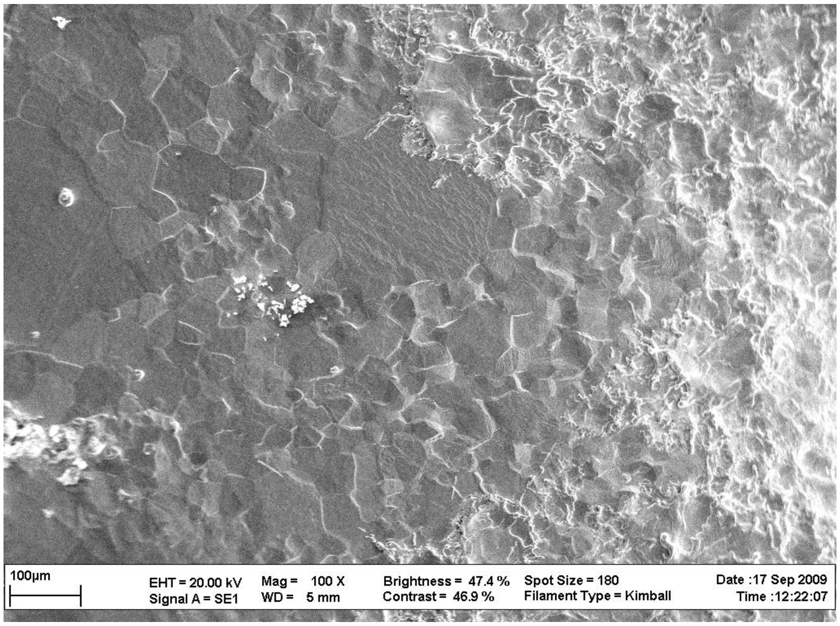

Figure 129 SEM image from the outer edge of the orifice plate (left) to the outer edge if the orifice (right) at 100X magnification

Closer inspection of the sputtered region also reveals the existence of sputter-induced ripple patterns and cone development typical of high temperature sputtering with surface diffusion. A detailed view of the ripple patterns is shown in Figure 130.

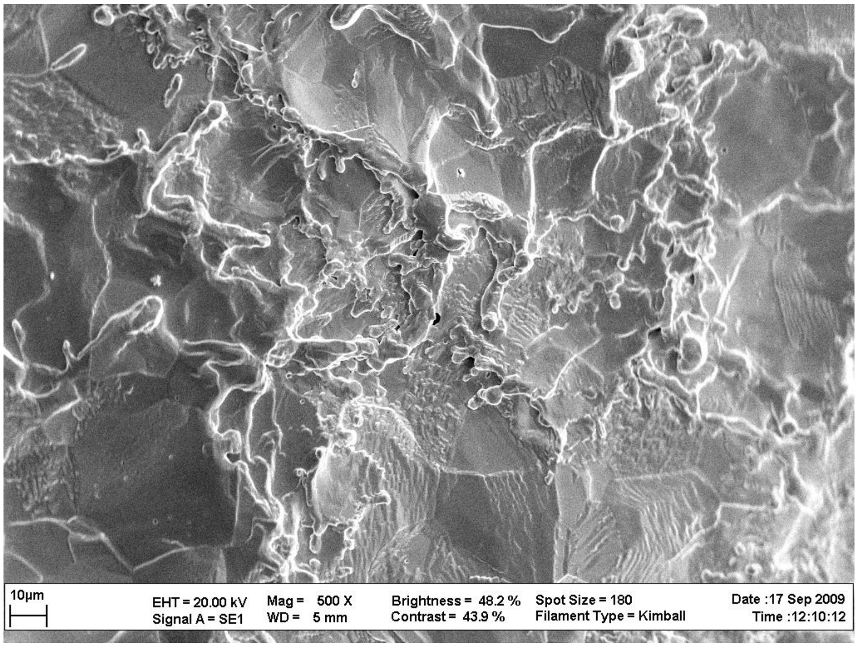

Figure 130 SEM image of an intensely sputtered region adjacent to the cathode orifice showing ripple pattern and cone formations at 500X magnification

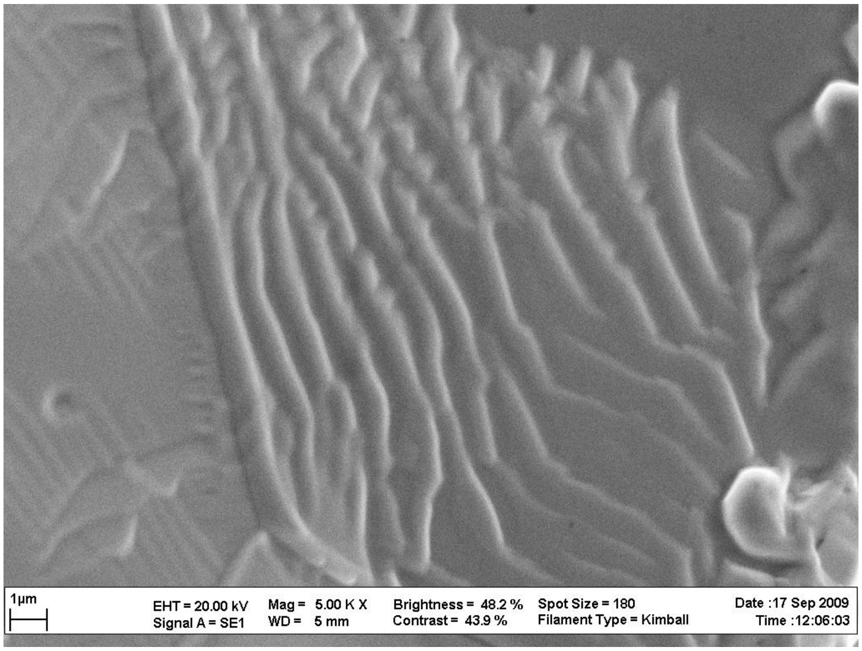

Figure 131 SEM image showing sputter ripple patterns as a result of surface diffusion at 500X magnification

Within the orifice there is also evidence of re-deposition of relatively large globules of sputtered material on the inner edge of the orifice walls. Such a pattern is shown in Figure 130 and in more detail in Figure 131. The particle was measured to be 4.3µm in diameter. Clogging of the orifice has been found to be more of a problem when cathodes are operated at low power for long periods. By the conclusion of the NSTAR 5700-hr THO segment, inspections revealed that the orifice was over 50% blocked however after extended operation at the higher TH15 power point for approximately 5000-hrs the deposits within the orifice were removed suggesting that the deposition mechanism is likely power-level dependent, specifically manifesting itself during low-power operation.[182] It is also worth noting that by the conclusion of the test, the periphery of the plate was only 28% of the BOL plate thickness.

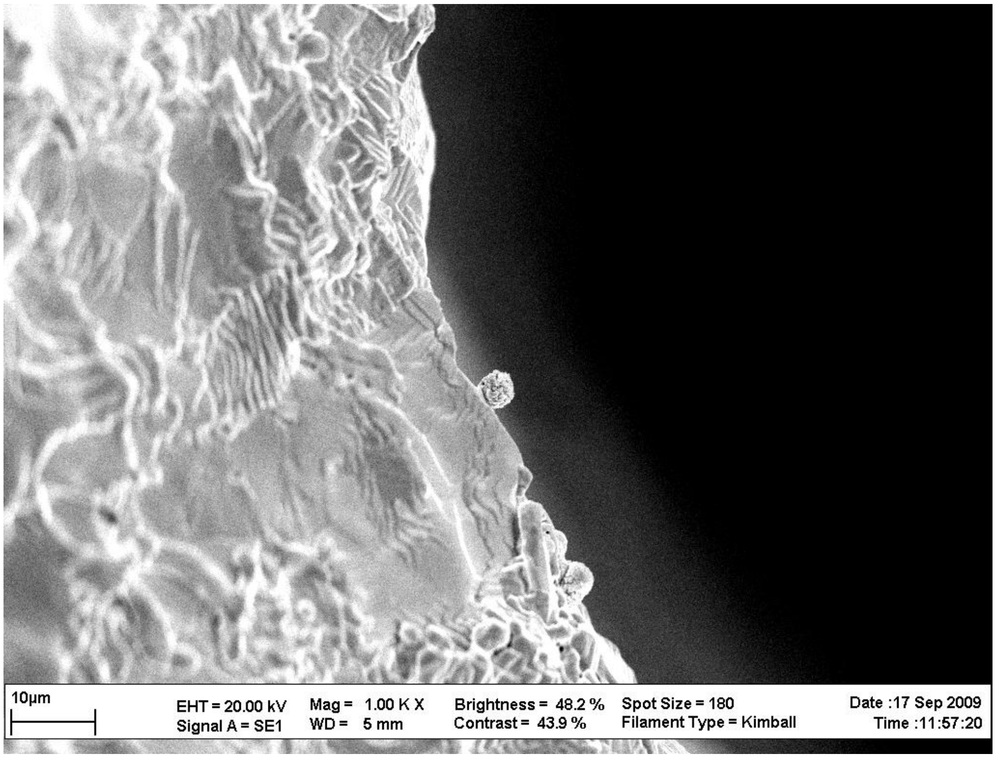

Figure 132 SEM image showing deposition of sputtered material within the orifice wall. Image also shows more evidence of sputter induced ripple formation on the orifice plate at 1000X magnification

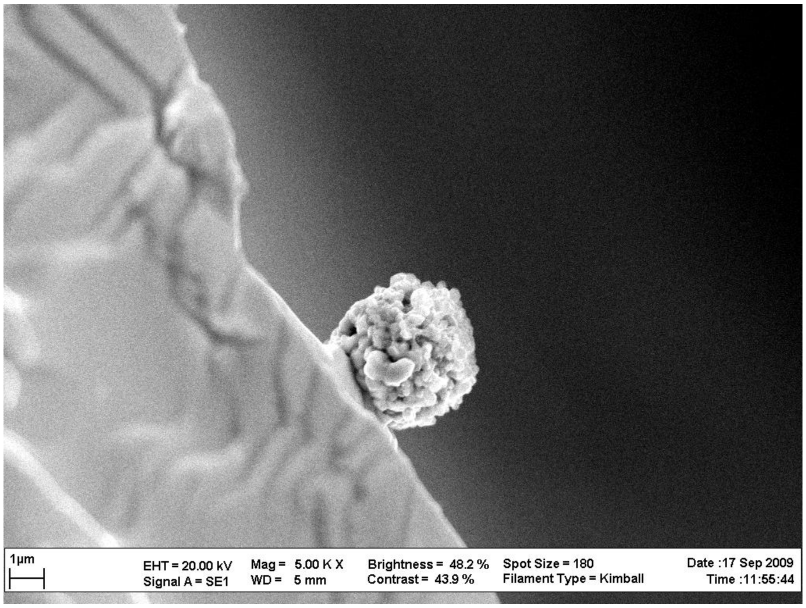

Figure 133 SEM image showing deposition of sputtered material within the orifice wall at 5000X magnification

The NSTAR ELT cathode showed extensive sputter erosion of the downstream keeper electrode where up to 47% of the wall thickness was removed. In addition to the net erosion, deposits of varying morphology were also found adhered to the interior of the cathode tube. Figure 132 and Figure 133 shows an image of large particles (20-40µm) adhered to the outer edge of the orifice plate with some smaller particles (5-10µm) located 100µm in towards the orifice in Figure 134.

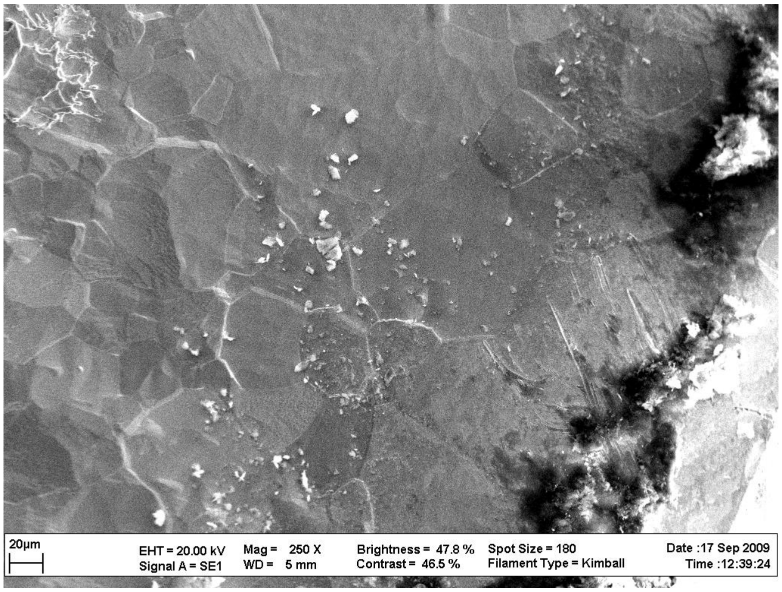

Figure 134 SEM image of large deposits on the outer edge of the orifice plate with some smaller particles towards the centre at 250X magnification

A backscattered electrons (BSE) technique was applied to the same sample area to attain an assessment of the chemical composition of the deposited particles. The BSE technique applies high-energy electrons originating in the electron beam, which are or back-scattered out of the specimen interaction volume by elastic scattering interactions with specimen atoms. Since heavy elements (high atomic number) backscatter electrons more strongly than light elements (low atomic number), and thus appear brighter in the image and we can identify areas with different chemical compositions. The result of the BSE techniques on the same sample area as in Figure 104 is shown in Figure 135. The affected area can also be observed at the edge of the cathode orifice plate in Figure 98.

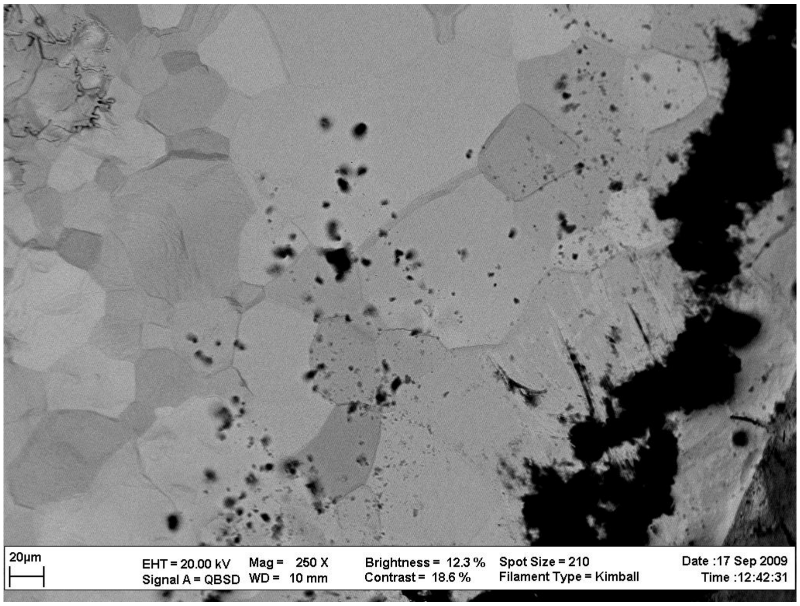

Figure 135 BSE technique applied to the outer edge of the orifice plate at 250X magnification. Dark regions represent areal of low atomic mass with lighter areas representing heavier elements

The technique is able to identify that the majority of particles on deposited on the orifice plate are of very low atomic number in comparison to the underlying molybdenum. In this case we can state that the deposited material must be carbon graphite sputtered from the anode electrode. The fact that these deposits are concentrated round the edge of the cathode suggests that the deposits are a phenomenon related to startup, since the orifice plate presents sharp outer edge located at the closest point to the anode. It is fair to assume that these deposits are therefore not a product of steady state operation but are related to use of a strike voltage to initiate startup. The use of a strike voltage to initiate startup should be given more consideration in future operation. The image also highlights the grain boundaries in the non-sputtered regions of the molybdenum plate.

Due to time constraints it was not possible to gain SEM images of the T6 cathode however a large scale image is shown in Figure 136. The image shows large quantities of sputter erosion to the cathode outer shield and also possibly indicates that the cathode orifice has significantly enlarged. The texture of the chamfer may also indicate that at some point the tip material may have come close to the melting temperature and thus formed a shiny surface appearance.

Figure 136 T6 discharge cathode tip post test image

REFERENCES

---

[1] Gray, H L, "*Development of ion propulsion systems*", *GEC Rev*, 12, 3, 154-168, 1997.

[2] Wallace N C and Fearn D G, "*The design and performance of the T6 ion thruster*", AIAA Paper 98-3342, Joint Propulsion Conference, 1998.

[3] Fearn D, Singfield A, Wallace N, Gabriel S and Harris P, "*The operation of ion thruster hollow cathodes using rare gas propellants*", AIAA Paper No. 90-2584, 21st International Electric Propulsion Conference, 1990.

[4] Latham P M, Martin A R, and Bond A, "*Design, manufacture and performance of the UK-25 engineering model thruster*", AIAA Paper 90-2541, Jul. 18-20, 1990, pp. 1-7

[5] Harris P T, and Gair S, "*A review of the cathode construction for the RAE 10/25 mN thruster*", International Electric Propulsion Conference, Paper No.88-078, 1988.

[6] Philip C M, and Fearn D G, "*Recent hollow cathode investigations at the Royal Aircraft Establishment*", AIAA paper 73-1137, (1973); AIAA Journal Vol. 12, No.10, 1974, pp.1319-25.

[7] Fearn D G, "*The operation of hollow cathodes under conditions suitable for ion beam neutralization*", Proceedings of the Conference on Electric Propulsion of Space Vehicles, Culham Laboratory, UK, (1973). Institute of Electrical Engineers Conference Publication 100, pp.146-150, 1973.

[8] Pottinger S, Gessini P, Webb D, Intini Marques R and Gabriel S B, "*Electric Propulsion Research at the University of Southampton*", Journal of the British Interplanetary Society, Vol. 59, No. 5, (2006)

[9] Gessini P, Gabriel S B and Fearn D G, "*Thrust Characterization of a T6 Hollow Cathode*", IEPC Paper 05-257, 29th International Electric Propulsion Conference, Princeton, NJ, 2005

---

[10] P. Gessini, S. B. Gabriel and D. G. Fearn, “*The T6 Hollow Cathode as a Microthruster*”, AIAA Paper 2005-4078, 41st AIAA/ASME/SAE/ASEE Joint Propulsion Conference & Exhibit, Tucson, AZ, 2005

[11] Walker R, *“The SIMONE Mission: low-cost Exploration of the Diverse NEO Population via Rendezvous with Microsatellites”*, IAC-03-Q.5.05 54th International Astronautical Congress of the International Astronautical Federation, 2003

[12] Rayman M D, and Lehman D H, *“NASA’s First New Millennium Deep-Space Technology Validation Flight,”* Second IAA International Conference on Low-Cost Planetary Missions, Laurel, MD, 1996

[13] Bodin P, Berge S, Bjork M, Edfors A, Kugelberg J and Rathsman P, “*The SMART-1 Attitude and Orbit Control System: Flight Results from the First Mission Phase*”, AIAA-2004-5244 AIAA Guidance, Navigation, and Control Conference and Exhibit, Providence, Rhode Island, 2004

[14] Kuninaka H, Shimizu Y, Yamada T, Funaki I and Nishiyama K, ”*Flight Report During Two Years on HAYABUSA Explorer Propelled by Microwave Discharge Ion Engines”*, AIAA-2005-3673, 41st AIAA/ASME/SAE/ASEE Joint Propulsion Conference and Exhibit, Tucson, Arizona, 2005

[15] Rayman, M D, Fraschettia T C, Raymonda C A, Russell C T, “*Preparing for the Dawn Mission so Vesta and Ceres”*, IAC-05-A3.5.B.011, 56th International Astronautical Congress, Fukuoka, Japan, 2005

[16] Moerel J, Marée T, Bombelli V, Simon D, “*Economic Benefits of the Use of Non-Toxic Mono-Propellants for Spacecraft Applications*”, AIAA-2003-4783 39th AIAA/ASME/SAE/ASEE Joint Propulsion Conference and Exhibit, Huntsville, Alabama, 2003

[17] Gessini P, “*Hollow Cathode Thrust Measurements Using a Target”*, PhD Thesis, University of Southampton, Southampton, UK, 2007

[18] Finke R C, *“Electric Propulsion and Its Applications to Space Missions”*, Progress in Astronautics and Aeronautics, Vol. 79, AIAA, (1981)

[19] Jahn R G, “*Physics of Electric Propulsion*”, McGraw-Hill, New York, 1968

[20] Moss J B, “*Propulsion Systems*”, ed. Fortescue P and Stark J, Spacecraft Systems Engineering, 2nd ed. J. Wiley & Sons, 1995, UK, pp.171-180

---

[21] Sackheim R L, Wolf R S, Zafran S, "*Space Propulsion Systems*", Space Mission Analysis & Design, 2nd ed., eds. W. J. Larson & J. R. Wertz, , pp.644-645, 653-655 (1992)

[22] Stuhlinger E, "*Ion Propulsion for Space Flight*", McGraw-Hill, New York, (1964)

[23] Patterson M J, and Rawlin VK, "*Derated Ion Thruster Design Issues*," IEPC Paper No. 91-150 (1999)

[24] Fearn D G, "Economical remote sensing from a low altitude with continuous drag compensation", Acta Astronautica, Volume 56, Issue 5, pp.555-572, (2005)

[25] Patterson M J, and Foster J E, "*Performance and Optimization of a 'Derated' Ion Thruster for Auxiliary Propulsion*," AIAA-91-2350 (1991)

[26] Wirz R "Discharge Plasma Processes *of Ring-Cusp Ion Thrusters*", Ph.D. Thesis, California Institute of Technology (2005)

[27] Young M, Muntz E P, Ketsdever A D and Wadsworth D C, "*Unique Hollow Cathode as a Code Validation Experiment and Candidate Non-Magnetic Ion Micro-Thruster*," AIAA-99-2854, 35th AIAA/ASME/SAE/ASEE Joint Propulsion Conference and Exhibit, 1999

[28] Crofton M W, "*The Feasibility of Hollow Cathode Ion Thrusters: A Preliminary Characterization*," AIAA-2000-5354, 36th AIAA/ASME/SAE/ASEE Joint Propulsion Conference and Exhibit, 2000

[29] Crofton M W and Boyd I D, "*Plume Measurement and Modeling Results for a Hollow Cathode Micro-Thruster*," AIAA-2001-3795, 37th AIAA/ASME/SAE/ASEE Joint Propulsion Conference and Exhibit, 2001

[30] Patterson M J, and Foster J E, "*Hollow Cathode Micro-Thruster Performance*," IEPC-01-226, 27th International Electric Propulsion Conference, 2001

[31] Morozov A I and Savelyev V V, "*Fundamentals of stationary plasma thurster theory*," Reviews of Plasma Physics, edited by B.B. Kadomtsev and V.D. Shafranov, Vol. 21, Consultants Bureau, New York, 2000, pg. 203.

[32] Khayms V and Martinez-Sanchez M, "*Fifty-Watt Hall thruster for microsatellites*," Micropropulsion for Small Spacecraft, edited by Micci M M and Ketsdever A D, Vol. 187, Progress in Astronautics and Aeronautics, AIAA, Reston, VA, , pp. 233-254 (2000)

---

[33] Raitses Y and Fisch N J, “*Parametric investigations of a nonconventional Hall thruster*,’ Physics of Plasmas, Vol. 8, No. 5, pp. 2579-2586. (2001)

[34] Smimov, A., Raitses, Y., and Fisch, N.J., “*Parametric investigations of a miniaturized cylindrical and annular Hall thrusters*” Journal of Applied Physics, Vol. 92, No. 10, pp. 5673-5679 (2002)

[35] Warner N Z and Martínez-Sánchez M, ‘*Design and Preliminary Testing of aMiniaturized TAL Hall Thruster*,” AIAA 2006-4994, 42nd AIAA/ASME/SAE/ASEE Joint Propulsion Conference & Exhibit, , Sacramento, California, 2006

[36] Ito T, Gascon N, Crawford W and Cappelli M “Further Development of a Micro Hall Thruster”, AIAA-2006-4495, 42nd Joint Propulsion Conference, Sacramento, CA, 2006

[37] Jankovsk R S, Sankovic J M, Oleson S, “*Performance of a FAKEL K10K resistojet*”, AIAA-1997-3059, 33rd AIAA/ASME/SAE/ASEE Joint Propulsion Conference and Exhibit, Seattle, WA, 1997

[38] Coxhill I, Gibbon D,“*A Xenon Resistojet Propulsion System for Microsatellites*”, AIAA-2005-4260, 41st AIAA/ASME/SAE/ASEE Joint Propulsion Conference and Exhibit, Tucson, Arizona, 2005

[39] Gessini P, Gabriel S B and. Fearn D G, “*The T6 Hollow Cathode as a Microthruster*”, AIAA Paper 2005-4078, 41st AIAA/ASME/SAE/ASEE Joint Propulsion Conference & Exhibit, Tucson, AZ, 2005

[40] Baker A M, Da-Silva-Curiel A, Schaffner J, Sweeting M, “*Advanced Low Cost Propulsion Concepts for Small Satellites Beyond LEO*”, IAC Paper No. 04-IAF-S.1.08, 2004

[41] Manzella D H, Curran F M, and Zube D M, "*Preliminary Plume Characteristics of an Arcjet Thruster*," AIAA Paper No. 90- 2645 (1990)

[42] Inter-Agency Space Debris Coordination Committee, Space Debris Mitigation Guidelines, IADC 02-01 (2002)

[43] Rayman M D, Fraschettia T C, Raymonda C A, Russell C T, “*Preparing for the Dawn Mission so Vesta and Ceres*”, IAC-05-A3.5.B.011, 56th International Astronautical Congress, , Fukuoka, Japan, 2005

[44] Moerel J, Marée T, Bombelli V., Simon D, “*Economic Benefits of the Use of Non-Toxic Mono-Propellants for Spacecraft Applications*”, AIAA-2003-4783 39th AIAA/ASME/SAE/ASEE Joint

---

Propulsion Conference and Exhibit, Huntsville, Alabama, 2003

[45] Mueller J, “*Thruster Options for Microspacecraft” from “Micropropulsion for Small Spacecraft*” Volume 187, Progress in Astronautics and Aeronautics.

[46] Coletti M, Grubisic A, Wallace N, Wells N, “*European Student Moon Orbiter Solar Electric Propulsion Subsystem Architecture – An All–Electric Spacecraft*” IEPC-2007-111, 30th International Electric Propulsion Conference, Florence, Italy, 2007

[47] Walker R, “*The SIMONE Mission: low-cost Exploration of the Diverse NEO Population via Rendezvous with Microsatellites*”, IAC-03-Q.5.05, 54th International Astronautical Congress of the International Astronautical Federation, 2003

[48] Csiky G A, "*Investigation of a Hollow Cathode Discharge Plasma*," AIAA- 69-258, 7th AIAA Electric Propulsion Conference, 1969

[49] Philip C M, "*A Study of Hollow Cathode Discharge Characteristics*," *AIAA Journal*, Vol. 9, pp. 2191-2196 (1971)

[50] Fearn D G and Philip C M, "*An Investigation of Physical Processes in a Hollow Cathode Discharge*," AIAA Journal, Vol. 11, pp. 131-132, (1973)

[51] Krishnan M, Jahn R G, Jaskowsky W F and Clark K E, "*Physical Processes in Hollow Cathodes*," AIAA Journal, Vol. 15, pp. 1217-1223,(1977)

[52] Siegfried D E and Wilbur P J, "*Studies on an Experimental Quartz Tube Hollow Cathode*," AIAA-79-2056, Princeton University/AIAA/DGLR 14th International Electric Propulsion Conference, 1979

[53] Siegfried D E and Wilbur P J, "*An Investigation of Mercury Hollow Cathode Phenomena*," AIAA-78-705, 13th AIAA/DGLR International Electric Propulsion Conference, 1978

[54] Rehn L, and Kaufman H R, "*Correlation of Inert Gas Hollow Cathode Performance*," AIAA-78-707, 13th AIAA/DGLR International Electric Propulsion Conference, 1978

[55] Csiky G A, "*Investigation of a Hollow Cathode Discharge Plasma*," AIAA- 69-258, AIAA 7th Electric Propulsion Conference, 1969

---

[56] Csiky G A, "*Measurements of Some Properties of a Discharge from a Hollow Cathode*," NASA TN D-4966, 1969

[57] Csiky G A, "*Langmuir Probe Measurements in a Discharge from a Hollow Cathode*," Journal of Spacecraft and Rockets, Vol. 7, pp. 474-475 (1970)

[58] Jack T M, Patterson S W, and Fearn D G, "*The Effect of the Keeper Electrode on Hollow Cathode Characteristics*," AIAA-2000-3533, 36th AIAA/ASME/SAE/ASEE Joint Propulsion Conference and Exhibit, 2000

[59] Patterson S W and Fearn D G, "*The Generation of High Energy Ions in Hollow Cathode Discharges*," IEPC-99-125, 26th International Electric Propulsion Conference, 1999

[60] Fearn D G and Patterson M J, "*The Compatibility of Hollow Cathode Characteristics with a Variety of Ion Thruster Designs*," IEPC-99-133, 26th International Electric Propulsion Conference, 1999

[61] Fearn D G, and Patterson S W, "*Characterization of the High Current Hollow Cathode for the T6 Ion Thruster*," AIAA-98-3346, AIAA/ASME/SAE/ASEE 34th Joint Propulsion Conference and Exhibit, 1998

[62] Patterson S W, Malik A K, and Fearn D G, "*Noise and Oscillatory Disturbances in the T6 Ion Thruster Hollow Cathode*," AIAA-99-2577, 35th AIAA/ASME/SAE/ASEE Joint Propulsion Conference and Exhibit, 1999

[63] Patterson S W, "*Discharge Physics and Associated Phenomena in an Ion Thruster Type Hollow Cathode*," PhD Thesis, Imperial College (2003)

[64] Fearn D G, and Patterson S W, "*The Hollow Cathode - a Versatile Component of Electric Thrusters*," ESA SP-465, ESA/CNES International Conference on Spacecraft Propulsion, 2000

[65] Polk J E, Anderson J R, Brophy J R, Rawlin V K, Patterson M J, Sovey J and Hamley J, "*An Overview of the Results from an 8200 Hour Wear Test of the NSTAR Ion Thruster*" AIAA 99-2446, 35th Joint Propulsion Conference, Los Angeles, CA, 1999

[66] Personal communication with David Fearn. January, 2006

[67] Malik, A K and Fearn D G, "*A study of the physics of hollow cathode discharges*", IEPC Paper 93-026 (1993)

---

[68] Chanda S, Mawdsley F, Brown R D, Watson S D, Malik A K and Fearn D G, "*Measurements of the electromagnetic emissions from the T5 ion thruster*", IEPC Paper 93-234 (1993)

[69] Fearn D G, "*The operation of hollow cathodes under conditions suitable for ion beam neutralisation*", Proc. Conf. on Electric Propulsion of Space Vehicles, Culham Laboratory, UK, (April 1973). Inst of Electrical Engineers Conference Publication 100, pp 146-150, 1973

[70] Fearn D G. Martin A R, and Smith P, "*Ion propulsion development in the UK*". AIAA Paper 93-2603 (1993)

[71] Siegfried D E, "*A Phenomenological Model for Orificed Hollow Cathodes*", Ph.D. Dissertation, Colorado State University, 1983

[72] Salhi A, "*Theoretical and Experimental Studies of Orificed, Hollow Cathode Operation*", Ph.D. Dissertation, Ohio State University, 1993

[73] Rawlin V K, and Pawlik E V, "*A Mercury Plasma-Bridge Neutralizer*," Journal of Spacecraft and Rockets, Vol. 5, No. 7, pp. 814-820 (1968)

[74] Ferreira C M and Delcroix J L, "*Theory of the Hollow Cathode Arc*," Journal of Applied Physics, Vol. 49, No. 4, pp. 2380-2395 (1978)

[75] Sarver-Verhey T R, "*Destructive Evaluation of a Xenon Hollow Cathode After a 28,000 Hour Life Test*," NASA/CR—1998-208678

[76] Fearn D G, and Philip C M, "*An Investigation of Physical Processes in a Hollow Cathode Discharge*," AIAA Paper No. 72-416, AIAA 9th Electric Propulsion Conference, Bethesda, MD, 1972

[77] Rehn L A, "*Argon Hollow Cathode*," NASA CR-135102, 1976

[78] Rehn L, and Kaufman H R, "*Correlation of Inert Gas Hollow Cathode Performance*," 13th AIAA/DGLR International Electric Propulsion Conference, San Diego, CA, 1978

[79] Rawlin V K, "*Operation of the J-Series Thruster Using Inert Gas*," NASA Technical Memorandum 82977, 1982

---

[80] Capacci M, Minucci M, and Severi A, "*Simple Numerical Model Describing Discharge Parameters in Orificed Hollow Cathode Devices*," AIAA Paper No. 97-2791 (1997)

[81] Cirri G F, "*Review of Qualification Activities on the Neutralizer for the RIT 10 Ion Thruster*," IEPC Proc, Vol. 2, pp. 1015-1022 (1993)

[82] Domonkos M, "*Evaluation of Low-Current Orificed Hollow Cathodes*," Ph.D. Thesis, University of Michigan, 1999

[83] Domonkos M, "*An Evaluation of Hollow Cathode Scaling to Very Low Power and Flow Rate*," IEPC Paper No. 97-189 (1997)

[84] Domonkos M, "Low-Current Hollow Cathode Evaluation," AIAA Paper No.99-2575 (1999)

[85] Siegfried D E, "*A Phenomenological Model for Orificed Hollow Cathodes"*, Ph.D. Dissertation, Colorado State University, 1983

[86] Kaufman H R, "*Technology of Electron Bombardment Ion Thruster*," in Advances in Electronics and Electronic Physics, Vol. 36, Academic Press, New York, , pp. 265-373 (1974)

[87] Siegfried D E, and Wilbur P J, "*A Phenomenological Model Describing Orificed Hollow Cathode Operation*," AIAA Paper No. 81-0746 (1981)

[88] Siegfried, D.E. and Wilbur, P.J., "*A Model for Mercury Orificed Hollow Cathodes: Theory and Experiment*," *AIAA Journal*, Vol. 22, No. 10, Oct. 1984, pp. 1405-1412

[89] Turchi, P. J., Salhi, A., "*Low Power Plasma Thrusters Based On Hollow Cathode Discharge*", 30th AIAA/ASME/SAE/ASEE Joint Propulsion Conference, Indianapolis, 1994

[90] Domonkos M T, Patterson M J, Gallimore A D, "*Low-Current, Xenon Orificed Hollow Cathode Performance for In-Space Applications* NASA Center for AeroSpace Information (CASI) NASA/TM-2002-211574; NAS 1.15:211574, 2002

[91] Domonkos, T A, "*Particle and Energy Balance Model of the Orificed Hollow Cathode*" AIAA 2002-4240, 38th Joint Propulsion Conference and Exhibit, Indianapolis, IN, United States, 2002

---

[92] Salhi A and Turchi P J, "*Scaling Relations for Design and Operation of Orificed Hollow Cathodes*," AIAA Paper No. 94-3133, 30th AIAA Joint Propulsion Conference, Indianapolis, IN, 1994

[93] Salhi, A. and Turchi, P.J., "*Theoretical Modeling of Orificed, Hollow Cathode Discharges*," Proceedings of the 23rd International Electric Propulsion Conference, Vol. 1, 1993, pp. 253-260

[94] Snyder A and Banks B A, "*Thrust Measurements of a Hollow-Cathode Discharge*," NASA TN D-6705, 1972

[95] Grubisic A N, "*Temperature Characterization and Optimization of an NSTAR Discharge Cathode for the Deep Space-1 Gridded Ion-Engine*" Masters Thesis, International Space University, Strasbourg, France 2005

[96] Compton K T, "*On the Theory of the Mercury Arc*," Physical Review, Vol. 37, pp. 1077-1090 (1931)

[97] Tanberg R, "*On the Cathode of an Arc Drawn in Vacuum*," Physical Review, Vol. 35, , pp. 1080-1089 (1930)

[98] Rawlin V K, "*Internal Erosion Rates of a 10-kW Xenon Ion Thruster*," AIAA-88-2912, AIAA/ASME/SAE/ASEE 24th Joint Propulsion Conference and Exhibit, 1988

[99] Kameyama I and Wilbur P J "*Zenith-Angle Distributions of Erosion Rates near High-Current Hollow Cathodes*". AIAA 96-3208, 32nd Joint Propulsion Conference, Lake Buena Vista, FL 1996

[100] Latham P M, Pearce A J, and Bond R A, "*Erosion Processes in the UK-25 Ion Thruster"*. IEPC 91-096, 22nd International Electric Propulsion Conference, Viareggio, Italy, 1991

[101] Friedly V and Wilbur PJ "*High Current Hollow Cathode Phenomena*" Journalof Propulsion and Power, 8(3):635–643 (1992)

[102] Kameyama I, and Wilbur P J, "*Measurements of Ions from High-Current Hollow Cathodes Using Electrostatic Energy Analyzer*". Journal of Propulsion and Power, 16(3):529–535 (2000)

[103] William G, Smith T, Domonkos M, Shand K, and Gallimore A, "*Laser Induced Fluorescence Characterization of Ions Emitted from a Hollow Cathode*," AIAA Paper No. 99-2862 *(*1999)

---

[104] Patterson S W, and Fearn D G, "*The Generation of High Energy Ions in Hollow Cathode Discharges*," IEPC-99-125, 26th International Electric Propulsion Conference, 1999

[105] Patterson S W, "*Discharge Physics and Associated Phenomena in an Ion Thruster Type Hollow Cathode*," PhD Thesis, Imperial College, 2003.

[106] Kameyama I and P. J. Wilbur, "*Characteristics of ions emitted from high-current hollow cathodes*," IEPC-93-023, Proc. 23rd Int. Electric Propulsion Conf. 1993

[107] Kameyama I, "*Effects of Neutral Density on Energetic Ions Produced Near High-Current Hollow Cathodes*," NASA CR-204154, 1997

[108] Katz I, Mikellides I G, Goebel D M, Jameson K K, Wirz R and Johnson L K, "*Production of High Energy Ions Near an Ion Thruster Discharge Hollow Cathode*," AIAA Paper 06-4485 (2006)

[109] Gallimore A D, Rovey J L and Herman D. A, "*Erosion Processes of the Discharge Cathode Assembly of Ring-Cusp Gridded Ion Thrusters*," Journal of Propulsion and Power, Vol. 23, No. 6, pp. 1271–1278 (2007)

[110] Williams G J, Domonkos, M T and Chavez J M, "*Measurement of Doubly Charged Ions in Ion Thruster Plumes*," International Electric Propulsion Conference Paper 01-310, 2001

[111] Foster J E, and Patterson M J, "Downstream Ion Energy Distributions in a Hollow Cathode Ring Cusp Discharge," Journal of Propulsion and Power, Vol. 21, No. 1, pp. 144–151 (2005)

[112] Goebel D M, Jameson K K, Katz I, and Mikellides I G, "*Energetic Ion Production and Electrode Erosion in Hollow Cathode Discharges*," International Electric Propulsion Conference Paper 05-269, 2005

[113] Crofton M W, "*The Feasibility of Hollow Cathode Ion Thrusters: A Preliminary Characterization*" AIAA 2000-3273, 36th Joint Propulsion Conference, Huntsville, AL, 2000

[114] Sengputa A, "*Destructive Physical Analysis of Hollow Cathodes from the Deep Space 1 Flight Spare Ion Engine 30,000Hr Life Test*". 29th International Electric Propulsion Conference, IEPC-2005-026, 2005

[115] Crofton M W, and Boyd I D, "*Plume Measurement and Modeling Results for a Xenon Hollow Cathode*," AIAA-2002-4103, 38th Joint Propulsion Conference, 2002

---

[116] Davis W D, and Miller H C, "*Analysis of the Electrode Products Emitted by DC Arcs in a Vacuum Ambient*," J. Appl. Phys, Vol. 40, No. 5, , pp. 2212-2221 (1969)

[117] Williams J D and Wilbur P J, "*Electron Emission from a Hollow Cathode-Based Plasma Contactor*," J. of Spacecraft and Rockets, Vol. 29, No. 6, pp.820-829 (1992)

[118] Kameyama, I., and P.J. Wilbur, "Measurement of Ions from High-Current Hollow Cathodes Using Electrostatic Energy Analyzers," J. of Propulsion and Power, Vol. 16, No. 3, 2000, pp. 529-535.

[119] Swift PD, "Cathode- and Anode-Spot Tracks in a Closed Magnetic Field," J. Appl. Phys, Vol.67, No.4, pp. 1720-1724 (1990)

[120] Rusteberg C M, Lindmayer B, Juttner and Pursch H, "*On the Ion Energy Distribution of High Current Arcs in Vacuum*," IEEE Trans. on Plasma Science, Vol. 23, No. 6, pp. 909-914 (1995)

[121] Foster J E and Patterson M J, "*Plasma Emission Characteristics from a High Current Hollow Cathode in an Ion Thruster*," AIAA-2002-4102, 38th Joint Propulsion Conference, 2002

[122] Casey C, Farnell J, Williams D, and Wilbur P J, "*Characteristics of Energetic Ions Emitted from Hollow Cathodes"* IEPC-03-072 at the 28th Int'l Electric Propulsion Conf., Toulouse, France, 2003

[123] Przybylowski J N, Polk J E, "*Dependence of the Energetic Ion Distribution on Propellant Composition in Hollow Cathodes*" AIAA 2007-5169, 43rd AIAA/ASME/SAE/ASEE Joint Propulsion Conference, 2007

[124] Herman D and Gallimore A, "*Near discharge cathode assembly plasma potential measurements in a 30-cm NSTAR type ion Engine*", AIAA Paper 2004-3958, 40th Joint Propulsion Conference, Ft. Lauderdale, FL, 2004

[125] Jameson K, Goebel DM, Watkins R, "*Hollow cathode and keeper region plasma measurements*", AIAA Paper 2005- 3667, 41th Joint Propulsion Conference, Tucson, AZ, 2005

[126] Sengupta A, "*Experimental investigation of discharge plasma magnetic field confinement in an NSTAR thruster*", AIAA Paper 2005-4069, 41th Joint Propulsion Conference, Tucson, AZ, 2005

[127] Goebel D M, Jameson K, Katz I, Mikellides I, Polk J, "*Energetic Ion Production and Keeper Erosion in Hollow Cathode Discharges*" IEPC-2005-266, 29th International Electric Propulsion Conference, Princeton University, 2005

---

[128] Goebel D M, Jameson K, Watkins R, Katz I, "*Hollow Cathode and Keeper-Region Plasma Measurements Using Ultra- Fast Miniature Scanning Probes*" AIAA Paper 2004-3430, 40th Joint Propulsion Conference, Ft. Lauderdale, FL, 2004

[129] Cronin, J L, "*Modern Dispenser Cathodes*" IEEE Proc. 128, 19–32 (1981)

[130] Fridman A, Kennedy L A, "Plasma Physics & Engineering" CRC Press; 1 edition, 2004

[131] Simmons J G, "*Richardson-Schottky Effect in Solids*", Physical Review Letters, Vol. 15, No.25, pp. 967-968 (1965)

[132] Willinst D J, and Boyd R, "*A study of the electron emission processes in a hollow cathode discharge*", J. Phys. D: Appl. Phys., Vol. 6 (1973)

[133] Martin R, "*Atomic Excitation Processes in the Discharge of Rare Gas Ion-Engines*," J. Phys. Atom. Molec. Phys., Vol. 7, No. 10 (1974)

[134] Katz I, Mikellides I G, Goebel D M, Polk J E, "*Plasma Heating of Inert Gas hollow Cathode Inserts*", IEPC-2007-017, 30th International Electric Propulsion Conference, Florence, Italy, 2007

[135] Crofton M, Boyd I D, "*Plume Measurement and Modelling Results for a Hollow Cathode Micro-Thruster*," AIAA Paper No. 2001-3795 (2001)

[136] Patterson M J, Foster J E, "Performance Testing of a Hollow Cathode Microthruster" IEPC-01-226, 27th International Electric Propulsion Conference, Pasadena, CA, 15-19 October, 2001

[137] Polk J E, Grubisic A N, Goebel D, "*Emitter Temperature Distributions in the NSTAR Discharge Hollow Cathode*" AIAA-2005-4398, 41st AIAA/ASME/SAE/ASEE Joint Propulsion Conference, Tucson, AZ, 2005

[138] Sarver-Verhey T R, "*28,000 Hour Xenon Hollow Cathode Life Test Results*," IEPC Paper No. 97-168 (1997)

[139] Rawlin V K, "*A 13,000 Hour Test of a Mercury Hollow Cathode*," NASA TM X-2785 (1973)

[140] Mandell M J and Katz I, "*Theory of Hollow* Cathode *Operation in Spot and Plume Modes*," AIAA.

Paper No. 94–3134, 30th AIAA/ASME/SAE/ASEE Joint Propulsion Conference, 1994

[141] Pottinger S J and Gabriel S B, IEPC-2001-182, Int. Electric Propulsion Conf, 2003

[142] Malik, A K, Montarde P, Haines MG, “*Spectroscopic measurements on xenon plasma in a hollow cathode*”, J App. Phys. Vol 33, pp2037–2048, 2000

[143] Mikellides I, Katz I, Goebel D M, Polk J E, “*Theroretical Model of a Hollow Cathode Plasma for the Assesment of Insert and Keeper Lifetimes*”, 41st AIAA Joint Propulsion Conference, Arizona, 2005

[144] Goebel D M, Jameson K K, Katz I and Mikellides I, "*Potential fluctuations and energetic ion production in hollow cathode discharges*", Phys. Plasmas, Vo1.l4, 103508 (2007)

[145] Riethof T R, Acchione B D, Branyan E R, ‘*High-Temperature Spectral Emissivity Studies on Some Refractory Metals and Carbides*.’ Temperature; Its Measurement and Control in Science and Industry, Volume Three. Charles M. Herzfeld, Editor in Chief. Part 2, Applied Methods and Instruments, edited by A. I. Dahl. With the cooperation of the American Institute of Physics, the Instrument Society of America, and the National Bureau of Standards. Published by Reinhold Publishing Corp., London, 1962, p. 515

[146] Deltschew R, Tartz M V, Plicht E, Hartmann H, Neumann H.J, Leiter J, Esch L, “*Sputter characteristics of carboncarbon compound material”*, Paper IEPC-01-118, 27th Int. Electric Propulsion Conf., Pasadena, CA, 2001

[147] Williams J, Gardner M, Wilbur P, “*Xenon sputter yield measurements for ion thruster materials”*, IEPS paper IEPC-03-130, 28th Int. Electric Propulsion Conf, Toulouse, March, 2003

[148] Leiter L, “*The "New Grid Systems for Ion Engines" Technology Project - Results and Conclusions*”, IEPC 2005-132, 29th Int. Electric Propulsion Conf., 31.10.-4.11, Princeton, 2005

[149] Tartz M, Hartmann E, Neumann H, “*Evolution of extraction grid erosion with operation time”*, AIAA-2004-3787, 40th Joint Propulsion Conference, Fort Lauderdale, FL, 2004

[150] Katz I, Mandell M J, Patterson M and Domonkos M 1999 *AIAA-99-2576, 35th AIAA/ASME/SAE/ASEE Joint Propulsion Conf. and Exhibits*

[151] Domonkos M T, Gallimore A D, Williams G J and Patterson M J, AIAA-99-2575, 1999

---

[152] Rashkovan V M *J. Phys. D: Appl. Phys.* 38 2817-2824 (2005)

[153] Malik A K, Monterde M P and Haines *J. Phys. D: Appl. Phys.* 33 2037 (2000)

[154] V M Rashkovan *et al* 2005 *J. Phys. D: Appl. Phys.* 38 2817-2824

[155] Mikellides I G, Katz I, Goebel D M, Polk J E, and Jameson, K K, "*Evidence of Non-Classical Plasma Transport in Hollow Cathodes for Electric Propulsion*," Journal of Applied Physics, Vol. 101, No. 6, p. 063301. doi:10.1063/1.2710763 (2007)

[156] Spitzer L Jr, "*Physics of Fully ionized Gases"*. Interscience Publishers Inc. New York, 1956

[157] Jack T M, "*The characterization of the STRV small satellite charge alleviation cathode*", Proc Third Workshop on Transient Hollow Cathode Discharge Phenomena, Paris, September 1994

[158] Crofton MW, "*Evaluation of the United Kingdom Ion Thruster*" J. Spacecraft and Rockets, Vol. 33, No. 5, pp. 739-747 (1996)

[159] Edwards C H, "Discharge *Characteristics and Instabilities in the UK-25 Ion Thruster Operating on Inert Gas Propellants*" PhD. Thesis, University of Southampton, 1997

[160] Marhold K, Tajmar M, "*Micronewton Thrust Balance for Indium FEEP Thrusters"* AIAA-2005-4387, 41st AIAA/ASME/SAE/ASEE Joint Propulsion Conference and Exhibit, Tucson, Arizona, 2005

[161] Gamero-Castaño M, Hruby V, "*Using a Torsional Balance to Characterize Thrust at Micro-Newton Levels*", AIAA 2003-4537, 39th AIAA/ASME/SAE/ASEE Joint Propulsion Conference and Exhibit, Huntsville, Alabama, 2003

[162] Ziemer J K, "*Performance measurements using a sub-microNewton resolution thrust stand*" IEPC-01-238, Proc. 27th Int.Electric Prop. Conf. Pasadena, CA, 2001

[163] Wiederick H H, Gauthier N, Campbell D A, and Rochon P, "*Magnetic Braking: Simple Theory and Experiment*," Am. J. Phys, 55,6, pp. 500– 503 (1987)

[164] T. M. Jack, S. W. Patterson, and D. G. Fearn, AIAA- 2000-3533, *36th AIAA/ASME/SAE/ASEE Joint Propulsion Conference and Exhibit*, Huntsville, AL, 2000

---

[165] Goebel D M, Jameson K, Katz I, Mikellides I G, "*Plasma Potential Behaviour and Plume Mode Transition in Hollow Cathode Discharges*", IEPC-2007-027, 39th International Electric Propulsion Conference, Florence, Italy, September, 2007

[166] Meezan B, Hargus W A, and Cappelli M A, "*Anomalous electron mobility in a coaxial Hall discharge plasma*", Physical Review E., Volume 63, 026410 (2001)

[167] Janes G C, and Lowder R S, "*Anomalous Electron Diffusion and Ion Acceleration in a Low-Density Plasma*", The Physics of Fluids, Vol. 9, No. 7 (1966)

[168] Sahli, A, Turchi P J, "*Low Power Plasma Thruster Based on a Hollow Cathode Discharge*", AIAA Paper No. 94-3126 (1994)

[169] Katz I and Patterson M J, "*Optimizing Plasma Contactors for Electrodynamic Tether Missions*," Tether Technology Interchange, Huntsville, AL, 1997

[170] Hill P G, and Peterson C R, "*Mechanics and Thermodynamics of Propulsion"* Addison-Wesley Publishing Company, 1965

[171] Turchi P J, "*Molecular Theory of Gas Flow"* Lecture Notes: The Ohio State University, 1996-97

[172] Patterson S W and Jugroot M, 'Discharge Initiation in the T6 Ion Thruster Hollow Cathode", A00-36720, AIAA Joint Propulsion Conference, Alabama, 2000

[173] Sutton G, "*Rocket Propulsion Elements*," 2d ed., John Wiley & Sons, Inc., New York, 1956

[174] Cohen-Zur A, Fruchtman A, Gany A, "*The Effect of Pressure on the Plume Divergence in the Hall Thruster*", IEEE transactions on plasma science, Vol. 36 (1), n^{o} 5, p.253, 2008

[175] Fruchtman A, "*The Plume in the Hall Thruster*", American Physical Society, 46th Annual Meeting of the Division of Plasma Physics, Savannah, GA, 2004

[176] Choueiri E, "*On the Thrust of Self-Field MPD Thrusters*" IEPC-97-121, International Electric Propulsion Conference, 1997

---

[177] Choueiri E Y, "*Scaling of Thrust in Self-Field Magnetoplasmadynamic Thrusters*," Journal of Propulsion and Power, Vol. 14, No. 5, pp. 744-753 (1998)

[178] Diamant K D, Choueiri E Y and Jahn R G, "*Spot mode transition and the anode fall of pulsed magnetoplasmadynamic thrusters*," Journal of Propulsion and Power, Vol. 14, No. 6, pp. 1036–1042 (1998)

[179] Choueiri, E Y, Kelly A J and Jahn R G, "*MPD thruster instabilities studies*," AIAA-87-1067, 19th International Electric Propulsion Conference, Colorado Springs, CO, 1987

[180] Kameyama I and Wilbur P. J, "Potential-hill model of high-energy ion production near high-current hollow cathodes," in *Proc. 21st Int. Symp. Space Technology Science*, ISTS-98-Aa-2-17, 1998

[181] Moore J, Davis C and Coplan M, "*Building Scientific Apparatus*", Perseus Books, 1991

[182] SenguptaA, "*The 30,000-Hour Extended-Life Test of the Deep Space 1 Flight Spare Ion Thruster, Final Report*," NASA/TP 2004-2 13391, 2004

[183] Hutchison, K G, 'Development of a Micro Hollow Cathode for use as a Ion Micro Propulsion Electron Source' PhD Thesis, University of Southampton, 2006

[184] Stockhausen G and Kock M 2001 *J. Phys. D: Appl. Phys.* 34 1683

[185] Katz I, Anderson J R, Polk J E, Brophy J R, "*A model of hollow cathode plasma chemistry*" AIAA-2002-4241, 2002

[186] Salhi A and Turchi PJ, AIAA Paper No. 92-3742, 1992

[187] Rudwan I FM, "*Physics of Hollow Cathode Breakdown and Steady-State Operation With Several Inert Propellants*", PhD Thesis, University of Southampton, 2003

[188] Song B, D'Angelo N and Merino, R L,"*On Anode Spots, Double Layers and Plasma Contactors*", Journal of Physics, Vol. 24, psg. 1789-1795, 1991

[189] Hershkowitz N, "*Review of Recent Laboratory Double Layer Experiments*" Space Science Reviews, Vol. 41, pp. 351-391, 1985

---

[190] Tighe K. Chien E, Solis P, Rebello D, Goebel D, and Snyder J, “Performance Evaluation of the XIPS Missions,” AIAA-2006-4666, 42nd AIAA/ASME/SAE/ASEE Joint Propulsion Conference and Exhibit Sacramento, California, July 9-12, 2006

[191] Loeb H W, Freisinger J, Groh K H, Scharmann A, “State-of-the-art of RIT-ion thrusters and their spin-offs” IAF International Astronautical Congress, 8-15 Oct. 1988. pp.17, 1988

[192] Collingwood C M, Gabriel S B, Corbett M H and Jameson P, “The MiDGIT Thruster: Development of a Multi-Mode Thruster”, In Proc. 31st Int. Electric Propulsion Conference, Ann Arbor, Michigan, September 20-24, 2009, IEPC-2009-171.

[193] Goebel D, et al., “Performance of XIPS Electric Propulsion in Station Keeping of the Boeing 702 Spacecraft”,AIAA-2002-5117, 38th Joint Propulsion Conference, Indianapolis, IN, 2002